The Electronic Structure of Vanadium Oxides as Catalysts in the Selective Oxidation of Small Alkanes

Christian Heine

Berlin 2014

The Electronic Structure of Vanadium Oxides as Catalysts in the Selective Oxidation of Small Alkanes

vorgelegt von
Dipl. Ing. Christian Heine
geboren in Wolfenbüttel

Von der Fakultät II - Mathematik und Naturwissenschaften
der Technischen Universität Berlin
zur Erlangung des akademischen Grades

Doktor der Naturwissenschaften
Dr. rer. nat.

genehmigte Dissertation

Promotionsauschuss:

Vorsitzender: Prof. Dr. Reinhard Schomäcker
Berichter/Gutachter: Prof. Dr. Robert Schlögl
Berichter/Gutachter: Prof. Dr. Peter Hildebrandt
Berichter/Gutachter: Prof. Dr. Thomas Risse

Tag der wissenschaftlichen Aussprache: 27.11.2014

Berlin 2014

The "paradox" is only a conflict between reality and your feeling of what reality "ought to be"

(Richard Feynman)

Acknowledgment

First and foremost, I want to thank Prof. Robert Schlögl who gave me the opportunity to write my PhD thesis at the Fritz-Haber-Institute of the Max-Planck-Society. It was a pleasure to work at the Fritz-Haber-Institute, also when I had to work until the night or things went wrong. When I came to the Institute in the morning, I always thought about the spirit, all the great scientist who worked here. It gave me a great inspiration and motivation. During my PhD, Prof. Schlögl gave me opportunity to follow my thoughts and ideas. However, he is always very critical which is in the end helpful to reflect the obtained results and conclusions.

I would like to particularly acknowledge the members of the doctoral board, Prof. Peter Hildebrandt and Prof. Thomas Risse for the review of the present work. Also gratitude goes to Prof. Reinhard Schomäcker for taking the chair of the examination board.

My special thanks go to my supervisor Dr. Maik Eichelbaum. We had a lot of fruitful discussions about microwave spectroscopy, (surface) chemistry/physics and science in general. He was always open minded for new ideas and supported me. Also, he gave me a good introduction in scientific writing.

I would like to particularly acknowledge Dr. Michael Hävecker for a lot of discussion about photoelectron spectroscopy , introduction in the photoelectron data analysis and the support at the ISISS beamline (synchrotron facility Bessy II), especially during the long time experiments with variable pressure near edge X-ray absorption setup. I want to thank Eugen Stotz together with Dr. Michael Hävecker for the planing and construction of the variable pressure near edge X-ray absorption setup.

Also great thanks go to my former group leader Dr. Annette Trunschke for the introduction in selective alkane oxidation catalysis. During my time in her group, I especially expanded my knowledge about catalyst synthesis. In this context, I would like to thank Dr. Maricruz Sanchez-Sanchez for the preparation of the defined MoVNbTeO$_x$ M1-phase sample.

I would like to acknowledge my office neighbour Dr. Frank Girgsdies for the pleasant atmosphere in the office, discussions about chemistry and X-ray diffraction and for the analysis of the X-ray diffraction data.

I am very grateful to Prof. R. Stößer (Humboldt-Universität zu Berlin) for his very helpful advice regarding measurements with microwaves and the German Federal Ministry of Education and Research (BMBF) as part of the ReAlSelOx project, grant number 033R028B for the financial support.

Abstract

The present work considers vanadium oxides catalysts in the selective oxidation of small alkanes. The dynamics of their (surface) electronic structure modulated by the chemical potential of reaction gases were investigated regarding charge carrier dynamics, surface valence/conduction band structure and work function modifications.

The charge carrier dynamics were studied with the in situ microwave cavity perturbation technique allowing the determination of the catalyst conductivity in a contact free manner in a fixed bed reactor geometry. An evaluation program based on the transmission line theory was developed for precise conductivity determination. The validity of the evaluation methods was tested with the n-type semiconducting vanadium pentoxide in the oxidation of n-butane. In agreement with literature, the experiments revealed an n-type conductivity. The addition of n-butane in the reaction feed leads to an increased conductivity corresponding to the abundance of electronically active V^{4+} defect states (corresponding to oxygen vacancies) in the forbidden bandgap of vanadium pentoxide increasing the mobile electron density.

Based on results of the reference study, the selective propane oxidation catalyst $MoVNbTeO_x$ M1-phase was investigated in the selective oxidation of ethane, propane and n-butane. Also the impact of water in the propane feed, triggering the abundance of the industrially important key product acrylic acid, on the $MoVNbTeO_x$ M1-phase electronic structure was studied. The in situ microwave cavity perturbation studies at ambient pressure were complemented with near ambient pressure X-ray photoelectron and X-ray absorption spectroscopy investigations at 0.25 mbar to understand the charge transfer processes according to semiconductor physics. The conductivity of $MoVNbTeO_x$ M1-phase increased with increasing propane to oxygen ratio identifying $MoVNbTeO_x$ M1-phase as an n-type semiconductor. In the alkane (ethane, propane and n-butane) exchange experiment, the number of electrons transferred to $MoVNbTeO_x$ M1-phase increased from ethane, to propane and finally to n-butane oxidation resulting in an increased conductivity. The X-ray photoelectron spectroscopy reveals that the exchange of the alkane leads to a modulation of the V^{4+}/V^{5+} redox couple at the surface corresponding to shifts of the valence band edge and electron affinity. Thus the surface of $MoVNbTeO_x$ M1-phase, being in dynamic equilibrium with the bulk electronic structure, is modified by the compositions (corresponding to the chemical potential) of the gas phase. The bulk charge carrier density is triggered by the barrier height of the surface induced space charge layer resulting in a modified conductivity. In contrast the modulated electron affinity can be explained by a change of the surface dipole.

Water in propane feed leads to a decreased conductivity of $MoVNbTeO_x$ M1-phase without a modification of the space charge layer. A drastic change of the surface elemental composition, in particular the abundance of V^{5+}, is induced by water, observable in the valence band, core level and vanadium $L_{2,3}$-edges X-ray absorption spectra. The surface modifications were accompanied with a decreased electron affinity corresponding to a decreased surface dipole. The drastically changed valence and conduction band structure likely affects the charge carrier mobility explaining the decreased conductivity in steam containing propane feed.

However, results from low pressure in situ photoelectron studies are debated according to their relevance for "real" catalysis at ambient pressures. In particular the oxygen pressure controls the oxidation state of transition metal oxide surfaces. The vanadium $L_{2,3}$ X-ray absorption edges of vanadyl pyrophosphate were investigated in the selective n-butane oxidation at 10, 100 and 1000 mbar to identify a possible pressure gap using the surface sensitive conversion electron mode. As a result, at low pressures the oxidation of the surface is controlled by the oxygen pressure. In contrast at higher pressures, the surface state of oxidation is triggered by the catalytic reaction providing a steady state between reduction of the catalyst during n-butane conversion and re-oxidation by molecular oxygen.

Zusammenfassung

Die vorliegende Arbeit befasst sich mit Vanadiumoxiden in der Selektivoxidation kleiner Alkane. Änderungen der elektronischen (Oberflächen-) Struktur, induziert durch das chemische Potential des umgebenden Reaktionsgases, wurden hinsichtlich der Ladungsträgerdynamik, der Valenz/ Leitungsbandstruktur und Austrittsarbeitsänderungen untersucht. Die Ladungsträgerdynamik wurde kontaktfrei mit Hilfe der Mikrowellen-Resonator-Störungs- Methode unter Verwendung einer Festbettreaktorgeometrie untersucht. Für eine präzise Bestimmung der Leitfähigkeit wurde ein Auswertungsprogramm geschrieben, das auf der Leitungstheorie beruht. Um das Auswertungsprogramm zu validieren, wurde das n-halbleitendende Vanadium(V)-oxid in der n-Butan-Oxidation vermessen. Wie in der Literatur beschrieben, zeigte sich in den Experimenten eine n-Halbleitfähigkeit. Durch die Zugabe von n-Butan zum Reaktionsgemisch erhöhte sich die Leitfähigkeit des Vanadium(V)-oxids. Die Leitfähigkeitserhöhung korreliert mit der Erzeugung elektronisch aktiver V^{4+} Defektzustände in der Bandlücke des Oxids, die mit Reduktion des Vanadium(V)-oxids und somit mit der Erzeugung von Sauerstofffehlstellen verbunden sind. Die Reduktion führt dadurch zu einer Erhöhung der mobilen Elektronenkonzentration. Gemäß der beschriebenen Vergleichsstudie wurde der Selektivoxidationskatalysator $MoVNbTeO_x$ M1-Phase in der Ethan-, Propan- und n-Butan-Oxidation untersucht. Zudem wurde der Einfluss von Wasserdampf, der die Acrylsäureproduktion steigert, auf die elektronische Struktur des Oxids studiert. Hierzu wurden neben der Mikrowellen-Resonator-Störungs-Methode, Hoch- druckröntgenphotoelektronenspektroskopie und Röntgenabsorptionsspektroskopie bei 0.25 mbar verwendet, um den Ladungstransport halbleiterphysikalisch beschreiben zu können. Die $MoVNbTeO_x$ M1-Phase ist ein n-Halbleiter, da ihre Leitfähigkeit mit zunehmendem Propangehalt im Reaktionsgemisch steigt. Durch Austausch des Alkans im Reaktionsgemisch, beginnend von Ethan über Propan zu n-Butan, erhöht sich die Anzahl der vom Alkan auf das Oxid übertragenen Elektronen, was wiederum in einer Erhöhung der Leitfähigkeit mündet. Die Hochdruckröntgenphotoelektronenstudie zeigte, dass der Austausch des Alkans in Reaktionsgemisch mit der Änderung des V^{4+}/V^{5+} Verhältnisses an der Oberfläche verbunden ist, das wiederum mit einer Energiepositionsänderung der Valenzbandkante und Elektronenaffinitätsänderung korreliert. Die durch das Reaktionsgemisch modifizierte Oberfläche der $MoVNbTeO_x$ M1-Phase ist in einem dynamischen Gleichgewicht mit ihrer Volumenstruktur. Die Volumenladungsträgerkonzentration ist durch die Barriere der oberflächennahen Raumladungszone gesteuert, was wiederum eine Änderung der Leitfähigkeit bewirkt. Die Elektronenaffinitätsänderung ist hingegen durch eine Modifizierung des Oberflächendipols zu erklären. Wasserdampf im Propanreaktionsgemisch senkt die Leitfähigkeit der $MoVNbTeO_x$ M1-Phase ohne die Raumladungszone zu verändern. Die chemische Zusammensetzung der Oberflächen wird durch die Zugabe von Wasser zum Reaktionsgemisch drastisch umgebaut, was sich im Besonderen in die Erhöhung der V^{5+} Konzentration äußert. Diesen Sachverhalt zeigten die Valenzband-, Rumpfniveau- und Vanadium $L_{2,3}$ Röntgenabsorptionsspektren. Die drastische Änderung der chemischen Zusammensetzung äußerte sich in einer Erniedrigung der Elektronenaffinität und somit einem geänderter Oberflächendipol. Eine wahrscheinliche Erklärung für die Senkung der Leitfähigkeit unter wasserhaltigen Reaktionsbedingungen kann die Modifizierung der Valenzbandstruktur gegeben sein, da die Krümmung der Energiebänder mit der effektiven Masse der Ladungs- träger verknüpft ist, die in die Leitfähigkeit eines Feststoffes eingeht. Die Ergebnisse, die unter Niederdruckbedingungen gewonnen wurden, müssen allerdings kritisch betrachtet werden, da sich das chemische Potential der Gasphase zu realkatalytischen Bedingungen, auf Grund des Druckunterschieds, unterscheidet. Um eine mögliche Druckabhängigkeit des Oxidationszustands eines Oxidationskatalysators zu verfolgen, wurden die Vanadium $L_{2,3}$ Röntgenabsorptionskanten von Vanadyl Pyrophosphat bei 10, 100 und 1000 mbar im oberflächensensitiven Elektronen Modus untersucht. Bei niedrigen Drücken wird der Oxidationszustand des Vanadyl Pyrophosphats durch den Sauerstoffgesamtdruck bestimmt. Im Gegensatz dazu, steuert die katalytische Reaktion durch die Reduktion des Katalysators auf Grund der n-Butan-Oxidation und seiner Reoxidation durch molekularen Sauerstoff den Oxidationszustand unter Normaldruckbedingungen.

List of Figures

Contents

1 Introduction

1.1 Selective Oxidation Catalysis

Selective oxidation of light alkanes (methane, ethane, propane and butanes) to olefines or oxygenates becomes increasingly important in chemical industry due to the scarcity of crude oil resources and the corresponding energy price increase [22]. Olefines and oxygenates are key intermediates to manufacture polymers, surfactants or pharmaceuticals. For instance, acrylic acid is industrially produced by a two step process with a yield of up to 80 % (global production of 4.7 million tonnes (2012)) [22]. In the first step, propylene is oxidized to acrolein followed by its oxidation to acrylic acid. Propylene is manufactured by steam cracking of the naphtha cruide oil fraction. For the highly energy-consuming steam cracking process, temperatures up to 850°C are needed. Propylene is also commercially used in epoxidation [22, 24, 25, 9]. However, technical realization of direct alkane oxidation is limited due to insufficient selectivity and conversion [23, 22, 8]. Only the selective oxidation of n-butane to maleic anhydride over a vanadyl pyrophosphate is industrially used providing typically selectivities of about 70% and conversions of 80%-85% [98, 28, 196, 103, 78]. The global production was 1.78 million tonnes in 2012 [1].

Development of efficient partial alkane oxidation catalysts is sophisticated because neither the reaction mechanism occurring at the catalyst surface nor the active sites on the active surface are unambiguously identified for any selective oxidation reaction. The geometric structure and its corresponding electronic structure of catalyst surface providing the active site are the subject of current research and scientific discussion.

It is generally believed that lattice oxygen of the transition metal oxide catalyst are involved in the oxidation reaction [167, 28]. The participation of lattice oxygen is associated with the so called Mars and van Krevelen reaction mechanism [144]. Mars and van Krevelen studied the oxidation of aromates as a function of the reactant partial pressure on promoted vanadium pentoxide. They assumed the reduction (removal of lattice oxygen) of the catalyst by aromates to form oxygenates followed by the reoxidation of the catalyst by molecular oxygen to obtain a macroscopic kinetic rate law.

During the Mars and van Krevelen redox cycle, a charge transfer between the catalyst and the gas phase reactants takes place. The reduction of the catalyst is associated with an electron transfer from the reducing agent to the catalyst. In the re-oxidation step, electrons are consumed to create metal oxygen bonds.

If free charge carriers participate in the catalytic reaction, the charge transfer between the reactant and the catalyst affects the conductivity of the catalyst. Herrmann et al. used the general concept of the Mars and van Krevelen reaction mechanism to explain the conductivity response of the vanadyl pyrophosphate (VPP) catalyst in the selective oxidation of n-butane to maleic anhydride [96, 95, 94].

$$\mathsf{C_4H_{10} + 7\ O_O^x + 14h^{\cdot} \rightarrow C_4H_2O_3 + 7\ V_O^{\cdot\cdot} + 4\ H_2O} \qquad \text{(reduction of VPP)} \tag{1.1}$$

$$\mathsf{3.5\ O_2 + 7\ V_O^{\cdot\cdot} \rightarrow 7\ O_O^x + 14h^{\cdot}} \qquad \text{(reoxidation of VPP)} \tag{1.2}$$

An n-butane molecule removes 7 lattice oxygen atoms $\mathsf{O_O^x}$ (formation of 7 oxygen vacancies $\mathsf{V_O^{\cdot\cdot}}$) and 14 electron holes $\mathsf{h^{\cdot}}$ from VPP to form maleic anhydride and 4 water molecules (equation 1.1). Molecular oxygen re-oxidizes the reduced surface and electron holes are created (equation 1.2) which is considered to be the rate determining reaction step [150]. It is assumed that vanadium undergoes a V^{4+}/V^{5+} redox cycle during the catalytic oxidation of n-butane. In terms of the V^{4+}/V^{5+} redox couple, the reduction or oxidation can be expressed in the following way:

$$\mathsf{V^{5+} \rightarrow V^{4+} + h^{\cdot}} \quad \text{(reduction of VPP)} \tag{1.3}$$

$$\mathsf{V^{4+} + h^{\cdot} \rightharpoonup V^{5+}} \quad \text{(oxidation of VPP)} \tag{1.4}$$

Herrmann et al. observed a decreasing/increasing conductivity in pure n-butane/oxygen atmosphere. In reaction atmosphere (oxygen+n-butane), the conductivity reached an intermediate level. According to the conductivity considering equation 1.1/1.3 and 1.2/1.4, electron holes are the majority charge carriers identifying vanadyl pyrophosphate as a p-type semiconductor. Herrmann et al. used the simplified semiconductor model to describe the redox reaction occurring at the catalyst surface triggering the Fermi level of vanadyl pyrophosphate. According to the described concept conductivity studies were performed for other oxidation catalysts, too, for instance, with $MoVNbTeO_x$ M2-phase in the selective oxidation of propylene to acrylic acid. $MoVNbTeO_x$ M2 was identified as n-type semiconductor [20].

Morrison [150], Schwab [170], Boudart [18] and Volkenshtein [195] assumed a more detailed picture of oxidation catalysis according to semiconductor concepts. In most cases, the geometric and electronic structure of a surface differs from the solid bulk structure. In case of vanadyl pyrophoshate the surface is substantially more oxidized than the bulk indicated by the abundance of V^{5+} species which are discussed to be essential for alkane activation (bulk vanadium oxidation state 4+) at the surface [51, 52]. A V^{5+} site is a defect site in general assigned to be a part of the active site in oxidation catalysis accepting electrons or donating electron holes [161]. Surface states corresponding to surfaces species are located, in general, in the forbidden bandgap of semiconductors. In order to achieve charge neutrality, bulk electrons diffuse in unoccupied (in vanadyl pyrophospate V^{5+}) states below the bulk Fermi level, achieving thermodynamic equilibrium at the surfaces [181, 137]. Details of the concept will be explained in the theory chapter. The bulk Fermi level is pinned between unoccupied and occupied surface states. The charge compensation generates an electric field in the so called space charge layer corresponding to a surface barrier. In case of vanadyl pyrophosphate, it can be assumed that the bulk Fermi level is pinned with respect to the V^{4+}/V^{5+} redox couple, where V^{4+} would be the occupied and V^{5+} the unoccupied surface state. Considering the above mentioned participation of lattice oxygen in the catalytic reaction, the redox couple and therefore the equilibrium between bulk and surfaces is modified by the gas phase reactants and products. These considerations agree with the concept of a catalytically active surface layer which is only formed under reaction conditions [167]. Regarding the conductivity response observed by Herrmann et al., in oxygen/n-butane atmosphere a gas phase dependent V^{5+}/V^{4+} ratio is induced modifying the surface barrier and therefore the distance between the Fermi level and the band edges. The bulk Fermi statistics and therefore the number of majority charge carriers is changed by the gas phase reactants resulting in an increased (oxygen atmosphere) or decreased (n-butane atmosphere) conductivity. The described concept is widely used in gas senor technology [198] and provides a (quantitative) understanding of the dynamics between the reactants/products in the gas phase, the molecular active site at the catalyst surface and its bulk electronic structure.

1.2 Selective Propane Oxidation to Acrylic Acid catalyzed by the MoVNbTeO$_x$ M1-Phase

The selective oxidation of propane to acrylic acid (AA) will be discussed according to the reaction network obtained from data on a phase pure MoVNbTeO$_x$ M1-phase catalyst [153]. Details about its geometric structure will be given in section 1.4. The proposed reaction network is depicted in figure 1.1. The AA formation proceeds via the oxidative dehydrogenation of propane (ODP) to propylene. The ODP is considered to be induced by the hydrogen abstraction from a methyl or methylene group by a vanadyl (O=V^{5+}) group forming a propyl radical bonded to a HO-V^{4+} group [161]. Thus V^{5+} is needed for the activation of the propane molecule. The second hydrogen abstraction from the alkoxy species or an isopropyl radical in the gas phase leads to the formation of propylene [161]. Alternative pathways are discussed as well [161]. It is an experimental fact, that propylene is the main product for short contact times and low propane conversion [153]. The consecutive oxidation of propylene to AA is supposed to occur at a different active site than the ODP requiring nucleophilic oxygen to accept hydrogen [161, 167]. In contrast, for the oxygen transfer to the propylene molecule an electrophilic oyxgen species is desired with a weaker metal center to oxygen interaction. The bridging oxygen between two edge linked pyramids [VO_5] in the $MoVNbTeO_x$ M1-phase structure is discussed in literature to fulfill these requirements [167]. Acetic acid formation starts only at maximum acrylic acid selectivity and therefore it was concluded that it is formed by oxidative degradation of acrylic acid [153]. Hence, this step could be also the main source for carbon monoxide and carbon dioxide formation. $MoVNbTeO_x$ M1-phase does not oxidize carbon monoxide to carbon dioxide. Therefore it was concluded that carbon monoxide is no carbon dioxide source. As deduced from the selectivity analysis, it was concluded that carbon monoxide also directly occurs due to the oxidation of the alkoxy species in contrast to carbon dioxide which is exclusively a secondary product.

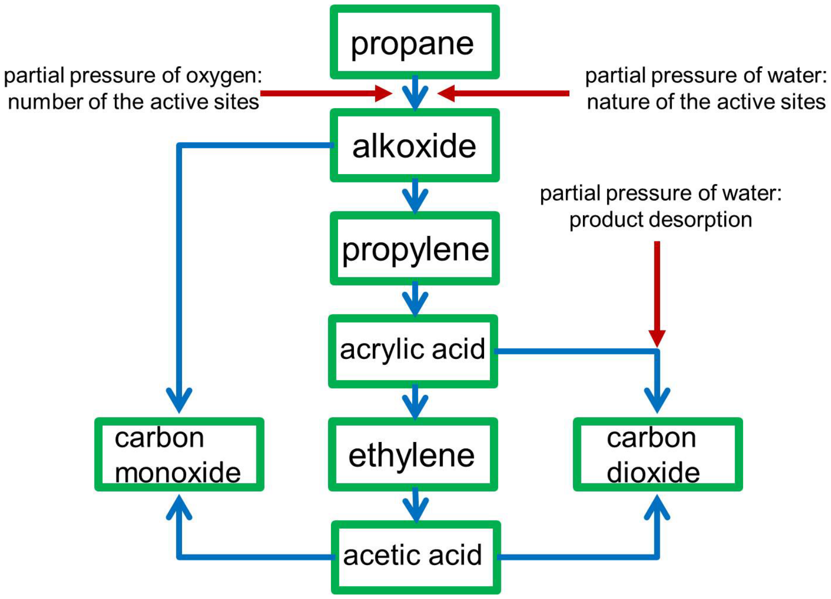

Figure 1.1: *Proposed reaction network from the AA formation catalyzed by the M1 phase (adapted from [153])*

A increasing amount of oxygen in the reaction feed increases the propane conversion but only hardly influences the selectivity to AA. According to these results, it was concluded that oxygen partial pressure modifies the number of active sites.

In contrast, steam in the reaction feed benefits the production of AA and decreases the apparent activation energy for the reaction on the $MoVNbTeO_x$ M1-phase. Additionally it is stated in literature that water blocks unselective catalytic sites by adsorption [13]. It is known from near ambient pressure X-ray photoelectron spectroscopy studies that steam in the reaction feed has a crucial impact on the $MoVNbTeO_x$ M1-phase surface composition [26, 87, 153]. The vanadium concentration (in particular the V^{5+}) concentration and the tellurium concentration is increased in steam containing feed while molybdenum is depleted. Therefore vanadium and tellurium are assumed to play an essential role in the active site for AA formation [167]. The surface modification induced by steam is mainly limited to the topmost layer of the surface [26, 87, 153]. In general, the $MoVNbTeO_x$ M1-phase surface is more oxidized than the bulk [26, 87, 153]. For instance, molybdenum is only found in the oxidation state 6+ while in the bulk a ratio of Mo^{5+} and Mo^{6+} is needed to form the crystal structure (see section 1.4). The bulk phase is not affected by reactions and transformations occurring at the surface proven by in situ X-ray powder diffraction [153].

1.3 Selective n-Butane Oxidation to Maleic Anhydride Catalyzed by Vanadyl Pryrophosphate VPP

Phase pure VPP is a highly active and selective and commercially used catalyst for the oxidation of n-butane to maleic anhydride [52, 51, 27]. In general, the structure of the catalytically active surface and the reaction mechanism of the maleic anhydride formation are still controversially discussed in literature [8]. The following statements about proposed reaction mechanisms, which proceed via an olefinic or alkoxide pathway, are assumed to occur at the bulk (100) basal plane of VPP. The bulk crystal structure will be described in section 1.4. The mechanisms involving an olefin (butene) was obtained from Temporal Analysis of Products (TAP) experiments [28, 16, 3]. According to the TAP experiments, n-butane is converted into maleic anhydride by the pathway of butenes, butadienes and furan as reaction intermediates. However, the experimental conditions (feed composition, temperature, total pressure etc.) are far from the industrially used state of operation [29]. According to section 1.2, the experimental conditions influence the product composition. Thus the intermediates formed in the TAP experiments have not necessarily to be formed under industrially applied reaction conditions.

In the proposed alkoxide route, activated n-butane (after cleavage of a C-H bond) forms a chelating configuration at a vanadium ion species on the surface via the coordination of methyl group carbon of butane. Afterwards the complete oxidation of n-butane to maleic anhydride shall take place at these vanadium site maintaining the chelating configuration [29].

Often a V^{5+}/V^{4+} redox couple is associated with the oxidation of n-butane to maleic anhydride involving lattice oxygen (of the catalyst) and/or activated oxygen [28]. V^{4+} sites are assumed to adsorb/activate n-butane. In contrast, phosphorous or in particular P-OH Bronsted acidic sites are considered to stabilize reaction intermediates or trigger the desorption of the product MA [98, 28, 196, 27, 155]. Moreover, it was also proposed that the alkane activation occurs directly at phosphates [33].
However, it could be shown with near ambient pressure photoelectron spectroscopy and X-ray absorption spectroscopy that the surface composition of VPP differs from the bulk and behaves dynamically depending on the reaction feed composition and temperature similar to the $MoVNbTeO_x$ M1-phase [122, 85, 14, 82, 114, 52, 51]. The average vanadium oxidation state at the VPP surface in reaction feed (n-butane/oxygen, 400°C) is significantly higher (+4.3) than in the bulk (+4.0) [52, 51]. Also the surface V/P/O ratio is different (1/1.5/6) in comparison to the bulk ratio of 1/1/4.5. A depth profile of the vanadium oxidation state indicates that only the topmost surface (within 1 nm) interacts with the gas atmosphere at 0.5 mbar, while the bulk phase remains intact which is in agreement with kinetic studies suggesting that only the surface layer(s) can exchange oxygen with the gas phase [155].

1.4 Bulk Crystal Structure of the Catalysts under Investigation

The crystal structure of vanadium pentoxide V_2O_5 provides the elementary coordination of vanadium in all catalysts under investigation. Based on the considerations for V_2O_5, the bulk crystal structure of vanadyl pyrophosphate $(VO)_2P_2O_7$ and the mixed metal oxide $MoVNbTeO_x$ M1 phase will be described. The bulk crystal structure of the catalysts provides the coordination and oxidation state of metal centers and acts therefore as a starting point to analyze the X-ray absorption and photoelectron spectra of the catalyst surfaces.
In figure 1.2a the orthorhombic cell (a= 11.512(3)Å, b= 3.564(1)Å, c= 4.368(1)Å, cell volume = 179.2(1) $Å^3$, crystal density = 3.4 g/cm^3) of V_2O_5 is shown [54]. Vanadium is in the oxidation state 5+ according to the chemical formula. V_2O_5 is a layer structure which is built of distorted square $[VO_5]$ pyramids sharing edges and corners. Vanadium is octahedrally coordinated by oxygen, forming a vanadyl bond perpendicular to the (001) plane, four single V-O bond in the (001) plane and a long V-O bonds to the next layer. Two distorted square $[VO_5]$ pyramids sharing edges (double pyramid) are oppositely orientated (mirror-inverted) resulting from the V^{5+}-V^{5+} repulsive interaction. Vanadium is displaced towards the oxygen of the vanadyl bond and in the opposite direction of the

oxygen atoms bridging the vanadium atoms of the pyramids (perpendicular to the vanadyl bond). The double pyramids form zigzag chains in the (001)-plane.
$(VO)_2P_2O_7$ shown in figure 1.2b crystallizes also in a orthorhombic unit cell (a = 7.7285(3)Å, b = 9.5842(4)Å, c = 16.5962(6) Å, cell volume = 1222.99(11)Å^3, crystal density = 3.3 g/cm^3) [69]. According to the chemical formula, vanadium is in the oxidation state 4+ and phosphorus in the oxidation state 5+. The $[VO_5]$ double pyramid structure is also present in $(VO)_2P_2O_7$. However, the distortion of the vanadium atom is less pronounced in comparison to V_2O_5. The double pyramids are bridged by tilted and untilted $[PO_4]$ tetrahedra and therefore separated from each other. Two (100) planes are linked by pyrophosphate groups.

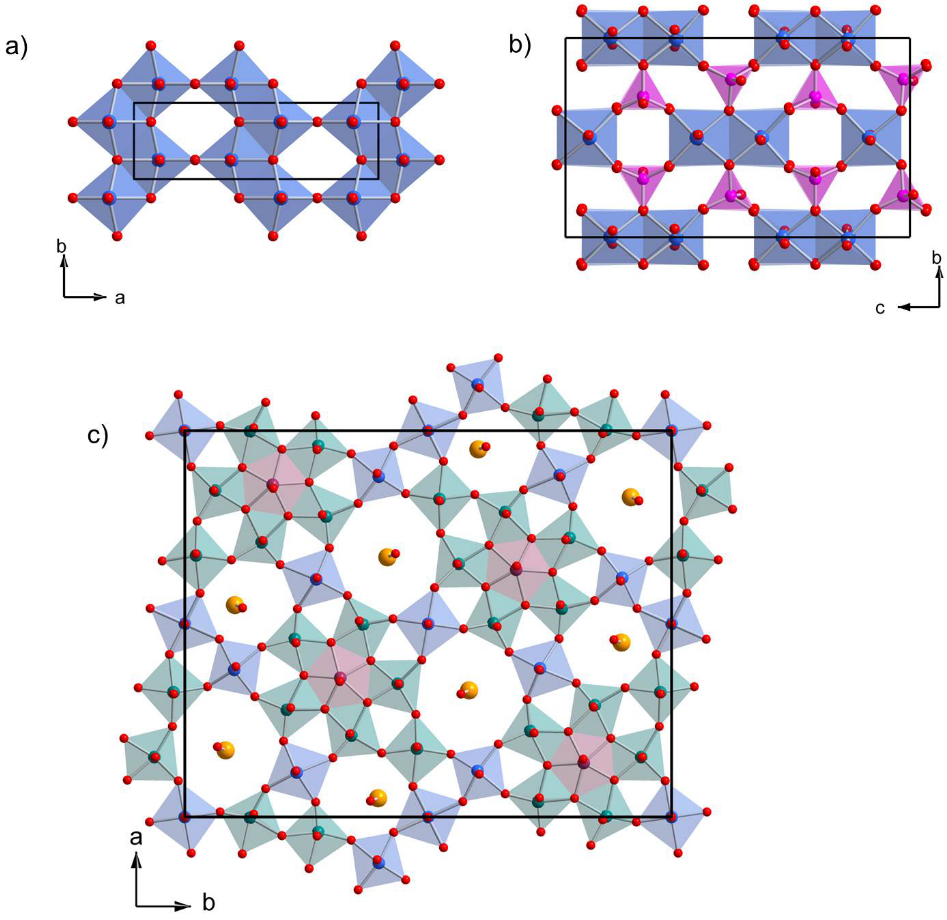

Figure 1.2: *Crystallographic unit cells of a) V_2O_5 ((001)-plane) b) $(VO)_2P_2O_7$ ((100)-plane) and c) $MoVNbTeO_x$M1-phase ((001)-plane): vanadium (blue), molybdenum (green), tellurium (yellow), oxygen (red), phosphorous (violet) and niobium (dark red)*

The $MoVNbTeO_x$ M1 phase bulk crystal structure is very complex. Similar to both above described oxides, M1 crystallizes in an orthorhombic unit cell (a = 21.134(2)Å, b = 26.658(2)Å, c = 4.0147(3)Å, cell volume = 2261,89(78) Å^3, crystal density = 4.4 g/cm^3) [46, 45]. The basal (001) plane is shown in figure 1.2c. The pentagonal bipyramids (dark red) mainly with niobium as centers are the main building blocks of the M1 structure [165]. Niobium is therefore coordinated by 7 oxygen atoms and its oxidation state is 5+ [152]. The pentagonal bipyramids are sharing edges with distorted square pyramids (green) occupied by molybdenum. Regarding charge neutrality, molybdenum is in the oxidation state 5+ and 6+ [46, 45, 152]. These pentagonal structural motifs are corner linked by distorted square pyramids (blue) occupied by molybdenum or vanadium forming the six or seven membered ring structure of the M1 (001) basal plane. Vanadium/molybdenum is found in the oxidation state 4+/5+ and 5+/6+ at these sites [46, 45, 152]. The MoVNbTeO$_x$ M1 phase has a certain phase width [26]. Thus it is not clearly defined which of the blue square pyramids is occupied with molybdenum or vanadium [46, 45]. The heptagonal and hexagonal channel along the [001] direction are partially filled with tellurium (oxidation state 4+ [152]) oxide zigzag chains. (001) planes are linked by oxygen to the neighbored planes. In general tellurium and niobium are not needed to build the M1 crystal structure. Also MoV oxides can be synthesized crystallizing in the M1 structure [117].

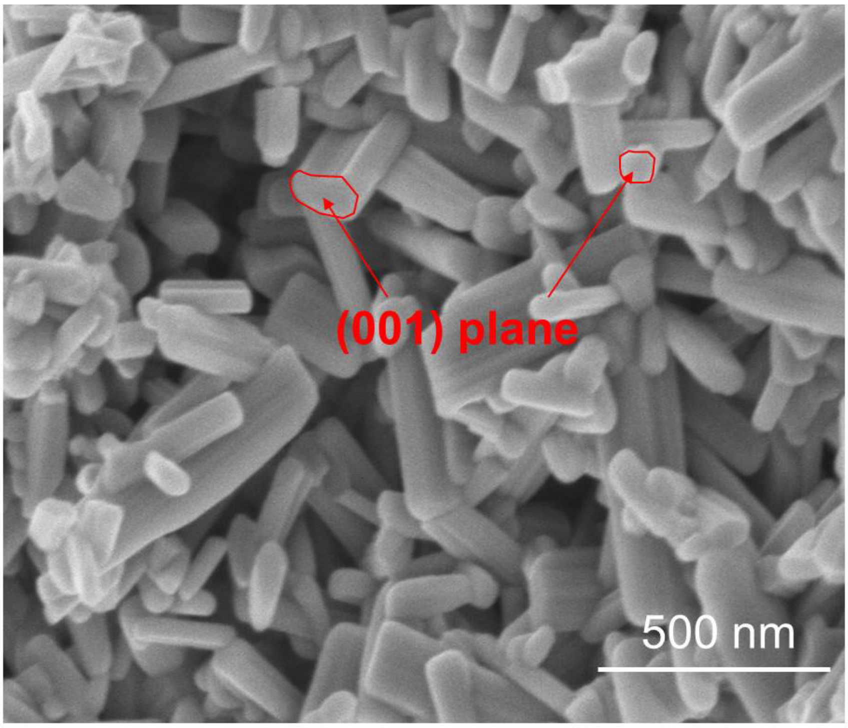

Figure 1.3: *Scanning electron microscope image of M1 needles (the image is provided by Gisela Weinberg, Fritz-Haber-Institut der Max Planck Gesellschaft)*

The morphology of the MoVNbTeO$_x$ M1 phase particles is strongly related to the bulk crystal structure. M1 forms needles along the [001] direction as seen in figure 1.3. Thus the (001) plane is also the basal plane of the needles.

1.5 Objectives and Outline of the work

In the present work, the dynamics of the catalysts electronic structure was investigated under reaction conditions in order to check if the working mode of oxidation catalysts can be described within the semiconductor concepts introduced in section 1.1. The goal was to study the influence of the reactive gas phase on the Fermi level, surface barrier, work function, electron affinity, metal oxidation states and charge carrier density (conductivity) for the unselective catalyst V_2O_5, and the selective catalysts MoVTeNbOx M1-phase and vanadyl pyrophosphate under catalytically relevant reaction conditions with proven formation of selective and unselective oxidation products. These studies should prove if the catalysts can be described in general as semiconductors with charge transfer between bulk and surface. Furthermore, the relevance of this working mode for the catalytic properties is to be identified. The applied methods were the in situ microwave cavity perturbation technique, near ambient pressure X-ray photoelectron spectroscopy and X-ray absorption spectroscopy.

In contrast to generally used DC conductivity measurements to monitor the gas phase response of transition metal oxides, the conductivity can be measured by the microwave perturbation technique in a contact free manner avoid contact artifacts [176, 32].

Near ambient pressure X-ray photoelectron spectroscopy is applied to monitor modifications of the surface barrier induced by the reaction atmosphere. In this manner, the photoelectron spectroscopy investigations were focused on the valence band region and work function measurements complemented by core level spectra to identify chemical modifications.

Near ambient pressure X-ray photoelectron spectroscopy is limited to the mbar range. At the low pressure conditions the chemical potential of the gas phase significantly differs from ambient pressure conditions. In particular, the oxygen pressure is a crucial factor influencing the surface termination of transition metal oxides [159]. Thereby, the significance of results obtained at low pressure for real catalysis is debatable. To bridge the pressure gap, a new X-ray absorption setup was introduced monitoring the pressure dependency of catalysts under reaction conditions up to 1 bar. The X-ray absorption data were obtained in the surface sensitive conversion electron yield mode to investigate modifications of surface terminations.

The catalysts introduced in section1.4 were investigated. The binary transition metal oxide V_2O_5 was used as a reference material.

$MoVNbTeO_x$ M1-phase is active in ethane [17, 22], propane [149, 152, 74, 26, 190](as mentioned in section 1.2) and n-butane selective oxidation [22].

Vanadyl phyrophosphate is industrially used in the n-butane oxidation to maleic anhydride

[98, 28, 196, 103, 78, 27].

The present work is divided in 4 chapters. In the theory chapter, the general physical concepts of microwave cavities and waveguides, the interaction of light and matter and semiconductor surfaces will be described. The introduced physical theories will be applied to photoelectron spectroscopy, X-ray absorption spectroscopy and the microwave perturbation method in the experimental chapter. The 4 sections of the result chapter are partially adapted from publications. The result chapter is arranged as followed:

Section 4.1 **The model oxidation catalyst α-V_2O_5: Insights from contactless in situ microwave permittivity and conductivity measurements** The section is adapted from the publication *"Christian Heine, Frank Girgsdies, Annette Trunschke, Robert Schlögl, Maik Eichelbaum; The model oxidation catalyst α-V_2O_5: Insights from contactless in situ microwave permittivity and conductivity measurements; Applied Physics A (Springer-Verlag Berlin Heidelberg 2013); 112; 289 - 296, August 2013; doi: 10.1007/ s00339-013-7800-6"* including the subsections abstract (4.11), introduction (4.12), experimental methods (4.13), results and discussion (4.14) and conclusions (4.15).

The microwave conductivity response of the semiconducting V_2O_5 was investigated depending on the applied reaction gas atmosphere (reducing or oxidizing conditions). The conductivity type of V_2O_5 was determined and compared with literature to verify the origin of the microwave response. In situ X-ray powder diffraction was used to exclude a possible phase transformation modifying the dielectric properties of the sample. Additionally the abundance of vanadium V-d^1 states was probed with in situ UV/VIS spectroscopy and compared with the microwave response to find a possible correlation between the V^{4+}/V^{5+} redox couple according to the statements in section 1.1.

Section 4.16 and 4.17 describes the theory and application of a fit-model to analyze the obtained microwave resonance curves.

Section 4.2 **Work Function, Band Bending and Microwave Conductivity Studies on the Selective Alkane Oxidation Catalyst MoVTeNb Oxide (Orthorhombic M1 Phase) under Operation Conditions** The section is adapted from the publication *"Christian Heine, Michael Hävecker, Maricruz Sanchez-Sanchez, Annette Trunschke, Robert Schlögl and Maik Eichelbaum; Work Function, Band Bending and Microwave Conductivity Studies on the Selective Alkane Oxidation Catalyst MoVTeNb Oxide (Orthorhombic M1 Phase) under Operation Conditions; Journal of Physical Chemistry C(American Chemical Society) 117; 26988 - 26997; December 2013; doi: 10.1021/jp409601h"*

The microwave conductivity of $MoVTeNbO_x$ M1 phase was probed depending of the propane feed composition and alkane (ethane, propane and n-butane) in a reaction feed with constant alkane to oxygen ratio. The valence band, core level and work function were investigated with near ambient pressure X-ray photoelectron spectroscopy under reaction conditions similar to the alkane variation microwave study. The obtained data were interpreted in terms of the semiconductor model introduced in section 1.1.

Section 4.3 **The Impact of Water on the Electronic Structure of the Selective Propane Oxidation Catalyst MoVTeNb Oxide (Orthorhombic M1 Phase)** The section is dedicated to the influence of water in the propane feed, increasing the selectivity to acrylic acid (see section 1.2), on the electronic structure of $MoVTeNbO_x$ M1 phase. It is also a combined microwave conductivity and near ambient pressure photoelectron study focused on the valence band structure. In particular, the section is focused on the redox active element vanadium. The abundance of vanadium states in the valence band was probed with resonant photoelectron spectroscopy. Possible coordination modifications of vanadium due to water content in the propane feed were investigated with X-ray absorption spectroscopy.

Section 4.4 **Ambient-Pressure Soft X-Ray Absorption Spectroscopy of a Catalyst Surface in Action: Closing the Pressure Gap in the Selective n-Butane Oxidation over Vanadyl Pyrophosphate** The section is adapted from the publication *"Christian Heine, Michael Hävecker, Eugen Stotz, Frank Rosowski, Axel Knop-Gericke, Annette Trunschke, Maik Eichelbaum and Robert Schlögl; Ambient-Pressure Soft X-Ray Absorption Spectroscopy of a Catalyst Surface in Action: Closing the Pressure Gap in the Selective n-Butane Oxidation over Vanadyl Pyrophosphate; Journal of Physical Chemistry C(American Chemical Society) 118; 20405 - 20412; August 2014; doi:0.1021 /jp506068x "* In this section the vanadium $L_{2,3}$ X-ray absorption edges of vanadyl pyrophosphate were investigated in the n-butane oxidation at different total pressures. Closing the pressure gap between low pressure experiments and real catalysis at ambient pressure was the aim of the work.

In Chapter 5 the final conclusions will be given.

2 Theory

2.1 Maxwell Equations

The Maxwell equations describe the distribution of electromagnetic waves in the limits of classical physics [59]. This set of equations can be expressed in a differential and integral form.

$$\nabla \cdot \mathbf{E} = \frac{\rho}{\varepsilon_0} \tag{2.1}$$

$$\nabla \times \mathbf{E} = -\frac{\partial \mathbf{B}}{\partial t} \tag{2.2}$$

$$\nabla \cdot \mathbf{B} = 0 \tag{2.3}$$

$$c^2 \nabla \times \mathbf{B} = \frac{\mathbf{j}}{\varepsilon_0} + \frac{\partial \mathbf{E}}{\partial t} \tag{2.4}$$

E is the electric field, **B** magnetic induction, **j** the current density, ρ the charge density, t the time, c the speed of light and ε_0 the vacuum permittivity. The differential expression can be transformed in the integral one with the Divergence (Gauss) theorem and Stokes' theorem.

$$\iiint\limits_{\mathbf{V}} \nabla \cdot \mathbf{A}\, d\mathbf{V} = \iint\limits_{\partial V} \mathbf{A}\, d\mathbf{O} \quad \text{(Divergence theorem)} \tag{2.5}$$

$$\iint\limits_{\mathbf{O}} \nabla \times \mathbf{A}\, d\mathbf{O} = \int_{\partial O} \mathbf{A}\, d\mathbf{S} \quad \text{(Stokes theorem)} \tag{2.6}$$

The Gauss theorem states that the sum over all sources and sinks (described by the divergence) of a vector field **A** in a volume **V** with a volume element $d\mathbf{V}$ equals the flux through its surface (boundary of the volume ∂V) with the surface element $d\mathbf{S}$. The Stokes theorem relates the surface **O** integral of the curl of a vector field with the line integral around the surface (boundary of the surface ∂O). Using the Gauss theorem for equation 2.1, 2.3 and the Stokes theorem for equation 2.3, 2.4 the Maxwell equations have the following form:

$$\oiint_{\partial \mathbf{V}} \mathbf{E}\, d\mathbf{O} = \iiint_{\mathbf{V}} \frac{\rho}{\varepsilon_0}\, d\mathbf{V} \tag{2.7}$$

$$\oint_{\partial \mathbf{F}} \mathbf{E}\, d\mathbf{S} = \iint_{\mathbf{F}} \frac{\partial \mathbf{B}}{\partial t}\, d\mathbf{O} \tag{2.8}$$

$$\oiint_{\partial \mathbf{V}} \mathbf{B}\, d\mathbf{O} = 0 \tag{2.9}$$

$$c^2 \oint_{\partial \mathbf{F}} \mathbf{B}\, d\mathbf{S} = \iint_{\mathbf{F}} \frac{\mathbf{j}}{\varepsilon_0} + \frac{\partial \mathbf{E}}{\partial t}\, d\mathbf{O} \tag{2.10}$$

According to the problem, the integral or differential form of the Maxwell equations can be used to find a solution. The shown equations can be interpreted in the following way:

Equation 2.1/2.7: The source and the sink of the electric field is the electric charge. Thus, the flux of an electric field through a closed surface is proportional to the electric charge in its volume.

Equation 2.2/2.8: The time derivative of the magnetic induction induces an electric vortex field. Hence, a time varying flux of the magnetic induction through a surface induces an electric field at its boundary and vice versa. This equation is the Faraday law of induction.

Equation 2.3/2.9: The magnetic field has no sources or sinks. Therefore, the flux of the magnetic induction through a closed surface vanishes. No magnetic monopoles exists in the limits of classical physics.

Equation 2.4/2.10: An electric current or a time varying electric field induces a magnetic vortex field. Thus, a flux of an electric current and/or a time varying electric field through a surface induces a magnetic induction at its boundary and vice versa.

In matter the electric field is substituted by the electric displacement field **D** [60]. The following equations relate the electric field to the displacement field.

$$\mathbf{D} = \varepsilon_r \varepsilon_0\, \mathbf{E} = \varepsilon_0 \mathbf{E} + \mathbf{P} \tag{2.11}$$

$$\text{with } \mathbf{P} = \Sigma q\delta = \chi_e \varepsilon_0 \mathbf{E} \tag{2.12}$$

$$\text{and } \varepsilon_r = 1 + \chi_e \tag{2.13}$$

ε_r is the relative permittivity, **P** the polarization, representing the sum of all dipole moments $q\delta$ and χ_e the electric susceptibility. Sometimes, the Maxwell equation are expressed in terms of the magnetic field strength **H**. **H** is proportional to **B** and the proportional constants are the relative μ_r and vacuum μ_0 permeability.

$$\mathbf{B} = \mu_r \mu_0 \mathbf{H} \tag{2.14}$$

2.2 Wave Equation

The Wave equation results from solving the Maxwell equations [61, 62]. The curl of any vector field **A** solves equation 2.3 and is a proper solution for the magnetic induction.

$$\nabla \cdot (\nabla \times \mathbf{A}) = 0 \tag{2.15}$$

$$\Rightarrow \mathbf{B} = \nabla \times \mathbf{A} \tag{2.16}$$

Now the expression for the magnetic induction can be used in equation 2.2 to find a solution for the electric field.

$$\nabla \times \mathbf{E} = -\frac{\partial}{\partial t}(\nabla \times \mathbf{A}) \tag{2.17}$$

$$\Rightarrow \nabla \times \left(\mathbf{E} + \frac{\partial \mathbf{A}}{\partial t} \right) = 0 \tag{2.18}$$

The gradient of any scalar field ϕ solves equation 2.18 and gives the expression for the electric field because the curl of any gradient field vanishes.

$$\mathbf{E} + \frac{\partial \mathbf{A}}{\partial t} = -\nabla \phi \tag{2.19}$$

$$\Rightarrow \mathbf{E} = -\nabla \phi - \frac{\partial \mathbf{A}}{\partial t} \tag{2.20}$$

Now, the expressions for the magnetic induction and the electric field can be used in equation 2.1 and 2.4.

$$-\nabla^2 \phi - \frac{\partial \nabla \mathbf{A}}{\partial t} = \frac{\rho}{\varepsilon_0} \tag{2.21}$$

$$c^2 \nabla \times (\nabla \times \mathbf{A}) - \frac{\partial}{\partial t} \left(-\nabla \phi - \frac{\partial \mathbf{A}}{\partial t} \right) = \frac{j}{\varepsilon_0} \tag{2.22}$$

$$\text{with the algebraic identity} \quad \nabla \times (\nabla \times \mathbf{A}) = \nabla(\nabla \cdot \mathbf{A}) - \nabla^2 \mathbf{A} \tag{2.23}$$

$$c^2 \nabla (\nabla \cdot \mathbf{A}) - c^2 \nabla^2 \mathbf{A} + \frac{\partial}{\partial t} \nabla \phi + \frac{\partial^2 \mathbf{A}}{\partial t^2} = \frac{j}{\varepsilon_0} \tag{2.24}$$

The vector and scalar potential can be separated with the Lorenz gauge condition and the result is the wave equation in the vector and scalar notation.

$$\nabla \cdot \mathbf{A} = -\frac{1}{c^2}\frac{\partial \phi}{\partial t} \quad \text{(Lorenz gauge condition)} \tag{2.25}$$

$$\nabla^2 \mathbf{A} - \frac{1}{c^2}\frac{\partial^2 \mathbf{A}}{\partial t^2} = -\frac{j}{\varepsilon_0 c^2} \tag{2.26}$$

$$\nabla^2 \phi - \frac{1}{c^2}\frac{\partial^2 \phi}{\partial t^2} = -\frac{\rho}{\varepsilon_0} \tag{2.27}$$

The inhomogeneity in both differential equations (equation 2.26 and 2.27 are the source or sink of the electromagnetic wave. In free space these inhomogeneities vanish because there are no source or sink.

$$\nabla^2 \mathbf{A} - \frac{1}{c^2}\frac{\partial^2 \mathbf{A}}{\partial t^2} = 0 \tag{2.28}$$

$$\nabla^2 \phi - \frac{1}{c^2}\frac{\partial^2 \phi}{\partial t^2} = 0 \tag{2.29}$$

The wave equation can be written in a general form with a variable ψ. ψ can be the vector or scalar potential and therefore also the electric field or magnetic induction because both are related to the potentials.

$$\nabla^2 \psi - \frac{1}{c^2}\frac{\partial^2 \psi}{\partial t^2} = 0 \tag{2.30}$$

A general solution is the sum of a progressive f and returning g wave with a wave vector $\mathbf{k}$ times the position $\mathbf{r}$ describing the spatial distribution and a angular frequency ω times the time t.

$$\psi = f(\mathbf{k}\,\mathbf{r} - \omega t) + g(\mathbf{k}\,\mathbf{r} + \omega t) \tag{2.31}$$

In free space, planar waves are proper solutions, in the case of point source spherical waves can be used.

2.3 Physics of Microwave Cavities and Waveguides

2.3.1 Microwave Cavities

The operating mode of microwave cavities will be explained starting with a capacitor in an AC electric circuit [58], as shown in figure 2.1. The amplitude of the electric field is spatially constant in the limit of AC voltage U with small angular frequency ω.

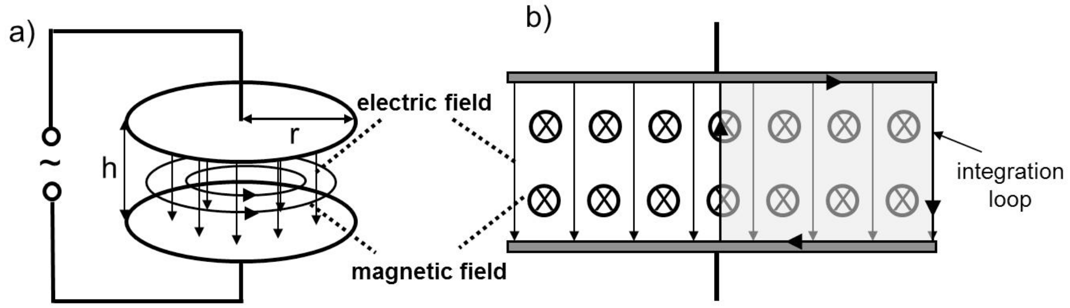

Figure 2.1: *AC electric circuit with a capacitor (similar to [58]): a) AC electric circuit and the capacitor geometry; b) capacitor (side view) with marked integration loop*

$$\mathbf{E}_1 = \mathbf{E_0} exp\{i\omega t\} \quad (\mathbf{E_0} : \text{constant}) \tag{2.32}$$

However, at higher angular frequencies the oscillating electric field induces a circular magnetic field perpendicular to it (see figure 2.1a). To compute the spatial distribution of the magnetic field, equation 2.10 is used. The current density vanishes because there is no current flux between the capacitor plates.

$$c^2 \mathbf{B} \cdot 2\pi r = \frac{\partial}{\partial t} \mathbf{E} \cdot \pi r^2 \implies \mathbf{B} = \frac{i\omega r}{2c^2} \mathbf{E_0} exp\{i\omega t\} \tag{2.33}$$

The magnetic field is a function of the time (like the electric field) and of the capacitor plate radius r, as seen from equation 2.33. It induces another electric field $\mathbf{E_2}$ which can be computed with equation 2.8. The new total electric field $\mathbf{E}$ is a superposition of the spatially constant electric field $\mathbf{E_1}$ (see equation 2.32) and the induced electric field $\mathbf{E_2}$.

$$\mathbf{E} = \mathbf{E_1} + \mathbf{E_2} \tag{2.34}$$

As seen from equation 2.32, $\mathbf{E_1}$ is spatially constant, thus the line integral around the loop (see figure 2.1 b) vanishes. In contrast, the integral of $\mathbf{E_2}$ gives $|-\mathbf{E_2}(r)\ h|$. The magnetic field is only a function of the capacitor plate radius but not of the plate distance h.

$$h\,\mathbf{E_2}(r) = h\,\frac{\partial}{\partial t}\int_0^r \mathbf{B}(r)\,dr \;\Rightarrow\; \mathbf{E_2}(r) = \frac{\partial}{\partial t}\frac{i\omega r^2}{4c^2}\mathbf{E_0}exp\{i\omega t\}$$
$$\Rightarrow\; \mathbf{E_2}(r) = -\frac{\omega^2 r^2}{4c^2}\mathbf{E_0}exp\{i\omega t\} \qquad (2.35)$$

The total electric field **E** is given with $\mathbf{E_2}$ by:

$$\mathbf{E} = \mathbf{E_1} + \mathbf{E_2} = \left(1 - \frac{\omega^2 r^2}{4c^2}\right)\mathbf{E_0}exp\{i\omega t\} \qquad (2.36)$$

The electric field $\mathbf{E_2}$ induces another magnetic field which induces another electric field and so forth. Thus a new component of the total electric field induces a new component of the total magnetic field and vice versa. The total electric field can be expressed with the Bessel function of the first kind for integer order of zero J_0.

$$\mathbf{E} = \mathbf{E_0}exp\{i\omega t\}\left[1 - \frac{1}{(1!)^2}\left(\frac{\omega\, r}{2\, c}\right)^2 + \frac{1}{(2!)^2}\left(\frac{\omega\, r}{2\, c}\right)^4 - \frac{1}{(3!)^2}\left(\frac{\omega\, r}{2\, c}\right)^6 + \ldots\right]$$
$$\mathbf{E} = \mathbf{E_0}exp\{i\omega t\}\, J_0\left(\frac{\omega r}{2c}\right) \qquad (2.37)$$

The electric field as a function of the capacitor plate radius is shown in figure 2.2. The first node of the electric field is located at $r = 2.405c/\omega$. Ideally, there is no current

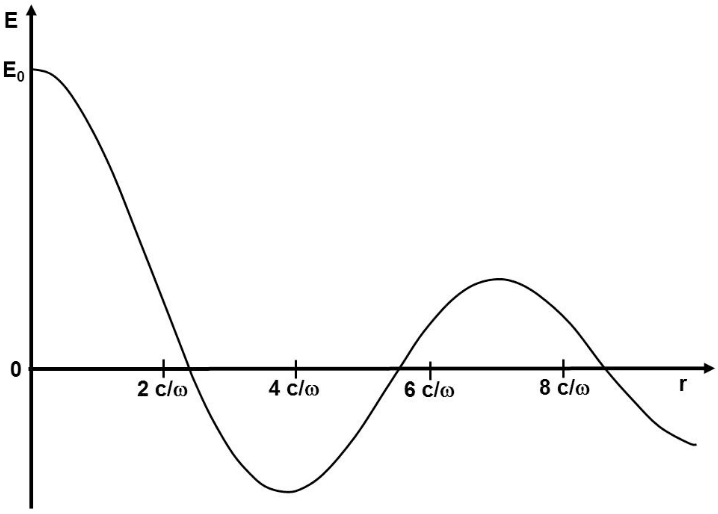

Figure 2.2: *Electric field distribution as a function of the radius r of the capacitor*

flux at the node even in the case of a shortcut (metallic wall at the node). If the electric and the magnetic field suffer no losses inside the cylinder, the energy is stored inside the cylinder and commuted between the electric and magnetic field and the cylinder behaves like a resonant circuit (LC circuit). The electric/magnetic field can be described by a capacitance/inductance. The resonance angular frequency is determined by the nodes of the electric field.

$$\omega_0 = 2.405\; c/r \tag{2.38}$$

In reality, both fields suffer losses, as shown in figure 2.3. The electric field separates charges at the inner surface of the cylinder (top electrons, bottom electron holes). These charges oscillate with the electric field and generate losses resulting from the resistance of the cylinder walls. Additionally the magnetic field is 90° out of phase relative to the electric field, as seen from equation 2.4, figure 2.3 b) and c). It has no node at $r = 2.405c/\omega$ and vanishes outside the cylinder ($r > 2.405c/\omega$). The drastic change of the magnetic field induces a current (see equation 2.4) which causes also Ohmic losses. The energy

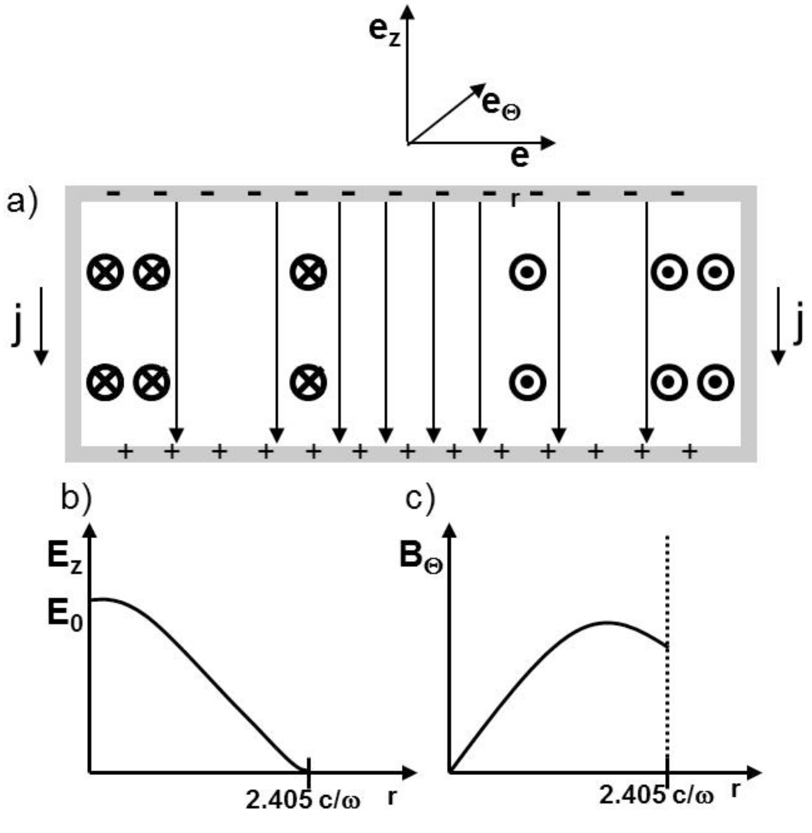

Figure 2.3: *a) Electric and magnetic field with the corresponding current flux at the walls of the cylinder; electric b)and magnetic c) field distribution as a function of the radius r of the cylinder*

losses of a cavity (cylinder) are characterized by the quality factor Q which will be described in a separate section.

In general, a cavity can be stimulated by an electromagnetic wave which can be coupled into the cavity, for instance, trough a hole in a wall of the cavity. The frequency has to be equal to the resonance frequency of the cavity to induce a standing electromagnetic field inside. In the case of microwave cavities, its radius ranges from millimeters to centimeters. The described mode of operation is the so called transverse magnetic TM(010) mode. TM means that the magnetic field in the z-direction (see figure 2.3) vanishes. The z-direction is the direction of propagation of an electromagnetic wave in a waveguide and is used for the definition. 010 means that a resonant half-wave stands in e_r direction but not in e_θ or in e_z direction.

In addition to the TM mode, also TE modes can be stimulated in a microwave cavity. TE means that the electric field in the z-direction vanishes.

Every mode has its own resonance frequency and field distribution which can be computed with the Maxwell equations.

2.3.2 Waveguides

To explain the operation mode of a wave guide, a rectangular waveguide will be explained [63], as seen in figure 2.4. The inner surface of the waveguide walls are made of an ideal conductor. For simplicity, the electric field has only a y-component and is constant in the y-direction (transversal electric field). Concerning the described boundary conditions, the

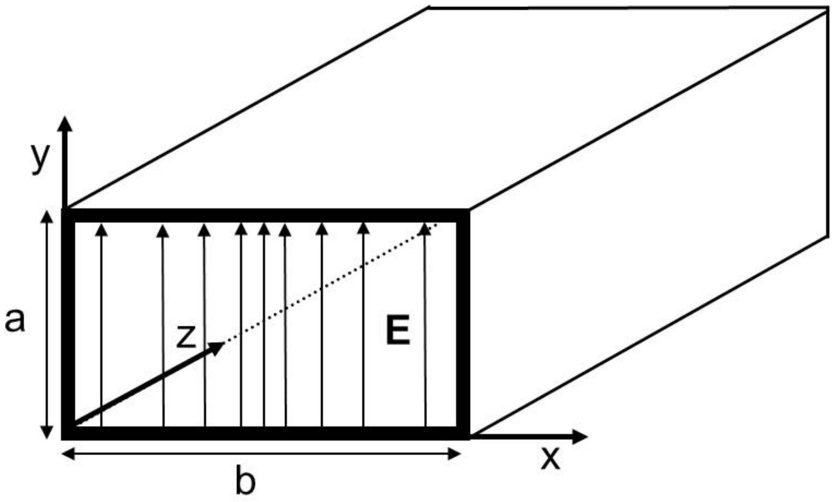

Figure 2.4: *Rectangular waveguide with the electric field distribution*

wave equation can be expressed in the following form:

$$\frac{\partial^2}{\partial x^2}E_y + \frac{\partial^2}{\partial z^2}E_y = \frac{1}{c^2}\frac{\partial^2}{\partial t^2}E_y \tag{2.39}$$

The electromagnetic wave propagates in the z-direction (see figure 2.4) and can be described with a planar wave along z. At the waveguide walls (x=0; b), the electric field vanishes because the tangent component of an electric field vanishes at the surface of an ideal conductor. Thus its x-component can be described with a sinus function.

$$E_y = E_0\, sin\{k_x\, x\}\; exp\{i(k_z\, z - \omega\, t)\} \tag{2.40}$$

k_x and k_z are the wave vectors in the x- and z-direction. k_x has to be n multiples of π in order that equation 2.40 fulfills the mentioned boundary conditions. The dispersion relation for an electromagnetic wave in a rectangular waveguide derives from the wave equation (equation 2.39) and its solution (equation 2.40).

$$k_x^2 + k_z^2 = \frac{\omega^2}{c^2} \Rightarrow k_z = \pm\sqrt{(\omega^2/c^2) - (n^2\pi^2/a^2)} \tag{2.41}$$

The algebraic sign in front of the square root defines the direction of propagation. The smallest value for n is unity which means that a half-wave stands in the waveguide in the x-direction.

$$k_z = \pm\sqrt{(\omega^2/c^2) - (\pi^2/a^2)} \text{ (for n=1)} \tag{2.42}$$

In the case of $\omega < \omega_g = \sqrt{c^2\left(\frac{\pi^2}{a^2}\right)}$, k_z is an imaginary number. Then, the exponent in equation 2.40 becomes negative. Thus equation 2.40 describes an over-damped wave. Consequently, an electromagnetic wave with an angular frequency smaller than the critical frequency ω_g cannot propagate in the waveguide. For instance, AC current cannot be transported in a waveguide.

2.3.3 Equivalent Circuit of a Waveguide

The equivalent circuit of a waveguide [32] is shown in figure 2.5. The coil (inductance L) represents the magnetic, the capacitor (capacitance C) the electric field and resistance R/conductance G the Ohmic losses of a waveguide element Δz. The current $\Delta j(z,t)$ and the voltage $\Delta u(z,t)$ can be described with the following expressions according to

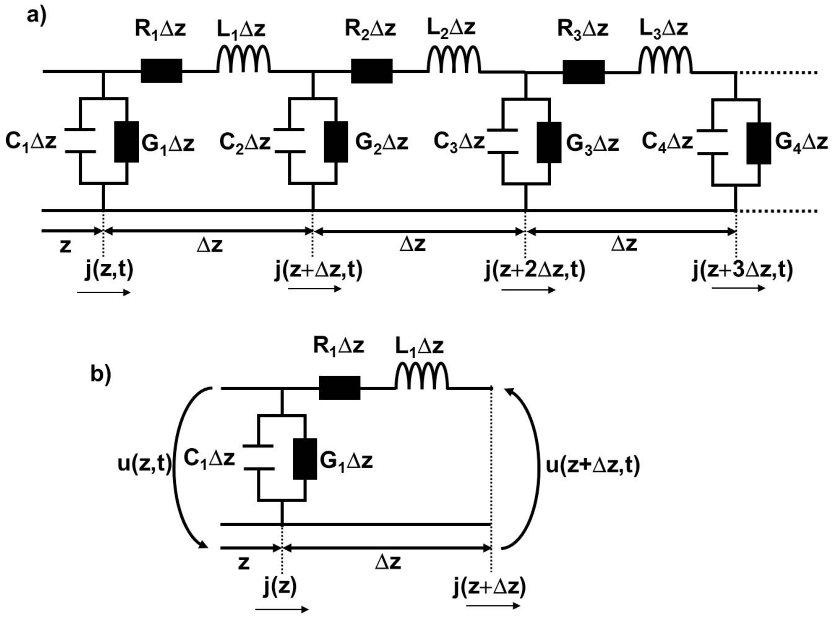

Figure 2.5: *Equivalent circuit of a waveguide*

the Kirchhoff's circuit laws.

$$-\Delta u(z,t) = u(z+\Delta z,t) - u(z,t) = R_1 \Delta\, z\; j(z,t) + L_1\;\Delta z\;\frac{\partial i(z,t)}{\partial t} \tag{2.43}$$

$$-\Delta j(z,t) = j(z+\Delta z,t) - j(z,t) = G_1 \Delta z u(z,t) + C_1 \Delta z \frac{\partial u(z,t)}{\partial t} \tag{2.44}$$

In the limiting case of $\Delta z \longrightarrow 0$, equations 2.43 and 2.44 are transformed to:

$$\frac{\partial u(z,t)}{\partial z} = R_1 j(z,t) + L_1 \frac{\partial j(z,t)}{\partial t} \tag{2.45}$$

$$\frac{\partial j(z,t)}{\partial z} = G_1 u(z,t) + C_1 \frac{\partial u(z,t)}{\partial t} \tag{2.46}$$

with $u(z,t) = U_0(z)\; exp\{i\;\omega\; t\}$ and $j(z,t) = J_0(z)\; exp\{i\;\omega\; t\}$

The current and the voltage can be separated by differentiating equation 2.45 and 2.46 with respect to z.

$$\frac{\partial^2 V(z)}{\partial z^2} = \gamma^2 V(z) \tag{2.47}$$

$$\frac{\partial^2 I(z)}{\partial z^2} = \gamma^2 I(z) \tag{2.48}$$

$$\text{with } \gamma^2 = \underbrace{(R_1 + i\omega L_1)}_{Z_1}\underbrace{(i\omega C_1 + G_1)}_{Y_1}$$

Equations 2.47 and 2.48 are the Fourier-transformed wave equations (equation 2.30). The incident I_+ and reflected current I_- can be derived from the incident V_+ and reflected voltage V_- with the wave impedance Z_c of the waveguide (Ohmic law). The wave impedance is given by the chain network in figure 2.5.

$$I = \overbrace{\frac{1}{Z_c}\underbrace{\widehat{V}_+ exp\{-\gamma z\}}_{V_+}}^{I_+} - \overbrace{\frac{1}{Z_c}\underbrace{\widehat{V}_- exp\{\gamma z\}}_{V_-}}^{I_-} \tag{2.49}$$

$$\text{with } Z_c = \frac{\sqrt{R_1 + i\omega L_1}}{\sqrt{G_1 + j\omega C_1}} = \sqrt{\frac{Z_1}{Y_1}}$$

The ratio of the reflected to the incident voltage is the reflection factor Γ.

$$\Gamma = \frac{V_-}{V_+} = \alpha + i\beta \tag{2.50}$$

$$V(z) = V_+(1+\Gamma) \tag{2.51}$$

$$I(z) = I_+(1-\Gamma) \tag{2.52}$$

The normalized impedance $\bar{z}$ is the ratio of the input/output resistance Z_i to the wave impedance Z_C. For instance, the output resistance can be a microwave cavity. The input/ output resistance represents the ratio of the voltage and the current at the beginning and end of the waveguide.

$$\bar{z} = \frac{Z_i}{Z_c} = \frac{(1+\Gamma)}{(1-\Gamma)} = x + iy \tag{2.53}$$

$$\text{with } Z_i = \frac{V(z)}{I(z)}$$

The reflection factor is the Möbius transformation of the normalized impedance. The reflection factor and the normalized impedance can be plotted in a Smith chart which is the projection of right half-plane of the complex plane on the unit circle, as shown in figure 2.6. The coupling of an electromagnetic wave from a waveguide into a microwave cavity can be described with the reflection factor. The reflection factor of a microwave cavity is inter alia a function of the resonance frequency and the quality factor. By fitting the reflection factor in the Smith chart [32] both values can be determined. The fitting procedure will be described in the result chapter.

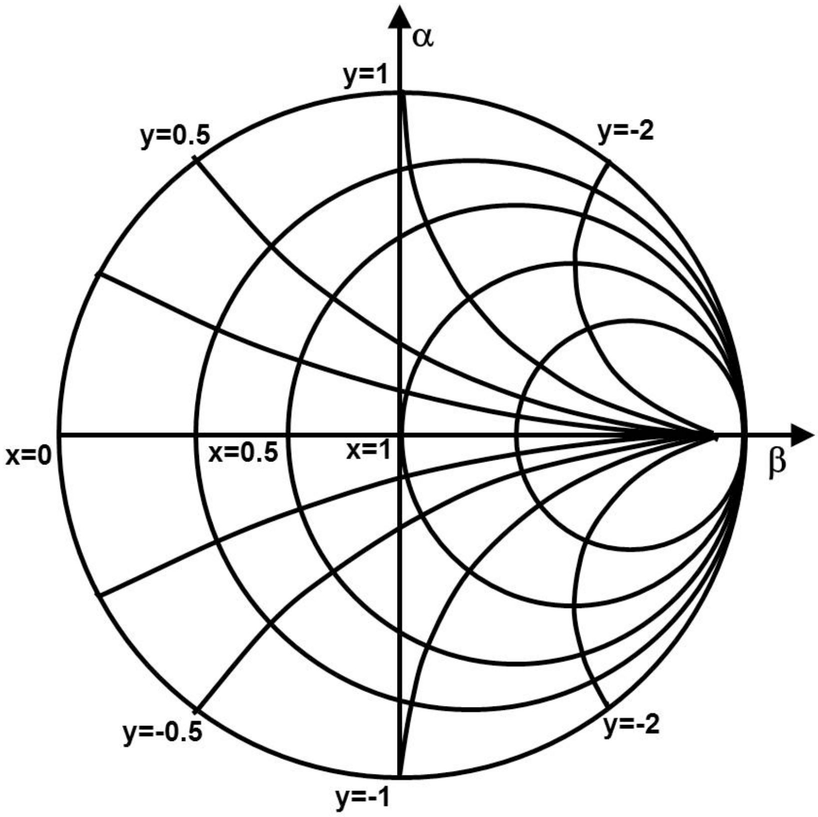

Figure 2.6: *Smith chart*

2.3.4 Quality Factor

The quality factor is defined as the ratio of the stored work W to the averaged losses P_L per period $T_0 = 1/\omega_0$ and equal to the ratio of the reactive P_B and active power P_W (absolute value), respectively.

$$Q = 2\pi \frac{W}{P_L\, T_0} = \omega_0 \frac{W}{P_L} = \left| \frac{P_B}{P_W} \right| \tag{2.54}$$

As mentioned in section 2.3.1, a microwave cavity can be described with a resonant circuit. A detailed description will be given in the result part. Now, the quality factor of a parallel and series resonant circuit will be derived.
The impedance Z_S and admittance Y_P of a series and a parallel resonant circuit is given by:

$$Z_s = R + j\left(\omega\, L - \frac{1}{\omega\, C}\right) \quad \text{(series resonant circuit)} \tag{2.55}$$

$$Y_p = G + j\left(\omega\, C - \frac{1}{\omega\, L}\right) \quad \text{(parallel resonant circuit)} \tag{2.56}$$

In a parallel/series resonant circuit, the root mean square of voltage U_eff/current I_eff reaches its maximum at $\omega = \omega_0$.

$$\left.\frac{\mathrm{d}I_\text{eff}}{\mathrm{d}\omega}\right|_{\omega=\omega_0} \overset{!}{=} 0 \implies \left(\frac{\mathrm{d}}{\mathrm{d}\omega}\frac{U_\text{eff}}{\sqrt{R^2 + \left(\omega\, L - \frac{1}{\omega\, C}\right)^2}}\right)_{\omega=\omega_0} \overset{!}{=} 0$$

$$\implies \omega_0 = \frac{1}{\sqrt{LC}} \quad \text{(series resonant circuit)} \tag{2.57}$$

$$\left.\frac{\mathrm{d}U_\text{eff}}{\mathrm{d}\omega}\right|_{\omega=\omega_0} \overset{!}{=} 0 \implies \left(\frac{\mathrm{d}}{\mathrm{d}\omega}\frac{I_\text{eff}}{\sqrt{G^2 + \left(\omega\, C - \frac{1}{\omega\, L}\right)^2}}\right)_{\omega=\omega_0} \overset{!}{=} 0$$

$$\implies \omega_0 = \frac{1}{\sqrt{LC}} \quad \text{(parallel resonant circuit)} \tag{2.58}$$

In both resonant circuits, the resonance angular frequency is $\frac{1}{\sqrt{LC}}$. The quality factor of both resonant circuits can be expressed in terms of electronic components of an electric circuit using equation 4.18.

$$Q = \frac{\omega_0\, I_{\text{eff}}^2 L}{I_{\text{eff}}^2 R} = \frac{1}{R}\sqrt{\frac{L}{C}} \text{ (series resonant circuit)} \tag{2.59}$$

$$Q = \frac{\omega_0\, U_{\text{eff}}^2 C}{U_{\text{eff}}^2 G} = \frac{1}{G}\sqrt{\frac{C}{L}} \text{ (parallel resonant circuit)} \tag{2.60}$$

In a series resonant circuit the quality factor decreases/increases with the resistance/conductance. In a parallel resonant circuit the relationship is inverted. The quality factor can also be expressed in terms of the resonance angular frequency and the full half width of the resonance peak $\Delta\omega$ which is at $\frac{1}{\sqrt{2}}$ of the current or voltage maximum.

$$\frac{I_{\text{eff}}}{I_{\text{eff}}(\omega_0)} = \frac{1}{\sqrt{2}} \implies \Delta\omega = \frac{R}{L} \text{ (series resonant circuit)} \tag{2.61}$$

$$\frac{U_{\text{eff}}}{U_{\text{eff}}(\omega_0)} = \frac{1}{\sqrt{2}} \implies \Delta\omega = \frac{G}{C} \text{ (parallel resonant circuit)} \tag{2.62}$$

$$\implies Q = \frac{\omega_0}{\Delta\omega} \tag{2.63}$$

In general, the quality factor is the ratio of the resonance frequency and the full half width of the resonance peak as it is exemplary shown with equations 4.19, 2.62 and 2.63.

2.4 Interaction of Light and Matter

2.4.1 Dielectric Function

In classical physics the dielectric function (permittivity) ε describes the dielectric response of matter interacting with electromagnetic waves [105]. Equation 2.4 is the starting point to derive the dielectric function. In matter the electric field is replaced by the dielectric displacement field (see equation 2.11).

$$\nabla \times \mathbf{H} = \mathbf{j} + \frac{\partial \mathbf{D}}{\partial t} \tag{2.64}$$

If the current density is assumed to be Ohmic, it can be expressed in terms of the electric field and the conductivity.

$$\mathbf{j} = \sigma \mathbf{E} \tag{2.65}$$

The Fourier transforms of **H**, **E** and **D** are only functions of ω. The conductivity and the dielectric function are complex numbers and frequency-dependent. In the Fourier representation, equation 2.64 has the following form:

$$\nabla \times \mathbf{H}(\omega) = \sigma_1(\omega)\mathbf{E}(\omega) + i\varepsilon_0\varepsilon_1\omega\mathbf{E}(\omega) = -i\varepsilon_0\varepsilon(\omega)\omega\mathbf{E}(\omega) \tag{2.66}$$

According to equation 2.66, the conductivity and the dielectric function (permittivity) are coupled in the following way.

$$\sigma(\omega) = \sigma_1 + i\underbrace{\omega\varepsilon_0\varepsilon_1}_{\sigma_2} \tag{2.67}$$

$$\varepsilon(\omega) = \varepsilon_1 + i\underbrace{\frac{\sigma_1}{\varepsilon_0\omega}}_{\varepsilon_2} \tag{2.68}$$

The real part of the conductivity $\sigma_1(\omega)$ depends on the energy losses during a charge transport process. Thus the imaginary part of the dielectric function $\varepsilon_2(\omega)$ describes the dielectric losses (see equation 2.67). In contrast, $\varepsilon_1(\omega)$ and $\sigma_2(\omega)$ describe the reversibly stored energy in matter. In the case of $\omega > 0$, equation 2.67 and 2.68 can be applied to bound and free charge carrier systems because the charge carrier can oscillate with the electric field in both case.

The described macroscopic quantities conductivity and dielectric function can also be expressed in terms of atomic processes which will be shown in the next section.

2.4.2 Interaction of Light and Matter on the Atomic Level

In quantum mechanics, the interaction of electromagnetic waves with matter can be expressed in terms of a perturbation of the ground state system (atom, molecule or solid) [64, 36]. The problem is time dependent due to the time dependency of the electromagnetic wave. In the present section an approximation will be discussed to describe the mentioned process on the atomic scale. In the ground state, the system can be described with the Hamiltonian $\mathbf{H_0}$, its eigenvalues E_n and eigenstates $\{|\phi_n\rangle\}$ (base states of the system) solving the stationary Schrödinger equation:

$$\mathbf{H_0}\,|\phi_n\rangle = \mathbf{E_n}\,|\phi_n\rangle \tag{2.69}$$

The Hamiltonian $H(t)$ of the perturbed system can be expressed in terms of the ground state Hamiltonian H_0 and the perturbation $W(t)$.

$$\mathbf{H}(t) = \mathbf{H_0} + \mathbf{W}(t) \quad \text{with} \quad \mathbf{W}(t) = \lambda \hat{\mathbf{W}}(t),\ \lambda \ll 1 \tag{2.70}$$

λ is a dimensionless parameter and $\hat{\mathbf{W}}(t)$ an observable which can be, for instance, the vector potential of the electromagnetic wave (see section 2.2). The system is transferred from an initial state $|\phi_i\rangle$ (t=0) to a final state $|\phi_f\rangle$ at time t. $|\phi_i\rangle$ and $|\phi_f\rangle$ are stationary states of the unperturbed system.

$$i\hbar \frac{\mathrm{d}}{\mathrm{d}t} |\psi(t)\rangle = \mathbf{H}(t)\, |\psi(t)\rangle \tag{2.71}$$

$$\text{with} \quad |\psi(t)\rangle = \sum_n c_n(t)\, |\phi_n\rangle\, ;\ c_n(t) = \langle \phi_n | \psi(t)\rangle \tag{2.72}$$

$$\text{and} \quad \langle \phi_n | \, \hat{\mathbf{W}}(t)\, |\phi_k\rangle = \hat{W}_{nk}(t) \ \ \text{(matrix element)};\ \langle \phi_n | \, \mathbf{H_0}\, |\phi_k\rangle = \mathbf{E_n} \delta_{nk} \tag{2.73}$$

$|\psi(t)\rangle$ is the state vector and $c_n(t)$ the probability amplitude finding the system in $|\phi_n\rangle$ at time t. Using the relations 2.72 and 2.73 in the Schrödinger equation (equation 2.71), a set of differential equations coupled by the perturbation is generated.

$$i\hbar \frac{\mathrm{d}}{\mathrm{d}t} c_n(t) = E_n c_n(t) + \sum_k \lambda \hat{W}_{nk} c_k(t) \tag{2.74}$$

The components $c_n(t)$ of $|\psi(t)\rangle$ can be determined solving equation 2.74. If the perturbation is much smaller than the Hamiltonian of the ground state meaning that the system is close to the ground state, the solution has the following form:

$$c_n(t) = b_n(t) exp\{-iE_n\, t/\hbar\} \tag{2.75}$$

Using the solution (equation 2.75) another set of equations depending on $b_n(t)$ is obtained.

$$i\hbar \frac{\mathrm{d}}{\mathrm{d}t} b_n(t) = \lambda \sum_k exp\{i\omega_{nk} t\}\, \hat{W}_{nk}(t) b_k(t) \tag{2.76}$$

$$\text{with } \omega_{nk} = \frac{E_n - E_k}{\hbar} \text{ (Bohr angular frequency)} \tag{2.77}$$

A power series expansion in λ ($b_n(t) = b_n^{(0)} + \lambda\ b_n^{(1)}(t) + \lambda^2 b_n^{(2)}(t) + ...$) is used to approximately find the $b_n(t)$ factors which provides the solution for $\psi(t)$. $b_n^{(0)}$ is not time dependent. Thus for the zeroth-order solution the equations 2.74 are decoupled if $\lambda = 0$ and their solution are stationary. The first-order solution can be found using a recurrence relation (equation 2.78).

$$i\hbar\frac{\mathrm{d}}{\mathrm{d}t}b_n^{(1)}(t) = \sum_k exp\left\{i\omega_{nk}t\right\}\hat{W}_{nk}(t)\underbrace{\delta_{ki}}_{=b_k^{(0)}} = exp\left\{i\omega_{ni}t\right\}\hat{W}_{ni}(t) \tag{2.78}$$

$$\Longrightarrow b_n^{(1)} = 1/i\hbar\int_0^t exp\left\{i\omega_{ni}\acute{t}\right\}\hat{W}_{ni}(\acute{t})\mathrm{d}\acute{t}$$

At the time before the perturbation is introduced (t<0), the system is in the initial state ($|\phi_i\rangle$) and all coefficients $b_n(t)$ vanish except $b_i(t)$. When the perturbation affects the system (t=0), $\lambda\hat{\mathbf{W}}(t=0)$ is nonzero, starts acting on the state ϕ_i and remains finite for any time t. The probability $\wp_{if}$ to find the system in the final state $|\phi_f\rangle$ can be expressed in terms of $b_f^{(1)}(t)$ when the final state differs from the initial one.

$$\begin{aligned}\wp_{if} &= \left|\langle\phi_f|\psi(t)\rangle\right|^2 = \left|c_f(t)\right|^2 = \left|b_f(t)\right|^2 = \lambda^2\left|b_f^{(1)}(t)\right|^2 \\ &= 1/\hbar^2\left|\int_0^t exp\left\{i\omega_{fi}\acute{t}\right\}W_{fi}(\acute{t})\mathrm{d}\acute{t}\right|^2\end{aligned} \tag{2.79}$$

The result (equation 2.79) exhibits that the transition probability is a function of the Fourier transform of $W_{fi}(t)$.

A very important special case is a sinusoidal perturbation. As mentioned at the beginning of the present section the perturbation can be an electromagnetic wave with a sinusoidal oscillating electric field (neglecting the magnetic field and spatial variation of the electromagnetic wave: electric dipole approximation) which induces a transition of, for instance, an electron from the initial to the final state (discrete states). The matrix element has then the following form.

$$\hat{W}_{fi}(t) = \hat{W}_{fi}\,sin\left(\omega t\right) = \hat{W}_{fi}/2i\left(exp\left\{i\omega t\right\} - exp\left\{-i\omega t\right\}\right);\ \hat{W}_{fi}:\text{amplitude} \tag{2.80}$$

Using the expression for the transition probability (see equation 2.79), it becomes:

$$\wp_{if}(t,\omega) = \frac{\left|W_{fi}\right|^2}{4\hbar^2}\left|\underbrace{\frac{1-exp\left\{i(\omega_{fi}+\omega)t\right\}}{\omega_{fi}+\omega}}_{\text{anti resonant term}} + \underbrace{\frac{1-exp\left\{i(\omega_{fi}-\omega)t\right\}}{\omega_{fi}-\omega}}_{\text{resonant term}}\right|^2 \tag{2.81}$$

The first term in equation 2.81 is called anti resonant because it becomes important in the case of stimulated emission of a photon (-$\omega_{fi} = \omega$). In the case of a resonant absorption process ($\omega_{fi} = \omega$) the anti resonant term is negligibly small and only the resonant term is important because its denominator approches to zero. Close to the resonance

($\left|\omega_{fi}-\omega\right| \ll \left|\omega_{fi}\right|$) the transition probability can approximately be expressed by:

$$\wp_{if}(t,\omega) \approx \frac{\left|W_{fi}\right|^2}{4\hbar^2}\left|\frac{sin(\omega_{fi}-\omega)t/2}{(\omega_{fi}-\omega)/2}\right|^2 \; ; \; \wp_{if}(t,\omega_{fi}) = \frac{\left|W_{fi}\right|^2}{4\hbar^2}t^2 \qquad (2.82)$$

The transition probability as a function of the angular frequency for a fixed point in time is shown in figure 2.7. The amplitude at the resonance position is $\frac{\left|W_{fi}\right|^2}{4\hbar^2}t^2$ which exhibits two important properties of the transition probability. First it increases with time. For an infinite time the probability goes also to infinity which is a physically wrong solution and exhibits the limits of the first order approximation. Its maximum is unity and therefore the approximation is only valid for $t \ll \hbar/\left|W_{fi}\right|$. For too short times ($t = 1/\left|\omega_{fi}\right|$ the anti resonant term from equation 2.81 has to be considered. The lower time limit is $t \gg 1/\left|\omega_{fi}\right|$. Thus the electromagnetic wave have to oscillate a number of times in the interval t.
Second the transition probability increases with increasing intensity of the incident electromagnetic wave $\left|W_{fi}\right|$ having in mind that the first order approximation is only valid for small perturbations.

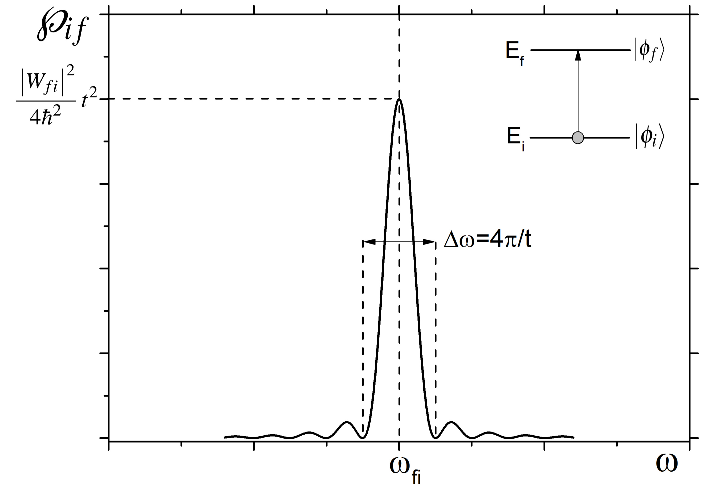

Figure 2.7: *First order transition probability of a discrete two state system affected by a sinusoidal perturbation*

Beside the transition between two discrete states, it can also occur between a discrete state (initial state) and a continuum (final state). Then, the final state is no longer a well defined state. It can be described by a density of final states $\rho(E,\mathbf{p})$ characterized by, for instance, their moment $\mathbf{p}$ and energy E. The transition probability is then exchanged by a transition probability density per unit time Ξ. Assuming that the variation of final states

δE_f with the energy is large compared to the width of the sinusoidal term in equation 2.82 ($\delta E_f \ll 4\pi\hbar/t$) (see figure 2.7), it can be approximated by a delta function.

$$\Xi(\phi_i, E, \mathbf{p}) = 2\pi/\hbar \left|\langle E, \mathbf{p}| W |\phi_i\rangle\right|^2 \rho\left(\mathbf{p}, E_f = E_i + \hbar\omega\right) \tag{2.83}$$

This result is known as Fermi's golden rule.
The absorption coefficient μ is a function of the cross section o_x (the ratio of the transition probability (density) and the photon flux) and the atomic density ς. Additionally μ can also be expressed in terms of the imaginary part of the dielectric function ε_2.

$$\mu = o_x\, \varsigma = \varepsilon_2\, \omega/c \implies \varepsilon_2 = o_x \varsigma\, c/\omega \tag{2.84}$$

Thus ε_2 describing in classical physics the dissipation of energy can be expressed in terms of quantum mechanic observables.

2.5 Electric Conductivity

In the first part of the present section the electronic band structure of solids will be described providing the base for the description of the electronic conductivity.
In an ideal crystalline solid, total translation invariance is obtained [106]. The solid is an infinitely expanded single crystal without any surface. The smallest periodic unit of the solid is the Wigner-Seitz-cell. The Fourier transform of the Wigner-Seitz-cell (real space) is the first Brillouin zone (reciprocal space). It contains all physical information of the entire solid. This fact can be explained with the Bloch theorem. An electron in a solid can be described with a Bloch-function $\psi_{\mathbf{k}}(\mathbf{r})$ considering the stationary Schrödinger equation (see equation 2.69) with a periodically modulated potential $V(\mathbf{r})$ characterized by the reciprocal lattice vector $\mathbf{G}$.

$$\begin{aligned} \mathbf{H}\psi_{\mathbf{k}}(\mathbf{r}) &= \left[-\frac{\hbar^2}{2m}\nabla^2 + V(\mathbf{r})\right]\psi_{\mathbf{k}}(\mathbf{r}) = E(\mathbf{k})\psi_{\mathbf{k}}(\mathbf{r}) \\ \text{with} \quad V(\mathbf{r}) &= \sum_{\mathbf{G}} V_{\mathbf{G}} exp\{i\, \mathbf{G}\, \mathbf{r}\} \\ \text{and} \quad \langle \mathbf{r}|\psi_{\mathbf{k}}\rangle &= \psi_{\mathbf{k}}(\mathbf{r}) = u_{\mathbf{k}}(\mathbf{r}) exp\{i\, \mathbf{k}\, \mathbf{r}\} \end{aligned} \tag{2.85}$$

$u_{\mathbf{k}}(\mathbf{r})$ is the periodic modulation factor of $\psi_{\mathbf{k}}(\mathbf{r})$. With the total translation invariance, the following relation for this factor is obtained:

$$u_{\mathbf{k}}(\mathbf{r}) = u_{\mathbf{k}}(\mathbf{r} + \mathbf{r_n}) \iff \psi_{\mathbf{k}}(\mathbf{r}) = \psi_{\mathbf{k}+\mathbf{G}}(\mathbf{r}) \tag{2.86}$$

$\mathbf{r_n}$ is the translation vector of the lattice. Applying the previous relation to the Schrödinger equation (equation 2.85), the dispersion relation $E(\mathbf{k})$ is reduced to the first Brillouin zone.

$$\begin{aligned} \mathbf{H}\psi_{\mathbf{k}}(\mathbf{r}) =& \mathbf{E}(\mathbf{k})\psi_{\mathbf{k}}(\mathbf{r}) \Longleftrightarrow \mathbf{H}\psi_{\mathbf{k+G}}(\mathbf{r}) = \mathbf{E}(\mathbf{k}+\mathbf{G})\psi_{\mathbf{k}}(\mathbf{r}+\mathbf{G}) \\ \Longleftrightarrow \mathbf{H}\psi_{\mathbf{k}}(\mathbf{r}) =& \mathbf{E}(\mathbf{k}+\mathbf{G})\psi_{\mathbf{k}}(\mathbf{r}) \qquad (2.87) \\ \Longrightarrow\ & \mathbf{E}(\mathbf{k}) = \mathbf{E}(\mathbf{k}+\mathbf{G}) \qquad (2.88) \end{aligned}$$

Now the electric conductivity will be discussed for a metal considering the previous results. Afterward the conductivity model will be transferred to semiconductors. In a isotropic solid the current density j can be expressed by [107]:

$$j = \frac{1}{8\pi^3}\int_{1.\mathrm{BZ}} v(\mathbf{k})\, f(\mathbf{k})\, d\mathbf{k} \qquad (2.89)$$

$$\text{with}\quad v(\mathbf{k}) = \frac{1}{\hbar}\nabla_{\mathbf{k}}E(\mathbf{k})$$

$$\text{and}\quad f(\mathbf{k}) \cong f_0(\mathbf{k}) + \frac{e}{\hbar}\,\tau(\mathbf{k})\,\mathrm{E}_i\,\frac{\partial f_0(\mathbf{k})}{\partial k_i} \qquad (2.90)$$

$v(\mathbf{k})$ is the group velocity of the electrons, $f(\mathbf{k})$ their occupation probability of a certain state characterized by $\mathbf{k}$ and E_i a component of the electric field. Considering Ohmic behavior, $f(\mathbf{k})$ can be expressed in terms of the linear Boltzmann distribution of non equilibration systems. After switching off the electric field, $f(\mathbf{k})$ turns back to $f_0(\mathbf{k})$ (Fermi distribution) during the relaxation time $\tau(\mathbf{k})$. The reasons for the relaxation are scattering processes occurring by electron electron, electron phonon interactions and lattice defects. Therefore the conductivity has the following form:

$$\sigma_1 = \frac{j}{\mathrm{E}_i} = -\frac{e^2}{8\pi^3}\int_{1.\mathrm{BZ}} \underbrace{\frac{f_0(\mathbf{k})v_i(\mathbf{k})}{e\mathrm{E}_i}\,d\mathbf{k}}_{=0} + v_i^2(\mathbf{k})\tau(\mathbf{k})\frac{\partial f_0}{\partial E} \qquad (2.91)$$

$$\text{with}\quad \frac{\partial f_0}{\partial k_i} = \frac{\partial f_0}{\partial E}\hbar v_i(\mathbf{k}) \qquad (2.92)$$

The derivative $\frac{\partial f_0}{\partial E}$ can be exchanged by a delta function because the expansion zone of the Fermi distribution is only $4kT$ broad:

$$\sigma_1 \approx \frac{e^2}{8\pi^3\hbar}\int df_E\, dE \left\langle \frac{v_i(\mathbf{k})}{v(\mathbf{k})}\tau(\mathbf{k}) \right\rangle \delta(E-E_F) = \frac{e^2}{8\pi^3\hbar}\int_{E=E_F} df_E \left\langle \frac{v_i(\mathbf{k})}{v(\mathbf{k})}\tau(\mathbf{k}) \right\rangle \quad (2.93)$$

$$\text{with} \quad d\mathbf{k} = df_E\, dk_\perp = df_E \frac{dE}{|\nabla_{\mathbf{k}}E|} = df_E \frac{dE}{\hbar\, v(\mathbf{k})} \quad (2.94)$$

df_E is a surface element with constant energy. The brackets denote the average of the value. In the case of quasi free electrons, their dispersion relation has a parabolic shape ($E = \frac{(\hbar\mathbf{k})^2}{2\,m^*}$), thus their effective mass is constant. The Fermi surface of quasi free electrons is a sphere and the average value $\left\langle \frac{v_i(\mathbf{k})}{v(\mathbf{k})}\tau(\mathbf{k}) \right\rangle$ equals $\frac{v(E_F)\ \tau(E_F)}{3}$, with E_F the Fermi energy. The group velocity becomes for $E = E_F$:

$$v(E_F) = \frac{\hbar k_F}{m^*} \quad (2.95)$$

k_F is the wave vector at the Fermi level. Every point (state) of the Fermi surface ($\int_{E=E_F} df_E = 2(4\pi k_F^2)$) is occupied with two electrons of opposite spin which can contribute to the conductivity of the metal. Now the conductivity can be expressed in the following way:

$$\sigma_1 = e\ \underbrace{\frac{k_F}{3\pi^2}}_{=n}\underbrace{\frac{e\tau(E_F)}{m^*}}_{=\mu} \quad (2.96)$$

n is the electron concentration which contributes to the current flux and μ their mobility. Equation 2.96 is an advancement of the Drude model [47, 48] developed by A. Sommerfeld and H. Bethe. In the Drude model all electrons contribute to the conductivity which is impossible concerning the Pauli exclusion principle. Only the states near the Fermi surface are affected by their displacement due to the applied electric field. In the described model only electrons in these states at the Fermi level contribute to the conductivity. In semiconductors the majority charge carriers are located at the conduction (n-type) or valence (p-type) band edge [108]. In the case of parabolic band edges and population inversion, equation 2.96 can be used with small modifications considering the location of the charge carriers. In general, the mobility of charge carrier in a semiconductor have a strong temperature dependency. At temperatures below the population inversion, the conductivity increases with the temperature due to the increasing number of ionized impurities (charge carriers). Beyond temperatures corresponding to the population inversion, the mobility decreases due to strong electron-phonon scattering. For intrinsic semiconductors, the charge carrier concentration and mobility of both charge carrier types have to be considered.

$$\sigma_1 = |e| \left(n\mu_n + p\mu_p \right) \tag{2.97}$$

$n/p; \mu_{n/p}$: electron/electron hole concentration; mobility

2.6 Surface Physics

At the surface, the translation symmetry of the bulk is distorted. The surface is, therefore, a defect of the bulk geometric structure. Regarding the Schrödinger equation (equation 2.85) describing the electronic structure of a solid, the symmetry break at the surface affects the periodic potential $V_{\mathbf{G}}$. It differs at the surface [133]. Thus also the energy eigenvalues must be different meaning that the electronic structure at the surface is different. This fact can also be understood from a chemical point of view. Considering a covalently bonded solid, bonds have to be broken to form the surface. The occurrence of unsaturated bonds (dangling bonds) is an electronically unfavorable situation. In general, the surface Gibbs free energy has to achieve its minimum [134]. This fact is the driving force for a restructuring of the surface. On the one hand a surface can relax. In this case of a relaxation, the periodicity of the bulk is kept constant parallel to the surface but perpendicular the inter atomic distance is changed in the topmost layers. On the other hand, a surface can reconstruct meaning the periodicity perpendicular and parallel to the surface is changed in the topmost layers.

Additionally, driven by a maximization of the entropy, a surface contains defects, like steps, adsorbed atoms or free vacancies which itself affects the periodicity and therefore the electronic structure of the surface. These defects generate new surface states.

2.6.1 Electronic Structure of the Surface

In the following section the previously introduced surface states will be described in more detail. In general, it is differed between intrinsic and extrinsic surface states [133]. Intrinsic surface states arise simply from the broken periodicity of the bulk geometric structure, relating to the model of the semi infinite atom chain in the quasi free electron approximation. The wave function of the bulk electron decays exponentially at the surface into the vacuum. The decay of the wave function at the surface modifies their energy eigenvalues which are located in the forbidden band gap at the boundary of the first Brillouin zone.

These surface states are called Shockley states. Details about this concept can be found in [41]. In a general three dimensional scenario the three dimensional first Brillouin zone is projected onto a particular surface. Thus only **k** vectors parallel to the surface are valid. States in the two dimensional Brillouin zone which are not degenerated with bulk states are true surfaces states.

Relating to the tight bound electron approach, which is very common in chemistry, surface states arise due to the lost binding partner at the vacuum side of the surface. Using the tight binding model, these surface states are called Tamm states. The missing bonding partner leads to a smaller overlap of surface atom wave functions with wave functions of the next neighbor atoms (in the bulk direction). The overlap of the wave functions causes the splitting and shift of their corresponding energy levels [65]. Thus a decreased overlap results in a decreased splitting/shift. By this reason, surface states at semiconductor surfaces (in general covalently bonded solids) are located in the forbidden band gap which is shown in figure 2.8. Beside dangling bonds states there are so called back bond states which arise from modification of chemical bonds in the topmost layers. As seen in figure 2.8, the high energy surface states located above the Fermi level have conduction band character. These states are unoccupied and therefore they are called acceptor states (they can accept electrons). Surfaces states near the valence band are occupied (below the Fermi level) and called donor states. In the case of an occupied/unoccupied acceptor/donor state, they are negatively/positively charged. Beside the intrinsic surface states also extrinsic surface states can occur at the surface of a solid. These states are related to

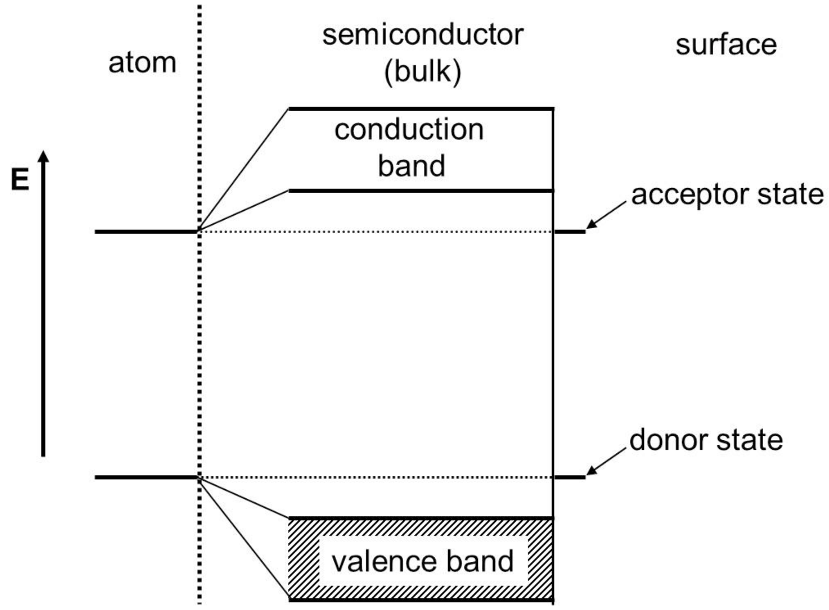

Figure 2.8: *Energy diagram of acceptor and donor surface states in comparison to the bulk electronic structure of a semiconductor*

defects like point defects, dislocations or steps and kinks. For instance, a missing atom at the surface changes the bonding geometry of its neighbor atoms. Details about the impact of a missing atom on the band structure of solids are given in Richards Feynmans Lectures on Physics 3 [65]. The changed potential $V(\mathbf{r}_{\text{defect}})$ at the location of the defects affects the wave functions of the electrons. They are more localized at the position of the defect. Depending on the type of the point defect, it acts as an electron trap (acceptor state) or a source of electrons (donor state). At the end of dislocations, steps or kinks, a particular atom is under-coordinated resulting in an increased number of broken bonds (dangling bonds).

Also adsorbates can affect surface states. In a simplified picture of chemisorption, a so called charge transfer state is formed between a state of the molecule and the solid during a redox reaction taking place at the surface, where a charge is transferred from the molecule to the solid or vice versa.

2.6.2 Space Charge Layer at Semiconductor Surfaces

The formation of a space charge layer at an n-type semiconductor surface will be described for the limiting case of a strong depletion layer (Schottky depletion layer) using the rigorous band model [137]. In an n-type semiconductor, the electron donor states are located in the forbidden band gap of the semiconductor. These states can be formed by doping of the semiconductor or result from lattice defects occupied with electrons. The Fermi level is shifted to the conduction band edge in comparison to the intrinsic semiconductor. In the case of impurity exhaustion all donor states are ionized (positively charged) because the electrons located in these states are transferred to the conduction band of the semiconductor by thermal excitation. Assuming that the donor state concentration is considerably higher than the intrinsic charge carrier concentration, the number of mobile electrons in the conduction band n equals approximately the ionized donor state concentration N_D^+.

As mentioned in the previous section, the surfaces states at semiconductor surfaces are located in the forbidden band gap. In the case of acceptor surface states which are located below the bulk Fermi level, electrons located in the conduction band diffuse in the surface acceptor states bringing the semiconductor in the thermodynamic equilibrium at the surface. However, localized positively charged donor states of the bulk remain and the semiconductor is positively charged near the surface. A so called depletion layer (depletion of electrons) is formed. The diffusion current causes a diffusion voltage U_D and generates an electric field. The resulting field current has the opposite direction of the diffusion current. In the thermodynamic equilibrium the net current vanishes and charge neutrality is achieved. The positively charged donor state concentration in the depletion

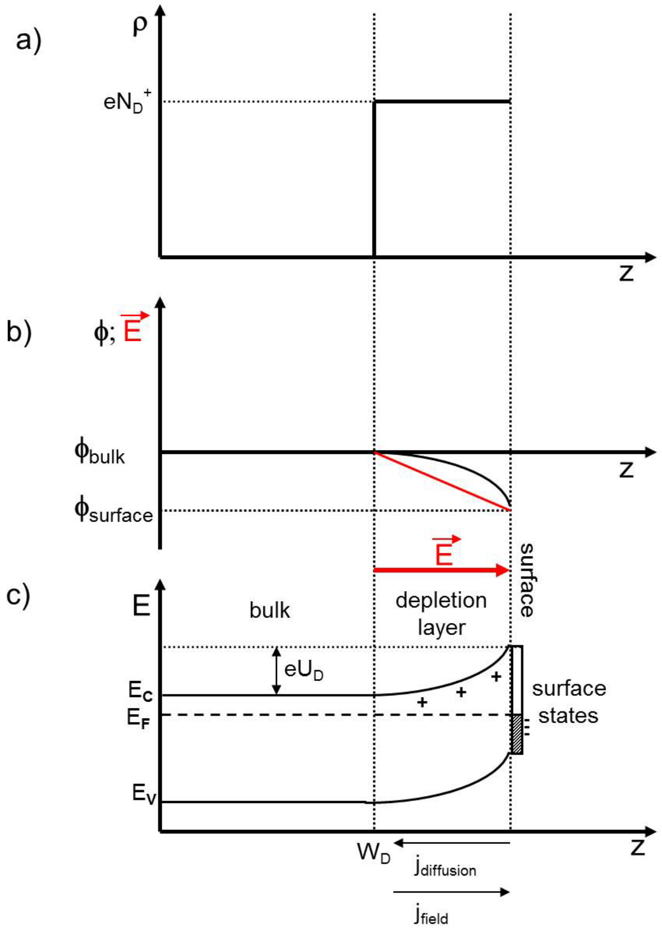

Figure 2.9: *Depletion layer near the surface of an n-type semiconductor in the limits of a Schottky depletion layer: a) spatial charge density distribution, b) spatial electric field and potential distribution; c) band diagram*

layer equals the surface charge Q_{SS}, however with opposite algebraic sign. The situation can be described with the Poisson equation (see equation 2.1) and is illustrated in figure 2.9.

$$-\frac{\mathrm{d}\mathbf{E}(z)}{\mathrm{d}z} = -\frac{\mathrm{d}^2\mathbf{U}(z)}{\mathrm{d}z^2} = \frac{e\,N_D^+}{\varepsilon\,\varepsilon_0} \tag{2.98}$$

The electric field $\mathbf{E}$/potential drop U of the depletion layer results after single/double integration of the Poisson equation.

$$\mathbf{E}(z) = \frac{e\,N_D^+}{\varepsilon\,\varepsilon_0}\,(z - W_d) \tag{2.99}$$

$$\mathbf{U}(z) = \underbrace{-\frac{e\,N_D^+}{\varepsilon\,\varepsilon_0}\,(z - W_d)^2}_{\phi(z)} + \phi_{\mathrm{bulk}} \tag{2.100}$$

As equation 2.100 exhibits, the energy bands are parabolically bended near the surface in the limiting case of the Schottky depletion layer. Relating to equation 2.97, the conductivity is constantly decreased in the depletion layer by assuming that only electrons contribute to the charge transfer (see also equation 2.96).

In general, also an accumulation or inversion layer can be formed near the surface. In case of an n-type semiconductor an accumulation is related to a downward band bending meaning that the electron concentration is increased near the surface in comparison to the bulk concentration. In an inversion layer the Fermi level is at the surface closer to the energy band containing the minority charge carriers of the bulk. Hence, the concentration of the original majority charge carrier exceeds the concentration of the former majority charge carriers.

Besides the limiting case of a Schottky depletion layer, a band bending can also occur near the surface of an intrinsic or degenerated semiconductor. A general description is however difficult because the exact spatial charge carrier concentration is needed to solve the Poisson equation.

2.6.3 Work Function Modification Induced by Adsorbates

Physisorbed or chemisorbed molecules at the surface of a solid can induce changes in the work function Φ of the solid. If a solid emits an electron, for instance in a photoelectron emission experiment, the ground state of the solid containing N electrons is then transferred to a final state containing $N-1$ electrons. Regarding the Schrödinger equation, the effective potential $V(\mathbf{r})$ is modified. Thus the energy eigenvalues of the final state differs from the ground state of the solid. In the final state of the emitted electron, it is outside of the solid, where it has only electrostatic energy described by the vacuum level of the solid (E_{vac}). The work function is defined as the difference of the Fermi level and the vacuum level [128]. In semiconductors the Fermi level is located in the forbidden band gap. Thus the work function of semiconductors at its surface are the sum of the energy difference between the Fermi level and the conduction band edge and the electron affinity χ, which is the energy difference between the conduction band edge and the vacuum level.

$$\Phi = (E_C - E_F) + \chi \tag{2.101}$$

As described in the previous section a band bending can occur at the surface of semiconductors. Thus in comparison to the bulk the difference $E_C - E_F$ is modified by eU_D. In the case of chemisorption at semiconductor surfaces the band banding can be changed as described in the previous section due to induction of surface states, the formation of adsorbate surface states and/or a modification of the electron occupation of surface states. Adsorbates can also modify the dipole moment at the surface of metals or semiconductors [135]. The electrostatic forces at the surface are modified which affects the position of the vacuum level. In semiconductors the dipole modification at the surface affects the electron affinity. The described effects of adsorbates at semiconductor surfaces are illustrated in figure 2.10.

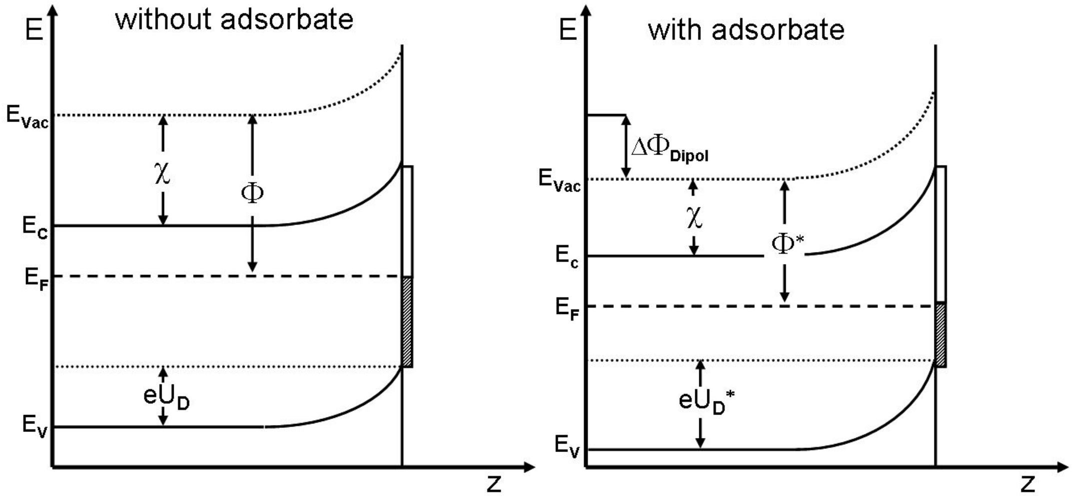

Figure 2.10: *Energy diagram near to the surface of a semiconductor with and without adsorbates*

3 Experimental Methods

3.1 Photoelectron Spectroscopy

At the beginning of this section the photoelectron emission process will be described with the three step model[11, 99] (one electron approximation).

In the three step model it is divided into the optical photoexcitation process, the transport of the photoelectron to the surface and the escape of the photoelectron into the vacuum. The photoexcitation process can be described by Fermi's golden rule as shown in section 2.4.2. In a photoelectron emission experiment, the excitation energy is constant and the kinetic energy of the escaped photoelectrons is measured. Assuming that the matrix element and the density of final states of the photoelectron is constant for a constant excitation energy, equation 2.83 has to be modified. Instead of the density of final states, the density of the occupied initial states is monitored in a photoelectron emission experiment. The photoexcitation process of an electron described by its wave vector k_i and its energy E_i in the reduced band diagram of a solid is shown in figure 3.1 a. The translation symmetry of the lattice ensures the momentum conservation in the electron excitation process and therefore a vertical transition is shown in figure 3.1a. The final state is assumed to be a free electron state and therefore the energy dispersion of the final states is the free electron parabola. The kinetic energy of the photoelectron in the vacuum is the energy difference between the vacuum level and the energy of the final state. The wave vector of the electron above the vacuum level is marked with $\mathbf{p}/\hbar$ to separate it from the wave vector in the reduced band diagram.

After the photoexcitation, the excited electron with E_f has to travel to the surface to escape into the vacuum. On its way, it can be inelastically scattered. The predominant scattering process is the electron-electron scattering. Only photoelectrons without energy losses contribute to the characteristic photoemission lines of a solid under investigation. In general the inelastically scattered electrons form the background of the photoelectron emission spectrum. However, for instance, in metals plasmons can be excited by inelastic scattering of photoelectrons. The photoemission line corresponding to the excited plasmon appears at lower kinetic energies (higher binding energies) compared to the characteristic photoemission line. The probability that an electron leaves the solid without energy at a certain distance from the surface can be characterized with the inelastic mean free path λ_{IMPF}. It defines the distance, an electron beam propagating through the sample before its intensity decays to 1/e of the initial intensity. In the present work the formalism of Tanuma[185, 184, 183] will be used to calculate λ_{IMPF} for the X-ray photoelectron spectroscopy studies of transition metal oxides, because it has been shown to be suitable for low density solids and photoelectrons with a kinetic energy (E_{kin}) between 50 eV and 2000 eV. The Tanuma formalism based on the modified Bethe equation[185, 184, 183] is:

$$\lambda_{IMPF} = \frac{E_{kin}}{E_p^2(\beta_{IMFP}\; ln(\gamma_{IMFP}\; E_{kin}) - C/E_{kin} + D/E_{kin}^2} \tag{3.1}$$

In equation 3.1 E_p is the plasmon energy of the free electron gas, E_{kin} the kinetic energy of the photoelectron. β_{IMFP}, γ_{IMFP}, C and D are parameters depending on the forbidden band gap, the plasmon energy, the density of the solid, numbers of valence electrons per atom and the atomic or molecular weight. In general, λ_{IMPF} mainly depends on the kinetic energy of the photoelectron as seen from equation 3.1. The general curve shape is related to the universal electron escape depth curve which has its minimum at around 40 eV[101]. λ_{IMPF} is limited to a few nanometers in the kinetic energy range from 50 eV to 2000 eV with the consequence photoelectron spectroscopy in the soft X-ray regime is a very surface sensitive method.

After the excited electron has arrived at the surface, it has to overcome the surface barrier $E_{vac} - E_0$ to escape into the vacuum as seen in figure 3.1b. The photoelectron excitation is shown in the extended band diagram indicated by the wave vector $\mathbf{K} = \mathbf{k} + \mathbf{G}$ consisting of a component perpendicular ($\mathbf{K}_\perp$) and parallel ($\mathbf{K}_\parallel$) to the surface. The energy E_0 is related to the Γ-point of the first Brillouin zone (the minimum of the valence band for a quasi free electron). Thus the photoelectron has to fulfill the following relation to escape into the vacuum:

$$(\hbar^2/2m)\mathbf{K}_\perp^2 \geq E_{\text{vac}} - E_0 \tag{3.2}$$

The component of the wave vector parallel to the surface is conserved because the surface barrier only affects the perpendicular component of the wave vector. The parallel component of the wave vector in vacuum $\mathbf{p}_\parallel/\hbar$ can be expressed in the following way, and as also depicted in figure 3.1c).

$$\mathbf{p}_{\|}/\hbar = \mathbf{k}_{f,\|} + \mathbf{G}_{\|} = \mathbf{K}_{\|} \tag{3.3}$$

$$\text{with } \mathbf{k}_{f,\|} = sin\,(\Lambda)\,\left[\frac{2m}{\hbar^2}E_{\text{kin}}\right]^{1/2} = sin\left(\acute{\Lambda}\right)\,\left[\frac{2m}{\hbar^2}\,\left(E_f - E_0\right)\right]^{1/2}$$

$$\Longrightarrow sin\left(\acute{\Lambda}_{max}\right) = \left[\frac{E_{\text{kin}}}{E_f - E_0}\right]^{1/2} \tag{3.4}$$

Equation 3.3 states that the escape angle Λ (with respect to the surface normal) outside the solid is larger than the traveling angle $\acute{\Lambda}$ to the surface (also see figure3.1c). Thus the maximum $\acute{\Lambda}$ ($\Lambda = 90°$) corresponding to a minimum $(\mathbf{K}_{\perp})_{\text{min}}$ is given in equation 3.4. Relating to the description of the photoelectron emission process, its kinetic energy can be expressed in the following way.

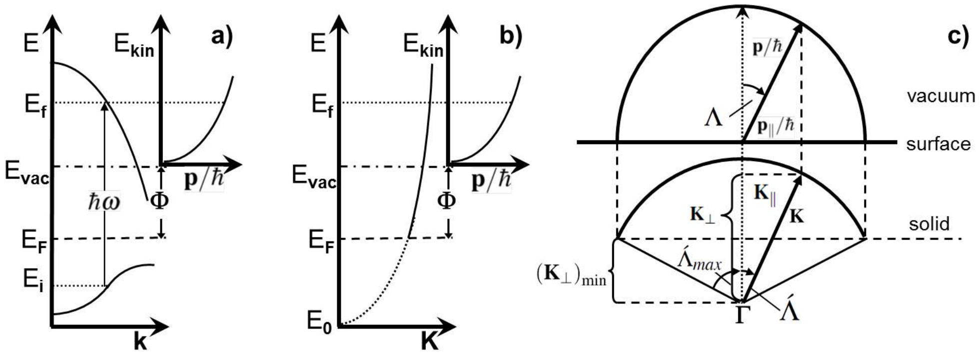

Figure 3.1: *a) Photoexcitation process in the reduced band diagram. b) Free electron model of photoelectron spectroscopy: wave vector of the electron in the final state is the difference of Γ-point and the intersection at $E = E_f$ with the free electron parabola. c) Escape cones inside and outside the solid for the free electron model (similar to [99])*

$$\begin{aligned} E_{kin} &= \hbar^2/2m\,\left[\mathbf{K}_{\|}^2 + \left(\mathbf{p}_{\perp}/\hbar^2\right)\right] = E_f - E_{\text{vac}} \\ &= \hbar\omega - \left(E_{\text{vac}} - E_F\right) - \left(E_F - E_i\right) = \hbar\omega - \Phi - E_B \end{aligned} \tag{3.5}$$

$E_F - E_i$ is the binding energy E_B of an electron in a solid. The description of the binding energy is a crucial topic because it corresponds to a core level or valence band level in the final state of the solid. After the photoelectron emission process, a positively charged electron hole is left in the solid. The electron hole can be screened in different ways (different screening channels). In some cases also two final states corresponding to different screening channels can be achieved resulting in so called satellite line(s) located at the high energy side (binding energy) of the characteristic photoelectron emission line(s) (main line)[100, 42]. Especially in transition metal (compounds) with open d-/f-shells, the described situation can occur. The Kotani-Toyozawa-model[119, 120, 121] will be used to exemplarily describe the problem for a metal (sp-valence band) and an insulator. In the following a core level is labeled with c, the valence d-levels with d and a ligand, for instance oxygen in NiO, with L like in a molecular orbital description which is often used to describe final state effects. The exponent of the valence d-levels exhibits the number of occupation and a exponent of -1 at a core level or ligand indicates an electron hole. For instance, the nomenclature $c^{-1}d^8L$ corresponds to a system with an electron hole in the core level, 8 electrons in the valence d-levels and neutral ligand.

Two possible final states for a metal can be seen in figure 3.2a. After the excitation of a core level electron, the effective Coulomb potential is increased leading to a shift of the unoccupied d-level below the sp valence band edge (Fermi level). Now a so called two electron hole state is generated because the unoccupied d-state is formally positively charged below the Fermi level. The two electron holes are screened by charge movement in the sp valence band (final state (1)). In the other final state, a charge transfer from the sp valence band to the d-level takes place resulting in a more effective screening situation (final state (2)). Thus the d-level has a smaller binding energy in the final state (2) than in the final state (1). The situation in an insulator is shown in figure 3.2b. The valence band consists of p-levels of the ligand. The d level and the upper sp band above the Fermi level are the conduction band states. After the excitation of the core electron the d level and parts of the sp band are located below the Fermi level quite similar to the situation shown for a metal. Now the screening can occur by a charge transfer from the p-states of the ligand into the sp band (final state (1)) or into the d-level (final state (2)). The insulator example can also be explained in the simple molecular picture by neglecting the sp band and considering only one p-level of the ligand. The final state (1) is similar to a $c^{-1}d^nL$ configuration. While the final state (2) corresponds to a $c^{-1}d^{n+1}L^{-1}$ configuration. In both examples (metal and insulator) the final state (2) is the energetically favored screening situation and corresponds to the main line. The final state (1) is the so called satellite line. The situation shown in figure 3.2 is an example for charge transfer satellites. In both final states the binding energy of the core level differs from its binding energy in the initial state (ground state) of the solid. Relating to section 2.4.2 the assumpution that the initial state (core level) and the final state (above the vacuum level) of the photoelectron can be described with states of the initial system is not absolutely valid in photoelectron spectroscopy (charge transfer effects were not considered in Fermi's golden role). The discussion above exhibits that in photoelectron spectroscopy the final state of a solid is monitored.

However, changes of the chemical environment of a certain element in a solid or at its sur-

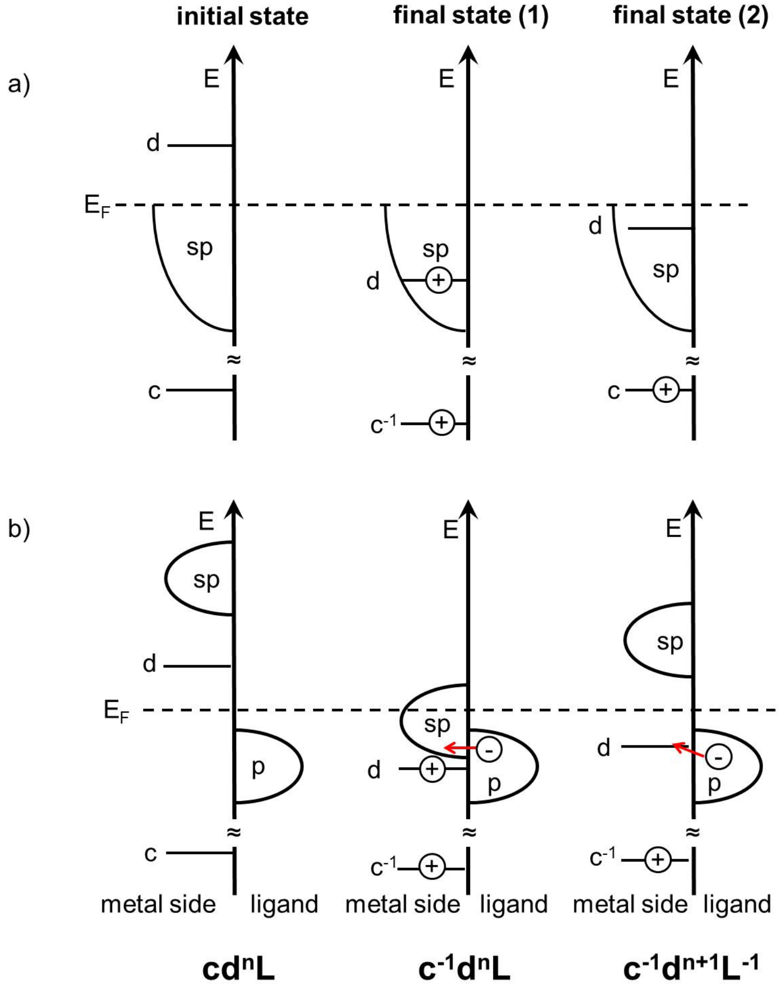

Figure 3.2: *Kotani-Toyozawa-model of charge transfer satellites: Two possible screening situations of a core electron hole in a metal (a) and an insulator (b)(similar to [100].*

face induce shifts of the characteristic photoelectron emission lines. The chemical shift is the difference between two chemical states of an atom. This fact can be explained, for instance, with an oxidation of a metal. In a simple model, a redox reaction takes place during the oxidation. The metal is oxidized and oxygen (ligand) is reduced. Thus an electron (valence electrons) transfer from the metal sites to the ligand takes place. At the metal site the Coulomb potential is screened by the core and valence electrons prior oxidation. After the redox reaction valence electrons are transferred to oxygen and the Coulomb potential is less well screened which, inter alia, leads to a shift of the core levels to higher binding energies in comparison to the metallic state before oxidation.

In semiconductors (insulators) a binding energy shift can also occur due to the formation of a space charge layer at the semiconductor surface (see section 2.6.2)[110, 135, 137]. The reference level of the binding energy is the Fermi level as shown before. In figure

3.3a the energy diagram of a semiconductor and the corresponding photoelectron emission spectrum is shown in the flat band situation. E_{core} denotes a core level, $E_{\text{cut off}}$ the secondary electron edge (cut-off) of the photoelectron emission spectrum, VB the valence band with the corresponding valence band edge E_v, E_g the forbidden band gap, E_F the Fermi level, $E_c$the conduction band edge, χ the electron affinity and E_{vac} the vacuum level. When an n-type semiconductor is depleted in electrons near the surface, the valence band edge, the core level and the secondary electron edge are shifted by the same absolute energy value towards the Fermi level in comparison to the flat band situation (figure 3.3 b). Thus the gradient of a space charge layer can be principally measured by photoelectron spectroscopy keeping in mind that photoelectron spectroscopy monitors the final state of the semiconductor, by the probing depth varying and determining the corresponding shift of the core level. However, the incident photon beam can generate electron-hole pairs inside the space charge layer. Its electric field separates the charge carrier and a so called surface photovoltage [168, 4] arises. The electric field of the surface photo voltage is contrary to the electric field of the space charge layer. Thus its diffusion voltage barrier height is lowered. The semiconductor is, strictly speaking, not in the thermodynamic equilibrium and therefore the term Fermi level is not valid and has to exchanged by quasi Fermi levels. A detailed study of the described effect was performed in [4].

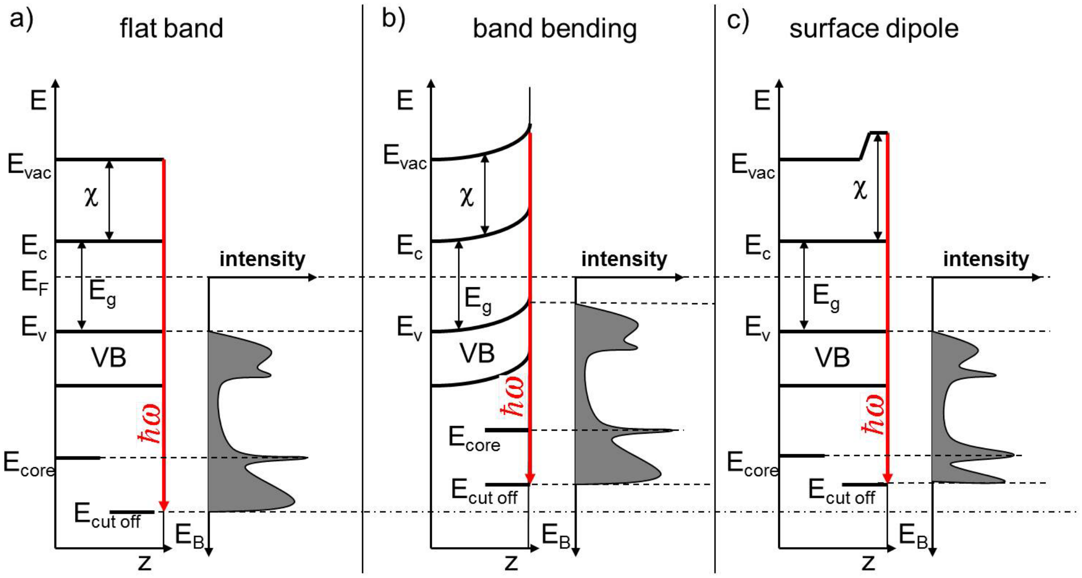

Figure 3.3: *Band diagram of a semiconductor and the corresponding photo electron emission spectrum: a) flatband situation, b) band bending and c) modification of the surface dipole*

If the electron affinity/work function is changed, for instance, due to an adsorbate at the surface as described in section 2.6.3, the secondary electron edge is shifted, while the valence band edge remains constant as shown in figure 3.3 c. Thus the electron affinity or work function can be measured by photoelectron spectroscopy.

$$\Phi = \hbar\omega - (E_{\text{cut off}} - E_F) \tag{3.6}$$

$$\chi = \hbar\omega - (E_{\text{cut off}} - E_v + E_g) \tag{3.7}$$

Experimental details about work function measurements using photoelectron spectroscopy will be given in the result part.
As seen from equation 3.5, the work function and the position of the Fermi level is needed to determine the kinetic energy of a photoelectron and the binding energy. If the electronic structure of an unknown sample is measured, also its work function Φ_s is unknown. However, the kinetic energies of the photoelectrons and their binding energies can still be determined by knowing the work function of the photoelectron spectrometer Φ_d. A schematic sketch of the photoelectron emission experiment and the corresponding energy diagram is shown in figure 3.4. The sample is electrically connected with the spectrometer (short cut situation). Thus in equilibrium the position of the sample Fermi level equals the detector Fermi level. The escaped photoelectrons in the final state E_f are selected by their kinetic energy with the analyzer (usually hemispherical electron analyzer). The kinetic energy of the photoelectrons is measured relative to the vacuum level of the detector.

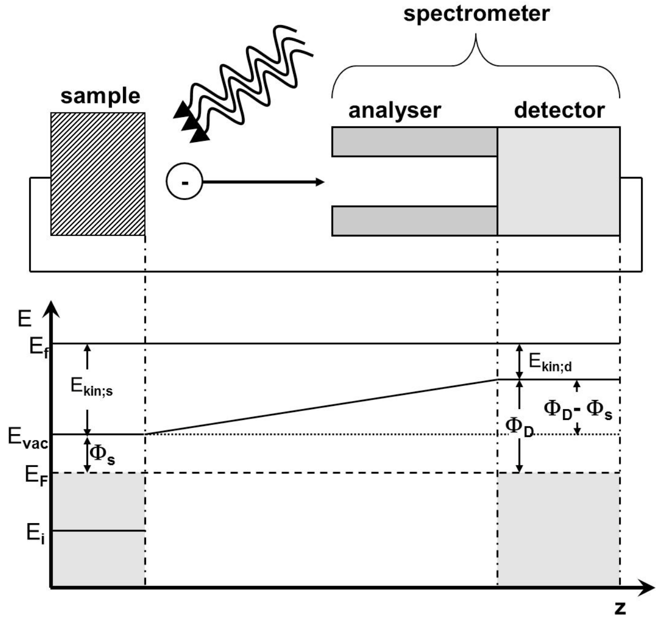

Figure 3.4: *A schematic sketch of the photoelectron emission experiment and the corresponding energy diagram.*

$$E_{\text{kin,d}} = E_f - E_{\text{vac}} = E_{\text{kin,s}} - (\Phi_s - \Phi_d) = \hbar\omega - \Phi_d - E_B \tag{3.8}$$

$E_{\text{kin,d}}/E_{\text{kin,s}}$ is the kinetic energy relative to the vacuum level of the detector/sample.

To precisely determine the photoemission core level line position, fitting of the spectrum is needed because in general lines corresponding to different chemical states of one element differ not much in energy[102, 42]. Therefore the line and background shape, which has to be subtracted, has to be known. The lifetime of the core hole causes an uncertainty in energy (Heisenberg uncertainty relation) resulting in a Lorentzian broadening of the photoemission line. Additionally, a Gaussian broadening occurs due to phonon scattering and the response function of the detector. The photo electron emission line, disregarding manybody effects like charge transfer effects, can be fitted with a convolution of a Gaussian and Lorentzian function. In metals the line shape is inherently unsymmetric caused by manybody effects which will not be explained here because in the present work only transition metal oxides were investigated.

A Shirley background[174] is often used for background subtraction. The correction assumes that the background is proportional to the weight of the photoemisson line at a given kinetic energy.

After the peak fitting procedure not only the peak position but also the concentration of a certain species in the sample can be determined[97]. However, the following assumptions have to be made to perform a quantitative analysis of core levels. The sample has to be homogeneous, flat and no interference effects occur. The angle between the incident photon beam and the escape vector of the photoelectrons has to be around 55°. The detector efficiency has to be constant and the influence of elastic scattering is negligible. Then, the photoelectron intensity J (peak area) of a core level corresponding to a chemical species is proportional to its concentration c.

$$\frac{\grave{J}_A}{\grave{J}_B} \approx \frac{c_A}{c_B} \quad \text{with } \grave{J} = \frac{J}{o_x\, \lambda_{IMFP}\, T} \tag{3.9}$$

In equation 3.9 o_x is the cross section, λ_{IMFP} and T the transmission function of the photoelectron spectrometer.

In the present work, in situ photoelectron spectroscopy was performed. In this case not only the scattering of electrons inside the solid but also scattering at gas atoms/molecules occurs[163, 115, 15]. The inelastic mean free path is inversely proportional to the pressure of the gas phase, resulting in an exponentially decreasing count rate of the photoelectrons with increasing distance between the sample an the spectrometer. Differentially pumped spectrometers are used to minimize the described effect. However, in situ photoelectron spectroscopy is still limited to the millibar pressure range.

3.2 Near Edge X-ray Absorption Fine Structure (NEXAFS) Spectroscopy

In contrast to photoelectron spectroscopy also amorphous and highly insulating samples can be investigated with NEXAFS spectroscopy[179]. It is highly sensitive to the coordination of a particular element under investigation in a compound.

In NEXAFS spectroscopy, an electron from a core level is excited to an unoccupied electronic level by irradiating a sample (atom, molecule or solid) with X-ray photons. The photoelectron excitation process can be described with Fermi's golden rule (equation 2.83). Thus the NEXAFS spectrum is related to the unoccupied density of states. Transitions to bound unoccupied states below the vacuum level and to quasi free electron levels above the vacuum level can occur. In general, the NEXAFS spectrum is dominated by dipole transitions which have to fulfill the dipole selection rules so that the matrix element does not vanish. Similar to photoelectron spectroscopy charge transfer and, especially for transitions to bound states, intra-atomic multiplet coupling effects have to be considered for the interpretation of NEXAFS spectra. NEXAFS can be performed in the absorption, fluorescence and photo/Auger-Meitner electron mode. In general, the signal, which is proportional to the X-ray cross section in the limit of weak absorption (similar to Lambert-Beer law, see equation 2.84), is measured as a function of the incident photon energy. In the absorption mode, the intensity of the incident photon beam and after transmission through the sample is measured. The signal is the absorption, thus the ratio of the transmitted and incident beam intensity. The absorption mode is therefore bulk sensitive.

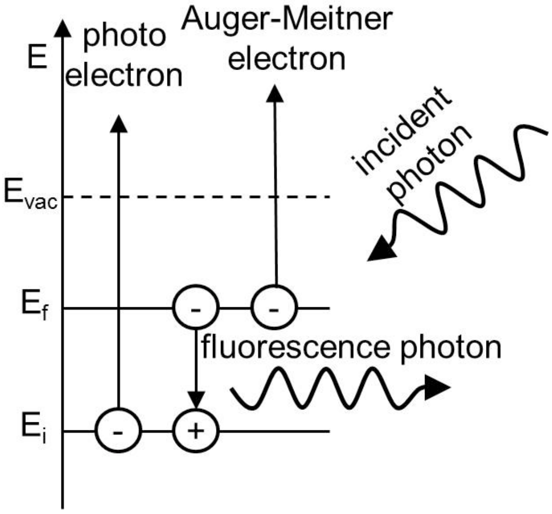

Figure 3.5: *Energy diagram of the fluorescence and photo/Auger-Meitner process to illustrate the physical principles of these detection modes*

The fluorescence mode and photon/Auger-Meitner electron mode is explained in figure

3.5. The number of generated electron holes/photoelectrons by absorption of the incident photon beam is proportional to the X-ray cross section. Therefore the most direct way of measuring NEXAFS in the electron mode is to monitor the number of photoelectrons as a function of the photon energy. However, transitions to bound levels below the vacuum level cannot be detected with the photoelectron mode. These transitions can be monitored by measuring the number of florescence photons or Auger-Meitner electrons resulting from annihilation of the created electron hole. The fluorescence mode is a so called "photon in, photon out" measurement obtained in reflection. In general, the probability of the fluorescence decay (radiative decay) increases with the atomic number in contrast to the Auger-Meitner decay. The sum of both decay yields is unity. In comparison to the electron mode, the measurement of fluorescence photons is bulk sensitive, because the interaction of matter with photons is much weaker than with electrons. The Auger-Meitner electron mode will be explained in the following general discussion about the electron mode.

The electron mode is the most surface sensitive one of all NEXAFS detection modes (see the discussion of inelastic mean free path in the previous section) and therefore suitable for studying surface modifications induced by chemical reactions. There are three different modes of operation to measure an electron yield. In the Auger-Meitner electron yield (AMEY), the electron analyzer is set to a window around a constant kinetic energy corresponding to a specific Auger-Meitner (AM) line in the photoelectron emission spectrum. The intensity of the AM lines changes with the photon energy according to the cross section of the AM line. In contrast to an AM line, the kinetic energy of a photoelectron emission line varies with the photon energy of the incident X-ray beam. Thus photoelectron emission lines can overlap with the AM-line under investigation and distorts the NEXAFS spectrum. One has to take care that no photoelectron emission line enters the kinetic energy window during the measurement.

The partial electron yield (PEY) mode is another NEXAFS detection mode. There, the analyzer is set to a certain threshold energy. Only electrons with a kinetic energy higher than the threshold will be detected. Besides the elastic AM-electrons also the inelastically scattered ones with a smaller kinetic energy contribute to the signal. The kinetic energy of the AM-line is independent of the photon energy and therefore the intensity of the inelastically scattered AM-electrons will follow the elastic one. A photoelectron emission line with a kinetic energy higher than the threshold contributes to the background of the signal and does not disturb the measurement when its is constantly detected during the measurement. However, photoelectron emission lines which enter the kinetic energy interval during the measurement distort the NEXAFS signal.

The third electron detection mode is the total electron yield (TEY) mode in which all escaped electrons irrespective of their kinetic energy are detected. The TEY is dominated by the inelastic tail of the photoelectron emission spectrum (below $E_{\mathrm{kin}} \approx$20 eV). The inelastically scattered AM electrons belonging to the inelastic tail are responsible for the NEXAFS signal. The total count rate in the TEY mode is very high in comparison to the PEY and AMEY mode. The signal to background ratio decreases from the AMEY to the TEY mode in contrast to the increasing signal to noise ratio. A gas atmosphere between the sample (grounded) and detector, which is normally a metal plate on a positive potential, can enhance the TEY signal. The escaped electrons are accelerated to the detector. On their way, they ionize gas atoms/molecules and generate a cascade of secondary electrons enhancing the signal. This measuring mode is called conversion electron yield (CEY) mode [203] and has the advantage that a surface sensitive electron mode can be measured under ambient pressure conditions. Details about the CEY mode will be given in the result part of the present work.

3.3 Conductivity Measurements Using the Microwave Cavity Perturbation Method

The introduction of a sample into a microwave cavity leads to a change of its resonance frequency and its quality factor. The field distribution of the electric and magnetic field are modified by the dielectric properties of the sample[32]. The Fourier transforms of equations 2.2 and 2.4 are used to express the changes of the electric and magnetic field in terms of the cavity resonance frequency ω_0 and quality factor Q. The Maxwell equations have to be considered for an empty (labeled with the index e) and a loaded (with a sample) cavity (labeled with the index l).

$$\nabla \times \mathbf{E}_e = -i\hat{\omega}_e \mu_e \mathbf{H}_e \tag{3.10}$$

$$\nabla \times \mathbf{H}_e = i\hat{\omega}_e \varepsilon_e \mathbf{E}_e \tag{3.11}$$

$$\nabla \times \mathbf{E}_l = -i\hat{\omega}_l \mu_l \mathbf{H}_l \tag{3.12}$$

$$\nabla \times \mathbf{H}_l = i\hat{\omega}_l \varepsilon_l \mathbf{E}_l \tag{3.13}$$

$\hat{\omega}$ is the complex frequency of the microwave inside the cavity. Its real part ω_1 denotes the resonance frequency ω_0 and the imaginary part ω_2 the frequency difference between the resonance frequency and the frequency at the full half widths of the resonance peak.

$$\hat{\omega} = \omega_1 + i\omega_2 \tag{3.14}$$

$$\omega_1 = \omega_0 \tag{3.15}$$

$$Q = \frac{\omega_1}{2\omega_2} \tag{3.16}$$

Solving the system of equations (equation 3.10 - 3.13), it can be reduced to the following equation:

$$\nabla \cdot (\mathbf{H}_l \times \mathbf{E}^{\star}{}_e + \mathbf{H}^{\star}{}_e \times \mathbf{E}_l) = j\,[(\hat{\omega}_l \varepsilon_l - \hat{\omega}_e \varepsilon_e)\mathbf{E}_l \mathbf{E}^{\star}_{\mathbf{e}} + (\hat{\omega}_l \mu_l - \hat{\omega}_e \mu_e)\mathbf{H}_l \mathbf{H}^{\star}_{\mathbf{e}}] \tag{3.17}$$

The variables labeled with a star are the conjugated complex number of the corresponding variable. The integral of equation 3.17 over the volume of the cavity $\mathbf{V_C}$ is the base equation to compute perturbation of the field distribution induced by a sample.

$$\begin{aligned} &\iiint\limits_{\mathbf{V_C}} \nabla \cdot (\mathbf{H}_l \times \mathbf{E}^{\star}{}_e + \mathbf{H}^{\star}{}_e \times \mathbf{E}_l)\ d\mathbf{V} \\ &= i \left[(\hat{\omega}_l - \hat{\omega}_e) \iiint\limits_{\mathbf{V_C}} \varepsilon_e \mathbf{E}_l \mathbf{E}^{\star}{}_e + \mu_e \mathbf{H}_l \mathbf{H}^{\star}{}_e + \omega_l \iiint\limits_{\mathbf{V_C}} \Delta\varepsilon \mathbf{E}_l \mathbf{E}^{\star}{}_e + \Delta\mu \mathbf{H}_l \mathbf{H}^{\star}{}_e \right] d\mathbf{V} \\ &\text{with} \quad \Delta\varepsilon = \varepsilon_l - \varepsilon_e \end{aligned} \tag{3.18}$$

Using the Divergence theorem (equation 2.5), the left side of equation 3.18 can be simplified to the following expression:

$$\iiint\limits_{\mathbf{V_C}} \nabla \cdot (\mathbf{H}_l \times \mathbf{E}^{\star}{}_e + \mathbf{H}^{\star}{}_e \times \mathbf{E}_l)\ d\mathbf{V} = \oint\!\!\oint\limits_{\mathbf{O_C}} \mathbf{H}_l \times \mathbf{E}^{\star}{}_e + \mathbf{H}^{\star}{}_e \times \mathbf{E}_l\ d\mathbf{O} \tag{3.19}$$

$$\text{with} \quad d\mathbf{O} = \left(\frac{\partial \mathbf{r}(u,v)}{\partial u} \times \frac{\partial \mathbf{r}(u,v)}{\partial v} \right) du dv = \mathbf{n}\ du\ dv$$

In equation 3.19 $\mathbf{r}$ is the position vector and $\mathbf{u}, \mathbf{v}$ are coordinates parameterizing the surface of the cavity. The vector product of the partial derivatives equals the surface normal and therefore the surface element $d\mathbf{O}$ is perpendicular to the surface of the cavity. Concerning this fact, equation 3.19 can be simplified to:

$$\frac{\hat{\omega}_l - \hat{\omega}_e}{\hat{\omega}_e} = -\frac{\iiint_{\mathbf{V_C}} \Delta\varepsilon \mathbf{E}_l \mathbf{E}^{\star}{}_e + \Delta\mu \mathbf{H}_l \mathbf{H}^{\star}{}_e}{\iiint_{\mathbf{V_C}} \varepsilon_e \mathbf{E}_l \mathbf{E}^{\star}{}_e + \mu_l \mathbf{H}_l \mathbf{H}^{\star}{}_e} \tag{3.20}$$

The sample is generally placed at the position of the electric field maximum to determine the permittivity of the sample. In the case of a large $\mathbf{V_C} : \mathbf{V_S}$ ratio, the electric field interacting with the sample is spatially constant and also the perturbation introduced by the sample can be assumed to be constant. The permeability of the sample should be close to the value of the vacuum that no direct modification of the magnetic field is induced by the sample. Moreover, the permittivity of the medium surrounding the sample has to be equal before and after the introduction of the sample so that the field distribution is only modified by the sample. With this assumptions, equation 3.20 can furthermore be simplified to:

$$\frac{\hat{\omega}_l - \hat{\omega}_e}{\hat{\omega}_e} = -\left(\frac{\varepsilon_r - 1}{2}\right) \frac{\iiint_{\mathbf{V_S}} \mathbf{E}_l \mathbf{E}^{\star}{}_e \, d\mathbf{V}}{\iiint_{\mathbf{V_C}} |\mathbf{E}_e|^2 \, d\mathbf{V}} \tag{3.21}$$

With the definition of $\hat{\omega}$, the left side of equation 3.21 can be separated in a real part providing the change of the resonance frequency and an imaginary part providing the change of the quality factor.

$$\begin{align}
\frac{\omega_l - \omega_e}{\omega_e} &= \frac{(\omega_{l1} - \omega_{e1}) + i(\omega_{l2} - \omega_{e2})}{\omega_{l1}\left(1 + i\dfrac{\omega_{l2}}{\omega_{l1}}\right)} \notag \\
\approx \left(\frac{\omega_{l1} - \omega_{e1}}{\omega_{l1}}\right) + i\left(\frac{1}{2Q_l} - \frac{1}{2Q_e}\right) &= -\left(\frac{\varepsilon_r - 1}{2}\right) \frac{\iiint_{\mathbf{V_S}} \mathbf{E_l} \mathbf{E}^{\star}{}_e \, d\mathbf{V}}{\iiint_{\mathbf{V_C}} |\mathbf{E}_e|^2 \, d\mathbf{V}} \tag{3.22} \\
\Longrightarrow \left(\frac{\omega_{l1} - \omega_{e1}}{\omega_{l1}}\right) &= (\varepsilon_1 - 1)\hat{C} \tag{3.23} \\
\frac{1}{Q_l} - \frac{1}{Q_e} &= \varepsilon_2 \hat{C} \tag{3.24} \\
\text{with } \hat{C} &= \frac{1}{2} \frac{\iiint_{\mathbf{V_S}} \mathbf{E_p} \mathbf{E_e^{\star}} \, d\mathbf{V}}{\iiint_{\mathbf{V_C}} |\mathbf{E_e}|^2 \, d\mathbf{V}} \notag
\end{align}$$

The constant $\hat{C}$ in equations 3.23 and 3.24 is a function of the electric field perturbed by the sample and depends therefore on its geometry and permittivity. Furthermore $\hat{C}$ couples equation 3.23 and 3.24 which makes a calculation in general difficult because a model for the permittivity, for instance Lorenz-Drude model[191], of the sample have to be assumed. A more practical way to determine the constants is the calibration of the cavity with standard samples (with comparable dielectric properties). In equations 3.23

and 3.24 the new constant A/B is introduced.

$$\left(\frac{\omega_{l1}-\omega_{e1}}{\omega_{l1}}\right)=(\varepsilon_1-1)\hat{A}\frac{V_S}{V_C} \tag{3.25}$$

$$\frac{1}{Q_l}-\frac{1}{Q_e}=\varepsilon_2\hat{B}\frac{V_S}{V_C} \tag{3.26}$$

The standard samples have to fulfill the following boundary conditions:

- The sample under investigation and the standard sample have to be similar in their geometry
- The sample under investigation and the standard sample have to be placed at the same position in the microwave cavity
- The permittivity measurements of the sample under investigation and the standard samples have to be performed in the same frequency interval and therefore with the same cavity mode

The conductivity can now be calculated from equation 2.68 with the known permittivity. In the present section many assumptions were used. Thereby, the design of the experiment has to fulfill these assumptions to calculate the permittivity of a sample under investigations with equation 3.25 and 3.26. Details about the permittivity determination of powder samples will be given in the result part.

4 Results and Discussion

4.1 The model oxidation catalyst α-V_2O_5: Insights from contactless in situ microwave permittivity and conductivity measurements [1]

Christian Heine[1], Frank Girgsdies[1], Annette Trunschke[1], Robert Schlögl[1] and Maik Eichelbaum[1]

[1]Department of Inorganic Chemistry, Fritz-Haber-Institut der Max-Planck-Gesellschaft, Faradayweg 4-6, 14195 Berlin, Germany

4.1.1 Abstract

The in situ microwave cavity perturbation technique was used to study the complex permittivity and conductivity of polycrystalline α-V_2O_5 in a tubular reactor under reactive high temperature conditions with a TM_{110} cavity resonating at 9.2 GHz. The sample was investigated at 400°C in flowing air and air/n-butane mixtures while simultaneously measuring the total oxidation products CO and CO_2 by gas chromatography. The V_2O_5 powder was identified as n-type semiconductor and the dynamic microwave conductivity correlated well with the near-infrared (NIR) absorption assigned to $V3d^1$ band gap states. Correlations between catalytic performance, real and imaginary part of the permittivity and NIR absorption allowed the differentiation between bulk and surface contributions to the charge transport in reactive atmospheres. The stability of the crystalline bulk phase was proven by in situ powder X-ray diffractometry for all applied testing conditions.

---

[1] The final publication is available at Springer via http://link.springer.com/article/10.1007/s00339-013-7800-6/[doi: 10.1007/ s00339-013-7800-6]

4.1.2 Introduction

The interaction between the electronic structure of semiconducting solids and the surrounding gas atmosphere due to chemisorption of gas molecules at the solid surface has for a long time been studied by electrical conductivity measurements [72]. Charge transfer at the solid/gas interface can significantly affect the charge carrier concentration in the conduction or valence band of a semiconducting solid, and thus its overall conductivity. This observation has found broad applications in the field of gas sensors. However, the same underlying mechanisms play a major role in heterogeneously catalyzed reactions, if reducible solids (such as many transition metal oxides) are at least part of the catalytically active phase [150, 80]. One prominent and industrially highly important class of reactions is the partial oxidation of alkanes to olefins and oxygenates requiring the transfer of a rather high number of charge carriers between catalyst and organic substrate [22]. The direct functionalization of light alkanes is in particular important in light of the upcoming raw material change in the dawning post-crude oil age. An already industrially applied example is the oxidation of n-butane to maleic anhydride, which is produced in a megaton per year range, at about 400°C on vanadyl pyrophosphate [8]. Vanadyl groups (V=O), either in monomeric or polymeric form, are discussed as redox-active species in the catalytic oxidation processes [167]. Hence binary vanadium oxides are highly interesting and structurally well-defined reference materials in order to understand fundamental principles, e.g. the influence of the electronic structure and of charge transfer properties on the catalytic performance [80].

However, 2-contact type electrical conductivity measurements often applied in catalytic in situ experiments are unfortunately rather undefined and provide many sources of error in reactive atmospheres. In particular, erratic contact resistances [180] between electrode and powder and between catalyst grains and particles, possibly even changing under reactive conditions due to water evaporation, catalyst sintering, electrode corrosion, etc., hamper the accurate determination of absolute conductivities and relative changes needed for a rigorous and quantitative correlation of charge transport and catalytic properties.

In order to avoid most of such electrode contact-related problems the microwave cavity perturbation technique (MCPT) has been applied to measure the conductivity and permittivity of powder catalysts under reaction conditions in a contact free manner [53, 67]. Measurements at microwave frequencies have in addition the advantage of probing localized charge transfer processes being in particular important in catalytic reactions, whereas direct current (DC) or low frequency alternating current (AC) methods need macroscopic percolation paths to observe charge transport. In this paper we report on the application of MCPT to the in situ investigation of the complex permittivity and conductivity of vanadium(V) oxide powder under reactive catalytic n-butane oxidation conditions. The tests were run in air and in a reaction feed containing 1 vol% n-butane and 20 vol% oxygen at 400°C. This way, a direct comparison between the conductivity of the highly selective commercial VPP catalyst [52] and the total oxidation (i.e. unselective) catalyst α-V_2O_5 can be made. The results are explained in the context of further complementary in situ UV/Vis spectrocopy and in situ X-ray powder diffraction (XRPD) experiments under comparable reaction conditions.

4.1.3 Experimental

Sample

The sample under investigation was extra pure α-V_2O_5 powder from Riedel-de Haën. The phase purity was tested by X-ray powder diffractometry (XRPD). The Rietveld analysis of the XRPD pattern shown in figure 4.1, exhibits that the α-V_2O_5 powder is phase-pure. The crystal density of the V_2O_5 powder determined from the Rietveld analysis was 3.365 g/cm^3.

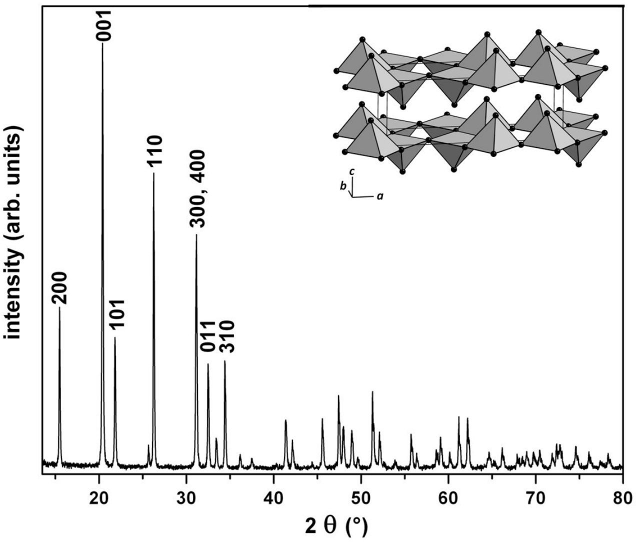

Figure 4.1: *X-ray powder diffractogram of α-V_2O_5 powder measured at room temperature (most prominent reflections indexed) and representative excerpt of the layered α-V_2O_5 crystal structure with vanadium coordination polyhedra.*

Microwave cavity perturbation measurement

The microwave conductivity setup is illustrated in figure 4.2. The microwave cavity (silver-plated brass X-band cavity from ZWG Adlershof) was used in a reflection configuration. One port of the vector network analyzer (Agilent PNA-L N5230C) was connected to the cavity by a coaxial cable and a waveguide. The microwave was coupled from the coaxial cable into the waveguide by an antenna. The coupling between the waveguide and the cavity was realized by an iris, consisting of an aperture and a coupling screw. The coupling screw is made of teflon with a brass tip. For the experiments the TM_{110} mode of the cylindrical cavity was used. The resonance frequency of the loaded and unloaded cavity was in the scan range from 9.21385 GHz to 9.26721 GHz. The scan step size was set to $4 \cdot 10^{-6}$ GHz. The complex reflection factor $\widetilde{\Gamma}(\omega)$, its amplitude being equal to the S_{11} parameter, was detected by the vector network analyzer. The fixed-bed reactor

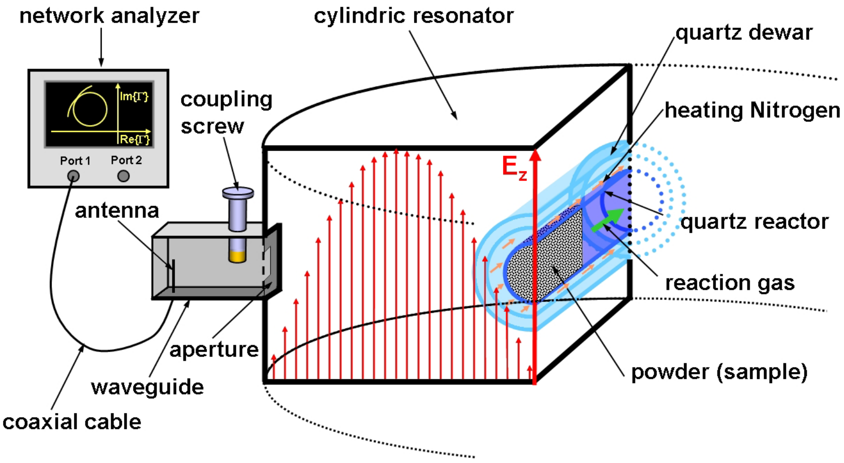

Figure 4.2: *Schematic presentation of the experimental setup including the network analyzer as microwave source and detector, coupling elements, the microwave cavity, the catalytic quartz reactor with sample position and the double-walled quartz dewar vessel to protect the cavity from convection heat from the reactor.*

for catalytic measurements consisted of a 4 mm outer diameter quartz tube located between the two maxima of the electric field. It was connected to a gas supply (mass flow controller manifold) and a gas analytics system (gas chromatograph Agilent 7890). Preheated nitrogen flowing around the reactor was used to heat the sample. The temperature was measured with a K-type thermocouple just outside the cavity. The reactor was surrounded by a vacuum pumped quartz dewar to protect the cavity from convection heat. Additionally, the cavity was water-cooled and purged with dry air in order to avoid any effects of air humidity. A detailed description of the heating and gas delivery system was reported previously [53]. This setup offers the possibility to measure the complex permittivity of single crystal and powder samples as a function of time, gas atmosphere, and temperature.

Catalytic measurements

As for the catalytic and permittivity measurements run in the MCPT setup, the α-V_2O_5 powder was first pelletized, then crushed and sieved. For all measurements shown the sieve fraction between 100 μm to 200 μm was used. The quartz tube reactor with an inner diameter of 3 mm was filled with 71.8 mg of the sieved α-V_2O_5 powder and fixed between two small quartz wool plugs. The catalyst bed length was 10.5 mm corresponding to a powder density of 0.97 g/cm^3. Accordingly, the volume fraction factor f, which is computed from the ratio of the powder and crystal density, was 0.28. The sample was heated to 400°C with a heating rate of 10 K/min in a gas atmosphere of 20 vol% oxygen and 80 vol% nitrogen. After reaching 400°C the catalytic and permittivity data acquisition was started. The sample was kept for 110 min in 20 vol% oxygen and 80 vol% nitrogen. Afterwards, the gas atmosphere was changed to 1 vol% n-butane, 20 vol% oxygen, and 79 vol% nitrogen. After 115 min the mixture was re-seted to 20 vol% oxygen and 80 vol% nitrogen for 235 min. The total gas flow was always 20 ml/min. In the described experiment the complex reflection factor as a function of frequency was measured every 5 min and a gas chromatogram was taken every 20 min.

In situ X-ray powder diffraction (XRPD)

Ex situ diffractograms were recorded on a Bruker AXS D8 diffractometer. In situ XRPD data were collected on a STOE theta-theta X-ray diffractometer (CuK$\alpha_{1,2}$ radiation, secondary graphite monochromator, scintillation counter) equipped with an Anton Paar XRK 900 high temperature reactor chamber with gas dosing system and coupled Pfeiffer OmniStar quadrupole mass spectrometer to monitor the downstream gas composition. The total flow rate was 100 ml/min. The sample was heated to 400°C with a heating rate of 10 K/min in 20 vol% oxygen and 80 vol% helium. At 400°C it was kept in this atmosphere for 6.5 hours. Then the gas composition was changed to 1 vol% n-butane, 20 vol% oxygen, and 79 vol% helium for 40 hours. Subsequently, the intial gas atmosphere (20 vol% oxygen and 80 vol% helium) was re-applied for 55 hours. All XRPD data were analyzed by full pattern fitting according to the Rietveld method using the program TOPAS [TOPAS version 3, copyright 1999, 2000 Bruker AXS].

In situ UV-VIS spectroscopy

The in situ UV-VIS experiment was performed with a Perkin Elmer Lambda 650 spectrometer equipped with a Harrick in situ reaction cell. The UV-VIS spectra were measured in diffuse reflectance geometry from 800 nm (1.55 eV) to 200 mn (6.2 eV) with a stepsize of 1 nm. Every 5 min a spectrum was taken. The Kubelka Munk theory [124] was used to evaluate the data:

$$K/S = \frac{(1-R)^2}{2\,R}, \tag{4.1}$$

where K is the coefficient of absorption, S the coefficient of scattering, and R the measured reflectance.

α-V_2O_5 powder was heated to 400°C with a rate of 10 K/min in 20 vol% oxygen and 80 vol% helium. At 400°C the sample was kept for 110 min in this gas mixture. Afterwards, the atmosphere was changed to 1 vol% n-butane, 20 vol% oxygen, and 79 vol% helium for 110 min, followed by the re-application of the first mixture for 110 min. The total flow was always 20 ml/min. The CO_2 concentration was detected with a Varian CP-4900 micro gas chromatograph to monitor the catalytic performance of the sample.

4.1.4 Results and discussion

Microwave permittivity and conductivity of α-vanadium(V) oxide

The introduction of a sample into a resonant cavity leads to a shift of the angular resonance frequency ω_0 and a change of the quality factor Q. The quality factor is defined in terms of the maximum stored energy W_s and the average dissipated power P_d in the cavity at the resonance frequency. It can also be expressed as the ratio of the resonance frequency and the full width at half minimum (FWHM) $\Delta\omega$ of the power peak:

$$Q = \left[\omega \frac{W_s}{P_d}\right]_{\omega=\omega_0} = \frac{\omega_0}{\Delta\omega} \tag{4.2}$$

In the depolarization regime the real part $\varepsilon_{1,p}$ and imaginary part $\varepsilon_{2,p}$ of the complex powder permittivity is related to the resonance frequency shift and quality factor change, respectively, with and without sample [32]:

$$A\ \left(\varepsilon_{1,p} - 1\right)\ \frac{V_s}{V_c} = \frac{\omega_1 - \omega_2}{\omega_1} \tag{4.3}$$

$$B\ \varepsilon_{2,p} \frac{V_s}{V_c} = \left(\frac{1}{Q_2} - \frac{1}{Q_1}\right). \tag{4.4}$$

ω_1 and ω_2 are the resonance angular frequencies and Q_1 and Q_2 are the quality factors of the unloaded and loaded cavity, respectively. In consideration of the experimental setup described in section 4.1.3 and figure 4.2, the 'unloaded' cavity is already loaded with the quartz dewar and the empty reactor. When a sample is introduced in the reactor, the cavity is called 'loaded'. V_s and V_c are the volumes of the sample and the cavity, respectively. A

and B are proportionality factors determined from calibration measurements of standard samples with known permittivity [53]. The sample under investigation must have the same shape as the reference samples and must be placed at the same position inside the cavity [32].

In order to transform the complex permittivity of the powder $\widetilde{\varepsilon}_p = \varepsilon_{1,p} + j\ \varepsilon_{2,p}$ into the complex permittivity of the solid $\widetilde{\varepsilon}_s = \varepsilon_{1,s} + j\ \varepsilon_{2,s}$ an effective medium theory calculation has to be applied. We used the Landau-Lifshitz-Looyenga formalism [127, 132] which is reported to provide an accurate correlation between the dielectric constants of powder and bulk in the micro- and radiowave regime for a broad range of powder volume fractions f (ratio of powder density and crystallographic (bulk) density) [49], and which gave also reliable values for semiconductor powders such as rutile TiO_2 and $SrTiO_3$:

$$\varepsilon_{1,p}^{1/3} - 1 = f\left(\varepsilon_{1,s}^{1/3} - 1\right) \tag{4.5}$$

$$\varepsilon_{2,s} = \frac{\varepsilon_{2,p}}{f}\left(\frac{\varepsilon_{1,s}}{\varepsilon_{1,p}}\right)^{2/3} \tag{4.6}$$

The relationship between the complex permittivity $\widetilde{\varepsilon}_s$ and the complex conductivity $\widetilde{\sigma}$ is given by the following equation:

$$\widetilde{\sigma} = \sigma_1 + j\sigma_2 = \varepsilon_0\ \omega\left(\varepsilon_{s,2} + j\varepsilon_{s,1}\right) \tag{4.7}$$

σ_1 describes the dielectric and/or ohmic losses (due to bound and free charge carriers, respectively) and is hence comparable with the DC conductivity, if losses not caused by free carriers can be neglected, which is a good approximation for most semiconductors [10].

In figure 4.3 the complex permittivity and conductivity, as calculated with equations (4.3), (4.4), (4.5), (4.6), and (4.7), and reaction product concentrations (i.e. catalytic performance) of α-V_2O_5 are plotted. It has been reported that 20 vol% oxygen in inert gas above 300 °C are sufficient to fully oxidize α-V_2O_5 and remove surface defects [89]. The electrical conductivity in V_2O_5 single crystals was described by free and bound polarons, the latter being localized at vanadium sites associated with oxygen vacancies [164]. The decrease of the conductivity in the first 20 min of the experiment can thus be explained by the healing of defects. The change from oxidizing to more reducing conditions (1 vol% n-butane/20 vol% oxygen/79 vol% nitrogen) induced an increase of the conductivity, which is characteristic for an n-type semiconductor and is in agreement with literature [113, 109]. The n-type conductivity is induced from non-stoichiometries in the oxide [80]. It was proposed that oxygen vacancies are compensated by vanadium species in lower oxidation states than the stoichiometric oxidation state +5, namely +4 and +3 [66]. In an oxidizing atmosphere the conductivity of an n-type semiconductor with appropriate reactivity decreases, while it increases in reducing gases. In a common model, this effect is explained by the creation of acceptor like surface states in the band gap due to the chemisorption of oxygen [72, 150]. These states act as traps for mobile electrons. Hence the equilibrium between surface and bulk states is changed which modifies the surface state induced band bending. A further discussion of the physics of the conductivity will be given after presenting the results of the complementary UV-VIS reference experiment. When the inital atmosphere was re-applied the conductivity decreased and approached

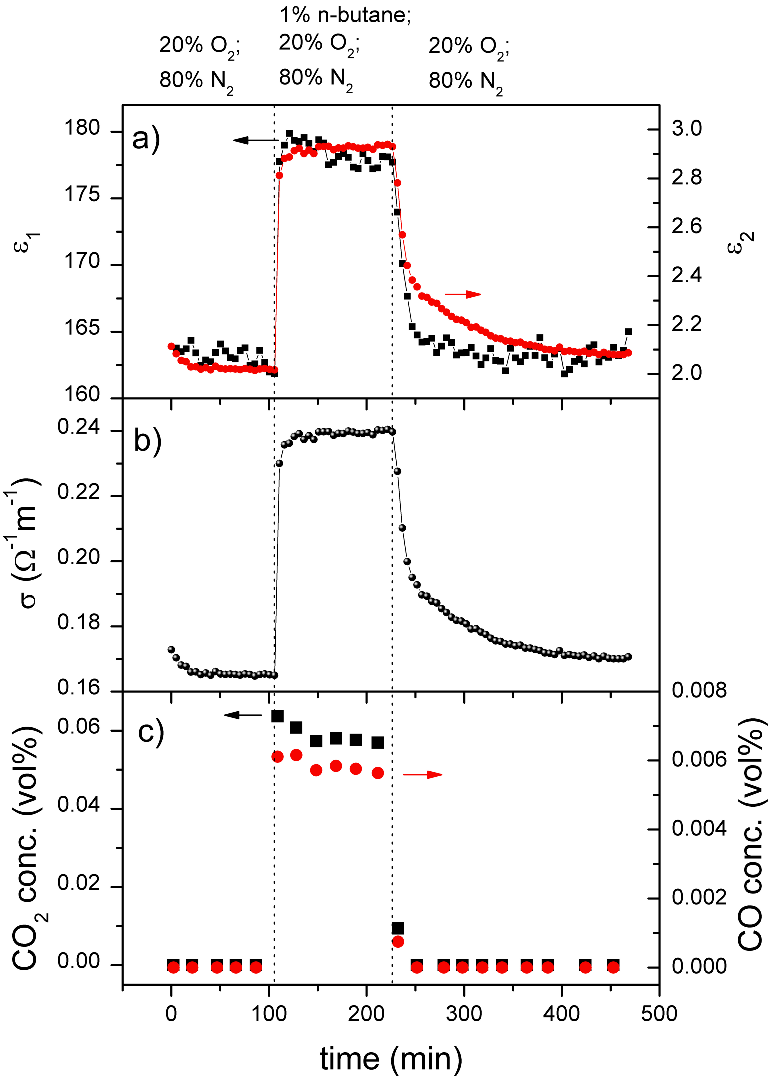

Figure 4.3: *a) ε_1, ε_2 and b) conductivity of α-vanadium(V) oxide in different reactive atmospheres at 400°C. c) Simultaneously measured CO and CO_2 concentrations evolved during the treatment of α-V_2O_5 in the different gas mixtures at 400 °C.*

only very slowly the value observed during the first atmosphere (figure 4.3b). This is in contrast to the very fast response observed in the reducing atmosphere. Interestingly, it has been reported that the re-oxidation of vanadia catalysts is the rate-limiting step in redox reactions [150, 34, 175]. For comparison, the much more active commercial catalyst vanadyl pyrophosphate (VPP), which catalyzes the selective oxidation of n-butane to the important basic chemical maleic anhydride with high selectivities, shows very fast reduction and slow oxidation kinetics as well [52]. However, the conductivity trends in the different gas mixtures are reversed, i.e. VPP exhibts a p-type conductivity behavior. An often discussed active site in oxidation catalysts is oxygen with the formal oxidation state -1 [150]. Such an ionic surface state could be formed by the trapping of an electron hole by (surface) lattice oxygen, which might explain the often observed higher catalytic activity (and probably selectivity) of p-type semiconducting oxides (in Kröger-Vink notation):

$$h^{\cdot} + \mathrm{O}_{\mathrm{O}}^{\mathrm{x}} \rightleftharpoons \mathrm{O}_{\mathrm{O}}^{\cdot} \tag{4.8}$$

This general statement is in agreement with other catalytically active vanadium phosphate samples investigated by the microwave conductivity technique [51].

The total value of the measured conductivity of V_2O_5 is orders of magnitudes higher than the conductivity of the selective catalyst VPP [52]. The absolute value of ε_2 for V_2O_5 being in the range between 2 and 3 and corresponding to a conductivity of 1.0-$1.5\cdot10^{-1}$ $(\Omega\mathrm{cm})^{-1}$ compares well with DC electrical conductivities of $3.7\cdot10^{-1}$ $(\Omega\mathrm{m})^{-1}$ for α-V_2O_5 single crystals measured at room temperature [164], though comparisons of microwave conductivities with DC values have to be taken with care due to potentially different probed processes.

In figure 4.3a the experimentally determined values of ε_1 and ε_2 are shown. As a result, both values increase similarly to the conductivity due to the change from oxidizing (20 vol% oxygen/80 vol% nitrogen) to reducing (1 vol% n-butane/20 vol%oxygen/79 vol% nitrogen) conditions and decrease when the oxidizing conditions are reapplied. This is not surprising for ε_2, since it is proportional to σ_1 after equation (4.7). The absolute value of ε_1 is in the range of 10^2, which compares well with values of 40 (b-axis) and 300 (c-axis) of single crystals measured at 10 kHz and about 200 K [88]. As for the catalytic reactivity, the parallel formation of CO and CO_2 indicates that the following combustion reactions took place at the surface of the catalyst:

$$C_4H_{10} + 6.5\ O_2 \longrightarrow 4\ CO_2 + 5\ H_2O \tag{4.9}$$

$$C_4H_{10} + 4.5\ O_2 \longrightarrow 4\ CO + 5\ H_2O \tag{4.10}$$

The maximum n-butane conversion was 8%. In detail, the time-dependent response of ε_1 and ε_2 show slight differences, in particular at the beginning and upon changing from the second to the third treatment. In the latter case ε_1 does not show the pronounced slow increase at the beginning and slow decline of σ at the end of the measurement cycle, but resembles the more rapid response of the CO and CO_2 concentration and hence the catalytic response measured simultaneously during the microwave conductivity measurement (figure 4.3c). In particular the parallel decrease at the beginning of the treatment in 1 vol% n-butane/20 vol% oxygen/79 vol% nitrogen is striking. This might point to a contribution of strong surface dipoles to ε_1 due to the adsorption of n-butane, CO_x and reaction intermediates on the surface. Moreover, the rapid stop of the reaction after switching off the n-butane gas does correlate with ε_1 but not with the conductivity change. Obviously, two processes are defining the re-oxidation behavior of the catalyst, indicated by a very fast and an underlying slow decay of the conductivty. This might point to a fast surface process (coinciding with the surface-sensitive catalytic activity and ε_1) and a slow bulk transformation, which will be examined by complementary experimental techniques presented in the next chapters.

In situ XRPD

In order to find a possible correlation between the conductivity and permittivity dynamics in oxidizing and reducing atmospheres and a possible phase transformation or a perturbation of the lattice due to the removal of oxygen from the bulk, in situ XRPD was performed. In figure 4.4a the diffractograms measured under reactive conditions (oxidizing, reaction/reducing, oxidizing conditions) are shown. In all patterns all diffraction peaks can be assigned to α-V_2O_5. In comparison to the diffractogram in figure 4.1 measured at room temperature the peaks are slightly shifted due to the anisotropic thermal expansion of α-vanadium(V) oxide [39]. However, the lattice parameters of the orthorhombic unit cell shown in figure 4.4b are indistinguishable in the different gas atmospheres. Hence the (major) increase of the conductivity in the 1 vol% n-butane/20 vol% oxygen/79 vol% nitrogen mixture cannot be assigned to a bulk phase transformation since no crystalline reduced phases such as V_4O_9 or V_6O_{13} have ben formed during the treatment. Furthermore, in figure 4.4c the ion currents (normalized to their intensity maximum) of CO (mass 28), CO_2 (mass 44), and n-butane (mass 43) recorded during the in situ XRPD experiment are

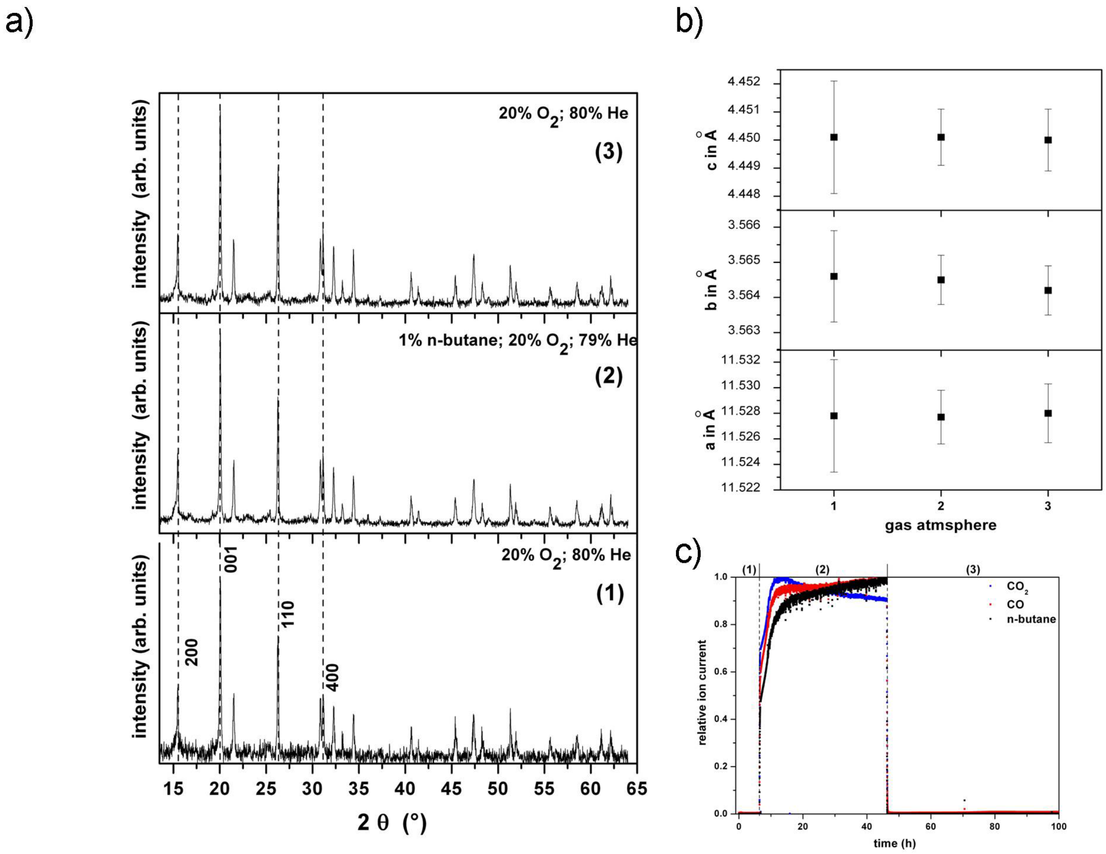

Figure 4.4: *In situ XRPD pattern (a), lattice parameters (b), and mass spectrometer data of CO, CO_2, and n-butane (c) evolved during the in situ XRPD measurement of the orthorhombic α-V_2O_5 powder in (1) 20 vol% oxygen/80 vol% helium, (2) 1 vol% n-butane/20 vol% oxygen/80 vol% helium, and (3) 20 vol% oxygen/80 vol% helium at 400°C.*

shown. Upon adding 1 vol% n-butane to the 20 vol% oxygen atmosphere, the evolution of CO and CO_2 was clearly detected indicating the catalytic activity of α-V_2O_5 under the applied experimental conditions.

In situ UV-VIS

The in situ UV-VIS experiment was performed to find indications for the presence of bulk point defects and electronic states in the band gap of α-V_2O_5 due to the proposed removal of (surface) lattice oxygen [80] that can explain the observed dynamic conductivity under different reaction conditions. In figure 4.5a three UV-VIS spectra are shown, each recorded after 1 hour in 20 vol% oxygen/80 vol% helium, 1 vol% n-butane/20 vol% oxygen/79 vol% helium, and again 20 vol% oxygen/80 vol% helium, respectively. The evolution of CO_2 during the treatment in the second mixture proved that the catalyst was working (not shown). α-V_2O_5 is characterized by an indirect optical bandgap [73]. Therefore, $(K/S\,h\nu)^{1/2}$ was plotted versus $h\nu$ and the band gap energy was determined by linear extrapolation of the low energy absorption edge as denoted in figure 4.5a. We found a value of 1.93 eV for the band gap, which is smaller than 2.2 eV reported in literature [73]. However, it is well known that the band gap of a semiconductor decreases with increasing temperature [192]. Additionally, diffuse reflection spectroscopy systematically underestimates the band gap for crystal sizes smaller than ca. 10 μm [44]. Thus, all features at photon energies smaller than 1.93 eV are assigned to band gap states. It can be seen that the K/S value is increased below 1.93 eV in 1 vol% n-butane/20 vol% oxygen/79 vol% helium compared to the K/S value measured in the 20 vol% oxygen/80 vol% helium atmosphere. It was reported that α-V_2O_5 single crystals exhibit absorption maxima at approximately 1.25 and 1.55 eV [113, 35, 66]. The increase of the 1.55 eV absorption observed under reducing conditions was assigned to electrons in vanadyl oxygen vacancies V_O (doubly ionizable donors) caused by the homogeneous loss of lattice oxygen without the formation of lower oxides. In the Kröger-Vink notation this can be expressed by the following formulae:

$$\mathrm{O_O^x} \rightleftharpoons \mathrm{V_O^x} + 1/2\mathrm{O_2} \tag{4.11}$$

$$\mathrm{V_O^x} \rightleftharpoons \mathrm{V_O^{\cdot}} + \mathrm{e}^{'} \rightleftharpoons \mathrm{V_O^{\cdot\cdot}} + 2\mathrm{e}^{'} \tag{4.12}$$

From electron paramagnetic resonance spectroscopy results it was concluded that one excess electron in the vacancy can interact with (i.e. is localized at) empty 3d-orbitals of adjacent vanadium atoms [66]. Moreover, the rather strong near-infrared (NIR) absorption was explained by charge transfer from the localized $3d^1$ (V^{4+}) states in the forbidden band gap to the conduction band or neighboring V orbitals. Consequently, we assign the increase of K/S in this range to the presence of oxygen vacancies and adjacent vanadium(IV) states perfectly rationalizing the increased conductivity. Moreover, this is in agreement with UV and X-ray photoelectron studies showing that an occupied vanadium(IV) state appears in the bandgap of α-V_2O_5 due to the removal of lattice oxygen under reducing conditions [89, 199]. When the 20 vol% oxygen/80 vol% helium was re-applied, K/S decreased again but did not reach the value of the first condition. If the absorption difference at 1.55 eV relative to the first measured spectrum at 0 min is plotted versus time and directly compared to the conductivity response (figure 4.5b) a remarkable agreement is achieved. The decrease of both absorption and conductivity at the beginning, the fast increase upon changing to reducing conditions, and the slowly falling values after re-applying the oxidizing atmosphere strongly indicate that the conductivity kinetics is governed by the (fast) formation and (slow) filling of oxygen vacancies, respectively. The latter process might be delayed due to the removal of OH groups and water

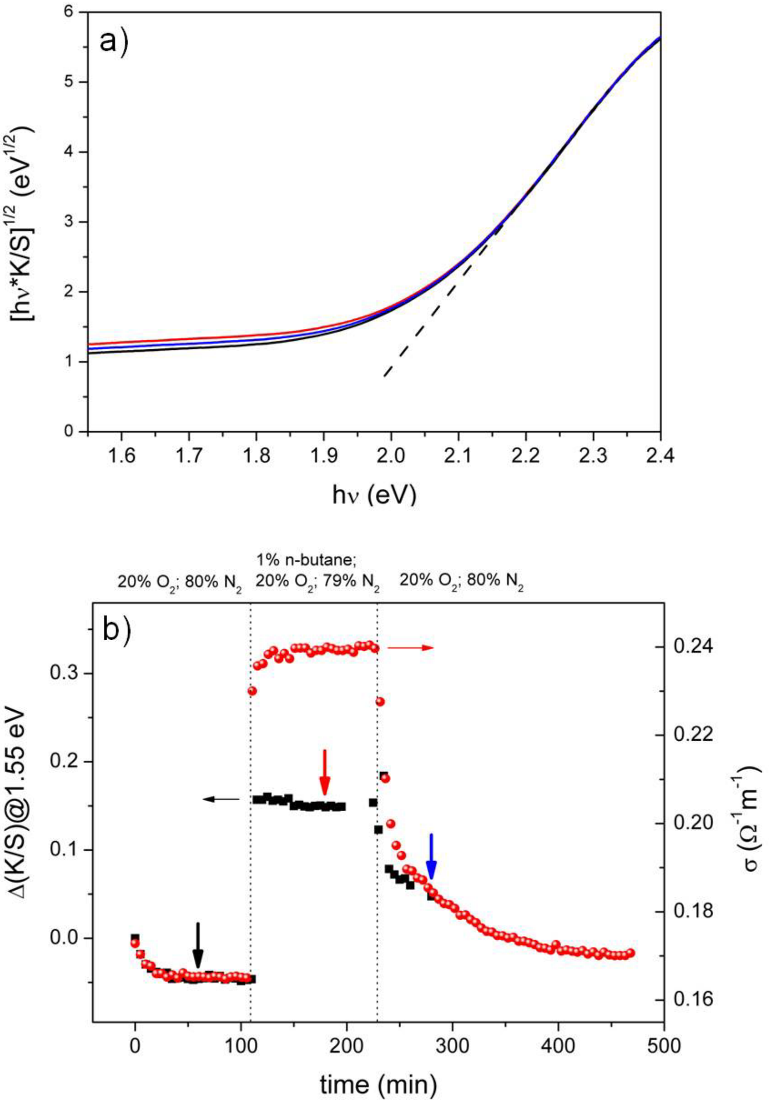

Figure 4.5: *(a) In situ UV-VIS spectra of α-V_2O_5 at 400°C measured after 1 hour in 20 vol% oxygen/80 vol% helium (black curve), 1 hour in 1 vol% n-butane/20 vol% oxygen/79 vol% helium (red), and 1 hour in 20 vol% oxygen/80 vol% helium (blue), respectively, as indicated by upright arrows in b), and extrapolation line of the band gap determination (broken line). (b) Absorption difference at 1.55 eV of α-V_2O_5 at 400°C during the different treatments compared to the first measured spectrum at 0 min (black squares). For comparison, the microwave conductivity measured under same conditions is shown (red circles).*

molecules in the vacancies produced during the alkane oxidation reaction. However, the maximum conductivity amplitude and the kinetic trend at the beginning of the treatment in the n-butane/oxygen gas mixture, as well as the initial fast decrease at the beginning of the third treatment differ from the relative time-resolved NIR absorption, but resemble more the fast response of the catalytic activity (figure 4.3c) and of ε_1 (figure 4.3a). Since the catalytic performance is associated with surface processes, e.g. formation of adsorbates, we suggest that chemisorbed reactant, intermediate and product molecules and/or active catalytic sites on the surface, very likely changing the work function of the surface due to their dipole moments (as also indicated by ε_1), are contributing to the observed conductivity under reaction conditions as well.

4.1.5 Conclusions

α-V_2O_5 powder was investigated at 400°C under reactive oxidation and reduction conditions with the in situ microwave cavity perturbation technique. As a result, we observed an increase of the micowave conductivity of V_2O_5 in the presence of a reducing agent (n-butane) in the gas feed, which is characteristic for an n-type semiconductor. Moreover, in the in situ X-ray powder diffraction experiment no phase transformation or any change of the lattice parameters were observed under reaction conditions. Hence we conclude that the bulk crystal phase is stable under the applied conditions. However, in an in situ UV-VIS reference experiment the optical absorption of α-V_2O_5 increased below the (theoretical) band gap energy in the n-butane/oxygen atmosphere, which can be attributed to the formation of oxygen vacancy point defects. Due to the perfect agreement between the time-dependent response of the absorption at 1.55 eV and the conductivity under oxidizing conditions an unambiguous correlation between the formation of point defects (and V3d band gap states) and the conductivity has been proven. Since under n-butane/oxygen conditions the absolute conductivity amplitude cannot be explained by oxygen vacancy formation alone, and since the difference correlates better with the CO/CO_2 formation, we assign this contribution to surface processes such as chemisorption. Thus, these results are suggesting the enormous potential of the microwave cavity perturbation technique for identifying and distinguishing surface and bulk processes and for elucidating their relevance for catalysis.

Acknowledgments

The authors thank Prof. R. Stößer (HU Berlin) for his continuing support of our microwave activities. Financial support by the German Federal Ministry of Education and Research (BMBF) within the framework of the ReAlSelOx project (Fkz 033R028) and by the Deutsche Forschungsgemeinschaft (DFG) are gratefully acknowledged.

4.1.6 Fit-Model Theory

Parallel resonant Circuit Model

In this section a resonant circuit model will be presented to analytically describe the MCPT setup introduced in section 4.1.3 and depicted in figure 4.2. The model is based on the work of Kajfez[111, 112] but extended by the additional perturbations due to gas phase and quartz reactor and describes the setup by an equivalent circuit (figure 4.6a)). The TM_{110} mode of the resonant cavity is represented by the parallel resonant circuit

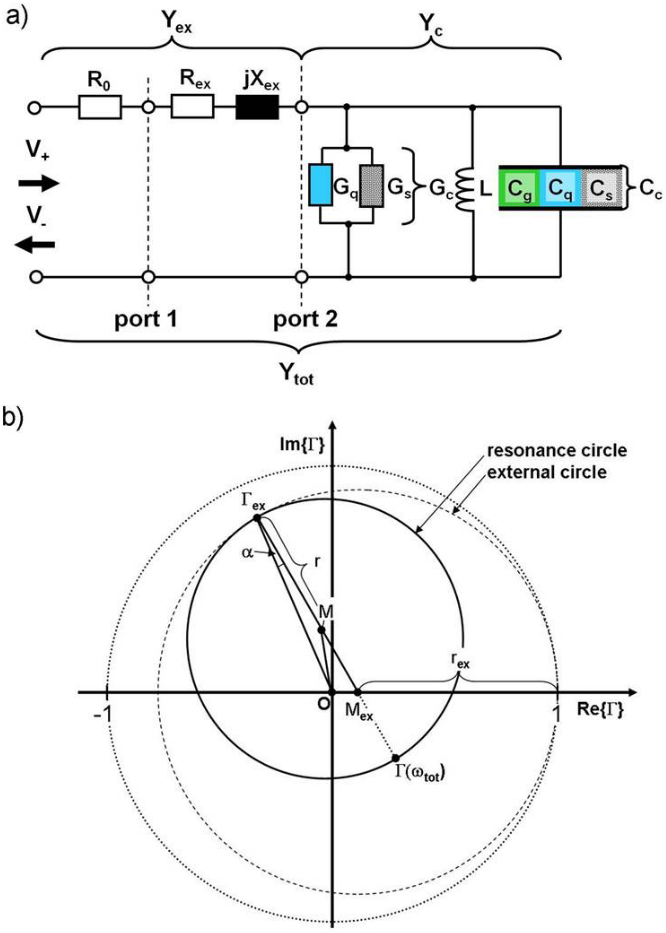

Figure 4.6: *a) Parallel resonant circuit model to analytically describe the experimental microwave cavity perturbation setup shown in figure 4.1. b) Smith chart of the complex reflection factor* $\widetilde{\Gamma}(\omega)$ *with positions of the external reflection factor* Γ_{ex} *and of the reflection factor* $\Gamma(\omega_{tot})$ *at the resonance frequency* ω_{tot}*. The definitions of the radii* r *and* r_{ex} *of the resonance and external circle, respectively, and of the centers of each circle are indicated as well.*

at port 2. The conductances G_q (quartz) and G_s (sample) describe the dielectric/ohmic losses of the quartz dewar/reactor assembly and the sample, respectively. Both conductances are summarized to G_c. The equations (4.3) and (4.4) base on the assumption that only the electric field (and not the magnetic field) of the cavity is directly perturbed by an introduced sample. Thus, the perturbation of the electric field is represented by the capacitances of the three dielectrics C_g (gas), C_q (quartz), and C_s (sample), which are summarized to C_c. The inductance L describes the magnetic properties of the cavity which are not directly affected by the sample and the quartz dewar/reactor assembly. The admittance Y_c of the parallel resonant circuit with the resonance angular frequency ω_c and the quality factor Q_c is then given by:

$$\begin{aligned} Y_c = G_c + j\left(\omega C_c - \frac{1}{\omega L}\right) &= G_c\left[1 + j\,Q_c\left(\frac{\omega}{\omega_c} - \frac{\omega_c}{\omega}\right)\right] \\ &\approx G_c\left[1 + j\,2\,Q_c\left(\frac{\omega - \omega_c}{\omega_c}\right)\right] \end{aligned} \tag{4.13}$$

$$\text{with}\quad \omega_c = \frac{1}{\sqrt{C_c\,L}} \tag{4.14}$$

$$\text{and}\quad Q_c = \frac{1}{G_c}\sqrt{\frac{C_c}{L}} = \frac{1}{G_c\,L\,\omega_c}. \tag{4.15}$$

The last term of equation (4.13) can be assumed, if the difference between ω and ω_c is small in comparison to ω_c.

According to equations (4.4) and (4.15) the quality factor is proportional to the reciprocal imaginary part of the complex permittivity and the reciprocal conductance, respectively. Consequently, in both equations the parameter representing the dielectric and/or ohmic losses is proportional to the reciprocal quality factor. Thus, the resonance frequencies ω_1 and ω_2 and the quality factors Q_1 and Q_2 of the loaded and unloaded cavity, respectively, can be expressed in the following way:

$$\omega_1 = \frac{1}{\sqrt{L\left(C_q + C_g\right)}} \tag{4.16}$$

$$\omega_2 = \frac{1}{\sqrt{L\left(C_q + C_g + C_s\right)}} \tag{4.17}$$

$$Q_1 = \frac{1}{G_q}\sqrt{\frac{\left(C_q + C_g\right)}{L}} \tag{4.18}$$

$$Q_2 = \frac{1}{G_q + G_s}\sqrt{\frac{\left(C_q + C_g + C_s\right)}{L}} \tag{4.19}$$

By insertion of the equations (4.16), (4.17), (4.18), and (4.19) in equation (4.4) a direct proportionality between $\varepsilon_{2,p}$ and G_s can be shown, assuming that the perturbation by the sample is small:

$$\varepsilon_{2,p} = \frac{L}{B}\frac{V_c}{V_s}\left[G_s\,\omega_2 + G_q\left(\omega_2 - \omega_1\right)\right] \approx \omega_2\frac{L}{B}\frac{V_c}{V_s}G_s \propto G_s \tag{4.20}$$

$$\text{with } \omega_1 \approx \omega_2$$

This equation is comparable with the real part of $\widetilde{\sigma}$ (equation (4.7)), which is also proportional to the imaginary part of the permittivity. Hence we prove here that the parallel circuit approach can be indeed used as physically meaningful model to describe the TM_{110} cavity and to separate perturbations by the quartz dewar, reactor, gas phase and sample for determining the complex permittivity of the studied material.

The resistance R_0 in figure 4.6a represents the wave resistance of the waveguide and the coaxial cable. Resistive losses in the coupling system (iris) and/or in the transmission line and waveguide are considered by the series resistance R_{ex} [70, 142]. The reactance X_{ex} describes a phase shift introduced by the coupling system. It is assumed to be constant for a single measurement [111]. The resulting admittance Y_{ex} of the external circuit is:

$$Y_{ex} = \overbrace{\frac{(R_{ex}+R_0)}{(R_{ex}+R_0)^2+X_{ex}^2}}^{G_{ex}} + j\,\overbrace{\frac{-\,X_{ex}}{(R_{ex}+R_0)^2+X_{ex}^2}}^{B_{ex}} \tag{4.21}$$

Thus, the resonant circuit at port 2 is additionally loaded by the external conductance G_{ex} and the resonance frequency is detuned by the external susceptance B_{ex}. The resulting total admittance Y_{tot} can be expressed by the following formulae:

$$\begin{aligned} Y_{tot} &= Y_{ex} + Y_c = G_{ex} + G_c + j\left[2\,Q_c\,G_c\left(\frac{\omega-\omega_c}{\omega_c}\right) + B_{ex}\right] \\ &= \left[G_{ex}+G_c\right]\left[1 + j\,2\,Q_{tot}\left(\frac{\omega-\omega_{tot}}{\omega_c}\right)\right] \end{aligned} \tag{4.22}$$

$$\text{with } \omega_{tot} = \omega_c\left(1 - \frac{B_{ex}}{2\,Q_c\,G_c}\right) \tag{4.23}$$

$$\text{and } Q_{tot} = \frac{G_c\,Q_c}{G_c+G_{ex}} \tag{4.24}$$

ω_{tot} and Q_{tot} are the total angular resonance frequency and quality factor, respectively.

In the transmission line theory the electric field is represented by a voltage and the magnetic field by a current. The reflection factor Γ measured by the vector network analyzer is the ratio of the reflected voltage V_- to the introduced voltage V_+ and can be expressed in terms of the impedance Z_i at port 1 and the wave resistance R_0 (cf. figure 4.6a).

$$\Gamma = \frac{V_-}{V_+} = \frac{Z_i - R_0}{Z_i + R_0} = \frac{R_{ex} + j\,X_{ex} + Y_c^{-1} - R_0}{R_{ex} + j\,X_{ex} + Y_c^{-1} + R_0} = \Gamma_{ex} + \frac{2\,R_0\,Y_{ex}^2}{Y_{tot}} \tag{4.25}$$

$$\text{with } \Gamma_{ex} = \frac{R_{ex} + \; jX_{ex} - R_0}{R_{ex} + j\,X_{ex} + R_0} \tag{4.26}$$

Γ_{ex} is the reflection factor of the external circuit.

The reflection factor is a function of frequency and describes a circle in the Smith chart [5] as shown in figure 4.6b. Γ_{ex} represents the point of the detuned resonance with a phase shift of 180° to the reflection factor of the total resonance frequency $\Gamma(\omega_{tot})$ relative to the center of the resonance circle (point M in figure 4.6b). It also describes a circle as a function of X_{ex}. Therefore, the complex equations (4.25) and (4.26) can be transformed into circle equations:

$$(\mathbf{Re}\{\Gamma\} - \mathbf{Re}\{M\})^2 + (\mathbf{Im}\{\Gamma\} - \mathbf{Im}\{M\})^2 = \underbrace{\left(\frac{R_0}{G_{ex} + G_c}|Y_{ex}|^2\right)^2}_{r^2} \tag{4.27}$$

$$\text{with } \mathbf{Re}\{M\} = |Y_{ex}|^2 \left(\frac{R_0}{G_c + G_{ex}} + R_{ex}^2 - R_0^2 + X_{ex}^2\right), \tag{4.28}$$

$$\mathbf{Im}\{M\} = 2\,R_0\,|Y_{ex}|^2\,X_{ex}\left(1 - \frac{G_{ex}}{G_{ex} + G_c}\right)$$

$$\left(\mathbf{Re}\{\Gamma_{ex}\} - \frac{R_{ex}}{R_0 + R_{ex}}\right)^2 + \mathbf{Im}\{\Gamma_{ex}\}^2 = \underbrace{\left(\frac{R_0}{R_0 + R_{ex}}\right)^2}_{r_{ex}^2} \tag{4.29}$$

Finally, equation (4.25), after considering an additional phase shift $e^{j\gamma}$, the total admittance Y_{tot}, and the radius of the resonance circle r, can be directly used as a complex fit function to determine Q_{tot}, ω_{tot}, and ω_c (without the need for linear fractional transformations highly dependent on the concrete pre-estimated fit parameters reported in earlier work [111, 112]):

$$\tilde{\Gamma}(\omega) = \Gamma(\omega) e^{j\gamma} = \Gamma_{ex}\,e^{j\gamma} + \frac{2\,r\,e^{j\,(2\phi\{Y_{ex}\}+\gamma)}}{1 + j\,2\,Q_{tot}\left(\dfrac{\omega - \omega_{tot}}{\omega_c}\right)} \tag{4.30}$$

$\phi\{Y_{ex}\}$ is the phase of Y_{ex}. $e^{j\gamma}$ considers a phase shift which is caused by the length of the waveguide and coaxial cable. It rotates the resonance and the external circle through the same angle. Thus, the angular relationship and the size ratio between the resonance and external circle is not affected by the rotation.
As mentioned above, the total quality factor can be determined with equation (4.30), but it is loaded by the resistive losses of the external circuit. To separate the dielectric and ohmic losses in the cavity $P_{d,c}$ from the resistive losses in the external system $P_{d,ex}$, equation (4.2) is used and the so called coupling factor κ is introduced:

$$\frac{1}{Q_{tot}} = \frac{P_{d,c} + P_{d,ex}}{\omega_c\, W_s} = \frac{1}{Q_c} + \frac{1}{Q_{ex}} \;\Rightarrow\; Q_c = Q_{tot}\,(1+\kappa) \tag{4.31}$$

$$\text{with}\;\; \kappa = \frac{Q_c}{Q_{ex}} = \frac{P_{d,ex}}{P_{d,c}} = \frac{G_{ex}}{G_c} = \frac{r}{r_{ex} - r} \tag{4.32}$$

Hence the quality factor of the cavity can be determined from the total quality factor and the radii of the resonance and the external circle, respectively.
The radius of the external circle r_{ex} can be determined from the triangles ($0\; M_{ex}\; \Gamma_{ex}$) and ($0\; M\; \Gamma_{ex}$) in the Smith chart (figure 4.6b). The points Γ_{ex}, M, $\Gamma(\omega_{tot})$ and M_{ex}, the latter being the center of the external circle, are located on one line because the tangent of the resonance circle is equal to those of the external circle in Γ_{ex}. From equation (4.29) it can be seen that the external circle touches the circle of unity in the point (1,0). Therefore, the distance $\overline{0M_{ex}}$ is equal to $(1 - r_{ex})$, and $\overline{0\Gamma_{ex}}$ is the absolute value of Γ_{ex}. Thus, r_{ex} can be computed with the law of cosines:

$$r_{ex} = \frac{1 - |\Gamma_{ex}|^2}{2 - \dfrac{r^2 + |\Gamma_{ex}|^2 - \overline{0M}^2}{r}} \tag{4.33}$$

Data Fit Method

The fit program is based on the Levenberg-Marquardt algorithm [129, 143] and was implemented using the LabVIEW environment. It fits the real and imaginary part of the measured reflection factor $\widetilde{\Gamma}_i$ as a function of frequency. An equal number of data points above and below the resonance frequency, which is first estimated with the frequency at the minimum of $\left|\widetilde{\Gamma}_i\right|$ (amplitude), is used for the fit. Equation (4.30) was slightly modified to stabilize the fit procedure:

$$\widetilde{\Gamma}(\omega) = \widetilde{\Gamma}_{ex} + \frac{2\, r\, e^{j\delta}}{1 + j\, 2\, Q_{tot} \left(\dfrac{\omega - \omega_{tot}}{\omega_{tot}} \right)} \tag{4.34}$$

$$\text{with } \widetilde{\Gamma}_{ex} = \Gamma_{ex}\, e^{j\gamma} \text{ and } \delta = 2\phi \left\{ Y_{ex} \right\} + \gamma \tag{4.35}$$

The fit parameters are the total angular resonance frequency ω_{tot}, the total quality factor Q_{tot}, the real and imaginary part of the external reflection factor $\widetilde{\Gamma}_{ex}$, the radius of the resonance circle r, and the phase shift δ. ω_c is exchanged by ω_{tot} in the denominator of the frequency term in equation (4.34), since the difference between ω_c and ω_{tot} is small in comparison to ω_c[111]. This modification reduces significantly the influence of the initial fit parameters on the fit result.

Another improvement of the fit procedure is the introduction of a square root radial weighting function W [156]:

$$W = \left[\frac{1}{\sqrt{\left(\mathbf{Re}\{M\} - \mathbf{Re}\{\widetilde{\Gamma}_i\} \right)^2 + \left(\mathbf{Im}\{M\} - \mathbf{Im}\{\widetilde{\Gamma}_i\} \right)^2}} \right]^{1/2} \tag{4.36}$$

The point M is the center of the resonance circle as shown in figure 4.6b. Equation (4.36) reduces the influence of noisy data points well outside the circle [156]. The center of the resonance circle is first estimated by a circle fit which is weighted with the following function, known as the standard weighting:

$$W_{st} = \left[\left(\mathbf{Re}\{\widetilde{\Gamma}_{ref}\} - \mathbf{Re}\{\widetilde{\Gamma}_i\} \right)^2 + \left(\mathbf{Im}\{\widetilde{\Gamma}_{ref}\} - \mathbf{Im}\{\widetilde{\Gamma}_i\} \right)^2 \right]^2 \tag{4.37}$$

The reference point $\widetilde{\Gamma}_{ref}$ is in the middle between the first and last data point. Thus the data points close to the resonance frequency are heavier weighted than those further away. By using the previously estimated resonance frequency, estimated diameter, and a quality factor which is estimated with the 3 dB method from $\left| \widetilde{\Gamma}_i \right|$(amplitude) as initial fit parameters, this new fit procedure runs very stable and is easiliy automated. The center of the resonance circle is determined from the best fit curve and Q_c can be computed using equations (4.31) and (4.33).

In order to determine the quality factor with the 3-dB method, the amplitude of the first data point (at the lowest measured frequency) is defined to estimate the background to calculate the value at $1/\sqrt{2}$ of the resonance peak minimum. The two frequencies of the data points which are the closest to the calculated value are used to estimate $\Delta\omega$. Using equation (4.2), the quality factor can be computed from the estimated resonance frequency and FWHM (i.e. $\Delta\omega$).

4.1.7 Data Evaluation with the parallel resonant Circuit Fit Method

In this section the data evaluation with the fit method is demonstrated for an in situ measurement of the complex permittivity of α-V_2O_5. First, the model was tested for different frequency intervals. In figure 4.7a the complex reflection factor of the V_2O_5 loaded cavity at 400°C and three Smith chart fits, calculated as described in the previous chapter, for different frequency intervals $\delta\omega$, are shown. The frequency interval is normalized to the FWHM $\Delta\omega = \omega_{\text{tot}}/Q$ of the cavity resonance peak (power) in order to compare fits of measured circles with different quality factors. The evaluated ω_{tot}, Q_{tot}, and Q_c from the three circle fits are summarized in table 4.1. It can be clearly seen that the Smith chart fit with the smallest normalized frequency interval gives the best agreement with the experimental data. Additionally, the calculated $\widetilde{\Gamma}_{ex}$ of this fit plotted in figure 4.4a is closest to the experimental value. Figure 4.4b shows the corresponding measured and fitted amplitude and phase of the complex reflection factor. A comparison of the residuals between the measured and fitted data confirms that the best fit is obtained with $\delta\omega/\Delta\omega = 0.8$. This result is caused by the limitations of equation (4.13). The simplifications of the imaginary part are only justified, if the frequency interval is small in comparison to the resonance frequency. From table 4.1 it can be seen that Q_c has a value larger than 1000 for every fit. Therefore, the FWHM of the resonance peak is smaller than the one thousandth part of the resonance frequency. A fit of the data within a frequency interval smaller than the FWHM of the resonance peak fulfills the assumption for equation (4.13). In order to have an adequate number of data points within the frequency interval, $\delta\omega/\Delta\omega$ is chosen close to one for the data evaluation of the experiment.

$\delta\omega/\Delta\omega$	$\omega_{\text{tot}}/2\pi$	Q_{tot}	Q_c	$\text{Re}\{\widetilde{\Gamma}_{ex}\}$	$\text{Im}\{\widetilde{\Gamma}_{ex}\}$
4.3	9.244063	2312	3028	-0.8	-0.51
2	9.244054	2151	2820	-0.8	-0.52
0.8	9.244014	2079	2752	-0.8	-0.54

Table 4.1: *ω_{tot}, Q_{tot}, and Q_c as calculated from the three Smith chart fits shown in figure 4.6a.*

In figure 4.8a Q_c, Q_{tot}, and Q(3 dB), the latter being calculated after the determination of the FWHM at 3 dB of the reflection amplitude (cf. chapter 4.1.6), determined from the measurement of V_2O_5 under the conditions described in section 4.1.3, are compared. At

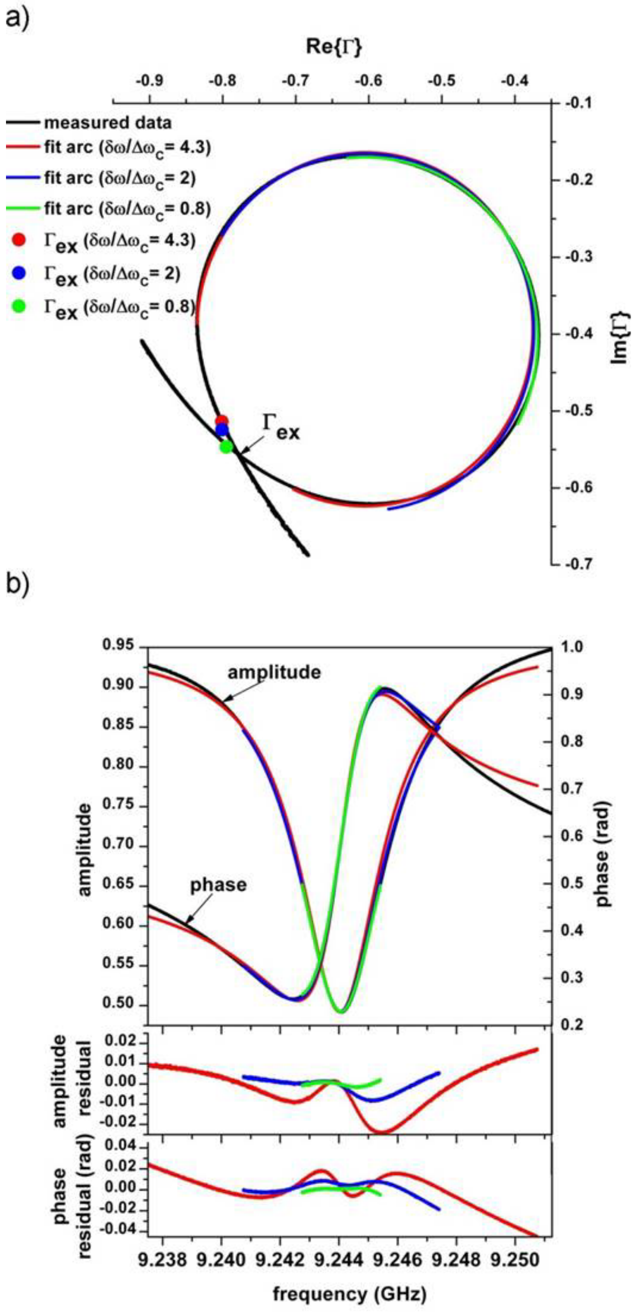

Figure 4.7: *a) Experimentally measured Smith chart of the complex reflection factor $\widetilde{\Gamma}(\omega)$ and three Smith chart fits calculated with the developed parallel resonant circuit model for three different normalized frequency intervals and resulting positions of the external reflection factor Γ_{ex}. b) Corresponding amplitude and phase of the experimental complex reflection factor, of the fitting results, and of the residuals of the difference between measured and calculated data points.*

the beginning of the experiment all quality factors increase slightly in the 20 vol% oxygen, 80 vol% nitrogen atmosphere. After 20 minutes the quality factors reach a constant value. When the gas atmosphere was changed to 1 vol% n-butane, 20 vol% oxygen, and

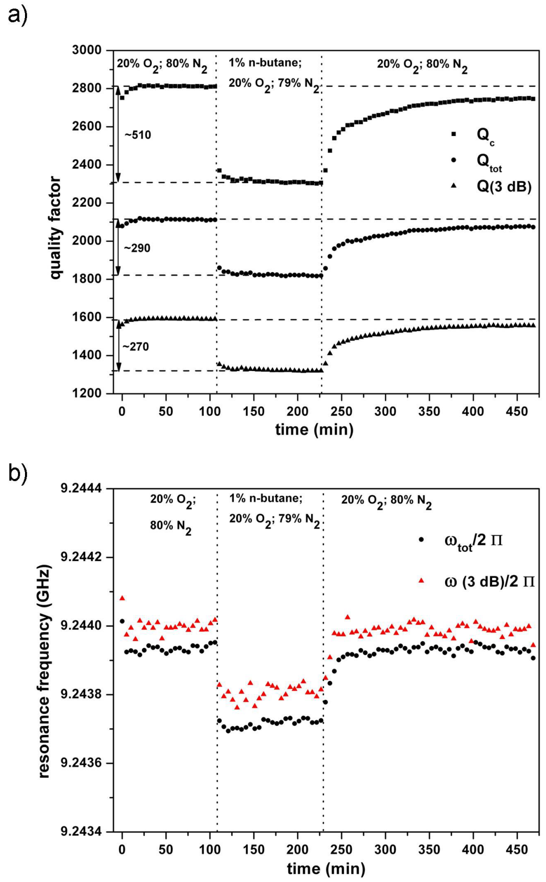

Figure 4.8: *a) Experimentally measured Smith chart of the complex reflection factor $\widetilde{\Gamma}(\omega)$ and three Smith chart fits calculated with the developed parallel resonant circuit model for three different normalized frequency intervals and resulting positions of the external reflection factor Γ_{ex}. b) Corresponding amplitude and phase of the experimental complex reflection factor, of the fitting results, and of the residuals of the difference between measured and calculated data points.*

79 vol% nitrogen, all quality factors decreased instantaneously and reached a steady-state after about 40 min. After applying the intial gas atmosphere (20 vol% oxygen, 80 vol% nitrogen), the quality factors rose rapidly within the first 25 min. Subsequently, they approached values being below the plateau observed during the first treatment in this gas mixture. It is to note, that no quality factor changes with gas atmospheres were observed, if only the empty reactor without catalyst was tested. Thus, all quality factors show qualitatively a similar behavior upon gas atmosphere changes. However, Q_c is always larger than Q_{tot}, while Q(3dB) is smallest. This observation can be explained with the influence of $\widetilde{\Gamma}_{\mathrm{ex}}$ and κ on Q_{tot} and Q_c. The background of Q(3 dB) is estimated with the amplitude at the first data point measured at the lowest frequency of the scan interval. However, figure 4.7b clearly indicates that the background is not constant in the frequency scan interval. Therefore, the background estimation is not accurate enough. In the fit model

the background is represented by $\widetilde{\Gamma}_{\text{ex}}$, which is the point of the detuned resonance. The external circuit illustrated in figure 4.6a) loads the cavity. From equation (4.31) it can be seen that the load, which is represented by $P_{d,ex}$, reduces Q_{tot} relative to Q_c. By considering the coupling factor κ, $P_{d,ex}$ can be subtracted from the denominator of Q_{tot} and Q_c is obtained. As a consequence, the losses caused by the sample are heavier weighted after the coupling factor correction. Thus, the difference of the quality factor values between the first and the second gas atmosphere is greater in the case of Q_c than for Q_{tot} (and Q(3 dB)). This is an important result of the fit approach since it has direct consequences on the obtained sensitivity of the method, as will be shown in the next chapter.

figure 4.8b shows the resonance frequencies evaluated with the 3 dB method (direct determination of the reflection amplitude minimum from measured data points) and the parallel resonant circuit model recorded during the catalytic experiment. ω_{tot} and ω(3 dB) decrease instantaneously upon changing the gas atmosphere from 20 vol% oxygen/80 vol% nitrogen to 1 vol% n-butane/20 vol% oxygen/79 vol% nitrogen. After applying the initial atmosphere both resonance frequencies increase again. Therefore, the qualitative behavior of the resonance frequencies is similar for both evaluation methods. However, the data scattering of ω_{tot} is much smaller than for ω(3 dB), proving again the major benefit of the fit model.

4.2 Work Function, Band Bending and Microwave Conductivity Studies on the Selective Alkane Oxidation Catalyst MoVTeNb Oxide (Orthorhombic M1 Phase) under Operation Conditions [2]

Christian Heine[1], Michael Hävecker[1,2], Maricruz Sanchez-Sanchez[1,3], Annette Trunschke[1], Robert Schlögl[1] and Maik Eichelbaum[1,4]

[1]Fritz Haber Institute of the Max Planck Society, Department of Inorganic Chemistry, Faradayweg 4-6, 14195 Berlin, Germany
[2]Helmholtz Centre Berlin / BESSY II, Solar Energy Research, Albert-Einstein-Straße 15, 12489 Berlin, Germany
[3]Present address: Technische Universität München, Department Chemie, Lichtenbergstraße 4, 85747 Garching, Germany
[4]BasCat, UniCat BASF JointLab, TU Berlin, Marchstraße 6, 10587 Berlin, Germany

4.2.1 Abstract

A systematic gas phase-dependence of the electron work function, electron affinity, band bending and the high frequency electrical conductivity of the prospective oxidation catalyst MoVTeNbO$_x$ with orthorhombic M1 structure was identified under selective alkane oxidation conditions. The conductivity measured in a fixed bed flow reactor at 1 bar with a noncontact microwave technique and the surface electronic properties studied by in situ X-ray photoelectron spectroscopy at 0.25 mbar were determined at 400°C in 2:1 mixtures of oxygen and the alkanes ethane, propane, and n-butane, respectively. The observed modulation of the surface electron affinity is explained by a gas phase dependent modification of the dipolar structure of the active surface, while the band alignment is interpreted

---

[2] Reprinted (adapted) with permission from [Christian Heine, Michael Hävecker, Maricruz Sanchez-Sanchez, Annette Trunschke, Robert Schlögl and Maik Eichelbaum; Work Function, Band Bending and Microwave Conductivity Studies on the Selective Alkane Oxidation Catalyst MoVTeNb Oxide (Orthorhombic M1 Phase) under Operation Conditions; 117; 26988 - 26997; December 2013; doi: 10.1021/jp409601h] Copyright [2013] American Chemical Society

in terms of the formation and modification of the space charge region due to pinning of the Fermi energy to the surface state energy as defined by the V^{4+}/V^{5+} oxide surface layer. The thus changed charge carrier density in the space charge region gives rise to the observed conductivity response. Consequently, the catalytic system and its working mode can be described as a semiconductor heterostructure comprising the semiconducting bulk phase, a V^{4+}/V^{5+} oxide termination layer, and the reactive gas phase modulating the Fermi energy of the whole system.

4.2.2 Introduction

The catalytic oxidation of natural gas, basically comprising methane, ethane, propane, and butanes, to the respective olefines and oxygenates is becoming increasingly important with the dawning raw material change in the chemical industry[22], but suffers still from the lack of highly selective catalysts for most reactions. Generally, understanding the electronic interaction between gas phase, the active catalyst surface and the crystalline bulk phase and the correlation with simultaneously measured catalytic data are prerequisites for identifying structure-function relationships that have the predictive power for suggesting better oxidation catalysts going beyond empirical trial and error research. Interestingly, most alkane oxidation catalysts are (transition) metal oxides with semiconducting or insulating collective electronic properties [150]. Consequently, since the advent of semiconductor physics attempts have been made to predict catalytic properties on the basis of the electronic (bulk) structure of the catalyst [18, 195]. This idea is based on the concept that the bulk electronic structure, namely the (electro-)chemical potential of electrons, i.e. Fermi potential, of the semiconductor, is influenced by 1) the bulk crystal structure, 2) the impurity (dopant) concentration, and 3) the temperature. Consequently, one could conclude that in oxidation catalysis the charge transfer between a semiconducting catalyst and the reactants, which is, besides the also very important local bonding effects, defined by the relative position of the Fermi potential and the redox potentials of the reactants. Thus the adsorption and catalytic properties could be modified by adjusting the ratio of electron (or hole) acceptors and donors in the bulk by doping or by the rational synthesis of a crystal structure with tailored Fermi energy. However, as already mentioned by Boudart in 1952 [18], a fourth parameter influencing the electronic chemical potential of a semiconductor is the partial pressure and the nature of the reactants and products, i.e. the gas phase chemical potential, that can form or modifiy surface states on the semiconductor. If these surface states, or the 'defect one-phase surface system' as it was called by Boudart [18], with a Fermi energy adjusted to the working conditions, are pinning the Fermi energy of the bulk to the surface state energy [150], the effect of dopants or even changes in the crystal structure on the Fermi level might be small. As a consequence, catalysis research in the last decades has concentrated on the search for the catalytically active site, mostly described by surface molecular models [75], with a strong emphasis on local bonding while ignoring collective properties of the catalyst as described within the rigid band model [150]. Many surface-sensitive studies on oxidation catalysts under operation conditions in the last years have shown indeed that the active surface is highly dynamic and deviates significantly in elemental composition and transition metal oxidation states from the bulk crystalline phase [87, 197, 52, 37, 26, 114, 85, 14]. Consequently, a picture of an active 2-dimensional surface phase with a sharp phase boundary to the bulk phase developing only under operation conditions has evolved [167]. Hence the questions arise why and how such a surface is formed on metal oxides, how it is stabilized and why it does not suffer from over-oxidation or -reduction, and how it interacts with the reactive gas phase leading to the desired partial oxidation instead of the thermodynamically favored product CO_2. The electronic properties of such a surface/bulk interface could be in principle described as well by semiconductor concepts, e.g. if the Fermi level of the bulk would be pinned by the surface layer, which itself is modified by the reactive gases. In this way, the developed phenomenological description of an oxidation catalyst could be rationalized by physical quantities. The alignment of the Fermi energy by the gas phase would manifest itself in a change of the work function and in the core and valence electron binding energies (band bending of the conduction and valence band). Electrical conductivity changes would indicate the modification of the charge carrier density in the bulk and hence give further evidence for band bending and the formation of a double layer comprising a (sub-surface) space charge region and an oppositely charged surface layer as described by rigid band semiconductor models [150]. In our contribution we are showing for the first time that by the complementary application of a contactless in situ conductivity method based on the microwave cavity perturbation technique [53] at ambient pressure, and of in situ X-ray photoelectron spectroscopy (XPS) at 25 Pa, the interaction between gas phase, surface, and bulk electronic structure can be probed under reaction conditions in order to provide evidence that the operation mode of the studied alkane oxidation catalyst $MoVTeNbO_x$ M1 can be described by principles of semiconductor physics. The mixed multi metal oxide $MoVTeNbO_x$, which is one of the most promising catalysts for various selective alkane oxidation reactions [22], was investigated in the selective oxidation of ethane, propane, and n-butane with molecular oxygen. The gas phase dependent vanadium oxidation state, work function, electron affinity and band alignment based on binding energy shifts of the valence band edge and core level states, were measured with XPS, and were correlated with the microwave conductivity measured in a fixed-bed flow reactor under proven operation conditions. The obtained information was used to develop a consistent model of the working mode of selective alkane oxidation catalysts.

4.2.3 Experimental Section

Catalyst synthesis

The MoVTeNb oxide composed of the M1 structure was prepared according to a precipitation-purification procedure described previously [116]. Briefly, $(NH_4)_6Mo_7O_{24}\cdot 4H_2O$ (22.95 g; grade: for analysis, Merck) was dissolved in MQ water (100 ml) at 353 K. Then, NH_4VO_3 (4.56 g; 99.0%, Fluka) was added and dissolved. Next, $Te(OH)_6$ (6.87 g; 97.5-102.5%, Aldrich) was added to the Mo/V-containing solution at 313 K. In parallel, the Nb-containing solution was prepared by dissolution of $NH_4[NbO(C_2O_4)_2]\cdot xH_2O$ (7.16 g; 99.99%, 20.17% Nb, H.C. Starck) in MQ water (30 ml) at 313 K. This solution was then added to the Mo/V/Te-containing solution. After stirring for 30 min at 313 K, the resultant slurry with a nominal molar Mo/V/Te/Nb ratio of 1:0.3:0.23:0.125 was spray-dried by using a Büchi B-191 mini spray-dryer. The as-prepared powder was calcined at 548 K for 1 h in synthetic air flow and then annealed at 873 K in an Ar flow by using a rotary tube furnace (Xerion) for 2 h. Thus, a biphasic crystalline M1 and M2 MoVTeNb oxide was generated. Next, M1 was isolated from M2 through treatment of the mixed-phase powder (15 g) by using a 15% H_2O_2 solution (425 ml) at room temperature while stirring continuously (400 rpm) for 24 h. The washed product was collected by using vacuum filtration using a glass filter (porosity 5), washed with MQ water, and dried at 368 K. Finally, the as-derived sample was heat-activated at 873 K in an Ar flow for 2 h by using the rotary tube furnace resulting in 9 g M1 (internal catalyst ID 10790). The Rietveld analysis of the X-ray powder diffraction pattern exhibited that the activated powder was phase-pure M1 (figure 4.9). The surface area was 9.2 m^2/g as measured by Brunauer-Emmett-Teller (BET) nitrogen adsorption. Relative metal contents of 65 at% Mo, 6 at% Te, 19 at% V, and 10 at% Nb have been determined by X-ray fluorescence analysis.

Microwave cavity perturbation technique

The electrical conductivity of the sample was measured in a contact free manner with the microwave cavity perturbation technique [176]. The introduction of a sample into the resonant cavity causes a perturbation of the standing electromagnetic wave inside. This perturbation causes a shift of the resonance frequency ω_0 and a change of the quality factor $Q = \omega_0/\Delta\omega$, which is the ratio of the resonance to the full half width of the resonance peak $\Delta\omega$. From these two quantities the complex permittivity of the powder $\varepsilon_p = \varepsilon_{p,1} + i\varepsilon_{p,2}$ can be computed. In the case of the semiconducting M1 phase the depolarization regime

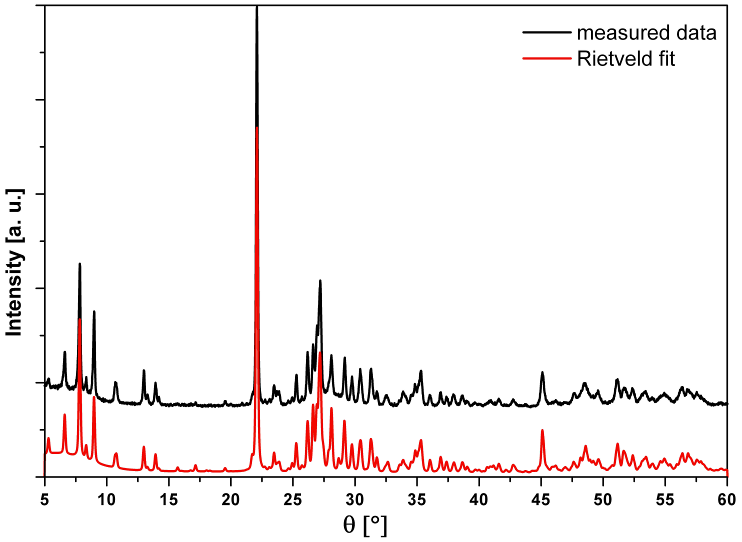

Figure 4.9: *X-ray powder diffraction pattern of M1 and the corresponding Rietveld fit of the M1 structure.*

[32] is considered for the calculation:

$$A\ \left(\varepsilon_{1,p}-1\right)\ \frac{V_s}{V_c}=\frac{\omega_1-\omega_2}{\omega_1} \tag{4.38}$$

$$B\ \varepsilon_{2,p}\frac{V_s}{V_c}=\left(\frac{1}{Q_2}-\frac{1}{Q_1}\right). \tag{4.39}$$

ω_1 and ω_2 are the resonance angular frequencies and Q_1 and Q_2 are the quality factors of the empty and sample-loaded cavity, respectively. V_s and V_c are the volumes of the sample and the cavity, respectively. A and B are proportionality factors determined by permittivity standards. After transforming the powder permittivity into the bulk permittivity ε_s with the Landau-Lifshitz-Looyenga effective medium model [132, 49], the conductivity σ can be calculated after:

$$\sigma=\varepsilon_0\omega_2\varepsilon_{s,2} \tag{4.40}$$

For the in situ studies the sample was placed in a fixed bed reactor (inner diameter of 3 mm) connected to a gas supply system and a gas chromatograph. To heat the sample, nitrogen gas was preheated in a resistive furnace and guided within a double walled quartz dewar system to the reactor tube. The reactor tube is located in the center of the cavity perpendicular to the resonator endplates. For the measurements the TM_{110} mode with a resonance frequency of about 9.2 GHz was used. A more detailed description of the method and the setup was reported previously [53]. In all experiments the gas flow through the reactor was 20 ml/min, corresponding to a gas hourly space velocity of 13333 ml/(g h) (with a catalyst mass of 90 mg and a bed length of 10.6 mm). For the measurements the powder catalyst was first pelletized, then crushed and finally sieved to use the sieve fraction between 100 and 200 μm. For the catalytic studies the gas flow was controlled with mass flow controllers (Bronkhorst) using gases with 99.95 vol% purity.

In situ photoelectron spectroscopy

In situ X-ray photoelectron spectroscopy (XPS) was performed at the synchrotron radiation facility BESSY II in Berlin. At the ISISS (Innovative Station for In Situ Spectroscopy) beamline monochromatic X-ray light was used to obtain high pressure XP spectra in the presence of reactive gases (alkane + oxygen) at elevated temperatures. Details of the vacuum system and the electronanalyser were reported before [193, 15]. For the XPS studies 10 mg of M1 powder were pressed into a self-supporting pellet (1 ton pressing pressure, diameter of pellet: 8 mm). In the experiment M1 was heated to 400°C with a heating rate of 5 K/min in the presence of propane/oxygen feed (volume flow ratio 1 sccm/ 2sccm). The total pressure was 25 Pa during the experiment. The following protocol was performed: $C3/O_2 \rightarrow C2/O_2 \rightarrow C3/O_2 \rightarrow C4/O_2 \rightarrow C3/O_2 \rightarrow C2/O_2 \rightarrow C4/O_2$. Alkanes, olefins (ethylene, propylene), CO, and CO_2 were analyzed with a micro gas chromatograph (micro-GC, Varian) after compressing the gas to atmospheric pressure. In parallel, the oxygenates (acetic acid, acrylic acid, maleic anhydride) were detected with a proton transfer reaction mass spectrometer (PTR-MS, IONICON).

Core level spectra of O1s, V2p, Mo3d, Nb3d, Te3d, and C1s were obtained with a constant kinetic electron energy of 150 eV corresponding to an inelastic mean free path (IMFP) of 0.6 nm.

Valence spectra and secondary electron cut-offs of the photoelectron spectra were recorded with a photon energy of 100 eV. To measure the cut-off a voltage of -18 V was applied between the sample and the photoelectron detector. The electron escape vector was normal to the surface of the pellet to avoid a distortion of the electron trajectories by the electric field [93]. To calculate the elemental composition and the vanadium oxidation state at the surface of M1, normalized core level intensities were evaluated after subtraction of a Shirley type background taking into account the photon energy dependence of the atomic subshell photo-ionization cross sections [200], using CASA data analysis software (Neil Farley, www.casaxps.com). A detailled description of the core level evaluations was reported before [87].

4.2.4 Results and Discussion

Conductivity and catalytic studies with propane feed variation

In order to check the semiconducting and catalytic properties of the phase-pure MoVTeNbO$_x$ M1 system, the electrical conducitivity was first tested in propane oxidation under dry conditions with different propane/oxygen ratios. Wet conditions were not included due to the known significant change of the surface termination and surface electronic structure [87] making correlations between different conditions and techniques more difficult. This will be reported in a subsequent publication. Conventional conductivity measurements of polycrystalline, 'real' catalysts under operation conditions are however very often difficult to be analyzed due to the high dependence on contact resistances between electrodes and catalyst particles and between catalyst grains. In particular, electrode contacts at elevated temperatures in flow-through reactors are challenging and hence complicate reliable and quantitative measurements. That is why we developed recently a contactless alternative for electrical (microwave) conductivity measurements of powder catalysts in a fixed bed flow through reactor based on the microwave cavity perturbation technique [53], which was also applied in the forthcoming studies. In figure 4.10a the microwave conductivity of M1 in propane/oxygen ratios of 1:2, 1:1, 2:1, and again 1:2 at 400°C and at a gas hourly space velocity (GHSV) of 16980 h^{-1} is shown. The corresponding catalytic data as measured with the in situ conductivity setup is depicted in figure 4.10b. As a result, the conductivity of M1 increased with rising relative propane concentrations. Under these dry feed conditions propane is mainly oxidized to propylene [201], while CO, CO$_2$, and in particular acrylic acid (AA) are formed as by-products. Under high propane-oxygen ratios the selectivity to acrylic acid increased substantially, the propylene selectivity rose slightly, while both the propane conversion and total oxidation product selectivities to CO$_\mathrm{x}$ declined. The latter products might thus be formed by the combustion of acrylic acid under oxygen-rich conditions. When the feed composition was set to the initial conditions, both the conductivity (figure 4.10a) and the catalytic performance (figure4.10b) returned nearly exactly to the initial values. From a defect chemistry point of view including lattice oxygen $\mathrm{O_O^x}$ of M1 (or most likely oxygen from the active surface [87, 26]), the oxidative dehydrogenation (ODH) of propane to propylene can be divided into two steps. First, lattice oxygen is removed from M1 and dehydrogenates propane to propylene and water. Hence oxygen vacancies $\mathrm{V^{\bullet\bullet}}$ and mobile electrons $\mathrm{e'}$ are generated:

$$\mathrm{C_3H_8 + O_O^x \longrightarrow C_3H_6 + V^{\bullet\bullet} + 2e' + H_2O} \qquad (4.41)$$

In a similar manner the oxidation of propane to the by-products can be formulated. In a subsequent step M1 is re-oxidized by gas phase oxygen, consuming oxygen vacancies

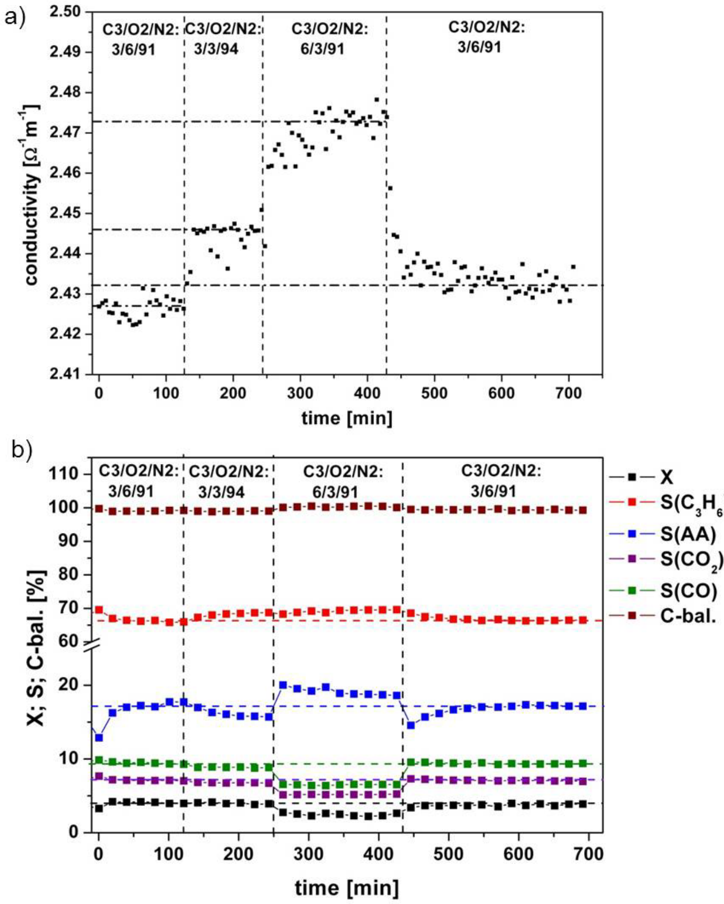

Figure 4.10: *a) Conductivity of M1 during the propane feed variation at 400°C. b) Simultaneously recorded catalytic data.*

and electrons:

$$V^{\bullet\bullet} + 1/2\mathrm{O}_2 + 2\mathrm{e}^{'} \longrightarrow \mathrm{O}_\mathrm{O}^\mathrm{x} \tag{4.42}$$

Since under more reducing, propane-rich conditions an increasing conductivity is observed, electrons are obviously the majority charge carriers basically defining the overall conductivity, i.e. the catalyst shows the conductivity response of an n-type semiconductor:

$$\sigma = e(n_\mathrm{e}\mu_\mathrm{e} + n_\mathrm{h}\mu_\mathrm{h}) \approx e n_\mathrm{e}\mu_\mathrm{e}, \tag{4.43}$$

with e being the elementary charge, n_e and n_h the number of electrons and electron holes, and μ_e and μ_h the mobility of electrons and holes, respectively. Within a rigid band model, this can be interpreted in terms of oxygen vacancies, or of associated reduced metal ions such as V^{4+} forming a partly doped d-band, generating occupied donor states (or a delocalized donor band) in the forbidden bandgap of M1 [146, 76, 123, 145, 68]. According to Fermi-Dirac statistics these donor states can release electrons into the conduction band where they are mobile and contribute to the overall conductivity. Interestingly, the behavior of the M1 phase as n-type semiconductor would be in agreement with the response found for the related M1 phase of the mixed metal oxide $\mathrm{MoVSbNbO_x}$ [162] and the M2 phase of $\mathrm{MoVTeNbO_x}$ [20]. Alternatively, since the reference compound V_2O_5 is usually described as small polaron conductor [90], the conduction mechanism could be also described by activated hopping of electrons between adjacent localized defect states. However, the description of the catalyst within classical semiconductor theory does not necessarily depend on the prerequisite of band conduction, but just on the applicability of Maxwell-Boltzmann (or Fermi-Dirac) statistics [18]. Therefore, we will use in the following the rigid band model to describe the electronic properties of M1 for the sake of its simplicity. If the oxygen vacancies are only formed at the surface, surface defect states, generally also located within the forbidden band gap of the semiconductor, are formed [138, 79]. These states can be filled with electrons as well. Hence even in the latter case the modification of the surface charge will induce an oppositely charged zone in the subsurface (i.e. space charge region) and influence the bulk conductivity [137]. Details concerning this effect will be discussed together with the photoelectron valence band and core level spectra later. Accordingly, since the microwave cavity perturbation technique is an integral method for semiconductors and insulators probing both surface and bulk [32], complementary investigations are needed for distinguishing between surface, subsurface, and bulk effects, as will be shown in the next chapters.

Conductivity and catalytic studies with alkane variation

The M1 phase is not only a prospective catalyst in propane oxidation, but can also catalyze the selective oxidation of n-butane to maleic anhydride and the ODH of ethane to ethylene with good and very good selectivities, respectively [22]. Thus M1 is an excellent candidate to study the influence of the alkane on the surface termination, the surface electronic structure and the charge transport properties of the solid catalytically active phase and to correlate these data with the catalytic performance. In figure 4.11a the conductivity of M1 is shown under different light alkane feeds (alkane/oxygen ratio always 1:2) at 400 °C and a GHSV of 16980 $\mathrm{h^{-1}}$. As a result, the conductivity responded reversibly on the different alkane feeds. It was with 2.60 $(\Omega\mathrm{m})^{-1}$ lowest in ethane, with 2.70 $(\Omega\mathrm{m})^{-1}$ highest in n-butane and returned always back to the intermediate value of 2.64 $(\Omega\mathrm{m})^{-1}$ in the propane feed. Hence referring to the discussion of the n-type semiconducting properties of M1 in the previous section, the mobile electron density of M1 is lowest in ethane and highest in n-butane relative to the state in the propane feed. Moreover, the simultaneously recorded catalytic data are shown in figure 4.11b. Independent of the alkane

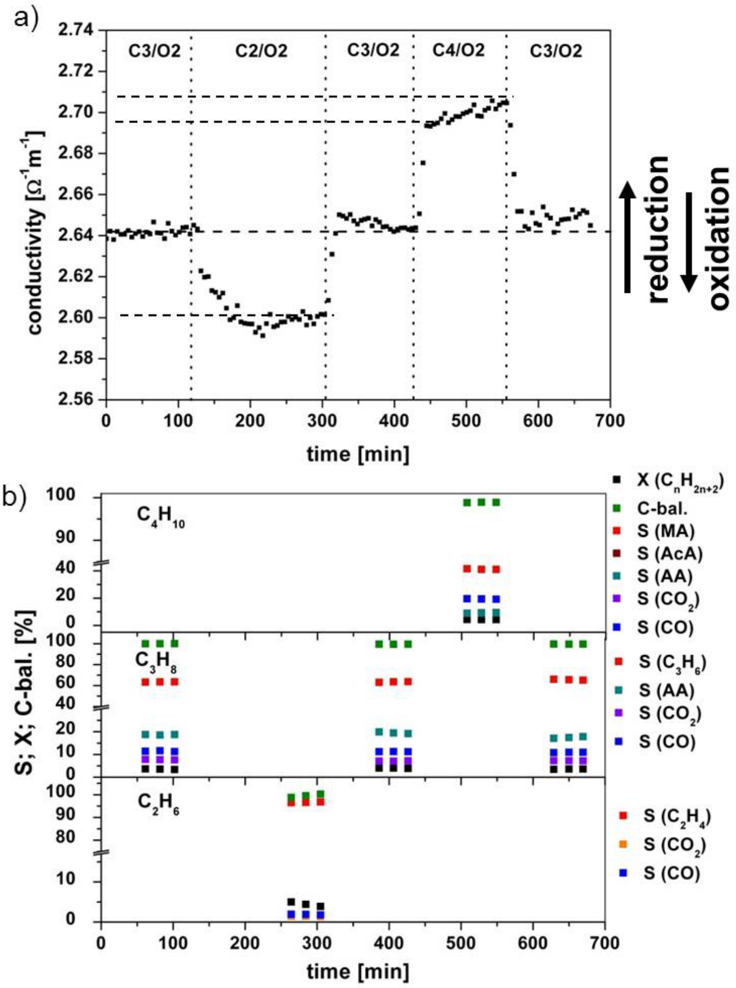

Figure 4.11: *a) Conductivity of M1 during the alkane variation at 400°C. b) Simultaneously recorded catalytic data.*

in the feed the alkane conversion was always approximately 4%. In the ethane feed the selectivity to ethylene was 97%, to CO 2%, and to CO_2 1%, being well in agreement with published catalytic data [17]. The catalytic performance in the propane feed, which was reproducibly achieved during all cycles, showed a selectivity to propylene of 64% and to acrylic acid of 19%, also being comparable with literature data [131]. This result agrees with the reproducible conductivity value in the propane feed (figure 4.11a). In the n-butane/oxygen mixture the selectivity to maleic anhydride (MA) was 41%, to acrylic acid (AA) 9%, and to acetic acid (AcA) 9%. Butylenes were not found in the product stream. The difference in the selectivities to 100% is for all reactions due to the formation of the total oxidation products CO and CO_2. As a general trend it can be deduced that the selectivities to the corresponding olefins decreased from ethane to n-butane oxidation while the selectivity to the desired oxygenates, and to the undesired deeper oxidation products CO and CO_2, was increasing. As already shown for the ODH of an alkane to the respective olefin (cf. equations 4.41 and 4.42) two electrons are formally needed per alkane molecule conversion. Furthermore, if ethane is oxidized to CO and CO_2, 10 and 14 electrons, respectively, would have to be transferred. The oxidation of propane would even necessitate the transfer of 8 electrons for acrylic acid, 14 for CO, and 20 electrons for CO_2 formation, while in the n-butane oxidation the transfer of even 14, 18, and 26 electrons is desired to produce maleic anhydride, CO, and CO_2, respectively. Hence the number of electrons which are formally transferred from the alkane to the catalyst increases from ethane to n-butane oxidation, if a direct charge transfer between adsorbed or gaseous species can be excluded and all catalytic cycles involve the participation of lattice oxygen (Mars-van Krevelen redox mechanism). Looking at these numbers and considering the constant alkane conversions but increasing selectivities to highly oxidized products, the increasing conductivity with alkane chain length can be understood, provided that the reduction step of the catalyst is faster than the re-oxidation. The latter statement is in particular supported by the longer time the catalyst needs to approach the steady state after switching from the more reducing propane to the more oxidizing ethane feed (figure 4.11a), whereas upon changing the gas mixtures in the reversed direction a much faster response is observed. The re-oxidation of vanadia catalysts has been discussed indeed as rate-determing step in oxidation catalysis [150].

XPS investigations

In order to understand the observed response of the microwave conductivity on the different reaction feeds in more detail, the electronic structure of M1 was investigated by XPS under comparable catalytic operation conditions. Since the bulk crystalline phase remained stable under the applied reaction conditions and no deterioration products were found, as tested by in situ X-ray diffraction, the surface sensitive XPS method was chosen to test the dynamic behavior of the surface under working conditions at 25 Pa. The simultaneously measured catalytic data recorded by micro-GC under these conditions are summarized in table 4.2. During the experiments the alkane conversions were always below 1%. In ethane oxidation the obtained selectivities to ethylene, CO, and CO_2 were comparable to the data recorded at atmospheric pressure in the conductivity study. In propane oxididation the selectivity to propylene was lower, while the selectivities to CO and CO_2 were higher in comparison to the ambient pressure data, but the trend of the decreasing selectivities to the olefins from ethane to propane oxidation was confirmed. Acrylic acid was not considered in the calculation of the selectivities, but was detected by mass spectrometry. In the n-butane feed maleic anhydride, acrylic acid, acetic acid, CO, and CO_2 were detected by mass spectrometry, but could not be quantified. In summary, all products observed in the ambient pressure experiments were alike identified in the low pressure in situ XPS studies, indicating that M1 was active and similarily selective in both studied pressure ranges. The normalized elemental ratios of Mo, V, Nb, Te, and the average V, Mo, Nb, and Te oxidation states were deduced from the measured core level spectra probed at a constant kinetic photoelectron energy of 150 eV (corresponding to an inelastic mean free path for detected photoelectrons of about 0.6 nm), i.e. within the same sample depth, and are summarized in figure 4.12. As a result of the data evalation, the surface of M1 contains 56-60 at% Mo (bulk: 65 at%), 8-11 at% Te (bulk: 6 at%), 15-16 at% V (bulk: 19 at%), and 16-18 at% Nb (bulk: 10 at%). Hence one can interpret these results as a relative depletion in Mo and V, and an enrichment in Te and Nb on the surface if compared to the bulk values measured by X-ray fluorescence. No clear systematic dependence of the elemental ratios on the alkane feed was observed. The average vanadium oxidation state was evaluated from the relative intensities at electron binding energies related to V^{4+} and V^{5+} in the $V2p_{3/2}$ spectrum. An exemplary fit of the $V2p_{3/2}$ spectrum measured in a 1:2 propane/O_2 feed is shown in figure 4.13. In the ethane feed more V^{5+} species are present at the surface in comparison to the n-butane feed, pointing to a more oxidized surface. Under all conditions the oxidation state was always above 4.5, which means that the number of V^{5+} species was larger than of V^{4+} species at the surface, which is in agreement with previous XPS studies [87]. According to the literature the vanadium oxidation state in the bulk phase of M1 is basically 4+ [7, 19]. Moreover, Mo was only found in the oxidation state 6+, Te as 4+, and Nb as 5+ on the surface, as deduced from the Mo3d, Te3d, and Nb3d core level spectra, respectively, and no changes were observed upon alkane exchange. Consequently, we conclude that vanadium is the only redox active metal ion under catalytic operation conditions, which has also been supported by XANES studies [172]. In addition, we calculated the work function ϕ of

	propane oxidation		ethane oxidation	
product	25 Pa	1 bar	25 Pa	1 bar
propylene	51%	64%	-	-
ethylene	-	-	98%	97%
CO_2	19%	8%	2%	1.5%
CO	29%	11%	<1%	1.5%

Table 4.2: *Comparison of product selectivities at 25 Pa (in situ XPS) and at 1 bar (in situ conductivity) in ethane and propane oxidation measured with GC. In the 25 Pa propane oxidation experiment oxygenates are not included in the selectivity calculation, since they could be detected, but not quantified by MS. The acrylic acid selectivity at 1 bar was 19%.*

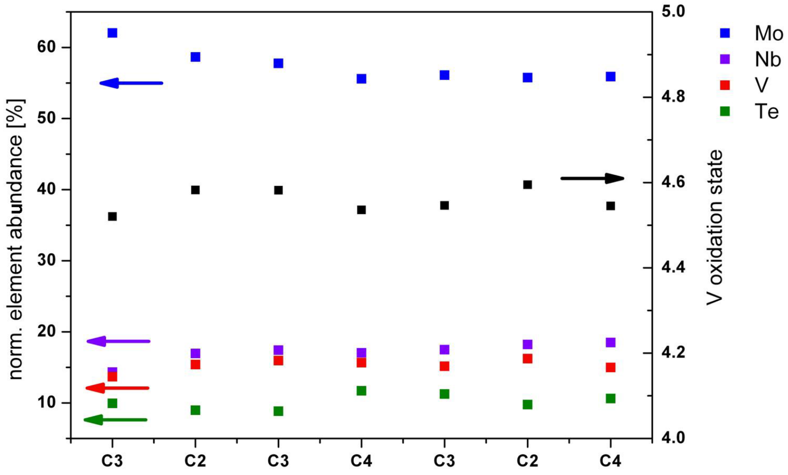

Figure 4.12: *Elemental composition and V oxidation state at the surface of M1 as evaluated from the respective core level spectra.*

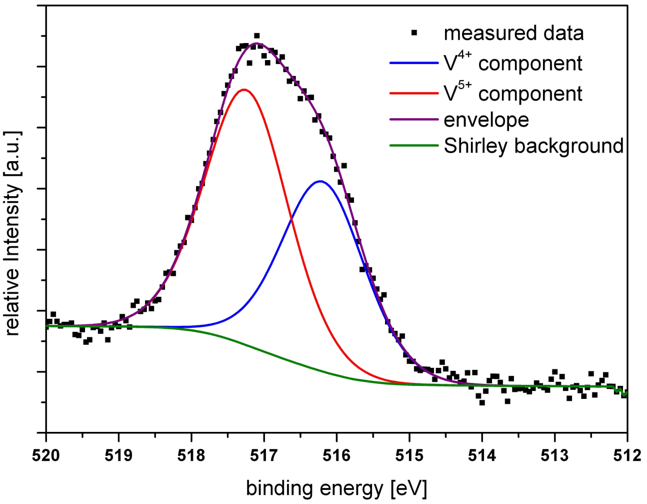

Figure 4.13: *V2p$_{3/2}$ spectrum of M1 in propane/O$_2$ 1:2 feed including the fit of the V^{4+} and V^{5+} component. A Shirley background was used for background correction.*

M1 under the different reaction conditions from the spectral width (SW) and the photon excitation energy (E_{photon}) [93, 138]:

$$\phi = E_{\text{photon}} - SW \tag{4.44}$$

The spectral width is the difference between the high binding energy end of the spectrum, which was determined by a linear extrapolation of the cut-off edge (figure 4.14), and the

Fermi level at 0 eV binding energy. Since the photoelectrons at the cut-off would theoretically have a kinetic energy of 0 eV, a bias of -18 V was applied for detection. The obtained work functions of M1 range between 6.4 eV and 6.7 eV. These numbers are well comparable with work functions of the reference binary oxides V_2O_5 (7.0 eV) [146] and MoO_3 (6.9 eV) [76]. The work function decreases from 6.66, over 6.57, to 6.46 eV in the order ethane, propane, and n-butane feed (figure 4.14). Furthermore, the work function changes are fully reversible, as could be proven for the propane feed, since ϕ always approached the value of 6.57-6.59 eV, irrespective of the previous treatment. It is well known that the work function of metal oxides decreases with increasing degree of reduction [76]. Hence from our work function measurements one could speculate that the reduction of the M1 surface increases from the ethane to the n-butane feed. This result, the observed reversibility and its interpretation are in full agreement with the findings of the conductivity study at atmospheric pressure (figure 4.11) and with the observed systematic change of the surface vanadium oxidation state (figure 4.12). In figure 4.15 the conductivity is plotted against the work function in the different alkane feeds. A clear correlation between the conductivity and the work function of M1 can be seen. An increasing conductivity and a decreasing work function both indicate a reduction of M1. The linear trend is in particular remarkable having in mind the different pressure ranges and sample preparations (pressed pellet versus powder) applied for the two methods. Moreover, valence band spectra in both ethane (most oxidizing) and n-butane (most reducing) feeds were measured (figure 4.20a). The intensities of all valence band spectra were normalized to their maximum. The band gap state between 0.25 and 2.25 eV binding energy (figure 4.20a, inset) is assigned to a partially filled V3d state based on resonant photoelectron spectroscopy studies on V_2O_5 [204], and since no other redox active transition metals were found under the probed conditions. Slightly higher peak intensities can be observed in the n-butane than in the ethane feed, though the resolution of the small differences is close to the accuracy limit of our measurement. An increase of the peak intensity indicates an increased occupation of the V3d valence level and hence a reduction of vanadium. This result is in agreement with the trends found in the XPS core level, work function, and conductivity studies. A closer analysis of the valence band spectra in the different alkane feeds reveals that the valence band edge, i.e. its linear extrapolation to the binding energy axis, is reproducibly shifted by 80 meV to smaller binding energies between the treatment in the n-butane and the ethane feed (figure 4.20a). In addition, core level spectra, e.g. O1s (figure 4.20b) and $Mo3d_{5/2}$ (figure 4.20c), also show a reproducible binding energy shift to smaller values between the n-butane and ethane feed by about 80 meV.

As reported before, the total change of the work function between the ethane and n-butane feed corresponds to 180 meV. Since the valence band edge and the core levels are only

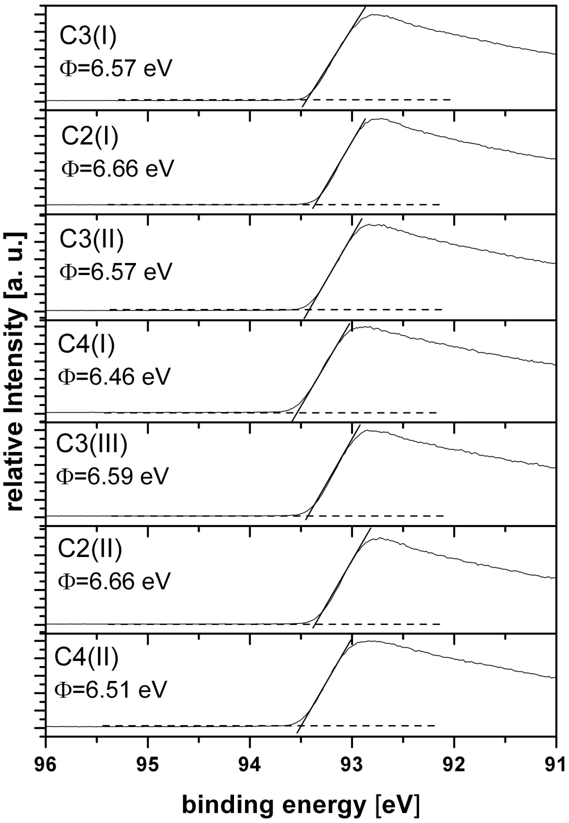

Figure 4.14: *Cut-off of the photoelectron spectra in the different alkane feeds measured with a photon energy of 100 eV, with Φ being the thus determined work function. Roman numerals indicate the order of the applied feeds referring to the measurement protocol in the experimental section.*

shifted by 80 meV, a change of the electron affinity by 100 meV between the two conditions can be concluded [150, 138]. A modification of the electron affinity can occur due to different adsorbates at the surface forming different surface dipoles [138], e.g. due to adsorbed water or OH groups, or a change in the surface termination [178]. Moreover, the contribution of the binding energy shift to the work function change can be explained by the simplified semiconductor/surface state concept (Schottky model) depicted in figure 4.17. The termination of the solid crystal lattice at the solid/gas interface does not only change the electron affinity, but can also create intrinsic (surface reconstruction with 2-dimensional translational symmetry) or in case of a very heterogeneous surface even extrinsic (surface with broken translational symmetry) localized electronic surface states. Experimental results from the actual investigation and from former studies [87, 167, 26] strongly indicate that the MoVTeNbO$_x$ M1 catalyst forms under alkane oxidation conditions a surface layer structurally and electronically strongly deviating from the bulk phase.

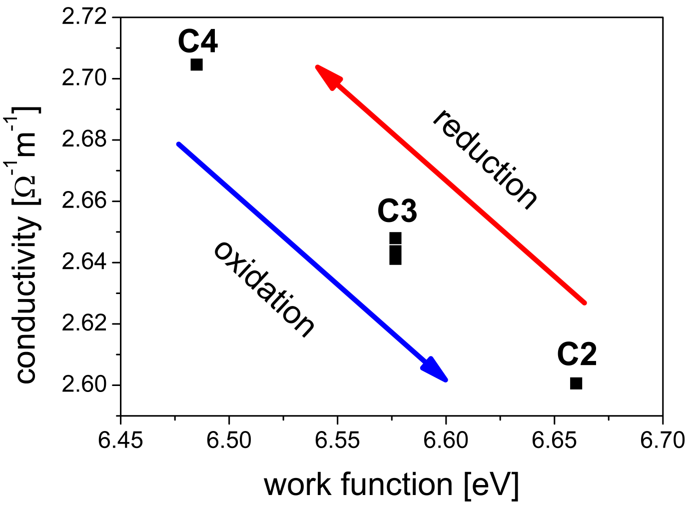

Figure 4.15: *Relation between work function (cf. figure 4.14) and conductivity (cf. figure 4.11) in the different alkane feeds.*

Moreover, the termination layer probed by XPS contains a significantly higher amount of V^{5+} species and showed a catalytic activity inversely proportional to the Mo and proportional to the V^{5+} surface concentration [87]. All these findings suggest that the M1 system under working conditions should be described as supported catalyst rather than as homogeneous system. Hence the complex system could be treated as heterojunction rather than as a homogeneous semiconductor according to semiconductor physis, with the n-type semiconducting M1 bulk phase as support, and an insulating or semiconducting overlayer basically consisting of a (2-dimensional) vanadium(IV,V) oxide as termination, which itself is modified by the reactive gas phase. Since the surface state energy (or surface layer Fermi energy) is usually different from the Fermi energy of the bulk electrons, charge transfer between surface and bulk follows in order to establish thermal equilibrium by equalizing the bulk and surface Fermi or surface state energy. In this way, charge is separated at the interface creating a surface charge and an oppositely charged space charge layer in the sub-surface region. The widths of the space charge region depends on the density of mobile charge carriers and the dielectric constant of the material [150, 137, 138]. Since the occupancy of the valence and conduction band by electrons is defined by Fermi-Dirac statistics and thus by the Fermi energy, the bands in the surface region bend relative to the Fermi level and depletion (upward band bending with decreased electron density) or accumulation layers (downward band bending with increased electron density) are formed. From the higher average V oxidation state on the surface in comparison to the bulk it can be concluded that more unoccupied (V3d band gap) states are present at the surface. These states act as traps for mobile electrons resulting in a deple-

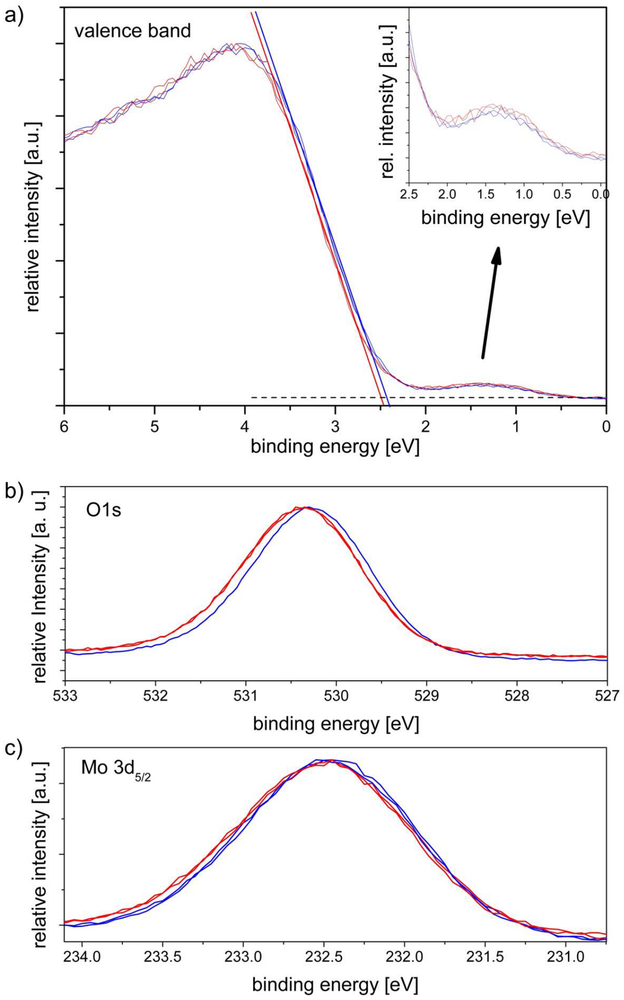

Figure 4.16: *a) Valence band (inset: V3d band gap states), b) O1s core level, and c) Mo3d$_{5/2}$ core level spectra of M1 in the ethane (blue curves) and n-butane (red curves) feeds.*

tion layer. Further support for the formation of a depletion layer is given by the rather small gap between valence band edge and Fermi level of approximately 2.4 eV and the previously [26] observed shift of the valence band edge to higher binding energies with higher excitation energies.

If the density of surface states is very high, the Fermi level can be even pinned at the surface state energy and thus becomes completely independent of the bulk impurity concentration. The occupation of (reactive) surface states is modulated by the applied gas phase modifying the band bending. In a simplified model, the surface state could be identified as V^{4+}/V^{5+} redox couple on the surface [150]. Then, the Fermi energy of the catalyst E_F

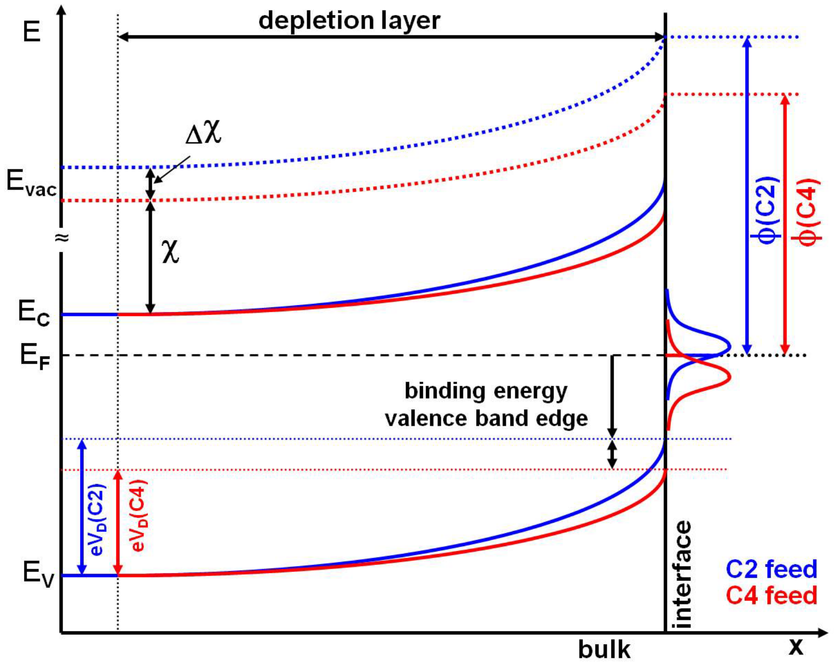

Figure 4.17: *Schematic band diagram of M1 in ethane (blue) and n-butane (red) feed.* ϕ *is the work function,* eV_D *is the diffusion energy,* $(\Delta)\chi$ *the electron affinity (difference),* E_{vac} *the vacuum level,* E_C *the conduction band edge,* E_F *the Fermi level, and* E_V *the valence band edge.*

would be pinned to the surface state energy E_t modified by the V^{4+}/V^{5+} concentration:

$$E_F = E_t + kT \ln \frac{[V^{4+}]}{[V^{5+}]} \tag{4.45}$$

E_t could in a first approximation be identified as redox potential of the couple in aqueous media, however local surface bonding of the couple at the gas/solid interface and possible structural re-arrangements during the redox processes have to be taken into account for a more precise description. Different adsorbates and in particular water could also change directly the surface state energy E_t. The proposed gas-phase dependent modification of the V^{4+}/V^{5+} couple is strongly supported by the observed change of the average vanadium oxidation state (figure 4.12) and by the intensity modulation of the partially filled V3d state located between the valence band edge and the Fermi level (E_F) (figure 4.20a). According to equation 4.45, for a change of the band bending due to Fermi level pinning by about 80 meV, as found in our experiments between the ethane and n-butane feed, the average vanadium oxidation state would have to vary between, e.g., 4.5 and 4.8 at the surface. This change does not seem to be unrealistic having in mind the probed information depth of 3x0.6 nm (86% of photoelectrons contributing to this signal are released within this depth) in the XPS experiment (figure 4.12), and is thus a strong support for the validity of the applied simple Schottky model with Fermi energy pinning to the redox couple surface state energy.

Due to the shift of the valence band edge to smaller binding energies in the ethane relative to the n-butane feed, the energy gap between the valence band edge (E_V) and the Fermi level decreases. Therefore, the number of occupied band gap states (V3d) and the degree of surface reduction must also decrease, which is in agreement with the V3d valence level spectra (figure 4.20c, inset). The band gap of a semiconductor is usually a material constant of the bulk and not affected by surface modifications [181]. Thus, the energy interval between the Fermi level and the conduction band edge has to increase resulting in an increase of the work function, which was indeed observed in the work function measurements (figure 4.14). The electrical conductivity $\sigma(x)$ depends on the spatially varying energy interval between E_C and E_F in the space charge region [138] after:

$$\sigma(x) \approx e n_{\mathrm{e}}(x) \mu_{\mathrm{e}}, \;\; n_{\mathrm{e}} = N_{\mathrm{eff}}^{C}\, exp\left[-\frac{E_C(x) - E_F}{k\,T}\right] \tag{4.46}$$

N_{eff}^{C} is the effective conduction band density of states, k the Boltzmann constant and T the temperature. Consequently, the electrical conductivity is directly influenced by the degree of band bending, modulated by the V^{4+}/V^{5+} ratio in the surface layer and hence by the gas phase chemical potential, as was observed in our experiments and explains its linear correlation with the work function (figure 4.15).

We believe that the developed model describing the active catalyst as semiconductor with a heterogeneous surface layer offers the possibility to understand the exceptional catalytic properties of the M1 phase and of selective oxidation catalysts in a more rational way. Such a heterostructure acts as chemical diode separating the free charge carriers from the location of the active layer. The active phase would be represented by the vanadium(IV,V) oxide surface layer, that can be also described as high lying acceptor state for electrons, being an important requirement to activate (oxidize) hydrocarbon molecules. Due to the surface barrier in the space charge region electron transfer to the surface is suppressed preventing the simultaneous activation of O_2 and the formation of reactive electrophilic oxygen species that could induce total oxidation of the activated hydrocarbon. Equation 4.45 shows that a high V^{5+}/V^{4+} ratio decreases the Fermi energy and can thus increase the band bending and surface barrier to values, where electron transport to the surface slows down to neglible rates. In this way, the reaction steps of alkane oxidation and oxygen activation are decoupled in time. One could even speculate about a decoupling of both reactions in space, provided that the VO_x termination layer does not cover the whole crystalline phase or if the formation and destruction of the surface layer is highly dynamic and oxygen can directly access and hence be directly activated at the (temporarily) uncovered electron rich bulk phase. This concept would be the physical representation of the site isolation and phase cooperation model often discussed in oxidation catalysis [75]. Moreover, an over-oxidation of the surface and finally a destruction of the catalyst is also prevented by the surface barrier.

4.2.5 Conclusions

The dynamic electronic structure of the orthorhombic M1 phase of the mixed multi metal oxide $MoVTeNbO_x$ was investigated by the noncontact microwave conductivity technique and XPS under working conditions for the selective oxidation of ethane, propane, and n-butane with molecular oxygen. By measuring the binding energies of the core and valence levels and the secondary electron cut-off energy under different reaction conditions the alkane dependent modulation of the work function, electron affinity, and band bending were determined. Whereas the alkane-dependent change of the electron affinity is explained by the formation or modification of the dipolar surface layer, the binding energy shifts and hence band bending are caused by Fermi energy pinning to the surface state energy of the V^{4+}/V^{5+} redox couple in the active layer. The complementary microwave conductivity studies indicate furthermore that the electron density in the conduction band (or in donor states) is modulated by the gas phase, too, which is in perfect agreement with the observed band bending and the thus induced Fermi level alignment. The correlation of the conductivity results, deduced without electrode contacts and under ambient pressure fixed bed flow reactor conditions, with the low pressure XPS measurements on pressed powder pellets, is a strong support for both the relevance and the validity of the XPS work function measurements under operation conditions. The identified relationships and the application of the heterojunction concept offer the possibility to understand 1) the formation of the surface layer governed by the electronic properties of the bulk and the gas phase, 2) the mechanism and relevance of charge transfer and charge separation at the gas-surface-bulk interface in selective oxidation reactions, and 3) to bridge the gap between low pressure electric contact-dependent surface science techniques and contactfree measurements under close-to-technical reaction conditions. Moreover, these ideas could open up new vistas in the prediction and synthesis of novel supported catalyst systems in order to engineer the charge separation at the solid-solid interface and the charge carrier density and type at the surface for optimized decoupling of alkane oxidation and oxygen activation, and hence catalytic performance.

Acknowledgement

The present work has been supported by the German Federal Ministry of Education and Research (BMBF) as part of the ReAlSelOx project, grant number 033R028B. The authors thank Dr. Frank Girgsdies for XRD measurements. The HZB staff is acknowledged for their continual support of the high-pressure electron spectroscopy activities of the FHI at BESSY II. We are very grateful to Prof. R. Stößer (Humboldt-Universität zu Berlin) for his very helpful advice regarding measurements with microwaves.

4.3 The Impact of Water on the Electronic Structure of the Selective Propane Oxidation Catalyst MoVTeNb Oxide (Orthorhombic M1 Phase)

Christian Heine[1], Michael Hävecker[1,2], Annette Trunschke[1], Robert Schlögl[1] and Maik Eichelbaum[1,3]

[1]Fritz Haber Institute of the Max Planck Society, Department of Inorganic Chemistry, Faradayweg 4-6, 14195 Berlin, Germany
[2]Helmholtz Centre Berlin / BESSY II, Solar Energy Research, Albert-Einstein-Straße 15, 12489 Berlin, Germany
[3]BasCat, UniCat BASF JointLab, TU Berlin, Marchstraße 6, 10587 Berlin, Germany

4.3.1 Abstract

The phase-pure selective propane oxidation catalyst MoVTeNb oxide M1 was investigated by microwave conductivity, X-ray photoelectron spectroscopy, X-ray absorption and resonant photoelectron spectroscopy under reaction conditions to identify the influence of steam on the electronic properties of the bulk and active surface layer. Steam increases significantly both the conversion of propane and the selectivity to the target product acrylic acid. The increased catalytic performance comes along with a decreased conductivity, a drastic modification of the surface chemical composition with an enrichment of covalently bonded V^{5+} species at the extent of Mo^{6+}, a decreased work function and hence polarity of the surface and a modified valence band structure. The higher degree of covalency in metal oxide bonds affects the mobility of the free charge carriers, and hence explains the steam-dependent conductivity of the sample. Hence we could prove that steam changes the electronic surface structure and charge carrier dynamics of the catalyst. The reversible changes in both electronic structure and acrylic acid selectivity suggest a structure-function relation and support the assignment of $V^{5+}=O$ as active surface species.

4.3.2 Introduction

Acrylic acid is with an annual global production of 4.7 million tonnes (2012) an important intermediate in the chemical industry to produce polyacrylates and methacrylate esters for diverse applications, e.g. for superabsorbers. It is currently mostly manufactured with a yield of up to 80% in a two step heterogeneous catalytic process starting with the oxidation of propylene to acrolein and followed by its oxidation to acrylic acid [22]. Propylene is produced by steam cracking of the naphtha destillation fraction of crude oil. The endothermic steam cracking process is highly energy-consuming due to the high temperatures needed (up to 850°C) and the necessary generation of steam. The upcoming scarcity of crude oil resources and the corresponding expected price increase are serious factors that will reduce the cost effectiveness of the current acrylic acid manufacture process. A competitive alternative could become the direct oxidation of propane from natural gas. The so far most promising catalyst for direct acrylic acid production from propane is with a current acrylic acid yield of about 50% the orthorhombic MoVTeNb oxide M1 phase (ICSD No. 5509) [45, 149, 152, 194]. M1 is a multimetal mixed oxide that can be synthesized with high phase purity according to powder X-ray diffractometry (XRD). Though it has to be noticed that XRD phase purity does not exclude inhomogeneities such as cation disorder or dynamic overlayers terminating the crystal surface, that can be different from the bulk structure [157, 26]. The crystal structure of M1 provides hexagonal and heptagonal channels perpendicular to the (001) basal plane partially occupied by tellurium. The (001) basal plane is formed by corner-linked MO_6 octahedra (M = molybdenum or vanadium) building a six and seven membered ring structure. MO_7 (M = mainly niobium) pentagonal bipyramids connect the ring structures by sharing edges with the octahedra. Along the c-direction the (001) basal planes are linked by oxygen atoms.

In the oxidation of propane with oxygen on M1, water (i.e. steam) plays a peculiar role for the selective oxidation reaction. In dry feed containing only propane and oxygen, propylene formed by oxidative dehydrogenation (ODH) is the main product (besides CO and CO_2), while the selectivity to acrylic acid is rather low [153]. However, the selectivity to acrylic acid is substantially increased up to 60% if steam is added to the reaction feed [153, 167]. It was proposed that water increases the desorption rate of acrylic acid on the catalyst surface preventing its over-oxidation (e.g. by transforming surface carboxylates into acrylic acid), but that it also changes the nature of the active sites [153]. In general, recent studies indicate that the bulk phase of M1 provides the framework of the active surface which is formed only under reaction conditions [26, 87, 167]. While during the catalytic reaction the bulk structure of M1 is unaffected [153], the surface structure changes depending on the composition of the gas phase. Near-ambient pressure X-ray photoelectron spectroscopy (NAP-XPS) exhibited that the average oxidation states of vanadium and molybdenum are substantially increased at the surface [26, 87]. Molybdenum is only found in the formal oxidation state of 6+ on the surface, while in the bulk a ratio of molybdenum(V) and (VI) is needed to form the crystal structure [152]. Vanadium is a redox active element in M1 with a gas phase-dependent oxidation state as known from a careful analysis of the vanadium $2p_{3/2}$ core level. The addition of water to the propane feed, triggering the production of acrylic acid, induces an increased V^{5+} concentration [26, 87] which is suggested to be essential for the alkane activation step [161, 87]. The V^{4+} concentration is unaffected by the water content of the propane feed [26, 87, 153] supporting the assumption of the unique role of V^{5+} in the acrylic acid formation. Moreover, the tellurium content is increased while the molybdenum content is depleted with steam [26, 87]. That is why it has been suggested that tellurium is also part of the active site [167].

In catalysis chemical modifications on the surface of the catalyst are in general interpreted in terms of a localized molecular model. However, regarding the crystalline, n-type semiconducting MoVTeNb oxide M1 [91] also the collective solid state properties such as the valence and conduction band structure, work function and electrical conductivity have to be taken into account. It was proven recently by microwave conductivity, which is a contactless technique allowing the investigation of the electrical properties of catalysts in a fixed-bed reactor without electrode contact resistance limitations [53], and NAP-XPS studies that M1 acts as a semiconducting gas sensor upon variation of the reaction conditions [91]. The conductivity, the work function and the valence band onset are adjusted reversibly to the applied chemical potential of the gas phase. Consequently, an active charge transfer between the bulk and the gas phase (or adsorbates) was proven indicating the relevance of the semiconducting properties of the bulk phase in controlling the catalytically active surface structure.

In our contribution we want to identify how steam modifies the active surface layer catalyzing the selective oxidation of propane to acrylic acid, and if it also changes the collective electronic properties of the M1 phase. The latter was investigated by microwave conductivity measurements under dry and wet feed conditions at ambient pressure. The results are compared and interpreted with surface sensitive in situ NAP-XPS and near-edge X-ray absorption fine structure (NEXAFS) investigations at 0.25 mbar under dry and wet propane oxidation conditions to identify structure-function relationships between the local electronic surface structure of M1, its collective electronic and catalytic properties. Core level spectra of vanadium $2p_{3/2}$, molybdenum 3d and oxygen 1s, valence band spectra and the work function were analyzed. Moreover, the contribution of vanadium to the electronic structure of the valence band and gap states was investigated in detail with resonant photoelectron spectroscopy (resPES) at the vanadium 2p threshold (vanadium

$L_{2,3}$-edge).

4.3.3 Experimental Section

Sample

The MoVTeNb multi metal mixed oxide M1 phase (internal ID.: 10790) was prepared according to a precipitation procedure described previously [91]. The Rietveld analysis of the X-ray powder diffraction (XRD) pattern proved the phase purity of the used M1 powder. It has also been proven by in situ XRD that the bulk phase is stable under all applied reaction conditions [153]. The surface area was 9.2 m^2/g measured with Brunauer-Emmett-Teller (BET) nitrogen adsorption. Relative metal contents of 65 at% Mo, 6 at% Te, 19 at% V, and 10 at% Nb were determined by X-ray fluorescence analysis.

Microwave Conductivity Measurements

The electric conductivity of M1 under reaction conditions was measured with the microwave cavity perturbation technique. In the depolarization regime, the sample (semiconductor or insulator) located in a microwave cavity causes a perturbation of the resonant electromagnetic field decreasing its quality factor Q and resonance frequency ω_0 [176]. The dielectric function (permittivity) of the sample ($\varepsilon = \varepsilon_1 + i\,\varepsilon_2$) can be computed with the quality factor/resonance frequency of the perturbed (Q_s/ω_s) and unperturbed cavity (Q_0/ω_0) [32].

$$A\,(\varepsilon_1 - 1)\,\frac{V_s}{V_c} = \frac{\omega_0 - \omega_s}{\omega_0} \tag{4.47}$$

$$B\varepsilon_2 \frac{V_s}{V_c} = 1/Q_s - 1/Q_0 \tag{4.48}$$

In equations 4.48 V_s/V_c is the sample/cavity volumes ratio. A and B are proportionality factors known from calibration standards [32, 53]. In the present study the sample was a powder and the evaluated dielectric function is related to the powder. To determine the conductivity of the bulk sample the powder values have to be transformed with an effective medium theory into the bulk values. We used the Landau-Lifshitz-Looyenga effective medium model because it was shown to be suitable for powders [132, 49]. The conductivity σ of the sample is a function of ω_s, ε_2 and the vacuum permittivity ε_0.

$$\sigma = \varepsilon_0\;\omega_s\;\varepsilon_2 \tag{4.49}$$

Details about the in situ microwave conductivity setup were reported previously [90, 53]. The measurement was performed with the TM_{110} mode of a cylindrical cavity at a resonance frequency of about 9.2 GHz. In the experiment the total gas flow controlled by calibrated mass flow controllers was 20 NmL/min. The corresponding gas hourly space velocity was 13333 NmL/(g h) (contact time: 0.27 $\mathrm{s\,g\,NmL^{-1}}$) with a catalyst mass of 90 mg and a bed length of 10.6 mm in a quartz tube reactor with 3 mm inner diameter. A particle sieve fraction between 100 and 200 μm was used for the experiment. The measurement was performed under wet and dry feed conditions containing 3% propane, 6% oxygen and 5% steam for the wet feed with residual N_2 gas at 350°C. We applied the following measurement protocol: dry feed → wet feed → dry feed → wet feed → dry feed.

Near-ambient X-ray Photoelectron and X-ray Absorption Spectroscopy

X-ray photoelectron spectroscopy (XPS), resonant photoelectron spectroscopy (ResPES) and near edge X-ray absorption fine structure (NEXAFS) studies were performed at the ISISS (Innovative Station for In Situ Spectroscopy) beamline at the synchrotron facility BESSY II in Berlin, Germany. Monochromatic light was used to record high resolution in situ XP and NEXAFS spectra. A detailed description of the differentially pumped hemispheric electron analyzer and the in situ vacuum chamber were reported before [15, 193]. For the measurements the sample powder was pressed into a self-supporting pellet of 8 mm diameter (1 ton pressing pressure). Details of the sample, the XPS, ResPES and NEXAFS measurements are described in the separate sections of the experimental part. The experiment was performed at 25 Pa and 400°C (heating rate 5 K/min). The reaction feed contained 1 Nml/min propane, 2 Nml/min oxygen and 3 Nml/min helium for the dry feed conditions and 1 Nml/min propane, 2 Nml/min oxygen and 3 Nml/min steam for the wet feed conditions. The experiment was started in wet feed, followed by dry and finally changed again to wet feed conditions.

In situ NEXAFS The NEXAFS experiments were performed in the total electron yield (TEY) mode and in the Auger-Meitner electron yield (AMEY) mode. The photon energy was varied from 505 to 560 eV by continuously moving the monochromator with a constant velocity of xxx meV/s to record the vanadium L-edges and oxygen K-edge. The data were also recorded continuously. The energy positions of every raw data point were read back from the monochromator control. The generated photoelectrons are accelerated to a Faraday cup by the electric field (applied voltage) and the photo current is measured.

The AMEY data were acquired with the electron spectrometer setting the kinetic energy at 385 eV (pass energy 20 eV) to suppress contributions of the gas phase to the AMEY, in particular from molecular oxygen. Details about the methodology to suppress gas phase contributions in the NEXAFS signal were reported before [81].

In situ XPS/ResPES measurements Core level spectra of O1s, V2p, Mo3d, Nb3d, Te3d, and C1s were performed with a constant kinetic electron energy of 150 and 650 eV, respectively, corresponding to an inelastic mean free path (IMFP) of 0.6 nm (surface sensitive) and 1.6 nm ("bulk" sensitive). The IMFP was calculated for MoO_3 using the model of Tanuma et al. [183]. To calculate the elemental ratios and the vanadium oxidation state at the surface of M1, normalized core level intensities were evaluated after subtraction of a Shirley type background taking into account the photon energy dependence of the atomic subshell photoionization cross sections, using CASA data analysis software (Neil Farley, www.casaxps.com). Valence spectra and secondary electron cutoffs of the photoelectron spectra were recorded with a photon energy of 100 eV. A voltage of -18 V was applied between the sample and the photoelectron detector to measure the cutoff of the photoelectron spectrum. The electron escape vector was perpendicular to the surface of the pellet to avoid a distortion of the electron trajectories by the electric field [93]. In the case of the ResPES measurements at the vanadium 2p threshold, the valence band spectra were recorded at characteristic points of the vanadium $L_{2,3}$-edges. Details about the measurement will be discussed in the results section.

4.3.4 Results and Discussion

Microwave conductivity measurements

Microwave conductivity measurements of M1 in a fixed-bed reactor under propane oxidation conditions were performed at 350°C and with a contact time of $0.27\ \mathrm{s\,g\,Nml^{-1}}$ to achieve a low propane conversion of $<5\%$ (differential conditions) for better comparison with the low pressure in situ XPS results (propane conversion of less than 1%) and to avoid concentration (and conductivity) gradients across the sample. Figure 4.18a shows the microwave conductivity of M1 obtained under dry and wet feed conditions, while the simultaneously measured catalytic performance is plotted in figure 4.18b. In the wet feed containing 3% propane, 6% oxygen and 5% steam the selectivity to acrylic acid is significantly increased from 10% to 30%, as compared to the conditions without steam. The propane conversion rises also from 3% to 4%. In contrast, the selectivities to propylene (from 80% to 60%) and to the undesired total oxidation products CO and CO_2 (from ca. 7% to 4%) decrease with steam. These reversible and stable trends and even the absolute values are basically in agreement with the catalytic data reported recently for similar conversions in a comprehensive reactivity study of M1 tested in a broad parameter field [153].

Based on these results the effect of water was interpreted in terms of the suppression of a decomposition of acrylic acid to CO and CO_2, explaining the increased selectivity of acrylic acid and the decreased selectivity to CO_x. However, the increased conversion has to be explained by an additional effect of water on the nature of the active sites with increased turn-over frequencies and decreased activation energies. The investigation of this latter effect is the focus of this present study. Upon reaching the final temperature of

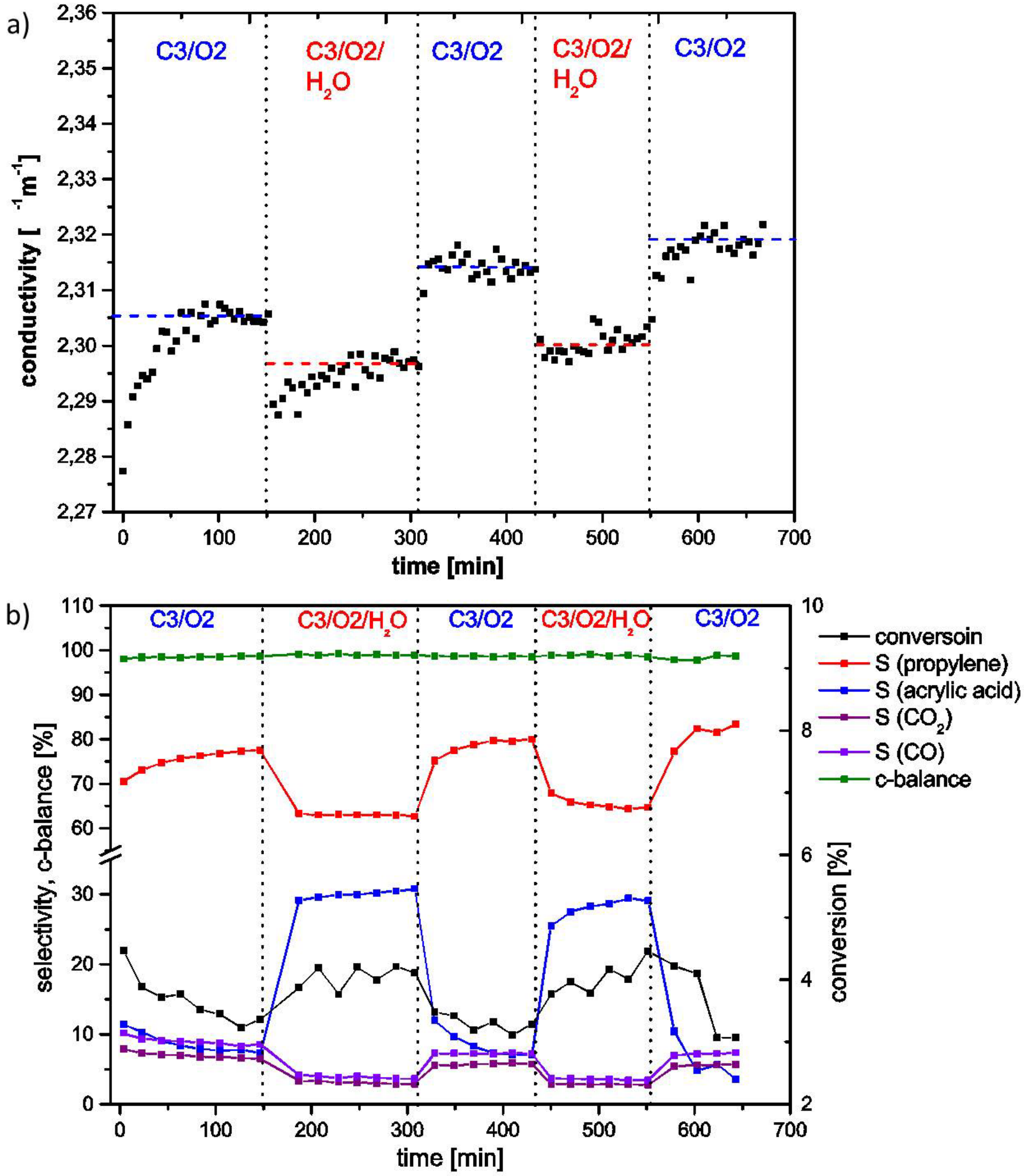

Figure 4.18: *a) Microwave conductivity of M1 under dry and wet propane feed conditions at 350°C and b) simultaneously measured catalytic data.*

350°C (time point "0" in figure 4.18a) the conductivity increased until it stabilized at a value of about 2.305 $\mathrm{S\,cm^{-1}}$ after 1.5 hours. This 110 value is in the range of the conductivity measured for pure silicon at 350°C [154], but is much smaller than for doped silicon samples, and four orders of magnitude higher than determined for the selective n-butane oxidation catalyst vanadyl pyrophosphate (VPO)[51]. The wet feed conditions were applied after the conductivity value remained constant for 1 hour. The feed change induced an immediate decrease followed by a slowly rising conductivity to a constant value still lower than the orignal conductivity in the dry feed. After applying the dry gas mixture for a second time the conductivity increased instantaneously to a constant value slightly above the value measured under the first dry conditions. The repeated change to wet and then again dry feed exhibited qualitatively the same results as observed before with a generally lower conductivity in the presence of steam.

In a previous study probing the microwave conductivity of M1 as a function of dry alkane oxidation feeds (with the different alkanes ethane, propane, n-butane and different alkane/oxygen ratios), the conductivity decreased while going from reducing to oxidizing conditions indicating the n-type semiconductivity of M1 with electrons as majority charge carriers [91]. In this study the work function, the valence band and core levels of M1 were additionally investigated by NAP-XPS. As a result, the work function of M1 increased from reducing to oxidizing gas atmospheres. The analysis of the core levels exhibited no significant changes of the surface elemental composition, but a slight change of the vanadium oxidation state. Furthermore, the core and valence levels shifted to lower energies in oxidizing and to higher energies in reducing feeds. This can be explained by a typical semiconductor response of a gas sensor, where the Fermi level of the solid phase is pinned to the surface state energy modified by the adsorbates [139]. As a consequence, the conduction and valence band and all core levels are bent towards the surface, because charge carriers are transferred between surface (adsorbates) and the bulk phase, while a subsurface space charge region and an oppositely charged surface are formed. The electrical conductivity $\sigma(x)$ depends on the spatially varying energy interval between the conduction band onset E_C and the Fermi energy E_F in the space charge region [139] after:

$$\sigma(x) \approx e n_{\mathrm{e}}(x) \mu_{\mathrm{e}}, \;\; n_{\mathrm{e}} = N_{\mathrm{eff}}^{C}\, exp\left[-\frac{E_C(x) - E_F}{k\,T}\right], \tag{4.50}$$

where e is the elemetary charge, n_e the free electron density, μ_e the free electron mobility, N_{eff}^{C} the effective conduction band density of states, k the Boltzmann constant and T the temperature. Consequently, the electrical conductivity is directly influenced by the degree of band bending, modifying the gap between E_C and E_F. This is the physical explanation for the found correlation between band bending (i.e. core and valence level shifts), work function and microwave conductivity being all dependent on the density of free charge carriers. If the decreased conductivity of M1 in the steam containing propane oxidation feed, as observed in our present study, can be as well explained by a steam-modified band bending, and hence by a modification of the charge carrier density in the bulk phase, is the rationale for the investigation of the catalyst by NAP-XPS in dry and wet feed that will be reported in the next sections.

Core level spectra

We analyzed oxygen 1s, vanadium 2p and molybdenum 3d core level spectra of M1 under dry and wet feed conditions with NAP-XPS. Two questions will be addressed by this study: 1) Can we prove a bending of bands under selective propane oxidation conditions and hence a space charge layer extending from the surface into the bulk by measuring the binding energy of photoelectrons in different depths of the catalyst? 2) If band bending is observed, does it depend on steam, which would allow a correlation between the selectivity to acrylic acid, showing a strong dependence on steam content, and the semiconducting response of the catalyst. The core levels were recorded in a surface sensitive (photoelectron kinetic energy: 150 eV; inelastic mean free path (IMFP): 0.6 nm, meaning that 63% of the photoelectrons were released within this depth) and "bulk" sensitive (650 eV, IMFP: 1.6 nm) mode to study the extension of the space charge region from the surface into the bulk and to discriminate between upward (i.e. formation of a depletion layer) and downward band bending (accumulation layer). In figure 4.19a the surface sensitively recorded O1s and V2p spectra are shown. It is obvious that the maximum of the O1s peak appears at the same binding energy position independent of the applied feed conditions. The O1s spectrum exhibits a shoulder at its high energy side, which could be a possible indication for the presence of different oxygen species such as OH groups. However, Zimmermann et al. analyzed the XP spectra of V_2O_3, VO_2 and V_2O_5 with a DFT calculation based on the Anderson impurity model [204]. As a result, satellites of the $V2p_{1/2}$ and $V2p_{3/2}$ core levels overlap with the O1s spectrum resulting in a high energy shoulder in all three transition metal oxides. These satellites have different distances to their main line subject to the oxidation state of vanadium. If vanadium is present in both oxidation states of 4+ and 5+, which is the case on the M1 surface [26, 87, 153], the satellites of the V^{4+} component of the $V2p_{1/2}$ spectrum, and of the V^{5+} component of the $V2p_{3/2}$ spectrum form the high energy shoulder of the O1s peak. The exact position of the satellites is unknown for M1 making it unreliable to fit the O1s spectrum in order to distinguish different oxygen species. Moreover, difference spectra between measurements in dry and wet feed gave no hint for a specific contribution to the O1s spectrum that is directly caused by the addition of steam to the gas phase (Figure 4.23, Supporting Information). Moreover, the satellite of

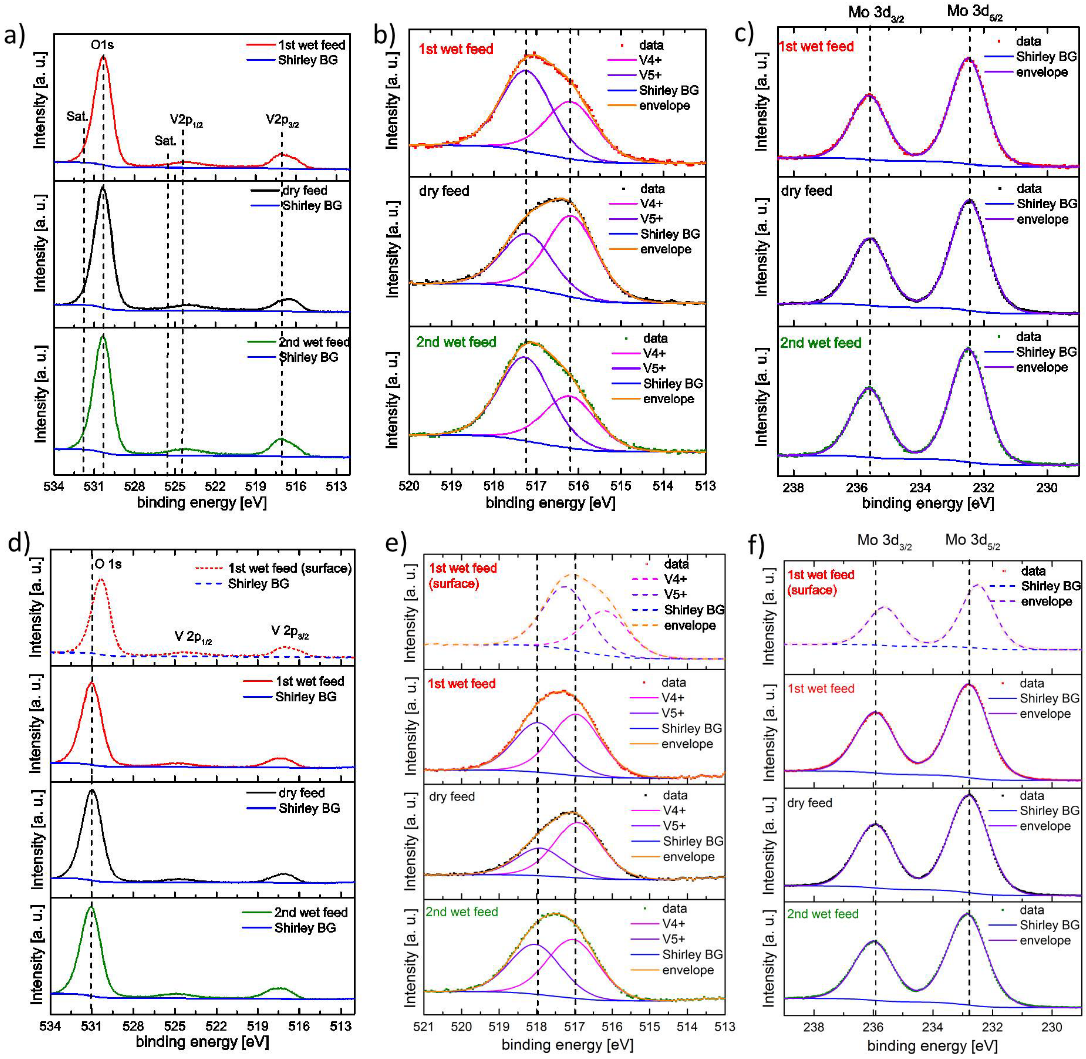

Figure 4.19: *Surface sensitively measured O1s and V2p (a), V2p$_{3/2}$ (b), and Mo3d (c), and bulk sensitively recorded O1s and V2p (d), V2p$_{3/2}$ (e) and Mo3d (f) core level spectra in dry and wet propane oxidation feed.*

the V^{4+} contribution to the $V2p_{3/2}$ spectrum overlaps with the $V2p_{1/2}$ peak. That is why only the undistorted $V2p_{3/2}$ core level can be used to analyze chemical shifts. The $V2p_{3/2}$ spectra are shown in detail in figure 4.19b. The spectra were fitted with two Gaussian-Lorentz peaks corresponding to V^{4+} and V^{5+} components [26, 87, 153]. Though a clear increase of the V^{5+} contribution is observed with steam, the absolute binding energies are for both oxidation state components independent on the feed.
The Mo3d doublet is depticted in 4.19c. Independent on the applied feed conditions this core level can be fitted with just one component[26, 87, 153] corresponding to Mo^{6+}[187]. Again, the maximum of this spectrum is not shifted between dry and wet propane oxidation feeds, which is in agreement with the other core level spectra, but in apparent contradiction to the previous assumption correlating the conductivity change with a gas phase dependent modification of the band bending, as indicated by 4.50.
In 4.19d, e and f the bulk sensitively recorded O1s, $V2p_{3/2}$ and Mo3d core level spectra are shown and compared with the surface sensitive investigations. The maxima of the bulk sensitively measured core level spectra of O1s, V2p, Mo3d and also Te3d (Figure 4.24, Supporting Information) are shifted by about 0.6 eV to higher binding energies. This trend shows clearly that the core levels measured in a deeper region of the catalyst are systematically shifted to higher binding energies, meaning that the difference between the respective core and Fermi level (at 0 eV binding energy per definition) increases with increasing probing depth. This effect can have two possible reasons. First, the core level shifts could be caused by a charging of the surface by the X-ray beam[186]. The photon intensity increases with increasing photon energy at the ISISS beam line. Thus a possible charging of the catalyst surface is more pronounced at higher photon energies. However, charging affects the peak shape of the core levels inducing asymmetries. Since the Mo3d spectra shown in 4.19c and 4.19f, that can be fitted with one component, are highly symmetric, charging can be excluded as explanation. Another possible reason for the binding energy shift is an upward bending of the valence and conduction bands at the M1 catalyst surface. In the case of the n-type semiconducting M1 phase the upward band bending is induced by the formation of an electron-depleted space charge region (depletion layer). The surface of M1 is indeed more oxidized than the bulk as was proven previously[91, 26, 87, 153]. This oxidized surface provides electron acceptor states which act as traps for mobile electrons in the bulk and obviously cause a positively charged depletion layer extending into the bulk. It has also to be mentioned that in XPS a surface photovoltage can arise due to an excitation of electrons by X-rays into higher states (final state effect)[168]. The induced electron and hole charge carriers are separated due to the band bending, i.e. electrons are accelerated into the bulk and holes to the surface, the electric field within the space charge region is compensated, and the upward bending of

the bands is decreased. The same circumstance can also be present in our study - even though the applied high temperature and the usage of a polycrystalline sample with a usually high electron-hole recombination rate should make it rather unlikely - but does not influence the conclusion, since it would only decrease the initial binding energy shifts.
Consequently, under propane oxidation conditions a depletion layer is formed proving the semiconducting response of the catalyst with charge transfer between surface and bulk under working conditions. However, this depletion layer or upward band bending is not influenced further by steam. This indicates that the absolute number of charge carriers in the catalyst is not affected by the presence of water in the gas phase.

Valence band spectra and secondary electron cutoff

Since steam does not influence the band bending, its influence on the valence band and the work function was elucidated. Changes in the valence band structure can denote modified bonding motifs of the surface metal oxide moieties, while a change in the work function would directly indicate a modification of the dipole moments and hence polarity of the surface. Valence band spectra of M1 in wet and dry feed are shown in figure 4.20a. The absolute intensities of the valence band measured in the wet feed were increased by a factor of two in comparison to the dry feet. Interestingly, this effect was also observed in ultra-high vacuum valence band studies of transition metal oxides investigating the effect of chemisorbed water [125, 126], though the reason remained unclear. For a better comparison all valence band spectra depicted in figure 4.20a were normalized to their maximum. As a result, no binding energy shifts of the valence band edge in dependence on steam are observed. This is in agreement with the non-shifted core level energies, hence definitely excluding an effect of water on the subsurface depletion layer and band bending. Besides, a clear difference between the relative contributions of the different components to the valence band is observed upon the addition of steam (bottom of figure 4.20). The relative spectral intensity between 4 and 8 eV is clearly enhanced in the wet feed. An increased intensity with steam is also measured above binding energies of 10 eV. The feature at 1.5 eV is basically not affected relative to the maximum of the valence band. The assignent of the different contributions to the valence band will be discussed in the chapter on resonant photoelectron spectroscopy.
The secondary electron cutoff of the photoelectron spectrum of M1 in wet and dry feeds recorded with an excitation energy of 100 eV is shown in figure 4.20b. The cutoff shifts reversibly to higher binding energies upon the addition of water to the feed. With the known energy position of the cutoff E_{cutoff}, measured at half maximum of the leading

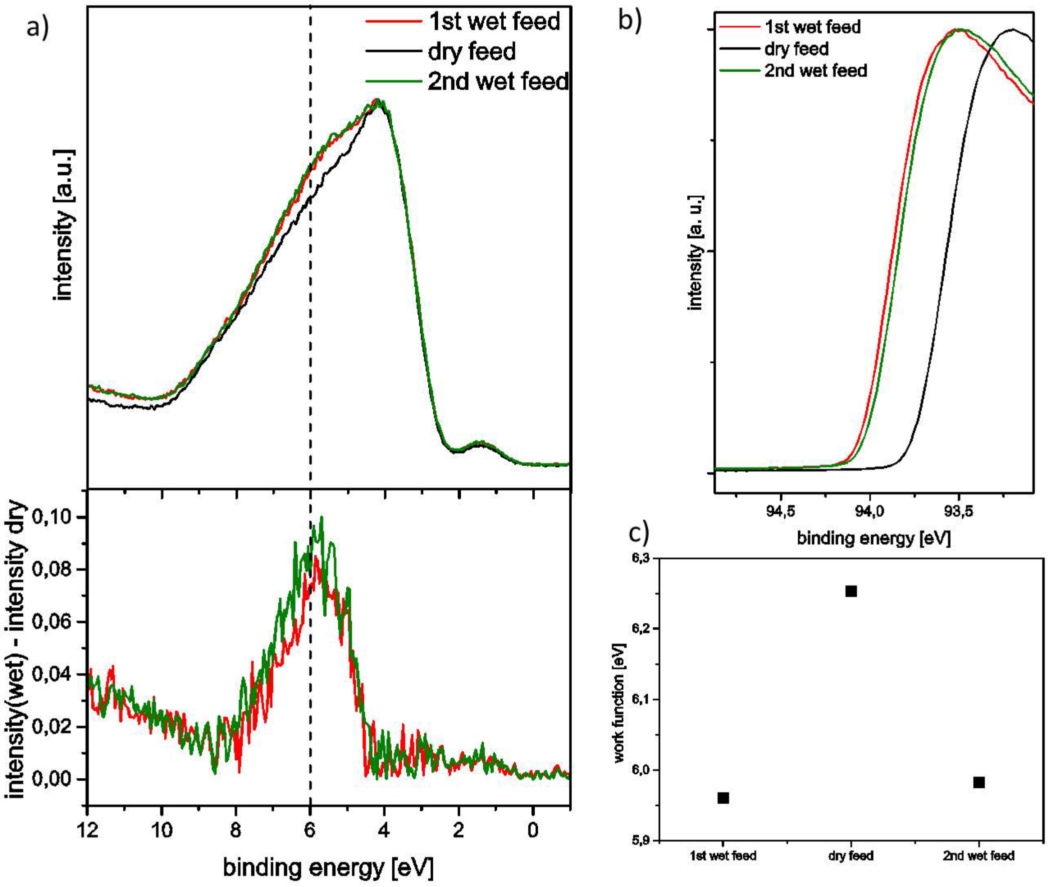

Figure 4.20: *a) Valence band spectra (normalized to their maximum) recorded at 100 eV photon energy, b) secondary electron cutoff, and c) calculated work function of M1 in dry and wet propane oxidation feed.*

edge, and the photon energy $E_{\hbar\omega}$, the work function Φ can be calculated [93]:

$$\Phi = E_{\hbar\omega} - E_{\text{cutoff}} \tag{4.51}$$

The work function of M1 in the first wet feed is 6.0 eV, in the dry feed 6.3 eV and in the second wet feed again 6.0 eV. Thus the work function of M1 is reversibly decreased in the steam containing mixture. In a previous study the work function of M1 probed under similar dry feed conditions was about 6.6 eV [91]. A possible reason for the deviation of the absolute values in dry feed between the two experiments could be a slightly different surface roughness [130] of the investigated pressed powder pellets. It is well known that the determination of precise absolute work functions is even for single crystals very difficult, since they depend very sensitively on the sample surface [92]. In either case, the determined values in dry feed (6.3-6.6 eV) are only slightly lower than the work functions of V_2O_5 (7.0 eV) [146] and MoO_3 (6.9 eV) [76] single crystals and are hence physically plausible. Moreover, during the measurement of one sample but in different gas mixtures the accuracy of the measurement is much higher (about 50 meV) and the reversible change by 0.3 eV between dry and wet feed is significant.

Work function changes can originate from a modification of the band bending and/or of the surface dipolar structure, i.e. by a change in the surface electron affinity [139]. Since an effect of steam on band bending can be excluded based on the valence and core level spectra, the work function change results obviously from modified surface dipoles. As reported previously, steam changes significantly the surface composition of M1 [26, 87, 153]. While the relative metal abundance of vanadium(V) (from 5 to 15%) and tellurium (from 16 to 25%) increases, a depletion in molybdenum from 55 to 35% was observed. It is therefore comprehensible that this drastic compositional change might impact the dipole momenta on the surface and hence changes also the work function of the catalyst. However, a decrease of the work function upon the adsorption of water was also observed in ultraviolet photoelectron spectroscopy studies of the binary oxides V_2O_3 [125] and α-Fe_2O_3 [126]. Hence also the formation of, e.g., OH groups that can neutralize polar surfaces, and/or probably trigger a surface reconstruction due to the reversible formation of metal hydroxides (e.g. of molybdenum), could give rise to the observed steam-induced reduction of the work function.

Summing up, steam does not change the charge carrier density of conduction electrons at the surface and subsurface of M1 since the band bending was not influenced. However, it modifies reversibly the valence band structure and surface polarity of the catalyst. In situ NEXAFS and resonant photoelectron spectroscopy were therefore performed to investigate these findings in more detail.

Near-edge X-ray absorption fine structure (NEXAFS) spectroscopy

The influence of steam on the electronic structure of M1 was further investigated by near-ambient pressure NEXAFS experiments. In figure 4.21a the vanadium L_3-edge spectrum of M1 measured in the total electron yield (TEY) mode is shown under dry and wet propane oxidation conditions at 400°C. For a better comparison, the linear-background corrected spectra were normalized to their maximum. Six prominent features can be identified. The intensities of the features I (514.9 eV) and II (515.5 eV) decrease under wet feed conditions, while features III (516.0 eV) and IV (516.4 eV) remain unaffected. Features V (dry: 517.4 eV, wet: 517.6 eV) and VI (dry: 517.9 eV, wet: 518.2 eV) are reversibly shifted by 0.2-0.3 eV to higher photon energies in steam containing feed. Moreover, the relative intensity of feature V is decreased in the wet feed and can then only be identified as a shoulder on the low energy side of the maximum. It could be shown that energetic shifts in the spectral weight of the V L_3-edge spectrum correlate with the average vanadium oxidation state of the material [83]. This relationship can be understood in terms of the effective nuclear potential which affects the position of the electronic states relative to the vacuum level and the relative position of the corresponding core level [31]. In case of vanadium in the oxidation state 5+ the effective nuclear potential is larger than for vanadium 4+. Thus, the vanadium(V) L_3-edge is shifted to higher photon energies in comparison to the spectrum of a vanadium(IV) or (III) compound. For a more quantitative discussion of such changes, the 1st momentum of the spectral distribution at the V L_3-edge can be calculated in order to precisely determine the spectral weight as a function of the gas composition [83]. The 1st momentum M is calculated after:

$$M = 1/A \int \hbar\omega \, TEY \, d\hbar\omega \,, \tag{4.52}$$

with $\hbar\omega$ being the photon energy, A the integral of the vanadium L_3-edge spectrum and TEY the total electron yield signal. The results of this calculation for M1 in dry and wet feed are depicted in figure 4.21b. A reversible shift by 0.08 eV to higher photon energies upon steam addition can be observed. This shift suggests an increase of the average vanadium oxidation state with steam, which is in agreement with the NAP-XPS experiments (cf. figure 4.19b).

The bulk crystal phase M1 is built of vanadium atoms with formal oxidation states of 4+ and 5+ in an octahedral coordination sphere [45, 152]. According to density functional theory/restricted open shell configuration interaction singles (DFT/ROCIS) calculations of V^{4+} and V^{5+} in distorted octahedral oxygen ligand fields, the low photon energy onset of the vanadium L_3-edge consists of transitions into $3d_{xy,xz}$ (in V^{5+} also $3d_{yz}$) orbitals [141, 140], which could correspond to features I and II in the experimental spectrum

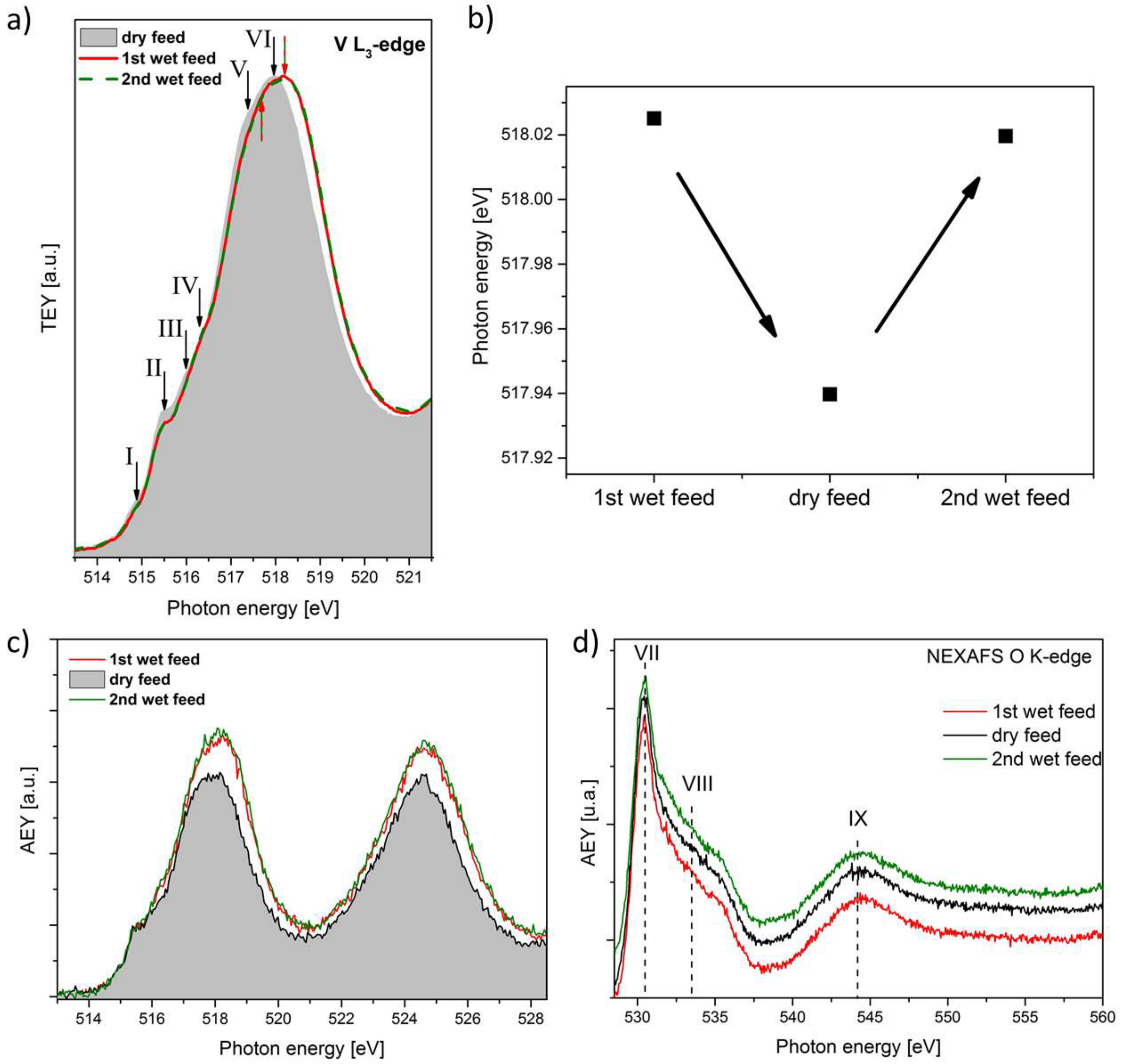

Figure 4.21: *a) Vanadium* L_3*-edge (TEY mode) b) 1st momentum of the vanadium* L_3*-edge c) vanadium* $L_{2,3}$*-edges (AMEY mode) and d) oxygen K-edge in both wet and dry feed (stacked plot with a constant off-set).*

(figure 4.21a). These orbitals are located between ($3d_{xy}$) or above and below ($3d_{xz}$, $3d_{yz}$) the V-O-V bridging bonds in the basal plane of the $[VO]_6$ coordination polyhedra. Thus the decreased intensity of features I and II under wet feed conditions could be assigned to a structural modification of the $3d_{xy}$, $3d_{xz}$, and $3d_{yz}$ orbitals, but a clear assignment to concrete bonding motifs in M1 is difficult. While according to the calculation the main peak of a V^{4+} L_3-edge contains transitions into $3d_{yz}$, $3d_{xy}$, $3d_{x^2-y^2}$ and $3d_{z^2}$ orbitals, it consists for V^{5+} species mainly of transitions into $3d_{x^2-y^2}$, while the contribution of $3d_{z^2}$ is mainly found at the high energy onset. Hence a predominant shift upon a change in the oxidation state of vanadium from 4+ to 5+ can be observed for the transition into $3d_{z^2}$. Thus the large shift of feature V to higher energies can be likely assigned to the $3d_{z^2}$ transition and hence to an increase of the vanadium(V) concentration on the surface. Since an increased energy for the transition into the $3d_{z^2}$ orbital correlates with a shortage of the vanadyl bond in a distorted octahedral oxygen ligand field [141, 140], steam obviously affects basically the V=O bond motif on the surface of M1.

Previous XPS measurements of M1 indicated that not only the average oxidation state, but that also the total vanadium content on the surface is increased in steam-containg feeds [153]. However, the aforementioned TEY NEXAFS mode cannot be used for a comparison of absolute signal intensities in different feeds due to a possibly gas phase dependent photon absorption and inelastic photoelectron scattering [171]. In figure 4.21c vanadium $L_{2,3}$-edge spectra measured in the Auger-Meitner electron yield (AMEY) mode, normalized to the ring current of the monochromator and linear-background corrected to the intensity value at 512 eV, are shown under wet and dry feed conditions in order to compare the absolute resonance intensities. In the AMEY mode Auger-Meitner electrons with a high kinetic energy are detected that are less strongly scattered by the gas phase. The analyzer was set to a kinetic energy of 385 eV to suppress contributions of the gas phase (mainly O_2) to the signal [81]. In wet feed the intensity of the vanadium $L_{2,3}$-edge is reversibly increased in comparison to the dry feed conditions. Assuming that the electron scattering and cascading processes in the M1 solid phase are hardly affected by the chemical modification of the surface due to the wet feed conditions, the AMEY intensity of the vanadium $L_{2,3}$-edge should be proportional to the number of absorption centers. Even if the gas phase phase still disturbs the absolute measurement, since in the wet feed helium is exchanged by steam which should induce an increased photon absorption and inelastic photoelectron scattering, the AMEY signal would then have to decrease with steam. Since the addition of water leads instead to an increased signal, the vanadium content is obviously indeed enriched at the surface, hence supporting the XPS results.

In figure 4.21d a stacked plot of the oxygen K-edge measured also in the AMEY mode is shown. In all spectra three dominant features can be identified. Feature VII is located at 531 eV, a shoulder (feature VIII) arises from 532 to 536 eV and a further feature IX at about 545 eV. No change in the shape of the spectra due to the addition of water to the feed can be identified. The oxygen K-edge of M1 is comparable with the oxygen K-edges of MoO_3 [21] and V_2O_5[204]. MoO_3 has also three features which nearly coincide in their positions and shape with the identified features in M1. Feature VII and VIII can also be observed in V_2O_5, in contrast to feature IX which differs in its position and shape. The main metal component in M1 is molybdenum. Its coordination to oxygen is similar as observed in MoO_3. In both oxides the molybdenum is coordinated by six oxygen atoms in a distorted octahedral ligand field. In this context the feature VII (π^* resonance) and VIII (σ^* resonance) can be assigned to transitions into orbitals with antibonding Mo4d-O2p character indicating covalent bonds between molybdenum and oxygen atoms [21], while feature IX is attributed to transitions into antibonding orbitals with Mo5s-O2p character [21]. In a pure ionic oxide, the oxygen 2p orbitals are completely filled and no resonance would occur. Thus the oxygen K-edge dominated by contributions from molybdenum-oxygen bonds indicates that the molybdenum is to a large extent covalently bonded in M1.

Resonant Photoelectron Spectroscopy (ResPES) at the Vanadium $L_{2,3}$-Edges

In order to investigate the electronic structure of the valence band in detail, resPES is the method of choice. In resPES contributions of a particular element to the valence band can be enhanced by selective excitation [151], if the normal photoelectron channel interferes with a second, element-specific excitation channel. In case of vanadium excited at the V2p threshold both processes can be described in the following way [204]:

$$2p^6 3d^n + \hbar\omega \rightarrow 2p^6 3d^{n-1} + e^- \qquad \text{(direct PES processes)} \tag{4.53}$$

$$2p^6 3d^n + \hbar\omega \rightarrow \left[2p^5 3d^{n+1}\right]^* \rightarrow 2p^6 3d^{n-1} + e^- \qquad \text{(second excitation process)} \tag{4.54}$$

In the second excitation process a 2p electron is excited to an intermediate state marked by the asterisk which is the final state in NEXAFS spectroscopy and decays by a Coster-Kronig or super-Coster-Kronig process [151]. Thus the final state of the direct PES (described by the amplitude A) and second excitation channel (described by the amplitude B) is the same and they can interfere:

$$|A+B|^2 = |A|^2 + |B|^2 + \text{cross term} \tag{4.55}$$

In the case of different final states, the cross term in figure 4.55 vanishes and no enhancement of the PES signal is observed. The valence band of M1 was recorded at photon energies corresponding to the vanadium $L_{2,3}$-absorption edge (figure 4.22a). To check whether an enhancement is due to a resPES process or just an overlap (incoherent enhancement) of the valence band with an Auger-Meitner decay channel, the valence band recorded at different photon energies is plotted versus the kinetic energy of the photoelectrons (figure 4.22c). The O KLL Auger-Meitner emission spectra, which could in principal overlap with the valence band, are shown in figure 4.22b. In case of a non-resonant overlap, the apparent enhancement appears at constant kinetic energies. This is however not observed in our experiment (figure 4.22c). The valence band spectra, normalized to the ring current of the monochromator, plotted versus the binding energy are shown in figure 4.22d. Since the onsets of the valence band spectra shown in figure 4.22 coincide, no background correction of the spectra was necessary. In all spectra the off-resonance valence band spectrum recorded at 512 eV is additionally plotted (dashed red line) to highlight the resonance enhancement. It can be clearly observed that features at binding energies in the range of 1.5 and 6-10 eV are enhanced, if they are excited at photon energies corresponding to the maxima of the vanadium $L_{2,3}$-edge. A plot of the valence band intensities at 1.5 and 6 eV versus the applied photon energy is shown in figure 4.22e. As a result, the excitation energy dependence of the enhancement of the valence band spectrum follows exactly the vanadium L_3- and L_2-edge spectra with maxima at 517.9 and 524.5 eV. Zimmerman et al. performed a resPES study of V_2O_3 and V_2O_5 [204]. In their investigation they identified a resonant enhancement for V_2O_3 at 1 eV binding energy which they attribute to an occupied vanadium 3d state with oxygen 2p admixture. Additionally, they found an enhancement above 6 eV, which was also observed for V_2O_5. In an ionic binding model of binary vanadium oxides the valence band is built of occupied O2p states while the conduction band is formed by unoccupied V3d states. In contrast, in a covalent model allowing a hybridization of V3d with O2p states, the valence band has O2p and V3d character. Thus even V_2O_5, without 3d valence electrons in an ionic model, contains partially occupied V3d (or mixed V3d/O2p) states [57, 166, 204]. Zimmermann et al. attributed the enhancement above 6 eV to the admixture of V3d states to the O2p valence band suggesting a strong covalent V-O bonding character in V_2O_5 [204]. Their conclusion is supported by DFT calculations [57, 204] and was also seen in resPES measurements at the V3p threshold [177, 173].

In M1 the situation is more complicated because besides vanadium, it contains also molybdenum, tellurium and niobium metal atoms. However, vanadium is coordinated by oxygen in a distorted octahedron as in V_2O_5 or V_2O_3. Thus the conclusion obtained for the resPES studies of V_2O_3 and V_2O_5 can be used to interpret the resonance spectra of M1 at

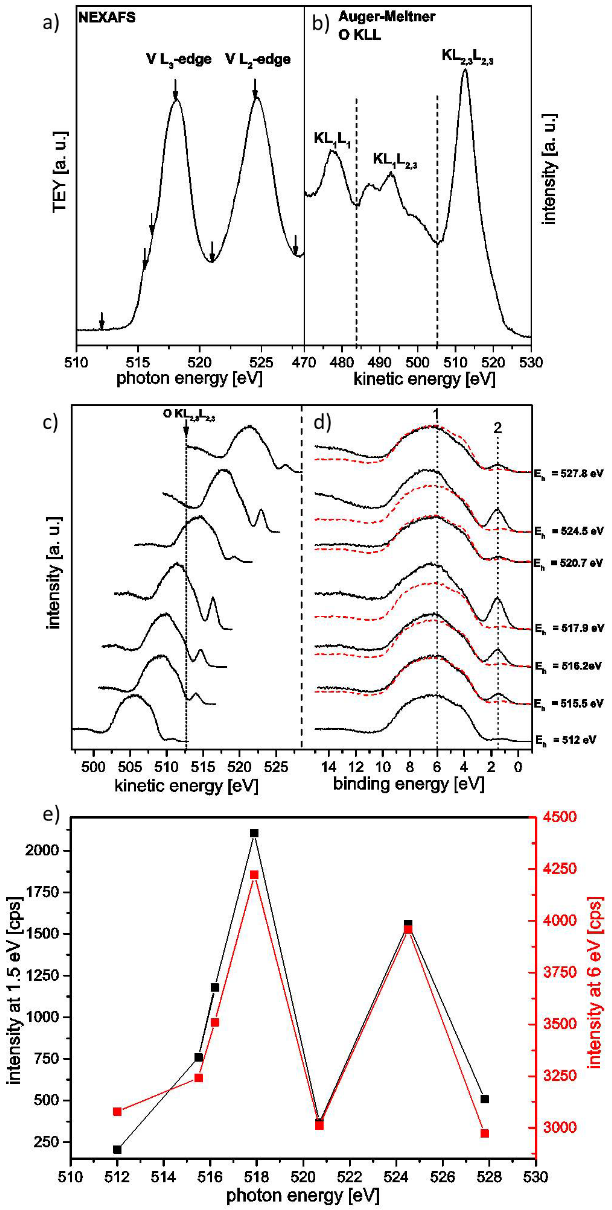

Figure 4.22: *a) Vanadium $L_{2,3}$-edge with marked (arrows) photon energies at which the resPES spectra were measured. b) Oxygen KLL Auger-Meitner spectrum, c) plot of resPES valence band spectra versus kinetic energy, d) resPES valence band spectra versus binding energy, e) intensity of the valence band at 1.5 and 6 eV binding energy versus excitation photon energy.*

the vanadium 2p threshold. Consequently, the enhancement at 1.5 eV binding energy in M1 can be assigned to a partially occupied V3d state. The enhancement between 6 and 10 eV binding energy can be interpreted in terms of a hybridization of V3d with O2p states similar to the results obtained for V_2O_3 and V_2O_5. Thus vanadium shows also in M1 a strong covalent bonding character. These results are in agreement with the interpretation of the oxygen K-edge spectra with a σ^* and π^* resonance component, which was mainly attributed to a hybridization between molybdenum 4d and oxygen 2p orbitals and hence points to a strong covalent molybdenum-oxygen bonding character.

As discussed before, steam induced a significant relative increase of the signal intensity at binding energies in the 6-10 eV range of the valence band (4.20a). This can now be interpreted as an enhancement of the vanadium 3d state admixture to the valence band. This observation agrees with the results obtained from NEXAFS AMEY mode measurements at the $L_{2,3}$-edge (4.21c) and from NAP-XPS results,[26, 87], where an increased vanadium abundance on the surface was observed upon the addition of water to the feed. In studies on the adsorption of water on metal oxides peaks in the valence band spectrum between 6 and 12 eV were assigned to undissociated, strongly chemisorbed, and dissociated water [158, 12]. E.g., for ceria on platinum signals at 10.8 and 7.6 eV were assigned to the 3s and 1p molecular orbital of hydroxyl groups [12]. Consequently, the increased emission above 10 eV observed for the M1 phase might be also arise from the formation of OH groups on the surface of the catalyst upon dissociative adsorption of water. However, in V_2O_5 a very broad satellite of the valence band, which is also seen in other transition metal oxides, occurs between the valence band and the oxygen 2s level above 10 eV [173, 71]. If a feature is enhanced in the valence band, also the corresponding satellite is enhanced because the main line(s) (valence band) and the satellite belong to the same ground state(s). Thus V3d states could also contribute to the increased intensity above 10 eV upon steam addition.

Since the peak at 1.5 eV binding energy can now be assigned to a (partially) filled vanadium 3d state, steam does obviously not influence its occupation (figure 4.20a). Interestingly, it is known from core level studies that only the V^{5+} concentration increases upon steam addition, while the V^{4+} concentration remains constant [87, 26, 153]. The constant and not steam-influenced intensity at 1.5 eV representing basically vanadium with 3d electrons such as V^{4+}, is therefore in good agreement with these findings, while the enhancement of the valence band at 6-10 eV might be due to surface-enriched, covalently bonded V^{5+} species. A changed valence (and likely conduction band) structure means also that the dispersion relation of the energy band and therefore the effective mass of the charge carriers is modified. According to the Drude-Lorentz model used to describe charge carrier dynamics in semiconductors [191], a modified effective mass m^* changes the plasmon frequency $\omega_p = n_e\ e^2/(\varepsilon_0\ m^*)$ (with n_e being the charge carrier density of conduction electrons, e the elementary charge and ε_0 the vacuum permittivity) and therefore the mobility of the charge carriers $\mu_e = e^2\ \tau/m^*$ (with τ being the relaxation time). This affects finally the conductivity given by the equation $\sigma = e\ n_e\ \mu_e$. Thus the modification of the effective mass and hence electron mobility would explain the decreased conductivity in steam containing propane oxidation feed (cf. figure 4.18a).

4.3.5 Conclusion

The selective propane oxidation catalyst $MoVTeNbO_x$ (orthorhombic M1 phase) was investigated by microwave conductivity, synchrotron X-ray photoelectron, soft X-ray absorption and resonant photoelectron spectroscopy under reaction conditions to identify the influence of steam on its bulk and surface electronic properties. The aim of this investigation was to understand the observed steam-induced increase of the selectivity to the target product acrylic acid. We found that steam decreases the electrical conductivity, increases the concentration of V^{5+} and Te^{6+} and decreases the relative amount of Mo^{6+} on the surface, decreases the work function and modifies the valence band structure. Furthermore, we could observe that the catalyst forms under reaction conditions a subsurface space charge region depleted in electrons (upward band bending). This proves that the catalyst acts like a semiconducting gas sensor (chemiresistor), where the (bulk) conductivity can be used to sensor electronic changes on the surface. However, since the addition of steam to the reaction feed does not affect the extent of the band bending, it does obviously not influence the number of charge carriers in the space charge region by an additional bulk surface charge transfer. This could mean that bulk charge carriers do not participate in the formation of acrylic acid. The presence of band bending and hence the formation of a high surface potential barrier, which electrons have to overcome on their way from the bulk to the surface, could be however necessary to terminate the bulk surface charge transfer, limit the formation of active oxygen species on the surface and to achieve finally the high selectivity to acrylic acid, while suppressing its total oxidation to CO_2. The surface potential barrier and the limited bulk surface charge transfer would also explain the extraordinary stability of the $MoVTeNbO_x$ M1 bulk phase under reaction conditions.

4.3.6 Supporting Information

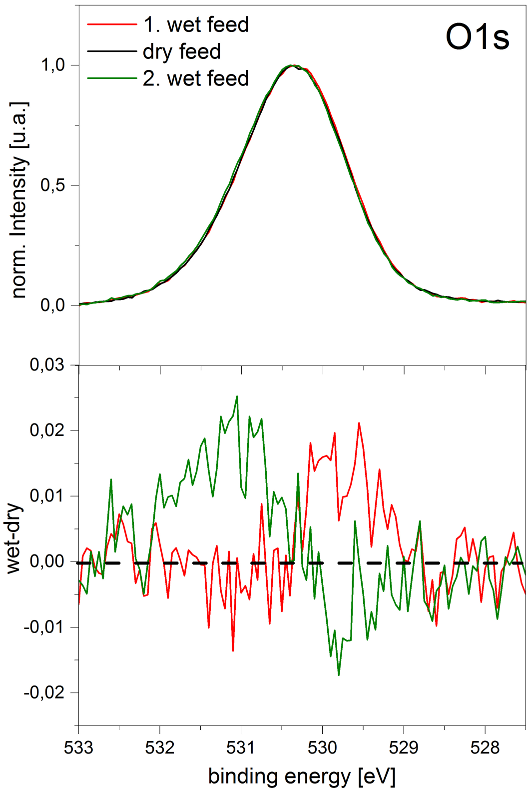

Figure 4.23: *O1s spectra of the MoVTeNbO$_x$ M1 phase at 400°C, 25 Pa in dry (1 Nml/min propane, 2 Nml/min oxygen and 3 Nml/min helium) and wet feed (1 Nml/min propane, 2 Nml/min oxygen and 3 Nml/min steam) and difference between the spectra measured in the two feeds*

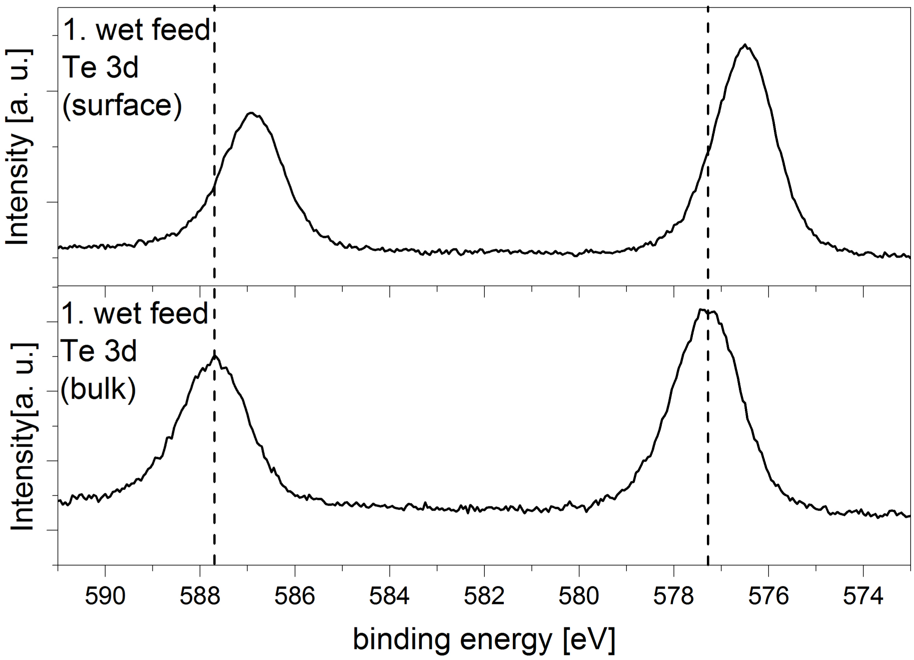

Figure 4.24: *Surface (kinetic energy: 150 eV) and bulk sensitively (kinetic energy: 650 eV) measured Te3d core level spectra of the MoVTeNbO$_x$ M1 phase at 400°C, 25 Pa in wet feed*

Acknowledgement

We thank Dr. Maricruz Sanchez-Sanchez for the preparation of the MoVTeNb M1 oxide sample. The HZB staff is acknowledged for their continual support of the high-pressure electron spectroscopy activities of the FHI at BESSY II.

4.4 Ambient-Pressure Soft X-Ray Absorption Spectroscopy of a Catalyst Surface in Action: Closing the Pressure Gap in the Selective n-Butane Oxidation over Vanadyl Pyrophosphate [3]

Christian Heine[1], Michael Hävecker[1,2], Eugen Stotz[1], Frank Rosowski[3,4], Axel Knop-Gericke[1], Annette Trunschke[1], Maik Eichelbaum[1,4] and Robert Schlögl[1]

[1]Department of Inorganic Chemistry, Fritz-Haber-Institut der Max-Planck-Gesellschaft, Faradayweg 4-6, 14195 Berlin, Germany
[2]Solar Energy Research, Helmholtz-Zentrum Berlin / BESSY II, Albert-Einstein-Straße 15, 12489 Berlin, Germany
[3]Process Research and Chemical Engineering, Heterogeneous Catalysis, BASF SE, Carl-Bosch-Straße 38, 67056 Ludwigshafen, Germany
[4]BasCat, UniCat BASF JointLab, TU Berlin, Marchstraße 6, 10587 Berlin, Germany

4.4.1 Abstract

In order to close the pressure gap in the investigation of catalyst surfaces under real operation conditions we have developed a variable-pressure soft X-ray ($h\nu \leq 1.5$ keV) absorption cell coupled to a gas analysis system to study the pressure dependency of the electronic and catalytic properties of catalyst surfaces in reactive atmospheres at elevated temperatures. With this setup we investigated the vanadium L_3-edge and catalytic performance of polycrystalline vanadyl pyrophosphate in the selective oxidation of n-butane to maleic anhydride between 10 and 1000 mbar at 400°C. As a result, major gas phase and pressure dependent spectral changes are observed at energies attributed to V 2p-3d$_{z^2}$ excitations assigned to vanadium atoms square-pyramidally coordinated to oxygen atoms.

---

[3] Reprinted (adapted) with permission from [Christian Heine, Michael Hävecker, Eugen Stotz, Frank Rosowski, Axel Knop-Gericke, Annette Trunschke, Maik Eichelbaum and Robert Schlögl; Ambient-Pressure Soft X-Ray Absorption Spectroscopy of a Catalyst Surface in Action: Closing the Pressure Gap in the Selective n-Butane Oxidation over Vanadyl Pyrophosphate; 118; 20405 - 20412; August 2014; doi:0.1021 /jp506068x] Copyright [2014] American Chemical Society

This can be interpreted in terms of a shortened vanadyl bond (V=O) and an increased vanadium oxidation state with higher pressures. Since this is accompanied by an increasing catalytic activity and selectivity, it indicates that vanadyl oxygen is actively involved in the selective oxidation of the alkane.

4.4.2 Introduction

Selective oxidation reactions are becoming increasingly important for the (petro-)chemical industry in the dawning post-crude oil era. Nevertheless, the direct oxidation of alkanes, e.g. from natural gas, to produce bulk and platform chemicals is still not established in industry due to a lack of efficient catalysts and processes. Only the selective oxidation of n-butane to maleic anhydride (MA) over vanadyl pyrophosphate (VPP) has been successfully commercialized [98, 28, 27, 196, 103, 78]. Hence, the comprehension of the working mode of VPP is of general interest to improve or even rationally design selective alkane oxidation catalysts. However, the active surface structure forming under reaction conditions and the function of each catalyst component in the reaction mechanism has not been clearly identified yet [8], though active site models on the basal plane of a VPP crystal in relation to the proposed reaction mechanism via an olefinic [28, 16, 3] or alkoxide route [29] have been suggested. Most often a vanadium(IV)-vanadium(V) redox couple, or even isolated V^{5+} (or V=O) sites are proposed to accomplish the 14-electron oxidation of n-butane to maleic anhydride via a Mars-van Krevelen mechanism, (V^{4+}) Lewis acid sites are considered to adsorb or activate the alkane, whereas phosphorous or in particular P-OH Bronsted acidic sites are suggested to stabilize reaction intermediates or trigger the desorption of the product MA [98, 155, 28, 27, 196]. Recently, it was even proposed that phosphates are directly involved in the C-H bond activation of n-butane [33]. Experimentally, it could be proven that the active surface differs tremendously in its electronic and compositional structure from the bulk crystal VPP phase, strongly depending on the applied gas composition and temperature [122, 85, 14, 82, 114, 52, 51]. VPP and its precursors are highly dynamic materials and can form a variety of metastable phases under n-butane oxidation conditions [104, 2, 122, 196, 38]. Near-ambient pressure X-ray photoelectron spectroscopy (XPS) measurements [52] indicate that the average surface vanadium oxidation state on VPP in feed gas (n-butane/oxygen) at the reaction temperature of 400°C is with +4.3 significantly higher than in the bulk (+4.0) and that the surface V/P/O ratio is with 1/1.5/6 different than the bulk ratio of 1/1/4.5. Moreover, the average vanadium oxidation state on the surface can fluctuate between 4.0 and 4.3 depending on the applied gas phase. A vanadium oxidation state profile recorded at different photoelectron escape depth exhibited, that only the topmost surface (within 1 nm depth) interacts with the gas atmosphere at 0.5 mbar, while the bulk phase remains intact, being in agreement with kinetic studies suggesting that only the surface layer(s) can exchange oxygen with the gas phase [155].

However, a disadvantage of the aforementioned surface-sensitive investigations is that they are typically limited to the millibar pressure range [115]. In XPS the excited photoelectrons are inelastically scattered at gas molecules on their way to the differentially pumped analyzer, thus increasingly diminishing the signal to noise ratio with higher pressures. It is however not clear, if in this pressure range the qualitative pressure gap limiting or influencing the chemical dynamics of the catalyst is already surpassed.

For the here relevant metal oxides, the Gibbs free energy, the related chemical potential and the surface energy are all a function of the oxygen pressure [136, 159]. Since the surface energy is related to the surface termination, surface reconstructions or relaxations are affected by the oxygen pressure, too. For VPP, the n-butane conversion in the in situ experiments at 0.5 mbar was below 1% [52], which considerably differs from the performance of VPP at 1 bar with a conversion in the range of $\geq$50% in an optimized reactor [28]. The reactor schemes (stagnation flow versus plug flow) cannot be directly compared, but an additional reason for the conversion discrepancy could be a surface layer depleted in oxygen at the VPP surface at 0.5 mbar, thus challenging the validity of the mechanistic interpretations of the near-ambient pressure measurements. Since the oxidation of n-butane to maleic anhydride involves the reduction of VPP by n-butane and its re-oxidation by gas phase oxygen [155, 2], a modification of the surface termination at steady state as function of the oxygen chemical potential could directly affect the kinetics of the oxidation and reduction reaction, respectively. A hint for a pressure-dependent VPP surface layer was given by recent microwave conductivity measurements at 1 bar [51]. Here, the conductivity increased significantly upon changing the feed from reaction gas (2% n-butane, 20% O_2) to air, indicating a strong oxidation of the p-type semiconducting catalyst. This strong effect was not observed with XPS at 0.5 mbar, where only a minor vanadium oxidation state change was monitored [52].

An alternative method for investigating the active surface is X-ray absorption spectroscopy (XAS). In the total electron yield (TEY) mode, the signal is dominated by Auger-Meitner (AM) electrons [55]. All elastically and inelastically scattered electrons are collected and detected at a given photon energy, independent on their kinetic energy. Here, the gas atmosphere can even enhance the signal [203]. Escaped primary electrons with high kinetic energy ionize gas molecules and generate a cascade of secondary electrons resulting in the so called conversion electron yield (CEY) [203]. This method was introduced by Shevchik and Fischer [171] and Kordesch and Hoffman [118]. It has been shown that in the CEY mode it is possible to measure XAS in the hard X-ray range under reaction conditions at ambient pressure [203, 171, 118]. E.g., Moggridge et al. applied the CEY technique to a

copper/zink oxide catalyst system under methanol synthesis reaction conditions at 1 bar [148]. They investigated the Cu K-edge at a photon energy of 9 keV and a kinetic energy of non-scattered photoelectrons of about 7 keV, corresponding to an inelastic mean free path length of the Cu KLL Auger electrons of about 8 nm. In the soft X-ray range ($<$1000 eV) the photoionization cross section is significantly higher [185] and the electron escape depth is in the range of only a few nanometers. The methodology has been applied in pioneering works, e.g., for the in situ investigation of the conversion of methanol to formaldehyde over copper catalysts at 0.5 mbar [84], the reaction of cobalt nanoparticles with hydrogen and carbon monoxide up to 1 bar [56, 189], and the investigation of an iron-based Fischer-Tropsch catalyst in a microelectromechanical system (MEMS) reactor with scanning transmission X-ray microscopy up to 1 bar [43].
Based on these concepts we have developed a variable-pressure in situ near-edge X-ray absorption fine structure (NEXAFS) setup to investigate absorption edges of pressed VPP powder pellets in a reaction cell in the soft X-ray range at pressures up to 1 bar and temperatures up to 400°C, while measuring the pressure dependent catalytic performance. This approach enables a much higher surface sensitivity (estimated inelastic mean free path length of AM photoelectrons: 1 nm) than previous designs optimized for the hard X-ray range [147, 169, 188]. With the variable pressure capability (1-1000 mbar) direct comparison with results obtained from low pressure methodologies [52, 51] is facilitated due to the overlap in pressure and surface sensitivity. In contrast to the hard X-ray regime, the low photon transmission through the gas phase is a major challenge in the soft X-ray range (cf. Supporting Information) and thus the X-ray path through the gas phase needs to be minimized. However, this results in small distances that create technical difficulties when approaching elevated sample temperatures, but were overcome in our system. More technical details of the setup are given in the Supporting Information.

4.4.3 Results and Discussion

In the present study we investigated the vanadium L-edges of polycrystalline VPP. The sample consists of phase-pure vanadyl pyrophosphate and its preparation and characterization was described recently [52, 51]. The bulk phase remained stable during all treatments as proven by powder X-ray diffraction and Raman spectroscopy. The pressure dependency of the catalyst surface was investigated by taking spectra at 10, 100 and 1000 mbar in a reducing (1.5% n-C_4H_{10} in He), reaction (1.5% n-C_4H_{10}, 20% O_2 in He) and oxidizing atmosphere (20% O_2 in He) at 400°C. A further complication is the $1\sigma_u \to \pi^*$ transition of O_2 at 531 eV that can enormously affect the background of the vanadium $L_{2,3}$-edge spectra. In the case of the experiments at 10 and 100 mbar it turned out that a simple linear background subtraction is suitable. Spectra at 1000 mbar in the presence of oxygen were corrected by the subtraction of an O_2 reference spectrum as shown in figure 4.25a. In the inset of figure 4.25a linear-background corrected spectra at 10 and 100 mbar are compared with the O_2-reference corrected spectrum at 1000 mbar. Since the low and high energy onsets of the vanadium L_3-edges of all data sets coincide, we conclude that both types of background correction are suitable and spectra at different pressures can be compared. The pressure-dependent activity and selectivity of VPP during the experiment was evaluated by analyzing the reaction gas with mass spectrometry (figure 4.25b). Mass spectrometry has been chosen here for the indispensable confirma-

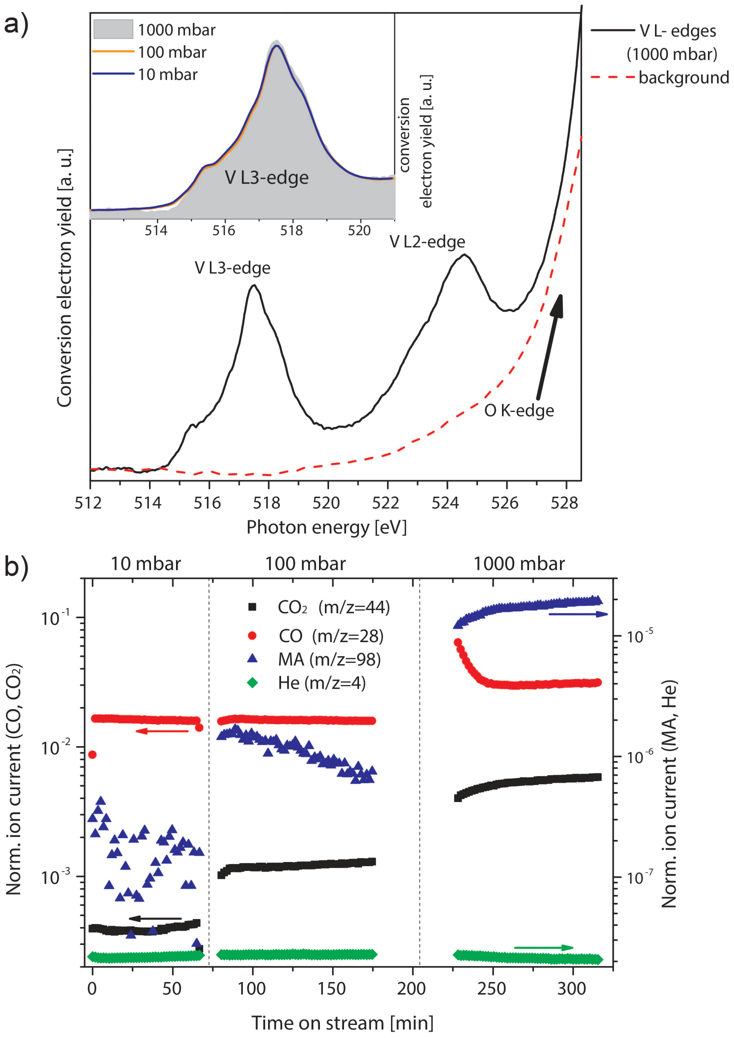

Figure 4.25: *a) Uncorrected V $L_{2,3}$-edge spectra of VPP in n-C_4H_{10}/O_2 at 1000 mbar and 400°C and the O K-edge onset of molecular oxygen. Inset: Background-corrected V L_3-edge spectra of VPP in n-C_4H_{10}/O_2 at 400°C at different pressures (10 and 100 mbar: linear background correction; 1000 mbar: subtraction of the K-edge spectrum of O_2). b) MS ion currents of CO, CO_2, maleic anhydride (MA) and He as detected under the conditions indicated in a). The CO, CO_2 and MA ion currents are normalized to the He ion current.*

tion of the functionality of the catalyst, and because it can be easily adapted to the variable cell pressure conditions. The pressure in front of the mass spectrometer was controlled by process pumps, and was kept constant at 5.5 mbar during all experiments, irrespective of the applied pressure in the reaction cell. By this way, the measured ion currents for the different products can be directly compared for all pressure ranges, as indicated by the stable He trace (figure 4.25b). As a result, in reaction feed (1.5% n-C_4H_{10}, 20% O_2 in He) the products CO, CO_2 and maleic anhydride were observed in the whole investigated pressure range, indicating that the catalyst was always active. The n-butane conversions could not be determined since only a small fraction of the gas phase is in contact with the catalyst pellet in the reaction cell (cf. Supporting Information), but qualitative trends can be deduced unambigously. Only a small increase in the production of CO_2 and maleic anhydride could be observed upon increasing the total pressure from 10 to 100 mbar. However, at 1000 mbar an enormous increase of all reaction products was detected. While the ion current and hence concentration of CO doubled, a five-fold increase was observed for CO_2 and an increase of MA by more than one order of magnitude, pointing to a significant MA selectivity gain with rising pressures. This can be explained by 1) a pressure-dependent reaction rate due to pressure-dependent sticking coefficients and hence surface coverages with reactive adsorbates on unchanged active sites and/or 2) by a dynamical pressure gap with structural changes of the active surface. The latter effect is being investigated by the NEXAFS experiments and is discussed in the next paragraphs.

In figure 4.26 the vanadium L_3-edge spectra of VPP in 1.5% n-butane in He ("n-C_4H_{10}"), 20% O_2 in He ("O_2") and 1.5% n-butane, 20% O_2 in He ("n-C_4H_{10}/O_2") at 10, 100 and 1000 mbar are shown. As a result, the spectral weight of the V L_3-edge in n-C_4H_{10} is clearly shifted to lower photon energies in comparison to the spectra in n-C_4H_{10}/O_2 and O_2, independent of the total pressure. At 10 and 100 mbar the spectra in n-C_4H_{10}/O_2 and O_2 nearly coincide. This is in clear contrast to the spectra at 1000 mbar. Here, in O_2 the spectral intensity at the high energy onset is significantly increased in comparison to the spectrum in n-C_4H_{10}/O_2. In order to precisely determine the overall position of the V L_3-edge as a function of the gas composition and the total pressure, the 1st momentum (M_1) of the V L_3-edge peak area was calculated:

$$M_1 = 1/A \int E\ CEY\ dE, \tag{4.56}$$

with E being the photon energy, CEY the conversion electron yield and A the V L_3-edge peak area. In a first approximation, the 1st momentum can be correlated with the vanadium oxidation state [182, 31, 30] as it was shown for different vanadium oxides and phosphates [83]. This relationship can be understood in terms of the effective nuclear potential which affects the position of the electronic states relative to the vacuum level and relative to each other. In case of vanadium in the oxidation state 5+ the effective nuclear potential is larger than for vanadium 4+. Thus, a vanadium(V) L_3-edge is shifted to higher photon energies in comparison to the L_3-edge of a vanadium(IV) or (III) compound [31, 30, 141]. figure 4.31a shows that at 10 mbar the 1st momentum of the V

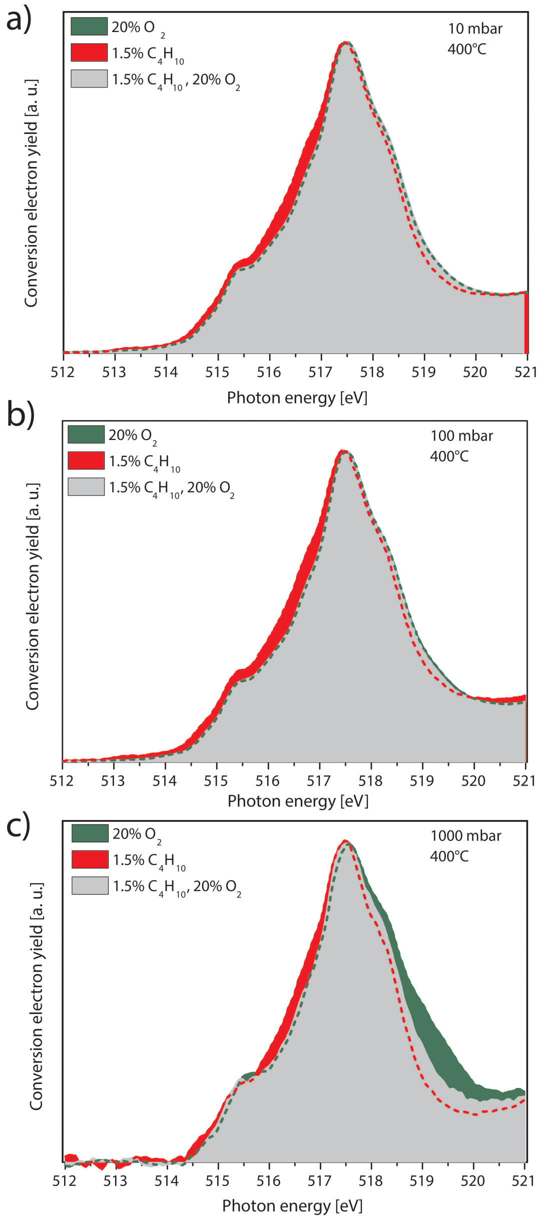

Figure 4.26: *V L_3-edge spectra of VPP in n-C_4H_{10}, n-C_4H_{10}/O_2 and O_2 atmosphere at a) 10 mbar, b) 100 mbar, c) 1000 mbar.*

L_3-edge in n-C_4H_{10} is shifted by about 0.1 eV to lower photon energies in comparison to the n-C_4H_{10}/O_2 and O_2 atmosphere. Only a very small difference is observed between the V L_3-edge in n-C_4H_{10}/O_2 and O_2. This is in agreement with recent XPS measurements at 0.5 mbar, showing a strong vanadium oxidation state change from 4.07 to 4.25 between n-

C_4H_{10} and n-C_4H_{10}/O_2, but only a small variation from 4.25 to 4.31 between n-C_4H_{10}/O_2 and O_2 [52]. Moreover, the pressure dependence of the V L_3-edge in n-C_4H_{10} is small, only slightly increasing by 0.05 eV from 10 to 1000 mbar (figure 4.31a). In the reaction feed n-C_4H_{10}/O_2 the position of the V L_3-edge is shifted by 0.05 eV to higher photon energies from 10 to 100 mbar, and increases further by 0.07 eV between 100 and 1000 mbar. An even more pronounced pressure dependence can be deduced from the 1st momentum shift in the pure O_2 atmosphere. While the V L_3-edge shifts from 10 to 100 mbar by only 0.04 eV, it increases by 0.20 eV between 100 and 1000 mbar. At 1000 mbar the 1st momentum cleary rises from the n-C_4H_{10} to the n-C_4H_{10}/O_2 atmosphere (difference 0.17 eV) and further from the n-C_4H_{10}/O_2 to the O_2 atmosphere (difference 0.13 eV). We

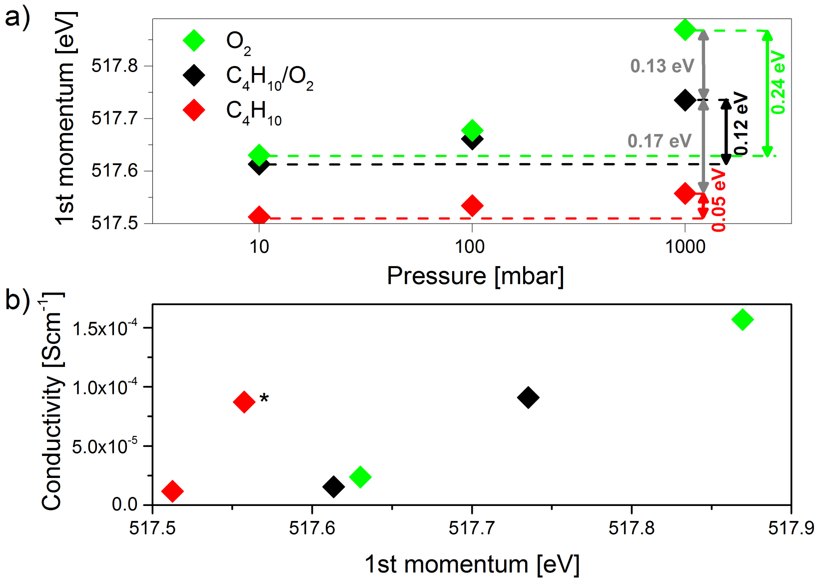

Figure 4.27: *a) 1st momenta of the V L_3-edge spectra and b) correlation plot between 1st momenta and microwave conductivtiy at 9.26 GHz of VPP measured under the same pressures (10 and 1000 mbar) and gas ratios (but with N_2 as inert gas) after ca. 100 min equilibration time except for *: Under this condition (1000 mbar, C_4H_{10}), recorded at the conductivity minimum after 20 min, coking was observed.*

use the 1st momentum of the V L_3-edge as a descriptor for the formal valence of vanadium and hence for the oxidation power of the surface. At low (10 mbar) and intermediate (100 mbar) pressures only the oxygen chemical potential affects the surface oxidation state, whereas the admixture of n-butane has no measurable influence. At 1000 mbar this changes and the presence of n-butane leads to a detectable reduction of the surface oxidation state despite the presence of oxygen in the gas phase. These novel pressure-resolved observations lead to the following conclusions. At 1000 mbar the surface state of the VPP catalyst is controlled by the catalytic reaction providing a steady state between reduction of the oxide during n-butane conversion and re-oxidation by oxygen. The fact that the reduction part of the reaction reduces the average surface oxidation state below the value expected for the oxygen chemical potential at 1000 mbar tells us that the re-oxidation is slower than the reduction and that we have a situation often indicated with the term "Mars-van Krevelen" mechanism. The generation of the reactive surface by re-oxidation is rate-limiting and controls the steady state of the surface electronic structure. The underlying reason for this is the fact that at the now prevailing levels of conversion the oxygen chemical potential is significantly consumed by the catalytic conversion and the tacit assumption that the supply of reactants is independent from the extent of conversion is invalid. We note that this effect can be observed at overall "differential reaction conditions" of a stagnant flow reactor. The consequence for the catalytic function is that only at 1000 mbar the dynamics of the catalyst is suitable of controlling the selectivity by site-isolation: oxidized patches as active sites isolated by reduced patches preventing over-oxidation of MA.

At lower pressures this is not the case and the steady state of the electronic structure of the catalyst is solely given by the chemical potential of oxygen. The extent of n-butane adsorption and conversion is low enough so that re-oxidation of the surface can always be achieved up to the state that is given by the oxygen chemical potential. The kinetics is not of "Mars-van Krevelen" but rather of "Langmuir-Hinshelwood" type. This observation has major implications for understanding diverging statements about the reaction kinetics in the literature as obtained under different regimes of partial and total pressures. This interpretation is also supported by pressure- and gas phase-dependent microwave conductivity experiments, depicted in a correlation plot with the 1st momenta of the NEXAFS measurements in figure 4.31b. The conductivity was measured with the in situ microwave cavity perturbation technique at 9.26 GHz [53]. This technique allows the contactfree measurement of the electrical conductivity of powder samples under reaction conditions and is described further in the Supporting Information. While the conductivity of VPP in n-C_4H_{10} at 1000 mbar is not directly comparable to the other values due to the formation of coke at higher pressures, which itself has a high electrical conductivity as it was shown recently [51], it can be clearly observed that there is a straightforward correlation with the NEXAFS signal in both n-C_4H_{10}/O_2 and O_2 atmosphere at the investigated pressure ranges of 10 and 1000 mbar. Since VPP is a p-type semiconductor [52], the increasing conductivity with higher pressures indicates a higher concentration of electron holes $h^{\cdot}$ as majority charge carriers due to the depletion of oxygen vacancies $V_O^{\cdot\cdot}$ by oxygen and the formation of lattice oxygen O_O^x, and hence a higher oxidation state:

$$V_O^{\cdot\cdot} + 1/2O_2 \rightleftharpoons O_O^x + 2h^{\cdot} \tag{4.57}$$

Moreover, while the effect of n-butane in reaction feed on the conductivity is small at low pressures (10 mbar), it significantly decreases the conductivity at 1000 mbar. This is exactly the same behaviour as deduced from the NEXAFS experiments giving a clear correlation between these two techniques. Only the values measured in n-C_4H_{10} deviate from this trend. This can be explained on the one hand by coke formation, as proven at least for 1000 mbar [51], but could be also due to structural or electronic changes only affecting the surface (e.g. formation of vanadium(III)) as only sensed by the NEXAFS signal. It is to be noted that the two methods do not necessarily probe the same, but closely related properties of the catalyst, namely the electronic surface structure and the absolute charge carrier density (or oxygen vacancies) of the whole catalyst, being related by the formation of a space charge region and a surface state modified band bending as observed in semiconductor gas sensors (chemiresistors) [91].

The spectral shape of the NEXAFS spectra can be also interpreted in more detail in order to develop a concept of the geometric structure of the active surface. In general, the V L_3-edge spectrum is mainly influenced by the coordination of vanadium by oxygen and its oxidation state. Though the exact structure of the catalyst surface is unknown, the crystal structure of VPP is taken as starting point in order to interpret the V L_3-edge spectrum of the working catalyst. The edge- and corner-sharing coordination polyhedra of vanadium in VPP separated by pyrophosphate groups are shown in figure 4.28a. VPP crystallizes in the orthorhombic space group $Pca2_1$ [50, 69]. All vanadium atoms are (4+1) square-pyramidally coordinated to 5 oxygen atoms and weakly bound to the apical oxygen atom of the $[VO_5]$ pyramid from the next layer (V-O bond length about 2.29 Å) parallel to the (100) crystal plane (represented by strongly distorted $[VO_6]$ coordination polyhedra in figure 4.28a and figure 4.28b). The two edge-sharing $[VO_5]$ pyramids in the (100) plane are mirror-invertedly arranged. The vanadium atom is shifted from the basal plane of the pyramid towards the oxygen atom at the top forming a short V=O vanadyl bond (1.60 Å). The four equatorial V-O bonds range from 1.95 to 2.07 Å. The oxygen coordination of vanadium in VPP is very similar to V_2O_5 (figure 4.28c), which crystallizes in the orthorhombic space group Pmmm with distorted $[VO_5]$ square pyramids as coordination polyhedra. The vanadium atom is bound to the top oxygen atom by a slightly shorter V=O bond (1.58 Å), and to the apical oxygen atom of the next layer by a much longer V-O bond (2.79 Å) as compared to VPP. In contrast to VPP, two mirror inverted edge-sharing square pyramids are directly connected via edges and corners to neighboring pyramid pairs. In general, higher oxidation states of the central atom cause a stronger distortion of the ligand field and consequently a stronger deviation of the coordination polyhedra from the ideal highly symmetric case. In a simple ligand field model the energetic order of V3d states in a square-pyramidal ligand field is $3d_{z^2} > 3d_{x^2-y^2} >$

$3d_{xz,yz}$ (degenerated) $>$ $3d_{xy}$ [140, 141]. Maganas et al. computed the V $L_{2,3}$-edge spectra of V_2O_5 and of vanadium(IV) and (V) oxide model complexes with square-pyramidal oxygen coordination with the density functional theory/restricted open shell configuration interaction singles (DFT/ROCIS) method including charge transfer and intra-atomic multiplet coupling effects [140, 141]. For V_2O_5 the energetic order of the main peaks corresponding to transitions into the respective 3d states is in agreement with the above described ligand field theory [140], with a low energy feature at 515 eV attributed to 2p-$3d_{xy}$, a shoulder at 516 eV mainly corresponding to 2p-$3d_{xz,yz}$, the most intense peak at 517 eV from 2p-$3d_{x^2-y^2}$, and a shoulder at 519 eV attributed to 2p-$3d_{z^2}$ single electron excitations. According to the DFT/ROCIS calculations [141], a reduction of the central vanadium atom from 5+ to 4+ in a square-pyramidal oxygen coordination is basically accompanied by a large energy shift of the spectral feature attributed to 2p-$3d_{z^2}$ excitations from 519 eV to 517 eV. This can be interpreted in terms of an elongated vanadyl bond (V=O) mainly affecting the energy of the $3d_{z^2}$ orbital pointing into the direction of the vanadyl oxygen atom. In contrast, contributions from 2p-$3d_{x^2-y^2}$ transitions are not much influenced by the vanadium oxidation state. The $3d_{x^2-y^2}$ orbital is situated in the equatorial plane of the coordination polyhedra (figure 4.28b and c) and strongly overlapping with 2p orbitals from the bridging oxygen atoms in this plane, that are hardly influenced by the distortion. The most prominent differences in the experimental V L_3-edge spectra of VPP due to the different gas mixtures are observed at 1000 mbar (figure 4.26). In

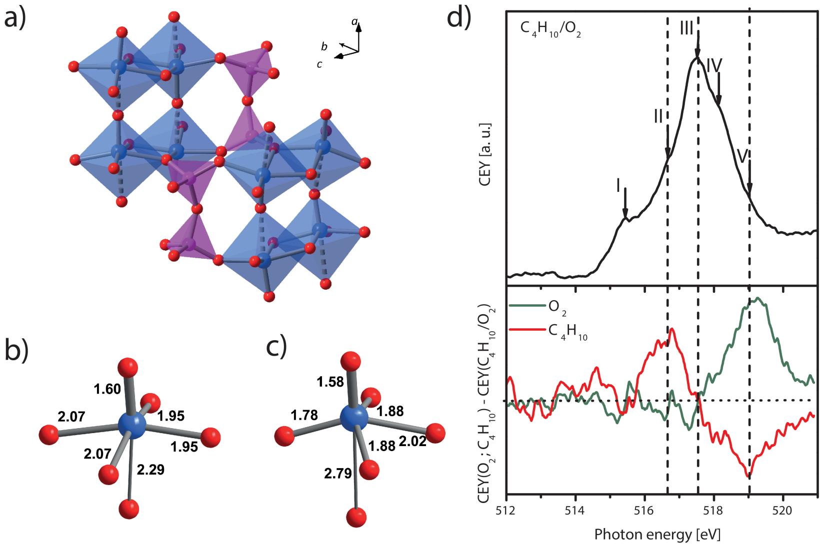

Figure 4.28: *Crystal structure (a) and characteristic single [VO_6] coordination polyhedron of VPP (b) and V_2O_5 (c) with V-O bond lengths in Å. Color code: blue: vanadium, red: oxygen, violet: phosphorous. d) Vanadium L_3-edge spectrum of VPP at 1000 mbar and 400°C in n-C_4H_{10}/O_2 atmosphere and difference spectra between spectra recorded in O_2 and n-C_4H_{10}/O_2, and between n-C_4H_{10} and n-C_4H_{10}/O_2, respectively.*

general, the shape of the measured V L_3 spectra of VPP is very similar to the V L_3-edge spectrum of V_2O_5 also exhibiting five distinct features (figure 4.28d) [140]. Feature III at 517.5 eV represents the maximum of the spectrum agreeing very well with the signal from 2p-3$d_{x^2-y^2}$ excitations in the DFT/ROCIS calculation. For a better comparison, difference spectra between the spectrum recorded in n-C_4H_{10}/O_2 and the spectra recorded in O_2 and n-C_4H_{10}, respectively, have been plotted in figure 4.28d. As a result, the maximum is not shifted in the different atmospheres, and neither in the different pressure ranges (figure 4.26), hence indicating that the bridging V-O-V bonds in the (100) plane are not much affected by the gas phase. Feature I of the experimental V L_3-edge spectrum at 515.5 eV, which is neither affected by the change of the gas atmosphere, agrees well with the 2p-3$d_{xz,yz}$ transitions. In contrast, large changes are observed for feature II at 517 eV and feature V at 519 eV. Since DFT/ROCIS predicts a shift from 517 to 519 eV for the signal assigned to 2p-3d_{z^2} transitions upon oxidation from V^{4+} to V^{5+} [140, 141], the decrease of feature V in n-C_4H_{10} (increase in O_2) and increase of feature II in n-C_4H_{10} can be perfectly interpreted in terms of an increasing (decreasing) vanadyl bond length due to a decreasing (increasing) vanadium oxidation state.

4.4.4 Conclusions

From the variable-pressure NEXAFS experiments of VPP a pressure dependency of the vanadium L_3-edge spectrum indicating a changing vanadium oxidation state on the surface can be clearly deduced. Moreover, also the activity and selectivity in the n-butane oxidation to maleic anhydride on VPP exhibit a pressure gap. Although a higher surface oxidation state with respect to the bulk under reaction conditions has been already obtained from low pressure XPS [52] and NEXAFS [51] experiments, the degree of oxidation is obviously a function of the total pressure, too, and hence the absolute surface oxidation state is being underestimated in the low pressure investigations. Interestingly, in all investigated pressure ranges and gas mixtures the general shapes of the V L_3-edge spectra are very similar, which indicates that the vanadium coordination and hence the geometric surface structure is not strongly affected by the total pressure. Basically, the vanadium 3d_{z^2} orbital and hence the vanadyl bond is mainly influenced by the reactive gas phase. The detected modification of the V=O bond at higher pressures is in line with its function as dynamical centre of activating the alkane. Tautomerisation into $V^{5+}{=}O \Longleftrightarrow V^{4+}{-}O^{*}$ could be a realistic formulation of the species creating a butyl radical as first reactive intermediate. Its further oxidation will proceed via acceptance of oxygen atoms from the interlinked polyhedra termed in the literature sometimes as "surface lattice oxygen". The resulting vacancies expose reduced vanadium centers to gas phase oxygen from where the re-oxidation process may begin. This process may be mainly sensed by the conductivity

measurements.
This is relevant with respect to the overall kinetic description of the VPP process providing an experimental molecular picture to the often discussed "Mars-van Krevelen" mechanism. The V=O species are activated with respect to the parent structure by the surface dynamical changes observed in this work to allow for facile radical formation from n-butane. This activation is made possible by the oxidation of V^{4+} to V^{5+}, which in turn requires restructuring of the VPP crystal structure in which no V^{5+} is possible. This restructuring may be associated with hydrolysis of the pyrophosphate being naturally a water-sensitive species. We observe a reaction-induced surface restructuring initiated by the catalytic reaction and confined in its extent to the surface, as defined by the information depth of our high-pressure NEXAFS experiment, by the underlying bulk structure and the presence of phosphate species as crystallization inhibitors for V_2O_5. The regeneration of the V=O species after transformation into a V-OH group is critical for maintaining the catalytic cyle and may represent the process limiting the re-oxidation kinetics. Finally, it is stressed that a combination of novel experimentation techniques with an in-depth theoretical analysis of the spectral shapes obtained through these new experiments allowed a fresh look at an old problem with the perspective to find a quantitative spectroscopic verification for a still hypothetical kinetic description of the selective oxidation of n-butane.

Acknowledgement

The present work has been supported by the German Federal Ministry of Education and Research (BMBF) as part of the ReAlSelOx project, grant number 033R028B. The HZB staff is acknowledged for their continual support of the high-pressure electron spectroscopy activities of the FHI at BESSY II. The work was conducted in the framework of the BasCat collaboration between BASF SE, the TU Berlin and the FHI. We thank the Berlin Cluster of Excellence Unicat for support.

4.4.5 Supporting Information

Variable-pressure NEXAFS setup

The experimental setup is shown in figure 4.29. The variable-pressure NEXAFS system is divided in a low pressure, a reaction and an optic section. The low pressure section consists of a differential pumping stage (CF 63/40 cross) connected by a flexible CF 40 metal tube with an x-y stage for X-ray beam alignment. It is connected to the Bessy II ISISS beamline and separated by an X-ray transparent Si_3N_4 membrane from the reaction section. The X-ray membrane (1.0 x 1.0 mm^2, thickness: 150 nm) mounted into a 17.5

x 17.5 mm^2, 200 μm thick wafer is glued with high temperature epoxy (EPO-TEK 353 ND) on a stainless steel tube. The epoxy has to seal the low pressure section and to resist the temperatures (400°C sample temperature) in front of the reaction cell. The distance between the X-ray membrane and the sample container (typically 2 mm) can be adjusted in order to minimize the X-ray path length while avoiding an overheating of the membrane. The stainless steel tube with the X-ray membrane is connected with a Swagelok ultra torr UHV fitting adapter to a CF 40 flange (figure S1b). The X-ray membrane is specified to resist a pressure differential of 1000 mbar under static conditions. The low pressure section is slowly pumped to 1 mbar ($\Delta p/\Delta t \approx 0.3$ mbar/s) by a diaphragm pump to achieve a quasi static force on the X-ray membrane. Afterwards the operation pressure of 10^{-7} mbar is reached with a turbo molecular pump.

The reaction and the optic section are mounted on a rack movable in the x, y and z direction and connected via a flexible CF 40 metal tube with the low pressure section. Thus, the alignment of the X-ray membrane is decoupled from the alignment of the X-ray beam. The reaction gas supply of the reaction chamber (CF 40 cube) is arranged by Bronkhorst mass flow controllers. For the supply and exhaust pipe system Swagelok VCR connectors are used. The exhaust pipe system is heated, preventing a condensation of reaction products. The reaction gas enters the reaction chamber via a CF 40/Swagelok adapter flange, flows through the central hole in the Faraday cup (diameter 1 mm) of the reaction cell, passes the sample pellet and leaves the reaction cell through a hole in its bottom pumped by the process pumps. Details about the reaction cell will be described in the respective section. A PID controller (RVC 300 Pfeiffer Vacuum) keeps the desired pressure in the reaction chamber constant via a feedback loop between the throttle valve and the capacitance pressure gauge at the gas inlet of the reaction chamber. After the gas passes the throttle valve the process pumps control the pressure in front of the mass spectrometer (Pfeiffer Omnistar GSD320 VARI), which was kept constant during the experiment (5.5 mbar). The used system is a conventional quadrupol mass spectrometer with a heated inlet valve, that automatically adapts the gas flow into the mass spectrometer recipient to obtain a constant recipient pressure of 2×10^{-6} mbar.

A 808 nm, cw infrared (IR) laser (LIMO Lissotschenko Mikrooptik) is used to heat the sample. The laser beam is guided through a fiber optic cable into the beam shaping module. The beam has a quadratic shape (5.0 x 5.0 mm^2 at sample position) when leaving the module. It illuminates a steel plate at the backside of the sample pellet, thus heating the sample (cf. figure 4.30). A PID feedback loop between a K-type thermocouple in front of the sample pellet and the laser source controls the sample temperature. The optical section is separated from the reaction section by a quartz window with anti-reflection coating optimized for 808 nm transmission.

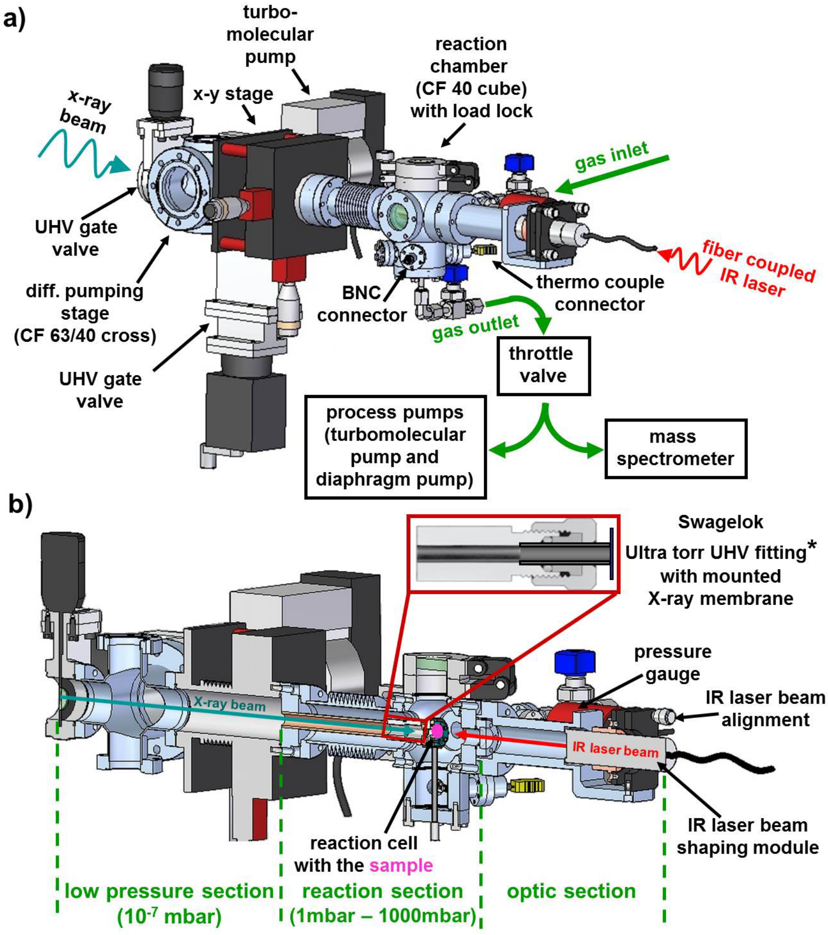

Figure 4.29: *Drawings of the high-pressure NEXAFS setup comprising the low pressure, reaction and optic section installed at the BESSY II ISISS beamline.*

Reaction cell

A schematic of the front and the cross section of the reaction cell, the sample carrier and the sample stage are shown in figure 4.30. The sample pellet mounted on a steel plate is gripped in a groove of a ceramic (MACOR) mold body and fixed with a nut from the rear. The distance between the Faraday cup like lid of the sample container and the sample surface is 900 μm creating a reaction volume of roughly 20 μl. A K-type thermocouple is fixed at the interface between the sample pellet and the ceramic mold body by a nut (figure 4.30a). The Faraday cup is fixed with two plates in front of the sample pellet on the ceramic mold body, which is itself mounted on a sapphire sample carrier by four screws. Spring loaded bolts mounted in a MACOR body of the sample stage realise the electric contact to the screws mounted at the sapphire sample carrier and allow connection to vacuum feedthroughs via wires. Two of the screws are connecting the thermocouple to the PID thermocontroller. The third screw is electrically connected with the Faraday cup via a metal plate to apply a potential. The fourth screw is electrically insulated from the Faraday cup like lid via a ceramic (MACOR) to avoid any leak current (figure 4.30b). The gas outlet at the sample stage is sealed to the reaction cell body via an O-ring. Thus, the complete reaction cell unit can easily be removed with the sapphire sample carrier from the sample stage for sample exchange without disassembling any connections. The sapphire sample carrrier and the IR laser heating are well proven concepts applied since a long time in the NAP-XPS setups of FHI [86, 202, 160].

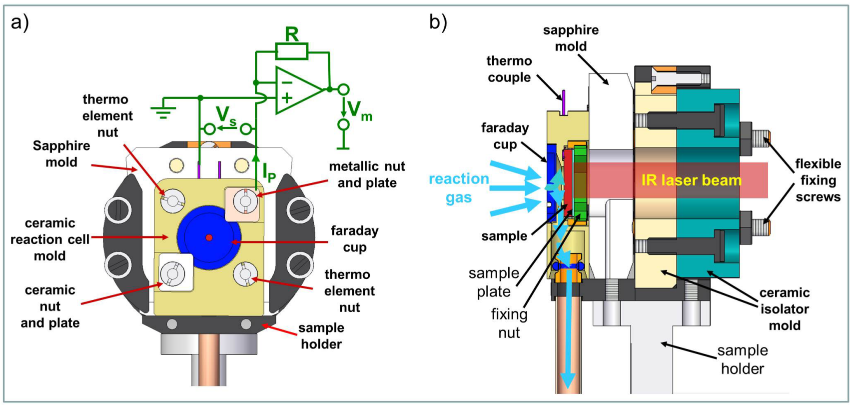

Figure 4.30: *Schematic of the front (a) and the cross section (b) of the reaction cell.*

Measurement principle (photocurrent measurement)

The impinging X-ray photon beam generates an electron hole pair in the solid. In the case of the vanadium $L_{2,3}$-edges transitions between occupied V 2p and unoccupied V 3d states take place. In the non-radiating decay process of the electron hole pair recombination, Auger-Meitner (AM) electrons are generated and mainly contribute to the total electron yield (TEY). Thus, the TEY mode is surface sensitive because the inelastic mean free path length of AM electrons is approximately 1 nm[185]. In addition to the absorption in the solid also X-ray absorption in the gas phase occurs resulting in two methodological challenges. On the one hand the photon number reaching the sample position decreases strongly with increasing X-ray path length in the gas. This is exemplified in figure S3 where the X-ray transmission in the photon energy range between 100 and 1000 eV is compared for a 10 mm path in air and 3 mm path in a butane/oxygen/helium reaction mixture. It becomes obvious that path lengths in the mm range are required for sufficient signal strength in the soft X-ray regime. The transmission of the X-ray membrane (150 nm Si_3N_4) used to seal the reaction part from the vacuum part of the beamline is shown for comparison. On the other hand the absorbed X-rays in the gas phase ionize the gas molecules and create electron-ion pairs. Electrons created by this process are detected as well. Thus, the K-edge of gas phase oxygen in addtion to the oxygen K-edge of VPP is visible in the spectra. For the detection of photoelectrons, a voltage V_S is applied between

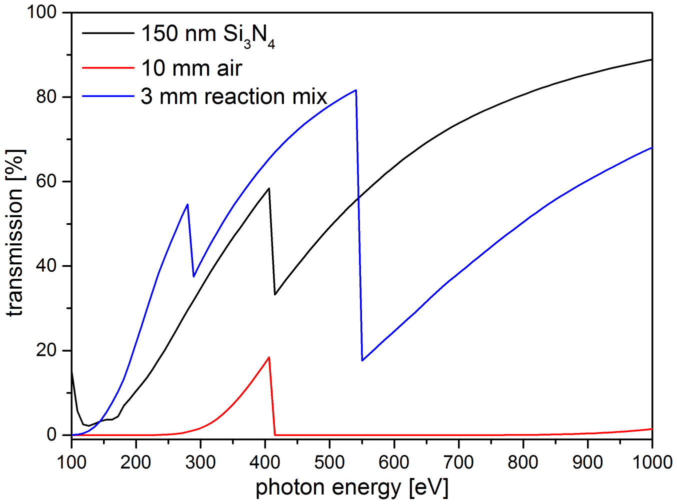

Figure 4.31: *X-ray transmission in a 10 mm path in air and 3 mm path in a n-butane/ oxygen/helium reaction mixture (always at 1000 mbar), and, for comparison, transmission of the X-ray membrane (150 nm Si_3N_4) used to seal the reaction from the vacuum section of the beamline.*

the sample (grounded by the thermocouple) and the Faraday cup (+108 V) (figure 4.30a). The by the absorption process generated primary Auger electrons and secondary electrons are moderately accelerated to the Faraday cup by the electric field and a photocurrent I_P is measured via a transimpedance amplifier (by measuring the voltage V_A = - R (resistance) I_P). On their way to the Faraday cup the high kinetic Auger electrons ionize gas molecules and a cascade of secondary electrons ("environmental secondaries") is generated until their energy is below the threshold for gas ionization, additionally enhancing the TEY. The described measurement principle is called conversion electron yield mode (CEY). Only fast electrons are able to ionize gas molecules. Thus, in contrast to the TEY mode where the spectrum is dominated by slow electrons, in the CEY mode the contribution of fast electrons to the spectrum might be enhanced.

NEXAFS experiments and data evaluation

In situ NEXAFS experiments were performed at the synchrotron radiation facility BESSY II in Berlin. The described instrument was connected to the ISISS (innovative station for in situ spectroscopy) beamline. The sample was probed with monochromatic light from 505 to 529 eV to investigate the vanadium L_2-, L_3- and oxygen K-edge. For the in situ NEXAFS experiments 10 mg of the VPP powder were pressed into a self-supporting pellet (1 ton pressing pressure, diameter of pellet: 8 mm). The sample pellet was heated to 400°C with a heating rate of 10 K/min in 1.5 % n-butane, 20 % oxygen and helium as balance at 3 mbar. Reference spectra were first taken at 3 mbar to test the CEY measurement and the stability of the X-ray membrane, which is not only strained by the pressure difference between the low pressure and reaction section, but also by the X-ray illumination and local heat transfer from the sample surface via the Faraday cup onto the membrane, in particular at higher pressures where heat conductivity via the gas becomes relevant. Afterwards the measurements at 10 mbar, 100 mbar and 1000 mbar were performed. The measurement protocol is shown in table figure 4.3. It is well known that the $1\sigma_u \rightarrow \pi^*$ transition of molecular oxygen at 531 eV can enormously affect the background of the vanadium $L_{2,3}$-edge spectra. In particular, the L_2-edge at 524 eV interferes heavily with the π^* resonance and the Coster-Kronig decay channel[40]. Therefore, only the L_3-edges at 517.5 eV were evaluated. In order to correct the L_3-edge spectrum of VPP for the π^* resonance of molecular oxygen, a gold foil, which does not form an oxide layer under the applied conditions, was mounted on the sample holder to measure the K-edge of molecular oxygen at room temperature as reference spectrum. The oxidizing conditions (20% oxygen in He) were applied and spectra were taken from 505 to 560 eV between 3 and 1000 mbar. These reference measurements were used for background correction. In the case of the experiments at 10 and 100 mbar it turned out that a simple linear background subtraction at the vanadium L_3-edge is suitable. Spectra at 1000 mbar in the presence of oxygen were corrected by the subtraction of the appropriate oxygen reference spectrum. All spectra are the sum over 5 raw data sets. The photon energy scale is adjusted to the π^* resonance of gas phase oxygen at around 531 eV.

index	T [°C]	p [mbar]	gas composition [%]			period [h]
			n-butane	oxygen	helium	
1	400	10	1.5	20	78	1
2	400	100	1.5	20	78	1
3	400	1000	1.5	20	78	2
4	400	10	1.5	20	78	0.5
5	400	10	0	20	80	1
6	400	100	0	20	80	1
7	400	1000	0	20	80	1
8	400	10	1.5	0	98	1
9	400	100	1.5	0	98	1
10	400	1000	1.5	0	98	1

Table 4.3: *Measurement protocol for the in situ NEXAFS measurement of VPP.*

Microwave conductivity measurements

The microwave cavity perturbation setup used to measure the conductivity and the measurement protocol were described in detail previously[53]. In short, as resonator a cylindrical X-band TM_{110} silver-plated brass cavity (ZWG Berlin-Adlershof) with a height of 19.5 mm and a diameter of 38.5 mm was used. A quartz tube reactor with 4 mm outer and 3 mm inner diameter containing the sample under investigation (powders were filled in with a bed height of 10 mm and embedded within quartz wool) and surrounded by a 10 mm outer diameter double-walled quartz dewar mantle was directly placed in the center of the cavity. As for the 1000 mbar measurement, the quartz tube flow through reactor was connected upstream to a gas delivery manifold equipped with mass flow controllers (Bronkhorst El-Flow) to supply the different gas mixtures. For the 10 mbar dynamic vacuum measurement a quartz cell equipped with Teflon Duran valves was used which was connected to a vacuum system that allows the dosing of gases and the adjustment of the total pressure in the reactor cell. Heating of the reactor was performed by preheating a stream of 8 l/min N_2 in a resistive furnace consisting of a Sylvania tungsten series I heater. The cavity was connected to a vector network analyzer (Agilent PNA-L N5230C-225) in order to record resonance spectra of S11-parameters in reflection mode (reflected power versus frequency) and to determine the resonance frequency and quality factor of the cavity with and without sample. The microwave power attenuation was set to 11 dBm. From the change of the quality factor with and without sample Q_2 and Q_1, respectively, the imaginary part of the permittivity ε_2 (after applying the Landau-Lifshitz-Looyenga effective medium theory to calculate the permittivity of the solid from the powder permittivity) and finally the conductivity σ were calculated after

$$B\varepsilon_2 \frac{V_s}{V_c} = \left(\frac{1}{Q_2} - \frac{1}{Q_1} \right) \tag{4.58}$$

$$\sigma = \varepsilon_0 \omega_2 \varepsilon_2 \tag{4.59}$$

with B being the calibration factor of the cavity determined with reference samples, V_c the volume of the cavity, V_s the volume of the sample, ε_0 the vacuum permittivity and ω_2 the resonance frequency of the cavity with sample.

5 Final Conclusions

In the present work, the charge carrier dynamics and the surface electronic structure of vanadium oxide catalysts in the selective oxidation of small alkanes were investigated. The major part focuses on the catalyst MoVNbTeOx (M1 phase) under propane oxidation conditions.

A dynamic charge carrier response was found in propane oxidation by varying the propane to oxygen ratio in the reaction feed. With increasing propane concentration the conductivity of MoVNbTeO$_x$ M1-phase also increased identifying MoVNbTeO$_x$ M1-phase as an n-type semiconductor (see section 4.2). Also when the alkane was exchanged in the reaction feed from ethane to propane and finally to n-butane the conductivity increased. The number of electrons transferred from the alkane to MoVNbTeO$_x$ M1-phase increases from ethane to n-butane oxidation. Thus in ethane oxidation MoVNbTeO$_x$ M1-phase is more oxidized than in n-butane oxidation. In the case of weakly conductive oxides like MoVNbTeO$_x$ M1-phase the electric field of the microwave radiation pervades the complete sample (depolarization regime) [32]. Therefore the bulk conductivity is monitored.

In selective oxidation catalysis the site isolation concept is discussed [167]. The catalytic reaction should occur at an isolated active site (ensemble of atoms) which interacts and exchanges electrons with reactants without participation of charge carriers from the bulk. Thus the results from the microwave studies are apparently in contradiction to the site isolation concept because the reactant (ethane, propane or n-butane) exchanges electrons with the bulk of the catalyst.

However, the X-ray photoelectron spectroscopy study reveals that the surface induced bend bending is modulated by the chemical reaction occurring at the surface via a modification of the V^{4+}/V^{5+} redox couple (see section 4.2). The reactants (alkane and oxygen) modify the abundance of the redox active V^{4+} and V^{5+} species on the surface. Vanadium is discussed to be an essential part of the active site [167]. One can assume that the alkane is adsorbed at a vanadium containing active site, corresponding to a surface state in the semiconductor model (compare section 2.6), and transfers electrons to the active site during the catalytic reaction. Consequently the surface charge is modified due to a reaction occurring at a molecular species (single site) at the surface. The surface charge is in equilibrium with the charge in the space charge layer (in the subsurface/bulk region) which affects the band bending and hence the surface barrier height (compare section 2.6). Thus also the charge carrier density in the space charge layer, being a part of the bulk charge carrier density monitored by the microwave conductivity experiment, underneath the MoVNbTeO$_x$ M1-phase surface is modified by the catalytic reaction occurring at a molecular active site.

In water containing propane feed the conductivity of MoVNbTeO$_x$ M1-phase is decreased compared to dry propane feed conditions (compare section 4.3). From the corresponding X-ray photoelectron spectroscopy experiment, no modification of the band bending could be determined. Thus the concept discussed above cannot explain the decreased conductivity. However, in addition to the charge carrier density also its mobility affects the conductivity of solids (compare section 2.5). The addition of water to the propane feed is accompanied by a drastic surface modification which also affects the valence band structure. The charge carrier effective mass depends on the bending of the energy bands (dispersion relation) and influences the charge carrier mobility. Chemically speaking, the chemical modification induced by water changes the bond strength of the charge carrier. Thus a changed valence band structure can also modify the conductivity of the solid. This hypothesis can be investigated with microwave Hall measurements in the future. According to the increased selectivity to acrylic acid in water containing propane feed, a changed charge carrier effective mass could influence the dynamics of the catalytic reaction at the surface and therefore influence the selectivity of the catalyst.

Furthermore, the results from resonant X-ray photoelectron spectroscopy investigations indicate that MoVNbTeO$_x$ M1-phase is a covalently bonded oxide which supports the application of a rigorous band model. Additionally solids with covalent bonding character tend to reconstruct at their surfaces (see section 2.6). This fact supports the idea that the catalytically active surface is not part of the bulk geometric structure. However, the bulk geometric structure is needed to achieve a particular surface reconstruction. Thus the MoVNbTeO$_x$ M1-phase study reveals that the bulk and the surface of MoVNbTeO$_x$ M1-phase are coupled in an electronic and geometric sense modulated by the chemical potential of the gas phase. The investigation could therefore show that this selective oxidation catalyst responds like a semiconducting gas sensor (chemiresistor) on the gas phase proving early semiconductor concepts suggested decades ago (see section 1.1). It proves furthermore that the bulk phase plays an essential role and cannot be described as "innocent" support. This explains why a vanadium [77] or molybdenum oxide monolayer [6] on inert supports does not show the same catalytic properties. In particular the high acrylic acid selectivity with the large number of transferred charge carriers necessitates a semiconducting bulk phase allowing a facile charge transport. However, the formation of the surface barrier might prevent a too facile transfer of electrons to the surface, probably preventing an overoxidation of acrylic acid to carbon oxides. This concept has to be proven by the investigation of other selective and unselective catalysts in the future.

However, results from low pressure X-ray photoelectron or X-ray absorption measurements are performed at different chemical potential than under real catalytic conditions which can affect the state of operation of transition metal oxide catalysts. In particular, the oxygen pressure has an influence on the oxide surface which is theoretically predicted [159] and was exemplarily revealed in the variable pressure near edge X-ray absorption fine structure spectroscopy study of vanadyl pyrophosphate in the selective oxidation of n-butane. The surface is drastically more oxidized at 1000 mbar than at 100 or 10 mbar which is accompanied with an increased n-butane conversion and selectivity to maleic anhydride (see section 4.4). Already under low pressure conditions the surface of vanadyl pyrophosphate is more oxidized than the bulk under reaction condition [52]. However, its surface state of oxidation is controlled by the oxygen pressure. At ambient pressure the interplay of surface reduction by n-butane and re-oxidation by molecular oxygen, thus the catalytic reaction, triggers the surface state of oxidation. The highly oxidized surface corresponds to a concentrated abundance of V^{5+} species which is a defect in terms of the bulk geometric structure. These results also support a restructuring of the vanadyl pyrophosphate surface under reaction conditions.

Bibliography

[1] http://mcgroup.co.uk/news/20131213/global-maleic-anhydride-consumption-registered-35-yoy-increase.html (28.08.2014).

[2] M. Abon, K. E. Bere, and P. Delichere. Nature of active oxygen in the n-butane selective oxidation over well-defined V-P-O catalysts: An oxygen isotopic labelling study. *Catal. Today*, 33:15–23, 1997.

[3] P. A. Agaskar, L. DeCaul, and R. K. Grasselli. A Molecular-Level Mechanism of n-Butane Oxidation to Maleic-Anhydride over Vanadyl Pyrophosphate. *Catal. Lett.*, 23(3-4):339–351, 1994.

[4] M. Alonso, R. Cimino, and K. Horn. Surface photovoltage effects in photoemission from metal-GaP(110) interfaces: Importance for band bending evaluation. *Phys. Rev. Lett.*, 64:1947–1950, 1990.

[5] W. Altar. Q Circles-A Means of Analysis of Resonant Microwave Systems. *Proc. IRE*, 35:355–361, 1947.

[6] K. Amakawa, L. Sun, C. Guo, M. Hävecker, P. Kube, I. E. Wachs, S. Lwin, A. I. Frenkel, A. Patlolla, K. Hermann, R. Schlögl, and A. Trunschke. How Strain Affects the Reactivity of Surface Metal Oxide Catalysts. *Angewandte Chemie International Edition*, 52(51):13553–13557, 2013.

[7] M. Baca and J. M. M. Millet. Bulk Oxidation State of the Different Cationic Elements in the MoVTe(Sb)NbO Catalysts for Oxidation or Ammoxidation of Propane. *Appl. Catal. A*, 288(1-2):243–243, 2005.

[8] N. Ballarini, F. Cavani, C. Cortelli, S. Ligi, F. Pierelli, F. Trifiro, C. Fumagalli, G. Mazzoni, and T. Monti. VPO catalyst for n-butane oxidation to maleic anhydride: A goal achieved, or a still open challenge? *Top. Catal.*, 38:147–156, 2006.

[9] P. Bassler, W. Harder, P. Resch, N. Rieber, W. Ruppel, J. Teles, A. Walch, A. Wenzel, and P. Zehner. US Patent 6,479,680, 2002.

[10] W. Bauhofer. Determination Of Semiconductor Energy Gaps Using The Microwave Cavity Perturbation Method. *J. Phys. E: Sci. Instrum.*, 14:934–938, 1981.

[11] C. N. Berglund and W. E. Spicer. Photoemission Studies of Copper and Silver: Experiment. *Phys. Rev.*, 136:A1044–A1064, 1964.

[12] U. Berner, K. Schierbaum, G. Jones, P. Wincott, S. Haq, and G. Thornton. Ultrathin ordered CeO2 overlayers on Pt(111): interaction with NO2, NO, {H2O} and {CO}. *Surface Science*, 467:201 – 213, 2000.

[13] M. Bettahar, G. Costentin, L. Savary, and J. Lavalley. On the partial oxidation of propane and propylene on mixed metal oxide catalysts. *Applied Catalysis A: General*, 145:1 – 48, 1996.

[14] H. Bluhm, M. Hävecker, E. Kleimenov, A. Knop-Gericke, A. Liskowski, R. Schlögl, and D. S. Su. In Situ Surface Analysis in Selective Oxidation Catalysis: n-Butane Conversion over VPP. *Top. Catal.*, 23:99–107, 2003.

[15] H. Bluhm, M. Hävecker, A. Knop-Gericke, M. Kiskinova, R. Schlögl, and M. Salmeron. In Situ X-Ray Photoelectron Spectroscopy Studies of Gas-Solid Interfaces at Near-Ambient Conditions. *MRS Bulletin*, 32(12):1022–1030, 2007.

[16] E. Bordes. Nature of the Active and Selective Sites In Vanadyl Pyrophosphate, Catalyst of Oxidation of n-Butane, Butene and Pentane to Maleic-Anhydride. *Catal. Today*, 16(1):27–38, 1993.

[17] P. Botella, A. Dejoz, M. C. Abello, M. I. Vazquez, L. Arrua, and J. M. L. Nieto. Selective Oxidation of Ethane: Developing an Orthorhombic Phase in Mo-V-X (X = Nb, Sb, Te) Mixed Oxides. *Catal. Today*, 142(3-4):272–277, 2009.

[18] M. Boudart. Electronic Chemical Potential in Chemisorption and Catalysis. *J. Am. Chem. Soc.*, 74:1531–1535, 1952.

[19] A. Brückner. Spin-Spin Exchange in Vanadium-Containing Catalysts Studied by In Situ-EPR: A Sensitive Monitor for Disorder-Related Activity. *Top. Catal.*, 38(1-3):133–139, 2006.

[20] M. Caldararu, M. Scurtu, C. Hornoiu, C. Munteanu, T. Blasco, and J. M. López Nieto. Electrical Conductivity of a MoVTeNbO Catalyst in Propene Oxidation Measured in Operando Conditions. *Catal. Today*, 155:311–318, 2010.

[21] M. Cavalleri, K. Hermann, S. Guimond, Y. Romanyshyn, H. Kuhlenbeck, and H.-J. Freund. X-ray spectroscopic fingerprints of reactive oxygen sites at the MoO_3 (010) surface. *Catal. Today*, 124:21 – 27, 2007.

[22] F. Cavani. Catalytic Selective Oxidation: The forefront in the Challenge for a More Sustainable Chemical Industry. *Catal. Today*, 157(1-4):8–15, 2010.

[23] F. Cavani, N. Ballarini, and A. Cericola. Oxidative dehydrogenation of ethane and propane: How far from commercial implementation? *Catal. Today*, 127(1-4):113–131, 2007.

[24] F. Cavani and A. Gaffney. *Synthesis of Propene Oxide: A Successful Example of Sustainable Industrial Chemistry*. 2009.

[25] F. Cavani and J. Teles. Sustainability in catalytic oxidation: An alternative approach or a structural evolution? *ChemSusChem*, 2(6):508–534, 2009.

[26] A. Celaya Sanfiz, T. W. Hansen, D. Teschner, P. Schnörch, F. Girgsdies, A. Trunschke, R. Schlögl, M. Hong Looi, and S. B. Abd Hamid. Dynamics of the MoVTeNb Oxide M1 Phase in Propane Oxidation. *J. Phys. Chem. C*, 114:1912–1921, 2010.

[27] G. Centi. Vanadyl pyrophosphate - A critical overview. *Catal. Today*, 16:5–26, 1993.

[28] G. Centi, F. Trifiro, J. R. Ebner, and V. M. Franchetti. Mechanistic Aspects of Maleic Anhydride Synthesis from C4 Hydrocarbons over Phosphorus Vanadium Oxide. *Chem. Rev.*, 88(1):55–80, 1988.

[29] B. Chen and E. J. Munson. Investigation of the Mechanism of n-Butane Oxidation on Vanadium Phosphorus Oxide Catalysts: Evidence from Isotopic Labeling Studies. *J. Am. Chem. Soc.*, 124:1638–1652, 2002.

[30] J. Chen. NEXAFS Investigations of Transition Metal Oxides, Nitrides, Carbides, Sulfides and other Interstitial Compounds. *Surf. Sci. Rep.*, 30:1 – 152, 1997.

[31] J. Chen, C. Kirn, B. Frühberger, B. DeVries, and M. Touvelle. A NEXAFS Determination of the Oxidation State of Vanadium Carbide on V(110): Observation of Charge Transfer from Vanadium to Carbon. *Surf. Sci.*, 321:145 – 155, 1994.

[32] L.-F. Chen, C. K. Ong, C. P. Neo, V. V. Varadan, and V. K. Varadan. *Microwave Electronics: Measurement and Materials Characterization*. Wiley, 2004.

[33] M. J. Cheng and W. A. Goddard. The Critical Role of Phosphate in Vanadium Phosphate Oxide for the Catalytic Activation and Functionalization of n-Butane to Maleic Anhydride. *J. Am. Chem. Soc.*, 135(12):4600–4603, 2013.

[34] H. Clark and D. Berets. 21 Vanadium Oxides as Oxidation Catalysts: Electrical Properties. In A. Farkas, editor, *Proceedings of the International Congress on Catalysis*, volume 9 of *Advances in Catalysis*, pages 204 – 214. Academic Press, 1957.

[35] P. Clauws and J. Vennik. Optical Absorption of Defects in V205 Single Crystals: As-Grown and Reduced V2O5. *Phys. Status Solidi B*, 66:553–560, 1974.

[36] C. Cohen-Tannoudji, B. Diu, and F. Laloe. *Quantum Mechanics*, chapter Approximation methods for time-depending problems. Quantum Mechanics. Wiley, 1992.

[37] P. Concepcion, S. Hernandez, and J. M. L. Nieto. On the Nature of Active Sites in MoVTeO and MoVTeNbO Catalysts: The Influence of Catalyst Activation Temperature. *Appl. Catal. A*, 391(1-2):92–101, 2011.

[38] M. Conte, G. Budroni, J. K. Bartley, S. H. Taylor, A. F. Carley, A. Schmidt, D. M. Murphy, F. Girgsdies, T. Ressler, R. Schlögl, and G. J. Hutchings. Chemically induced fast solid-state transitions of omega-VOPO4 in vanadium phosphate catalysts. *Science*, 313:1270–1273, 2006.

[39] I. Corvin and L. Cartz. Anisotropic Thermal Expansion of V2O5. *J. Am. Ceram. Soc.*, 48:328–329, 1965.

[40] D. Coster and R. D. L. Kronig. New Type of Auger Effect and its Influence on the X-Ray Spectrum. *Physica*, 2:13 – 24, 1935.

[41] S. Davison and M. Steslicka. *Basic theory of surface states*. Monographs on the physics and chemistry of materials. Clarendon Press, 1992.

[42] de Groot; Frank and A. Kotan. *Core Level Spectroscopy of Solids*. CRC Press, 2008.

[43] E. de Smit, I. Swart, J. F. Creemer, G. H. Hoveling, M. K. Gilles, T. Tyliszczak, P. J. Kooyman, H. W. Zandbergen, C. Morin, B. M. Weckhuysen, and F. M. F. de Groot. Nanoscale Chemical Imaging of a Working Catalyst by Scanning Transmission X-Ray Microscopy. *Nature*, 456:222–225, 2008.

[44] W. N. Delgass, G. L. Haller, R. Kellerman, and J. H. Lunsford. *Spectroscopy in Heterogeneous Catalysis*. Academic Press, New York, 1979.

[45] J. DeSanto, P., D. Buttrey, R. Grasselli, W. Pyrz, C. Lugmair, J. Volpe, A.F., T. Vogt, and B. Toby. Comparison of MoVTaTeO and MoVNbTeO M1 crystal chemistry. *Top. Catal.*, 38(1-3):31–40, 2006.

[46] P. DeSanto, J. B. Douglas, K. G. Robert, G. L. Claus, F. V. Anthony, H. T. Brian, and T. Vogt. Structural aspects of the M1 and M2 phases in MoVNbTeO propane ammoxidation catalysts. *Zeitschrift für Kristallographie/International journal for structural, physical, and chemical aspects of crystalline materials*, 219:152, 2009.

[47] P. Drude. Zur Elektronentheorie der Metalle. *Annalen der Physik*, 306(3):566–613, 1900.

[48] P. Drude. Zur Elektronentheorie der Metalle; II. Teil. Galvanomagnetische und thermomagnetische Effecte. *Annalen der Physik*, 308(11):369–402, 1900.

[49] D. C. Dube. Study of Landau-Lifshitz-Looyenga‘s Formula for Dielectric Correlation between Powder and Bulk. *J. Phys. D: Appl. Phys.*, 3:1648–1652, 1970.

[50] J. R. Ebner and M. R. Thompson. *Studies in Surface Science and Catalysis*, volume 68, pages 31–42. Elsevier, Amsterdam, 1991.

[51] M. Eichelbaum, R. Glaum, M. Hävecker, K. Wittich, C. Heine, H. Schwarz, C.-K. Dobner, C. Welker-Nieuwoudt, A. Trunschke, and R. Schlögl. Towards physical descriptors of active and selective catalysts for the oxidation of n-butane to maleic anhydride. *ChemCatChem*, 5:DOI: 10.1002/cctc.201200953, 2013.

[52] M. Eichelbaum, M. Hävecker, C. Heine, A. Karpov, C. K. Dobner, F. Rosowski, A. Trunschke, and R. Schlögl. The Intimate Relationship between Bulk Electronic Conductivity and Selectivity in the Catalytic Oxidation of n-Butane. *Angew. Chem. Int. Ed.*, 51:6246–6250, 2012.

[53] M. Eichelbaum, R. Stößer, A. Karpov, C.-K. Dobner, F. Rosowski, A. Trunschke, and R. Schlögl. The Microwave Cavity Perturbation Technique for Contact-free and In-Situ Electrical Conductivity Measurements in Catalysis and Materials Science. *Phys. Chem. Chem. Phys.*, 14:1302–1312, 2012.

[54] R. Enjalbert and J. Galy. A refinement of the structure of V_2O_5. *Acta Cryst. C*, 42(11):1467–1469, 1986.

[55] A. Erbil, G. S. Cargill III, R. Frahm, and R. F. Boehme. Total-Electron-Yield Current Measurements for Near-Surface Extended X-Ray-Absorption Fine Structure. *Phys. Rev. B*, 37:2450–2464, 1988.

[56] C. Escudero, P. Jiang, E. Pach, F. Borondics, M. W. West, A. Tuxen, M. Chintapalli, S. Carenco, J. Guo, and M. Salmeron. A Reaction Cell with Sample Laser Heating for In Situ Soft X-Ray Absorption Spectroscopy Studies under Environmental Conditions. *J. Synchrotron Rad.*, 20(3):504–508, 2013.

[57] V. Eyert and K.-H. Höck. Electronic structure of V2O5: Role of octahedral deformations. *Phys. Rev. B*, 57:12727–12737, 1998.

[58] R. P. Feynman, R. B. Leighton, and M. Sands. *The Feynman Lecture on Physics Volume II*, chapter Cavity Resonators. ADDISON-WESLEY PUBLISHING COMPANY INC., 1966.

[59] R. P. Feynman, R. B. Leighton, and M. Sands. *The Feynman Lecture on Physics Volume II*, chapter The Maxwell- Equations. ADDISON-WESLEY PUBLISHING COMPANY INC., 1966.

[60] R. P. Feynman, R. B. Leighton, and M. Sands. *The Feynman Lecture on Physics Volume II*, chapter Dielectrics. ADDISON-WESLEY PUBLISHING COMPANY INC., 1966.

[61] R. P. Feynman, R. B. Leighton, and M. Sands. *The Feynman Lecture on Physics Volume II*, chapter Solutions of Maxwell's Equations in Free Space. ADDISON-WESLEY PUBLISHING COMPANY INC., 1966.

[62] R. P. Feynman, R. B. Leighton, and M. Sands. *The Feynman Lecture on Physics Volume II*, chapter Solutions of Maxwell's Equations with Currents and Charges. ADDISON-WESLEY PUBLISHING COMPANY INC., 1966.

[63] R. P. Feynman, R. B. Leighton, and M. Sands. *The Feynman Lecture on Physics Volume II*, chapter Waveguides. ADDISON-WESLEY PUBLISHING COMPANY INC., 1966.

[64] R. P. Feynman, R. B. Leighton, and M. Sands. *The Feynman Lecture on Physics Volume III*, chapter The Ammonia Maser. ADDISON-WESLEY PUBLISHING COMPANY INC., 1966.

[65] R. P. Feynman, R. B. Leighton, and M. Sands. *The Feynman Lecture on Physics Volume III*, chapter Propagation in a Crystal Lattice. ADDISON-WESLEY PUBLISHING COMPANY INC., 1966.

[66] L. Fiermans, P. Clauws, W. Lambrecht, L. Vandenbroucke, and J. Vennik. Single crystal V2O5 and lower oxides. A survey of their electronic, optical, structural, and surface properties. *Phys. Status Solidi A*, 59:485–504, 1980.

[67] G. Fischerauer, M. Spörl, A. Gollwitzer, M. Wedemann, and R. Moos. Catalyst State Observation via the Perturbation of a Microwave Cavity Resonator. *Frequenz*, 62:180–184, 2008.

[68] M. V. Ganduglia-Pirovano, A. Hofmann, and J. Sauer. Oxygen Vacancies in Transition Metal and Rare Earth Oxides: Current State of Understanding and Remaining Challenges. *Surf. Sci. Rep.*, 62(6):219–270, 2007.

[69] S. Geupel, K. Pilz, S. v. Smaalen, F. Bullesfeld, A. Prokofiev, and W. Assmus. Synchrotron-radiation study of the two-leg spin-ladder (VO)2P2O7 at 120 K. *Acta Cryst. C*, 58(1):i9–i13, 2002.

[70] E. Ginzton. Microwave Q Measurements in the Presence of Coupling Losses. *IRE Trans. Microw. Theory Tech.*, 6:383–389, 1958.

[71] K. W. Goodman and V. E. Henrich. Assignment of a photoemission feature in the O-2s–O-2p band gaps of TiO2 and V2O5. *Phys. Rev. B*, 50:10450–10456, 1994.

[72] T. A. Goodwin and P. Mark. The influence of chemisorption on the electrical conductivity of thin semiconductors. *Prog. Surf. Sci.*, 1:1 – 64, 1971.

[73] C. Q. Granqvist, editor. *Handbook of Inorganic Electrochromic Materials*. Elsevier Science B.V., 2002.

[74] R. Grasselli, C. Lugmair, and J. Volpe, AnthonyF. Doping of MoVNbTeO (M1) and MoVTeO (M2) Phases for Selective Oxidation of Propane and Propylene to Acrylic Acid. *Topics in Catalysis*, 50(1-4):66–73, 2008.

[75] R. K. Grasselli. Fundamental Principles of Selective Heterogeneous Oxidation Catalysis. *Top. Catal.*, 21:79–88, 2002.

[76] M. T. Greiner, L. Chai, M. G. Helander, W. M. Tang, and Z. H. Lu. Transition Metal Oxide Work Functions: The Influence of Cation Oxidation State and Oxygen Vacancies. *Adv. Funct. Mater.*, 22(21):4557–4568, 2012.

[77] P. Gruene, T. Wolfram, K. Pelzer, R. Schlögl, and A. Trunschke. Role of dispersion of vanadia on SBA-15 in the oxidative dehydrogenation of propane. *Catalysis Today*, 157:137 – 142, 2010. 6th World Congress on Oxidation Catalysis Lille, France, 5-10 July 2009 Towards an integrated approach in innovation and development.

[78] V. Guliants and M. A. Carreon. Vanadium-Phosphorus-Oxides: From Fundamentals of n-Butane Oxidation to Synthesis of New Phases. *Catalysis*, 18:1–45, 2005.

[79] A. Gurlo. Interplay between O-2 and SnO2: Oxygen iInosorption and Spectroscopic Evidence for Adsorbed Oxygen. *ChemPhysChem*, 7(10):2041–2052, 2006.

[80] J. Haber. Fifty years of my romance with vanadium oxide catalysts. *Catal. Today*, 142:100–113, 2009.

[81] M. Hävecker, M. Cavalleri, R. Herbert, R. Follath, A. Knop-Gericke, C. Hess, K. Hermann, and R. Schlögl. Methodology for the structural characterisation of Vx Oy species supported on silica under reaction conditions by means of in situ O K-edge X-ray absorption spectroscopy. *Phys. Stat. Sol. b*, 246(7):1459–1469, 2009.

[82] M. Hävecker, A. Knop-Gericke, H. Bluhm, E. Kleimenov, R. Mayer, M. Fait, and R. Schlögl. Dynamic Surface Behaviour of VPO Catalysts under Reactive and Non-Reactive Gas Compositions: An In Situ XAS Study. *Appl. Surf. Sci.*, 230:272–282, 2004.

[83] M. Hävecker, A. Knop-Gericke, R. W. Mayer, M. Fait, H. Bluhm, and R. Schlögl. Influence of the Geometric Structure on the V L3 Near Edge X-Ray Absorption Fine Structure from Vanadium Phosphorus Oxide Catalysts. *J. Electron Spectrosc. Relat. Phenom.*, 125(2):79–87, 2002.

[84] M. Hävecker, A. Knop-Gericke, and T. Schedel-Niedrig. High-Pressure Soft X-Ray Absorption Spectroscopy: Application of a New In Situ Spectroscopic Method in Catalysis Research. *Appl. Surf. Sci.*, 142:438–442, 1999.

[85] M. Hävecker, R. W. Mayer, A. Knop-Gericke, H. Bluhm, E. Kleimenov, A. Liskowski, D. Su, R. Follath, F. G. Requejo, D. F. Ogletree, M. Salmeron, J. A. Lopez-Sanchez, J. K. Bartley, G. J. Hutchings, and R. Schlögl. In Situ Investigation of the Nature of the Active Surface of a Vanadyl Pyrophosphate Catalyst during n-Butane Oxidation to Maleic Anhydride. *J. Phys. Chem. B*, 107:4587–4596, 2003.

[86] M. Hävecker, N. Pinna, K. Weiß, H. Sack-Kongehl, R. E. Jentoft, D. Wang, M. Swoboda, U. Wild, M. Niederberger, J. Urban, D. S. Su, and R. Schlögl. Synthesis and Functional Verification of the Unsupported Active Phase of VxOy Catalysts for Partial Oxidation of n-Butane. *J. Catal.*, 236:221–232, 2005.

[87] M. Hävecker, S. Wrabetz, J. Kröhnert, L. I. Csepei, R. N. d'Alnoncourt, Y. V. Kolen'ko, F. Girgsdies, R. Schlögl, and A. Trunschke. Surface Chemistry of Phase-Pure M1 MoVTeNb Oxide During Operation in Selective Oxidation of Propane to Acrylic Acid. *J. Catal.*, 285:48–60, 2012.

[88] W. M. Haynes, editor. *CRC Handbook of Chemistry and Physics*. CRC Press, 93 edition, 2012.

[89] M. Heber and W. Gränert. Application of Ultraviolet Photoelectron Spectroscopy in the Surface Characterization of Polycrystalline Oxide Catalysts. 2. Depth Variation of the Reduction Degree in the Surface Region of Partially Reduced V2O5. *J. Phys. Chem. B*, 104:5288–5297, 2000.

[90] C. Heine, M. Hävecker, F. Girgsdies, A. Trunschke, R. Schlögl, and M. Eichelbaum. The Model Oxidation Catalyst alpha-V2O5: Insights from Contactless In Situ Microwave Permittivity and Conductivity Measurements. *Appl. Phys. A*, 112:289–296, 2013.

[91] C. Heine, M. Hävecker, M. Sanchez-Sanchez, A. Trunschke, R. Schlögl, and M. Eichelbaum. Work Function, Band Bending and Microwave Conductivity Studies on the Selective Alkane Oxidation Catalyst MoVTeNb Oxide (Orthorhombic M1 Phase) under Operation Conditions. *J. Phys. Chem. C*, 117:26988–26997, 2013.

[92] V. E. Heinrich and P. A. Cox. *The Surface Science of Metal Oxides*. Univ. Pr., Cambridge, 1996.

[93] M. G. Helander, M. T. Greiner, Z. B. Wang, and Z. H. Lu. Pitfalls in Measuring Work Function Using Photoelectron Spectroscopy. *Appl. Surf. Sci.*, 256(8):2602–2605, 2010.

[94] J. M. Herrmann. The electronic factor and related redox processes in oxidation catalysis. *Catal. Today*, 112:73–77, 2006.

[95] J. M. Herrmann, F. R. Rouvet, and J. C. Volta. Electrical Properties of Pure Vanadium Phosphate Phases and of VPO Catalysts used in the Partial Oxidation of n-Butane to Maleic Anhydride. *J. Chem. Soc. Faraday Trans.*, 90:1441–1448, 1994.

[96] J. M. Herrmann, P. Vernoux, K. E. Bere, and M. Abon. In situ study of redox and of p-type semiconducting properties of vanadyl pyrophosphate and of V-P-O catalysts during the partial oxidation of n-butane to maleic anhydride. *J. Catal.*, 167:106–117, 1997.

[97] R. Hesse, P. Streubel, and R. Szargan. Improved accuracy of quantitative XPS analysis using predetermined spectrometer transmission functions with UNIFIT 2004. *Surf. Interface Anal.*, 37(7):589–607, 2005.

[98] B. K. Hodnett. Vanadium-Phosphorus Oxide Catalysts for the Selective Oxidation of C-4 Hydrocarbons to Maleic-Anhydride. *Catal. Rev.*, 27(3):373–424, 1985.

[99] S. Hüfner. *Photoelectron Spectroscopy: Principles and Applications*, chapter Photoemission of Valence Electrons from Metallic Solids in the One-Electron Approximation. Advanced Texts in Physics. Springer, 2003.

[100] S. Hüfner. *Photoelectron Spectroscopy: Principles and Applications*, chapter Charge-Excitation Final States: Satellites. Advanced Texts in Physics. Springer, 2003.

[101] S. Hüfner. *Photoelectron Spectroscopy: Principles and Applications*, chapter Introduction. Advanced Texts in Physics. Springer, 2003.

[102] S. Hüfner. *Photoelectron Spectroscopy: Principles and Applications*, chapter Continuous Satellites and Plasmon Satellites: XPS Photoemission in Nearly Free Electron Systems. Advanced Texts in Physics. Springer, 2003.

[103] G. J. Hutchings. Vanadium phosphate: a new look at the active components of catalysts for the oxidation of butane to maleic anhydride. *J. Mater. Chem.*, 14:3385–3395, 2004.

[104] G. J. Hutchings, A. Desmartin-Chomel, R. Olier, and J.-C. Volta. Role of the Product in the Transformation of a Catalyst to its Active State. *Nature*, 368:41–45, 1994.

[105] H. Ibach and H. Lüth. *Festkorperphysik Einfuhrung in die Grundlagen*, chapter Dielektrische Eigenschaften der Materie. Springer-Lehrbuch. Springer, 2009.

[106] H. Ibach and H. Lüth. *Festkorperphysik Einfuhrung in die Grundlagen*, chapter Elektronische Bänder in Festkörpern. Springer-Lehrbuch. Springer, 2009.

[107] H. Ibach and H. Lüth. *Festkorperphysik Einfuhrung in die Grundlagen*, chapter Bewegung von Ladungsträgern in Bändern und Transportphänomene. Springer-Lehrbuch. Springer, 2009.

[108] H. Ibach and H. Lüth. *Festkorperphysik Einfuhrung in die Grundlagen*, chapter Halbleiter. Springer-Lehrbuch. Springer, 2009.

[109] V. A. Ioffe and I. B. Patrina. Comparison of the Small-Polaron Theory with the Experimental Data of Current Transport in V2O5. *Phys. Status Solidi B*, 40:389–395, 1970.

[110] W. Jaegermann. *Modern Aspects of Electrochemistry*, volume 30, chapter 1: The Semiconductor/Electrolyte Interface: A Surface Science Approach. Plenum, 1996.

[111] D. Kajfez. Linear fractional curve fitting for measurement of high Q factors. *IEEE Trans. Microw. Theory Tech.*, 42:1149–1153, 1994.

[112] D. Kajfez. *Q factor*. Vector Fields, Oxford, MS, 1994.

[113] N. Kenny, C. Kannewurf, and D. Whitmore. Optical absorption coefficients of vanadium pentoxide single crystals. *J. Phys. Chem. Solids*, 27:1237 – 1246, 1966.

[114] E. Kleimenov, H. Bluhm, M. Hävecker, A. Knop-Gericke, A. Pestryakov, D. Teschner, J. A. Lopez-Sanchez, J. K. Bartley, G. J. Hutchings, and R. Schlögl. XPS Investigations of VPO Catalysts under Reaction Conditions. *Surf. Sci.*, 575:181–188, 2005.

[115] A. Knop-Gericke, E. Kleimenov, M. Hävecker, R. Blume, D. Teschner, S. Zafeiratos, R. Schlögl, V. I. Bukhtiyarov, V. V. Kaichev, I. P. Prosvirin, A. I. Nizovskii, H. Bluhm, A. Barinov, P. Dudin, and M. Kiskinova. *Advances in Catalysis*, volume 52, chapter 4 X-Ray Photoelectron Spectroscopy for Investigation of Heterogeneous Catalytic Processes, pages 213–272. Elsevier Academic Press Inc, 2009.

[116] Y. V. Kolen'ko, W. Zhang, R. Naumann d'Alnoncourt, F. Girgsdies, T. W. Hansen, T. Wolfram, R. Schlögl, and A. Trunschke. Synthesis of MoVTeNb Oxide Catalysts with Tunable Particle Dimensions. *ChemCatChem*, 3:1597–1606, 2011.

[117] T. Konya, T. Katou, T. Murayama, S. Ishikawa, M. Sadakane, D. Buttrey, and W. Ueda. An orthorhombic Mo3VOx catalyst most active for oxidative dehydrogenation of ethane among related complex metal oxides. *Catal. Sci. Technol.*, 3:380–387, 2013.

[118] M. E. Kordesch and R. W. Hoffman. Electron-Yield Extended X-Ray Absorption Fine Structure with the Use of a Gas-Flow Electron Detector. *Phys. Rev. B*, 29:491–492, 1984.

[119] A. Kotani and Y. Toyozawa. Optical Spectra of Core Electrons in Metals with an Incomplete Shell. I. Analytic Features. *Journal of the Physical Society of Japan*, 35(4):1073–1081, 1973.

[120] A. Kotani and Y. Toyozawa. Optical Spectra of Core Electrons in Metals with an Incomplete Shell. II. Numerical Calculations of Overall Line Shapes. *Journal of the Physical Society of Japan*, 35(4):1082–1088, 1973.

[121] A. Kotani and Y. Toyozawa. Photoelectron Spectra of Core Electrons in Metals with an Incomplete Shell. *Journal of the Physical Society of Japan*, 37(4):912–919, 1974.

[122] G. Koyano, T. Okuhara, and M. Misono. Structural Changes of Surface Layer of Vanadyl Pyrophosphate Catalysts by Oxidation-Reduction and their Relationships with Selective Oxidation of n-Butane. *J. Am. Chem. Soc.*, 120(4):767–774, 1998.

[123] M. Kroger, S. Hamwi, J. Meyer, T. Riedl, W. Kowalsky, and A. Kahn. Role of the Deep-Lying Electronic States of MoO_3 in the Enhancement of Hole-Injection in Organic Thin Films. *Appl. Phys. Lett.*, 95(12):123301, 2009.

[124] P. Kubelka and F. Munk. Reflection characteristics of paints. *Z. Tech. Phys.*, 12:593–601, 1931.

[125] R. L. Kurtz and V. E. Henrich. Surface electronic structure and chemisorption on corundum transition-metal oxides: V2O3. *Phys. Rev. B*, 28:6699–6706, 1983.

[126] R. L. Kurtz and V. E. Henrich. Surface electronic structure and chemisorption on corundum transition-metal oxides: α-Fe2O3. *Phys. Rev. B*, 36:3413–3421, 1987.

[127] L. D. Landau and E. M. Lifshitz. *Electrodynamics of continuous media*. Pergamon Press, 1960.

[128] N. D. Lang and W. Kohn. Theory of Metal Surfaces: Work Function. *Phys. Rev. B*, 3:1215–1223, 1971.

[129] K. Levenberg. A method for the solution of certain non-linear problems in least squares. *Q. Appl. Math.*, 2:164–168, 1944.

[130] W. Li and D. Y. Li. On the correlation between surface roughness and work function in copper. *J. Chem. Phys.*, 122(6):064708, 2005.

[131] H. G. Lintz and S. P. Muller. The Partial Oxidation of Propane on Mixed Metal Oxides-A Short Overview. *Appl. Catal. A*, 357(2):178–183, 2009.

[132] H. Looyenga. Dielectric constants of heterogeneous mixtures. *Physica*, 31:401 – 406, 1965.

[133] H. Lüth. *Surfaces and Interfaces of Solid Materials*, chapter Electronic Surface States. Springer, 1995.

[134] H. Lüth. *Surfaces and Interfaces of Solid Materials*, chapter Morphology and Structure of Surfaces and Interfaces. Springer, 1995.

[135] H. Lüth. *Surfaces and Interfaces of Solid Materials*, chapter Adsorption on Solid Surfaces. Springer, 1995.

[136] H. Lüth. *Surfaces and Interfaces of Solid Materials*. Springer, 1995.

[137] H. Lüth. *Solid surfaces, Interfaces and Thin Films*, chapter Space Charge Layer, pages 329 – 380. Springer Verlag, 2001.

[138] H. Lüth. *Solid surfaces, Interfaces and Thin Films*. Springer Verlag, 2001.

[139] H. Lüth. *Solid surfaces, Interfaces and Thin Films*, chapter Electronic structure of Surfaces, pages 265 – 328. Springer Verlag, 2001.

[140] D. Maganas, M. Roemelt, M. Havecker, A. Trunschke, A. Knop-Gericke, R. Schlogl, and F. Neese. First principles calculations of the structure and V L-edge X-ray absorption spectra of V2O5 using local pair natural orbital coupled cluster theory and spin-orbit coupled configuration interaction approaches. *Phys. Chem. Chem. Phys.*, 15:7260–7276, 2013.

[141] D. Maganas, M. Roemelt, T. Weyhermuller, R. Blume, M. Havecker, A. Knop-Gericke, S. DeBeer, R. Schlogl, and F. Neese. L-edge X-ray absorption study of mononuclear vanadium complexes and spectral predictions using a restricted open shell configuration interaction ansatz. *Phys. Chem. Chem. Phys.*, 16:264–276, 2014.

[142] L. Malter and G. R. Brewer. Microwave Q Measurements in the Presence of Series Losses. *J. Appl. Phys.*, 20:918 – 925, 1949.

[143] D. W. Marquardt. An Algorithm for Least-Squares Estimation of Nonlinear Parameters. *J. Soc. Ind. Appl. Math.*, 11:431–441, 1963.

[144] P. Mars and D. W. van Krevelen. Oxidations carried out by means of vanadium oxide catalysts. *Chem. Eng. Sci. Spec. Suppl.*, 3:41–57, 1954.

[145] J. Meyer, M. Kroger, S. Hamwi, F. Gnam, T. Riedl, W. Kowalsky, and A. Kahn. Charge Generation Layers Comprising Transition Metal-Oxide/Organic Interfaces: Electronic Structure and Charge Generation Mechanism. *Appl. Phys. Lett.*, 96(19):193302, 2010.

[146] J. Meyer, K. Zilberberg, T. Riedl, and A. Kahn. Electronic Structure of Vanadium Pentoxide: An Efficient Hole Injector for Organic Electronic Materials. *J. Appl. Phys.*, 110(3):033710, 2011.

[147] G. Moggridge, S. Schroeder, R. Lambert, and T. Rayment. Environmental Cells for In Situ X-Ray Diffraction and X-Ray Absorption Spectroscopic Studies of Heterogeneous Catalysts. *Nucl. Instrum. Methods Phys. Res. B*, 97:28–32, 1995.

[148] G. D. Moggridge, T. Rayment, R. M. Ormerod, M. A. Morris, and R. M. Lambert. Spectroscopic Observation of a Catalyst Surface in a Reactive Atmosphere at High Pressure. *Nature*, 358(6388):658–660, 1992.

[149] Y. Moro-oka, W. Ueda, and K.-H. Lee. The role of bulk oxide ion in the catalytic oxidation reaction over metal oxide catalyst. *J. Mol. Catal. A*, 199:139 – 148, 2003.

[150] S. R. Morrison. *The Chemical Physics of Surfaces*. Plenum Press, New York, 1977.

[151] N. Mårtensson, O. Karis, and A. Nilsson. Resonant processes in the soft X-ray regime. *J. Electron Spectrosc. Relat. Phenom.*, 100:379 – 393, 1999.

[152] H. Murayama, D. Vitry, W. Ueda, G. Fuchs, M. Anne, and J. Dubois. Structure characterization of orthorhombic phase in MoVTeNbO catalyst by powder X-ray diffraction and {XANES}. *Appl. Catal. A*, 318(0):137 – 142, 2007.

[153] R. Naumann d'Alnoncourt, L.-I. Csepei, M. Hävecker, F. Girgsdies, M. E. Schuster, R. Schlögl, and A. Trunschke. The reaction network in propane oxidation over phase-pure MoVTeNb {M1} oxide catalysts. *J. Catal.*, 311(0):369 – 385, 2014.

[154] G. L. Pearson and J. Bardeen. Electrical Properties of Pure Silicon and Silicon Alloys Containing Boron and Phosphorus. *Phys. Rev.*, 75:865–883, 1949.

[155] M. A. Pepera, J. L. Callahan, M. J. Desmond, E. C. Milberger, P. R. Blum, and N. J. Bremer. Fundamental study of the oxidation of butane over vanadyl pyrophosphate. *J. Am. Chem. Soc.*, 107:4883–4892, 1985.

[156] P. J. Petersan and S. M. Anlage. Measurement of resonant frequency and quality factor of microwave resonators: Comparison of methods. *J. Appl. Phys.*, 84:3392–3402, 1998.

[157] W. D. Pyrz, D. A. Blom, N. R. Shiju, V. V. Guliants, T. Vogt, and D. J. Buttrey. The effect of Nb or Ta substitution into the {M1} phase of the MoV(Nb,Ta)TeO selective oxidation catalyst. *Catalysis Today*, 142:320 – 328, 2009.

[158] W. R. Flavell, A. G. Thomas, J. Hollingworth, S. Warren, S. C. Grice, P. M. Dunwoody, C. E. J. Mitchell, P. G. D. Marr, D. Teehan, S. Downes, E. A. Seddon, V. R. Dhanak, K. Asai, Y. Koboyashi, and N. Yamada. Electronic structure and surface reactivity of La1-SrCoO3. *Faraday Discuss.*, 114:407–420, 1999.

[159] K. Reuter and M. Scheffler. Composition, Structure, and Stability of RuO_2 (110) as a Function of Oxygen Pressure. *Phys. Rev. B*, 65:035406, 2001.

[160] T. Rocha, A. Oestereich, D. V. Demidov, M. Hävecker, S. Zafeiratos, G. Weinberg, V. Bukhtiyarov, K.-G. A., and R. Schlögl. The Silver-Oxygen System in Catalysis: New Insights by Near Ambient Pressure X-Ray Photoelectron Spectroscopy. *Phys. Chem. Chem. Phys.*, 14:4554–4564, 2012.

[161] X. Rozanska, R. Fortrie, and J. Sauer. Oxidative dehydrogenation of propane by monomeric vanadium oxide sites on silica support. *J. Phys. Chem. C*, 111(16):6041–6050, 2007.

[162] O. V. Safonova, B. Deniau, and J.-M. M. Millet. Mechanism of the Oxidation-Reduction of the MoVSbNbO Catalyst: In Operando X-ray Absorption Spectroscopy and Electrical Conductivity Measurements. *J. Phys. Chem. B*, 110:23962–23967, 2006.

[163] M. Salmeron and R. Schlögl. Ambient pressure photoelectron spectroscopy: A new tool for surface science and nanotechnology. *Surf. Sci. Rep.*, 63(4):169 – 199, 2008.

[164] C. Sanchez, M. Henry, J. C. Grenet, and J. Livage. Free and bound polarons in vanadium pentoxide. *J. Phys. C Solid State Phys.*, 15:7133, 1982.

[165] M. Sanchez Sanchez, F. Girgsdies, M. Jastak, P. Kube, R. Schlögl, and A. Trunschke. Aiding the Self-Assembly of Supramolecular Polyoxometalates under Hydrothermal Conditions To Give Precursors of Complex Functional Oxides. *Angewandte Chemie International Edition*, 51(29):7194–7197, 2012.

[166] G. A. Sawatzky and D. Post. X-ray photoelectron and Auger spectroscopy study of some vanadium oxides. *Phys. Rev. B*, 20:1546–1555, 1979.

[167] R. Schlögl. Active Sites for Propane Oxidation: Some Generic Considerations. *Top. Catal.*, 54:627–638, 2011.

[168] D. K. Schroder. Surface voltage and surface photovoltage: history, theory and applications. *Meas. Sci. Technol.*, 12(3):R16, 2001.

[169] S. Schroeder, G. Moggridge, R. Ormerod, R. Lambert, and T. Rayment. Conversion Electron Yield Detection as a Probe for In Situ XAFS Catalyst Studies. *Physica B*, 208-209(0):215 – 216, 1995.

[170] G.-M. Schwab. Mischkatalysatoren mit dotiertem Träger. *Angewandte Chemie*, 73(11):399–401, 1961.

[171] N. J. Shevchik and D. A. Fischer. Highpass Photocathode X-Ray Ionization Chamber for Surface EXAFS. *Rev. Sci. Instrum.*, 50(5):577–581, 1979.

[172] N. R. Shiju, A. J. Rondinone, D. R. Mullins, V. Schwartz, S. H. Overbury, and V. V. Guliants. XANES Study of Hydrothermal Mo-V-Based Mixed Oxide. M1-Phase Catalysts for the (Amm)oxidation of Propane. *Chem. Mater.*, 20(21):6611–6616, 2008.

[173] S. Shin, Y. Tezuka, T. Ishii, and Y. Ueda. Electronic structure of light transition metal compounds studied by photoemission. *Solid State Commun.*, 87(11):1051 – 1054, 1993.

[174] D. A. Shirley. High-Resolution X-Ray Photoemission Spectrum of the Valence Bands of Gold. *Phys. Rev. B*, 5:4709–4714, 1972.

[175] G. Simard, J. Steger, R. Arnott, and L. Siegel. Vanadium oxides as oxidation catalysts. *Ind. Eng. Chem.*, 47:1424–1430, 1955.

[176] J. C. Slater. Microwave Electronics. *Rev. Mod. Phys.*, 18:441–512, 1946.

[177] K. E. Smith and V. E. Henrich. Resonant photoemission in Ti2O3 and V2O3: Hybridization and localization of cation 3d orbitals. *Phys. Rev. B*, 38:9571–9580, 1988.

[178] R. Smoluchowski. Anisotropy of the Electronic Work Wunction of Metals. *Phys. Rev.*, 60(9):661–674, 1941.

[179] J. Stöhr. *NEXAFS Spectroscopy*. Springer Series in Surface Sciences. Springer, 1992.

[180] M. S. Sze and K. K. Ng. *Physics of Semiconductor Devices*, chapter Metal semiconductor contacts. Wiley Interscience, 2007.

[181] S. M. Sze and K. K. Ng. *Physics of Semiconductor Devices*. Wiley, Hoboken, 3 edition, 2007.

[182] J. Taftø and O. L. Krivanek. Site-Specific Valence Determination by Electron Energy-Loss Spectroscopy. *Phys. Rev. Lett.*, 48:560–563, 1982.

[183] S. Tanuma, C. J. Powell, and D. R. Penn. Calculations of electron inelastic mean free paths for 31 materials. *Surf. Interface Anal.*, 11(11):577–589, 1988.

[184] S. Tanuma, C. J. Powell, and D. R. Penn. Calculations of Electron Inelastic Mean Free Paths (imfps) .4. Evaluation of Calculated Imfps and of the Predictive Imfp Formula Tpp-2 For Electron Energies Between 50 and 2000 Ev. *Surf. Interface Anal.*, 20:77–89, 1993.

[185] S. Tanuma, C. J. Powell, and D. R. Penn. Calculations of Electron Inelastic Mean Free Paths .5. Data For 14 Organic-compounds Over the 50-2000 Ev Range. *Surf. Interface Anal.*, 21(3):165–176, 1994.

[186] B. J. Tielsch and J. E. Fulghum. Differential Charging in XPS. Part I: Demonstration of Lateral Charging in a Bulk Insulator Using Imaging XPS. *Surf. Interface Anal.*, 24(1):28–33, 1996.

[187] R. Tokarz-Sobieraj, K. Hermann, M. Witko, A. Blume, G. Mestl, and R. Schlögl. Properties of oxygen sites at the MoO3(1;0;0) surface: density functional theory cluster studies and photoemission experiments. *Surf. Sci.*, 489:107 – 125, 2001.

[188] G. Tourillon, E. Dartyge, A. Fontaine, M. Lemonnier, and F. Bartol. Electron Yield X-Ray Absorption Spectroscopy at Atmospheric Pressure. *Phys. Lett. A*, 121(5):251 – 257, 1987.

[189] A. Tuxen, S. Carenco, M. Chintapalli, C.-H. Chuang, C. Escudero, E. Pach, P. Jiang, F. Borondics, B. Beberwyck, A. P. Alivisatos, G. Thornton, W.-F. Pong, J. Guo, R. Perez, F. Besenbacher, and M. Salmeron. Size-Dependent Dissociation of Carbon Monoxide on Cobalt Nanoparticles. *J. Am. Chem. Soc.*, 135(6):2273–2278, 2013.

[190] W. Ueda, D. Vitry, and T. Katou. Structural organization of catalytic functions in Mo-based oxides for propane selective oxidation. *Catalysis Today*, 96(4):235 – 240, 2004.

[191] R. Ulbricht, E. Hendry, J. Shan, T. F. Heinz, and M. Bonn. Carrier dynamics in semiconductors studied with time-resolved terahertz spectroscopy. *Rev. Mod. Phys.*, 83:543–586, 2011.

[192] Y. P. Varshni. Temperature Dependence of the Energy Gap in Semiconductors. *Physica*, 34:149–154, 1967.

[193] E. M. Vass, M. Hävecker, S. Zafeiratos, D. Teschner, A. Knop-Gericke, and R. Schlögl. The Role of Carbon Species in Heterogeneous Catalytic Processes: An In Situ Soft X-Ray Photoelectron Spectroscopy Study. *J. Phys.: Condens. Matter*, 20(18):184016, 2008.

[194] D. Vitry, J.-L. Dubois, and W. Ueda. Strategy in achieving propane selective oxidation over multi-functional Mo-based oxide catalysts. *J. Mol. Catal. A*, 220(1):67 – 76, 2004.

[195] F. F. Volkenshtein. *The Electronic Theory of Catalysis on Semiconductors*. Pergamon Press, 1963.

[196] J. C. Volta. Vanadium phosphorus oxides, a reference catalyst for mild oxidation of light alkanes: a review. *Comptes Rendus De L Academie Des Sciences Serie Ii Fascicule C-chimie*, 3:717–723, 2000.

[197] I. E. Wachs and K. Routray. Catalysis Science of Bulk Mixed Oxides. *ACS Catal.*, 2:1235–1246, 2012.

[198] C. Wang, L. Yin, L. Zhang, D. Xiang, and R. Gao. Metal Oxide Gas Sensors: Sensitivity and Influencing Factors. *Sensors*, 10:2088–2106, 2010.

[199] Q.-H. Wu, A. Thissen, W. Jaegermann, and M. Liu. Photoelectron spectroscopy study of oxygen vacancy on vanadium oxides surface. *Appl. Surf. Sci.*, 236:473 – 478, 2004.

[200] J. Yeh and I. Lindau. Atomic Subshell Photoionization Cross Sections and Asymmetry Parameters: $1 \leq Z \leq 103$. *Atomic Data and Nuclear Data Tables*, 32(1):1 – 155, 1985.

[201] L. Yuan, V. V. Guliants, M. A. Banares, and S. J. Khatib. TIC-09-Mesoporous Niobium-Based Mixed Metal Oxides Containing Mo, V, and Te for Propane Oxidative Dehydrogenation. *Top. Catal.*, 49(3-4):268–280, 2008.

[202] D. Zemlyanov, B. Aszalos-Kiss, E. Kleimenov, D. Teschner, S. Zafeiratos, M. Hävecker, A. Knop-Gericke, R. Schlögl, H. Gabasch, W. Unterberger, K. Hayek, and B. Klötzer. In Situ XPS Study of Pd(1 1 1) Oxidation. Part 1: 2D Oxide Formation in 10^{-3} mbar O2. *Surf. Sci.*, 600:983–994, 2006.

[203] S. Zheng, S. Hayakawa, and Y. Gohshi. An Experimental Comparison of the Total-Electron-Yield and Conversion-Electron-Yield Modes for Near-Surface Characterization Using X-Ray Excitation. *J. Electron Spectrosc. Relat. Phenom.*, 87(1):81–89, 1997.

[204] R. Zimmermann, R. Claessen, F. Reinert, P. Steiner, and S. Hufner. Strong Hybridization in Vanadium Oxides: Evidence from Photoemission and Absorption Spectroscopy. *J. Phys.: Condens. Matter*, 10(25):5697–5716, 1998.

6 Appendix

List of Publications included in the Thesis

Christian Heine, Frank Girgsdies, Annette Trunschke, Robert Schlögl and Maik Eichelbaum; *The model oxidation catalyst α-V_2O_5: Insights from contactless in situ microwave permittivity and conductivity measurements*; Applied Physics A (Springer-Verlag Berlin Heidelberg 2013); 112; 289 - 296, August 2013; doi: 10.1007/ s00339-013-7800-6

Christian Heine, Michael Hävecker, Maricruz Sanchez-Sanchez, Annette Trunschke, Robert Schlögl and Maik Eichelbaum;*Work Function, Band Bending and Microwave Conductivity Studies on the Selective Alkane Oxidation Catalyst MoVTeNb Oxide (Orthorhombic M1 Phase) under Operation Conditions*; Journal of Physical Chemistry C(American Chemical Society) 117; 26988 - 26997; December 2013; doi: 10.1021/jp409601h

Christian Heine, Michael Hävecker, Eugen Stotz, Frank Rosowski, Axel Knop-Gericke, Annette Trunschke, Maik Eichelbaum and Robert Schlögl; *Ambient-Pressure Soft X-Ray Absorption Spectroscopy of a Catalyst Surface in Action: Closing the Pressure Gap in the Selective n-Butane Oxidation over Vanadyl Pyrophosphate*; Journal of Physical Chemistry C(American Chemical Society) 118; 20405 - 20412; August 2014; doi:0.1021 /jp506068x